Development and application of microanalysis systems in the environmental monitoring

Ting Wu

THESE DE DOCTORAT
DE L'ECOLE NORMALE SUPERIEURE DE CACHAN

Présentée par

Ting WU

pour obtenir le grade de

DOCTEUR DE L'ECOLE NORMALE SUPERIEURE DE CACHAN

Domaine :
SCIENCES PHYSIQUES et CHIMIQUES

Sujet de la thèse :

DEVELOPPEMENT ET APPLICATION DES SYSTEMES MICROANALYTIQUES DANS LE DOMAINE DE L'ENVIRONNEMENT

Thèse présentée et soutenue à Cachan le 17 juillet 2009 devant le jury composé de :

Yong CHEN	Professeur-ENS Paris	Rapporteur
Valérie PICHON	Maître de conférence -ESPCI	Rapporteur
Pingang HE	Professeur-ECNU	Examinateur
Bruno LE PIOUFLE	Professeur-ENS Cachan	Examinateur
Jacques DELAIRE	Professeur-ENS Cachan	Directeur de thèse
Isabelle LERAY	Chargée de Recherches-CNRS	Co-Directrice de thèse
Jiannong YE	Professeur-ECNU	Directeur de thèse

Laboratoire de Photophysique et Photochimie Supramoléculaires et Macromoléculaires
(ENS CACHAN/CNRS/UMR 8531)
61, avenue du Président Wilson, 94235 CACHAN CEDEX (France)

Acknowledgements

I would begin to thank my two supervisors. Words are simply not enough for expressing gratitude towards them. I would not have completed the PhD without the encouragement and sound advice of my two advisors, Prof. Jacques DELAIRE of Ecole Normale Supérieure de Cachan in France and Prof. Jiannong YE of East China Normal University in China. First, I would like to thank Prof. DELAIRE for accepting me in his team for my PhD study. I would like to thank him for everything that I have learned from him from research to life in general during my three years in France. He has given a lot of freedom and very insightful advice during the course of this work. I would like to thank Prof. YE for his continuous support, encouragement and guide during six years since my master studies. His wisdom, knowledge, commitment to the highest levels inspired and motivated me. This dissertation would not have been possible without their sincere dedications and their willingness to share their knowledge, motivations, and ideas.

I am also very grateful to my thesis committee members, for their valuable comments and suggestions on my thesis. I would like to thank Prof. Yong CHEN, Dr. Valérie PICHON, Prof. Bruno LE PIOUFLE and Prof. Pingang HE for being members of my committee and discussing my research time and again.

I would also like to express my gratitude to my thesis co-director Dr. Isabelle LERAY for her support during my thesis. She encouraged me to go ahead and helped me through all the stages of this work. I would like to thank Mr. Jean-Pierre LEFEVRE for his invaluable contribution during my PhD study. His knowledge about optics and microfluidics helped me a lot from fabrication of microchips to manipulation of microfluidics. His sense of humor made my working time easier. I would like to thank Dr. Valérie GENOT for giving me good suggestions and being always hospitable. You made me a feeling at home. I would like to thank Prof. Joseph ZYSS, Prof. Isabelle LEDOUX, Dr. Mélanie Lebental of LPQM for their helpful advices. I would like to thank Arnaud BROSSEAU for helping me for the AFM, SEM and FTIR measurements, and also for telling me more French culture. I would like to thank Prof. Pierre AUDEBERT and Dr. Fabien Miomandre for their fruitful advices for ASV measurements. I would like to thank Mr. Nguyen Chi Thanh for ellipsometric measurements and some very good advices in thin film research. I would

like to thank Mr. Patrick BOUTIN of CNAM (Conservatoire National des Arts et Métiers) for AAS measurements. I would like to thank Joseph LAUTRU for helping us fabricating our microfluidics mold and giving us advice about making devices. I would like to thank Prof. Jean-Michel El Hage Chahine, Dr. Thanh Ha-Duong and Alexandre of Université Paris Diderot for the discussion and manipulation about stopped-flow. I would like to thank Djibril, Sergey, Nadia as well for their help during the manipulation of microcavity laser.

My three years in such a welcoming lab will be memorable. I would like to acknowledge Prof. Joanne XIE, Prof. Keitaro Nakatani, Prof. Robert Pansu, who helped me during my whole stay here. I would ackowledge the extremely helpful Arnaud Spangenberg for the uncountable list of small favors and helpful answers he provided, and also for as so kind guide in Amsterdam. Thanks Rémi Métivier for his patient academic explanation. The time I shared the office with two Arnaud and Rémi in my first year in France made my life easy and colorful. I would like to thank Serge for sharing his knowledge in microfluidics. I would like to thank Jacky for his always kindness and help for many computer problems. Also, I would like to thank Andrée and Christian for their administrative responses and availability. I would like to thank other membres of PPSM, Aurélie, Thomas, Elena, Stephane, Laurent et al. People here are genuinely nice and I'm glad to have contacted with many. If I have forgotten anyone, I apologize.

This note would be incomplete if I do not mention my thanks to the collaboration program between ENS CACHAN and ECNU which favored me to complete this thesis. I would like to thank Ms. Bogdana Neuville, Ms. Christine ROSE, Ms. Brigitte Vidal of ENS CACHAN, for their help with all the official procedures in France. I would like to thank Mr. Wenhui YOU, Mrs. Yunhua QIAN, Mr. Haisheng LI of ECNU for all the administrative help. Also, I would like to thank all the colleagues in ECNU.

I extend my thanks to all my friends at ENS-CACHAN for their support and friendship. I extend my thanks to my lifetime friends including Hua REN, Xiaoju NI, Yaxin PENG, Zhiping LU, Na LI, Li LIN, Yingying CHEN, Hua YI, Chun LI, Xiaopeng HE, Yanchun GONG, Guanghua YANG, Jianxiao YANG, Zhongwei TANG, Sanjun ZHANG, Jing ZHANG, Chunyuan ZHOU and Tong WU et al, for their friendship and support over the years. Life would have been dull without you!

Lastly, but most certainly not least, I must thank my family. I would like to thank my parents for their support and encouragement in everything that I pursued. Everything I have accomplished is entirely due to the love and support of my parents, for their unconditional love and sacrifice. I would like to express my deep gratitude to my aunt and my uncle-in-law for their endless support and encouragement.

Contents

ABBREVIATIONS

AAS	Atomic absorption spectrometry
AFM	Atomic force microscopy
APS	3-aminopropyl functionalized silica gel
ASE	Amplified spontaneous emission
ASV	Anodic stripping voltammetry
β_n	Formation equilibrium constant
BCPs	Block copolymers
BP	4-tert-butylphenol
BPA	Bisphenol A
CE	Capillary electrophoresis
CMC	Critical micelle concentration
CZE	Capillary zone electrophoresis
DCM	[2-[2-[4-(dimethylamino)phenyl]ethenyl]-6-methyl-4H- pyran -4-ylidene]-propanedinitrile
Da	Daköhler number
DCP	2,4-dichlorophenol
EC	Electrochemical
EDC	Endocrine disrupting chemical
EE2	17α-ethynylestradiol
EOF	Electroosmotic flow
FAAS	Flame atomic absorption spectrometry
HPLC	High pressure liquid chromatography
GC-MS	Gas chromatography-mass spectrometry
K	Equilibrium constant
K_{sp}	Solubility product constant

λ	Wavelength
LED	Light emitting diode
LIF	Laser-induced fluorescence
LOC	Lab on a chip
μTAS	Micro-total-analysis-system
MEKC	Micellar electrokinetic chromatography
MEMS	Micro-electro-mechanical-systems
NMR	Nuclear magnetic resonance
NP	4-n-nonylphenol
P	Peclet number
PDMS	Polydimethylsiloxane
PMMA	Polymethylmetacrylate
PMT	Photo-multiplier tube
PS	Polystyrene
P(4-VP)	Poly(4-vinyl pyridine)
P(2-VP)	Poly(2-vinyl pyridine)
PMMA-b-PHEMA	Poly(methylmethacrylate)-b-Poly(2-hydroxyethyl methacrylate)
R_e	Reynolds number
RIE	Reactive ion etching
SAM	Self-assembled monolayer
SEM	Scanning electron microscope
SDS	Sodium dodecyl sulfate
SHM	Staggered herringbone mixer
SPA	solid phase extraction
STD	Standard Deviation
THF	Tetrahydrofuran
UV	Ultra-violet
WHO	World Health Organization
WGM	Whispering gallery mode

Abstract

This study describes the development and application of three microanalysis systems. The application domain is concentrated on environmental contaminations, mainly heavy metal ions in surface water and endocrine disrupting chemicals in sewage.

A microfabricated device has been developed for the selective detection of lead in water. It is based on the use of a selective and sensitive fluorescent molecular sensor (Calix-DANS4) for lead which contains a calix[4]arene bearing four dansyl groups. The principle of this sensor is photoinduced charge transfer (PCT) which can cause a slight blue shift of both the absorption and fluorescence spectra in acidic condition after binding with lead ion. The microchip-based lead sensor is a Y-shape microchannel structured with a passive mixer and stuck on a glass substrate. The detection is performed by using a configuration in which the sensing molecules are excited by two optical fibres, each connected to a 365 nm UV LED, and the emitted light is collected by another optical fibre coupled with a photomultiplier. A detection limit of 2.5×10^{-8} mol L^{-1} (i.e. 5.2 μg L^{-1}) could be reached, which is lower than the maximum level of lead allowed in drinking water after 2013, according to European regulation.

In order to improve the sensitivity of the previous microfluidic device and to get rid of interfering calcium ion, we developped a solid phase extraction preconcentration (SPE) stage with a micro-column filled with silica beads functionalized with aminopropyl groups (APS). During SPE, the APS groups selectively adsorb the lead ions at basic pH (pH = 10) which allows its separation from others (Ca^{2+}, Na^{+}). In acidic medium (pH = 2), lead is reversibly released and can be recovered in a 100 times more concentrated. The combination of SPE and previous fluorimetric microfluidic device was carried out for lead solutions of known concentrations in tap water. The results were proved by Atomic Absorption Spectroscopy.

The study of the mechanism of the complexation between fluorescence molecular sensor (Calix-DANS4) and lead ion allows us to optimize the chip where the complexation occurs. The large difference between the calibration curves obtained for reactants mixed inside the chip and for injection of a premixed solution shows that the complexation is not finished at the end of the microchannel. A new microchip with a longer channel has permitted to approach the equilibrium state. Conventional stopped-flow method was also applied

here to determine the real reaction kinetics and rate constants. The results show that this complexation at pH 3.2 is a relatively slow reaction, which takes several minutes for weak Pb^{2+} concentrations. It proves that the complexation in our microfluidic chips has not yet finished, as the transit times in all these microfluidic chips are less than 40 s.

Another microanalysis system for metal ion sensing is an optofluidic sensor which combines optical elements (such as waveguide, laser...) and microfluidics for biological and chemical assays. A preliminary study of polymer microcavity laser for metal ions sensor in microfluidic channel is introduced in this thesis. The search of the microcavity laser materials is focused on diblock copolymers, especially two diblock copolymers (PS-b-P2VP, PS-b-P4VP), which can form microphase separation to load laser dye (e.g. DCM) in the hydrophobic phase and metal ion in the hydrophilic phase. The morphologies and refractive index of their cast films are studied before fabricating the microcavity laser. Their responses to different environments (e.g. water, metal ion solutions...) are characterized by AFM and ellipsometry. The results show that PS-b-P4VP can exhibit remarkable changes both of morphology and refractive index when contacting with zinc ion solution, while zinc ion has no effect on PS-b-P2VP. The first optofluidic sensor is fabricated with a microcavity laser which is made of PS-b-P4VP doped with a laser dye (DCM) and placed in a PDMS microfluidic channel. Its laser spectral shifts in presence of pure water and zinc ion are both observed.

Endocrine Disrupting Chemicals (EDCs) are anthropogenic substances that can interfere with the endocrine systems of living organisms. Their harmful effects on human health, when they reach a certain amount, have been discovered and are still being studied precisely. An integrated analytical method to monitor five environmental endocrine disrupting chemicals (EDCs): 2,4-dichlorophenol (DCP), 4-tert-butylphenol (BP), bisphenol A (BPA), 17 α-ethynylestradiol (EE2) and 4-n-nonylphenol (NP), is developed for the first time. This third microanalysis system is based on a solid-phase extraction and miniaturized micellar electrokinetic chromatography (MEKC) with amperometric detection (AD). In order to get the optimum conditions of their separation and detection, several parameters including pH and concentration of running buffer, concentration of micelle, separation voltage and injection time are studied and optimized. The five EDCs are well separated under the optimum conditions within 12 min. This method is successfully applied for the determination of these five EDCs in sewage influent sample. Satisfactory extraction performances from sewage sample are obtained by solid-phase extraction (SPE), using a HLB (waters) cartridge. Quantitative analysis shows that DCP, BP and BPA exist at μg L^{-1} level in the selected sample, while EE2 and NP are not detected.

Résumé

Ce travail décrit le développement et l'application de trois micro-systèmes pour l'analyse. Les applications sont dédiées aux contaminations environmentales, principalement les ions des métaux lourds dans l'eau et les perturbateurs endocriniens dans les eaux résiduaires de ménage.

Un premier dispositif microfluidique a été mis au point pour la détection du plomb dans l'eau. Il utilise un senseur fluorescent (Calix-DANS4), sélectif et sensible pour le plomb, composé d'un calix [4] arene portant quatre groupes dansyl. Le principe de ce senseur est basé sur un transfert de charge photoinduit qui peut provoquer un léger déplacement vers le bleu à la fois des spectres d'absorption et de fluorescence en milieu acide après l'ajout des ions plomb. Le circuit microfluidique pour la detection du plomb est constitué d'un microcanal en forme de Y structuré afin d'assurer un mélange passif, moulé dans du PDMS, et collé sur un substrat de verre. Les molécules du senseur fluorescent sont excitées par deux fibres optiques chacune couplée à une LED UV à 365 nm, et la lumière émise est collectée par un faiseau de fibres optiques couplées à un photomultiplicateur. La limite de détection de 2.5×10^{-8} mol L^{-1} pour la solution entrante peut être ateinte, ce qui est inférieur la teneur maximale en plomb autorisée dans l'eau potable après 2013, selon réglementation européenne.

Afin d'améliorer la sensibilité du précédent dispositif et de se débarrasser des ions calcium, nous avons développé une étape de préconcentration par extraction en phase solide (SPE) à l'aide une micro-colonne remplie de billes de silice fonctionnalisées avec groupes aminopropyl (APS). Au cours de l'extraction en phase solide (SPE), les groupes APS retiennent sélectivement les ions plomb en milieu basique (pH=10). En milieu acide (pH=2), le plomb est libéré de manière reversible permettant de le séparer des autres ions majoritaires (Ca^{2+}, Na^{+}) et de le concentrer jusqu'à 100 fois. La combinaison de la SPE et du dispositif microfluidique a permis l'analyse de solutions de plomb de concentrations connues dans l'eau du robinet. Les résultats ont été confirmés par Spectroscopie d'Absorption Atomique.

L'étude du mécanisme de la complexation entre le senseur fluorescent (Calix-DANS4) et les ions plomb a permis d'optimiser le circuit microfluidique où a lieu cette complexation. En effet, la grande différence entre les courbes d'étalonnage obtenues après mélange des réactifs au sein du dispositif ou après injection d'un mélange montre que la complexation

n'est pas terminée à la sortie du microcanal. Un circuit fluidique avec un canal plus long a permis d'approcher l'état d'équilibre dans la zone de détection. La méthode "stopped-flow" conventionnelle a été appliquée pour déterminer les constantes de vitesse des réactions. Les résultats montrent que cette complexation à pH 3,2 est une réaction relativement lente, et qui prend plusieurs minutes pour de faible concentrations en Pb^{2+}. Le circuit fluidique plus long avec un temps transit de 40 secondes permet d'atteindre l'équilibre.

Un deuxième dispositif de détection des ions métalliques est envisagé: il s'agit d'un senseur optofluidique qui combine des éléments optiques (tels que les ondes, laser ...) et des éléments microfluidiques pour les dosages biologiques et chimiques. Une étude préliminaire de microcavité laser à base de polymère pour la détection des ions métalliques dans les canaux microfluidiques est présentée dans cette thèse. La recherche des matériaux pour la microcavité laser s'est focalisée sur des copolymères biblocs, en particulier deux biblocs (PS-b-P2VP, PS-b-P4VP), qui peuvent contenir un colorant laser (par exemple, DCM) dans la phase hydrophobe et piéger des ions métalliques dans la phase hydrophile, après séparation de microphases. La morphologie et l'indice de réfraction de films minces sont étudiées avant de fabriquer la microcavité laser. Leurs réponses à des environnements différents (par exemple l'eau, des solutions des ions métalliques ...) sont caractérisées par AFM et ellipsometrie. Les résultats ont montré que le PS-b-P4VP peut présenter à la fois de remarquables changements de morphologie et d'indice de réfraction lors du contact avec des solutions riches en ions zinc. Par contre les ions de zinc n'ont pas d'effets sur PS-b-P2VP. Un premier capteur optofluidique a été fabriqué avec un microcavité laser constituée de PS-b-P4VP dopé avec un colorant laser (DCM) et implantée dans un canal microfluidique. Les déplacements du spectre d'émission laser en présence d'eau et d'ions zinc sont observés.

Une méthode d'analyse intégrée pour la détection de cinq perturbateurs endocriniens existant dans les produits chimiques environnementaux: 2,4-Dichlorophénol (DCP), 4-tert-butylphénol (BP), bisphénol A (BPA), 17α- ethynylestradiol (EE2) et 4-n-nonylphénol (NP), est développée pour la première fois. Ce troisième système de microanalyse est basée sur une extraction en phase solide suivie d'une chromatographie capillaire électrocinétique micellaire (MEKC) miniaturisée avec détection ampérométrique (AD). Pour obtenir les conditions optimales de séparation et de détection, plusieurs paramètres dont le pH, la concentration de la solution tampon circulante, la concentration micellaire, la tension de séparation et le temps d'injection sont étudiés et optimisés. En 12 minutes, les cinq EDCs sont bien séparés dans les conditions optimales. Cette méthode est appliquée avec succès pour la détection de ces cinq EDCs dans des échantillons d'eaux usées. Les performances satisfaisantes de l'extraction en phase solide (SPE) à partir d'eaux usées sont obtenues, en utilisant une cartouche HLB (waters). L'analyse quantitative montre que les DCP, BP et BPA existent dans les échantillons à hauteur du μg L^{-1}, tandis que EE2 et NP n'ont pas été détectés.

摘要

本论文主要介绍了三种微分析系统的开发及对环境污染物的检测研究，包括地表水中重金属离子的检测和生活污水处理厂水体中环境雌激素的检测。

首先，我们研究了一种对铅离子进行选择性检测的流动注射微流控分析体系。其检测原理是基于一种荧光分子传感器（Calix-DANS4）对铅离子的高灵敏度和高选择性的响应。该荧光离子团是一种带有四个DANS1基团的杯芳烃。该铅离子检测微流控芯片由含有被动混合器的Y-型微通道和玻璃粘合而成。检测腔体的引入极大的提高了检测的灵敏度，检测时由光纤传导的两个365 nm 紫外发光二极管对腔体中荧光分子同时激发，然后另一光纤组在和激发光垂直的角度进行荧光采集，并与光电倍增管耦合放大进行检测。在pH 3.2, 乙腈/水=60/40，荧光分子浓度为1×10^{-6}摩尔/升时，该体系对铅离子的检测限可以达到2.5×10^{-8}摩尔/升，这已经低于世界卫生组织目前饮用水中铅离子含量指导标准中的最大值以及2013年的饮用水的欧洲标准。

为了改善我们的流动注射微流控分析体系的灵敏度和选择性，以及消除其共存离子钙离子的干扰，我们在微流控分析前加入了固相萃取富集前处理过程。萃取柱是自制的填充了功能化3-氨基丙烷硅胶的Teflon微柱。在进行微柱固相萃取时，功能化硅胶在碱性条件下（pH=10）选择性吸附痕量铅离子，从而能与其他的干扰离子分离，特别是水中大量存在的钙离子和钠离子。在酸性条件下，铅离子能被可逆地从微柱上洗脱下来，富集倍数可达100倍。固相萃取前处理过程和荧光法微流控装置相结合，已被成功地用于自来水中铅离子的检测。该检测结果已用常规用于检测痕量铅离子的原子吸收光谱法进行了证明。

在进行微流控体系分析检测时，我们发现体系外混合体系内检测和体系内由被动混合器混合再检测得到的滴定曲线存在很大的差异，初步表明该反应在我们的微流控体系中存在某些不完整性。利用一个快速反应模型在微流控体系中体系外混合和体系内混合的对比研究，我们证明了反应物在我们微流控分析体系中已经完全混合。为了更好地理解所研究荧光离子团和铅离子之间的络合作用，我们通过将微流控分析手段，停流方法(stopped-flow) 和计算机模拟相结合的方法从理论和实验的角度同时研究该络合反应的机理和反应动力学，并分析和验证了已有实验结果的合理性。首先，我们进一步改善了我们的微流控分析体系的操作参数，如降低流速以增加传输时间，从而延长反应时间，这明显地缩小了和体系外混合得到的滴定曲线的差距。另外，通过改变微流控体系的几何构型，如延长的微通道，同样为了延长反

应时间，两曲线已经接近重合，实验证明了该反应是个慢反应，在我们的微流控通道内，该络合反应尚未结束。然后，通过驰豫时间的分析方法，我们得到对于1:1络合反应，当荧光分子浓度远大于金属离子浓度时，铅离子浓度和驰豫时间的倒数成线性关系。

$$\frac{1}{\tau} = k_1[M] + k_{-1}$$

我们用停流方法研究了在该反应条件下的反应速率，实验数据也证明在铅离子浓度大于等于十倍荧光分子浓度时，该线性关系成立，并由此得到络合反应的结合常数(k_1)。我们通过用软件SPECFIT对荧光光谱的分析和拟合得到了该反应的平衡常数，从来计算得到其解离常数(k_{-1})。最后，我们用另一软件Chemical kinetics simulator对该反应进行计算机模拟，得到了对应于我们的微流控体系条件的理论曲线，和我们的实验曲线基本相符。

本论文中所研究的另一金属离子检测器是基于微腔激光的光流体传感器。该传感器的原理主要是微腔激光材料对金属离子的选择性吸附导致其折射率的改变，从来引起微腔激光光谱的移动。本论文的工作主要是对该微腔激光材料的研究。我们主要研究了嵌段共聚物，因为其微相分离的特殊性，疏水段可以容纳激光染料，而亲水段在水中溶胀后可以容纳金属离子，从而具有发激光和离子传感的双重性能。我们主要研究了两种嵌段共聚物(PS-b-P2VP, PS-b-P4VP)，PS能容纳染料分子(DCM), P2VP和P4VP 与金属离子间可能有相互作用。借助于原子力显微镜(AFM)，我们研究了两种聚合物薄膜的表面形态，以及经过水处理和金属离子处理后的形态变化。借助于椭偏仪(ellipsometry)，我们研究了两种聚合物薄膜的折射率，以及经过水处理和金属离子处理后的折射率变化。表面形态和折射率变化表明，PS-b-P4VP对锌离子有特殊的响应。该聚合物进一步用于制作微腔激光以及光流体，并在光流体中测试该微腔激光通过水和锌离子溶液后的光谱移动。初期的实验结果表明，锌离子能引起光谱移动，但真正的原因还需进一步证明和探索。

本论文中研究的最后一种微分析方法是关于微型毛细管电泳安培检测对污水厂中环境雌激素的检测研究。该小型化的毛细管电泳安培检测与固相萃取前处理相结合的方法首次成功地对五种环境雌激素：2,4-dichlorophenol (DCP), 4-tert-butylphenol (BP), bisphenol A (BPA), 17 α-ethynylestradiol (EE2) 和4-n-nonylphenol (NP)进行了分离和检测。毛细管电泳的分离模式采用的是胶束电动色谱(MEKC)，有效地改善了分离效果。为了改善灵敏度，在分析前采用了固相萃取将被分析物进行富集。我们对分离检测的条件（如缓冲液的pH值和浓度，胶束的浓度，分离电压，进样时间）进行了优化，在最优条件下，该五种分析物在12分钟内有效地得到分离和检测。该方法成功地用于污水厂中的该五种环境雌激素的检测。

Part I

General Introduction

Foreword

0.1 Motivation and objective

Environmental contamination by heavy metals is a worldwide problem. Heavy metals can be extremely toxic as they damage nerves, liver, kidney and bones, and also block functional groups of vital enzymes. The possible harmful effects of increasing levels of environmental heavy metals pollution on human health and the environment have been much accounted. So the detection of the trace content of these hazardous metals (e.g. lead, mercury, cadmium) in the environment becomes a major problem.

Endocrine disrupting chemicals (EDCs) are defined as substances that disturb the hormonal balance and can thus have deleterious effects in humans or animals, or their offspring. Most recently, the question has been intensively discussed as to what level of EDCs can interfere with the endocrine homeostasis of humans and animals, and what effects on individuals or populations may result. Until now, there is no regulation for the content of EDCs in the environment. But this domain is being worked on by the scientists all over the world, such as EPA in United States, and BKH Consulting Engineers in European Union.

Therefore, to develop sensitive, effective, and inexpensive methods which can efficiently monitor and determine the presence and amount of hazardous metals and endocrine disrupting chemicals in the environment is crucial. The emergency of lab-on-a-chip methods provides one solution to this need. The concept of μTAS (Miniaturized Total (chemical) Analysis System) was firstly suggested by Manz and Widmer in 1990, and it was typically a microchip or micro-device which can improve the performance of an analysis by reducing size. The miniaturisation of chemical analysis systems yields many functional and economical benefits. Recent advances in fabrication technology and growing demand for accurate, efficient, fast, automated analytical systems have provided a unique opportunity for a variety of applications of μTAS ranging from biological analysis to environmental monitoring.

This thesis is concerned with the issue of environmental pollution, particularly those of heavy metal ions and endocrine disrupting chemicals in the environment. Our objective is to develop effective microanalysis devices for the determination of heavy metal ions and endocrine disrupting chemicals in the environment.

0.2 Thesis Overview

This thesis presents the design and application of three miniaturized analysis systems for environmental monitoring:

- Fluorimetric microfluidic device;
- Optofluidic chemical sensor;
- Miniaturized capillary electrophoresis.

In this thesis, there are seven chapters and one appendix. References are provided at the end of all seven chapters.

Chapter 1 serves as an introduction of miniaturized analytical systems and as a review on the previous studies about environmental pollutants detection.

Chapter 2 describes a fluorimetric microfluidic device for lead ion detection. A fluoroionophore (Calix-DANS4) was used as a detection ligand to complex lead ion in a selective way. A calibration curve of fluorescence intensity versus lead ion concentration is plotted for lead ion detection.

Chapter 3 is an extensive research of lead ion detection in a fluorimetric microfluidic device. A home-made solid phase extraction (SPE) mini-column is applied to preconcentrate and purify trace lead ion. The detection of lead ion in real tap water is achieved with the combination of fluorometric microfluidic device and SPE.

In chapter 4, the chemical kinetics of the complexation between lead ion and fluoroionophore (Calix-DANS4) is studied. Stopped-flow method and theory modeling are used to better understand the reaction kinetics. Computational simulation is used to validate the previous results obtained in micro-devices.

In chapter 5, the design of an optofluidic device based on microcavity laser is presented. The research about the material for microcavity laser is the main point of this part in which diblock copolymers are chosen. Several characteristic methods such as AFM, ellipsometry, UV-Vis are applied for their morphology and optical quality studies. A preliminary performance of optofluidic sensor for metal ion is displayed.

Chapter 6 describes another microanalysis system - miniaturized capillary electrophoresis. The separation and detection of five endocrine disrupting chemicals are achieved with this system.

Chapter 7 concludes the thesis with a brief conclusion and some suggestions for future research.

Part II

Microfluidic devices for lead ion sensing

Chapter 1

Lab-on-a-chip: principles and methods

1.1 Microfluidics and lab-on-a-chip devices

Miniaturization and MEMS (Micro-Electro-Mechanical-Systems) gave birth to microfluidics in the 1990s and today still constitute a large portion of this young discipline. Microfluidics can be defined as the study of flows that are simple or complex, mono- or multiphasic, which are circulating in artificial microsystems, i.e. systems that are fabricated using new technologies [1, 2]. The term microfluidics is used here not to link the fluid mechanics to any particular length scale, such as the micron, but rather to refer in general to situations in which small size scale causes changes in fluid behavior, some of which are beneficial. The main advantage of microfluidics is the use of scaling laws for new effects and better performance.

Microfluidics can have a revolutionizing impact on chemical analysis and synthesis, similar to the impact of integrated circuits on computers and electronics. Making analysis instruments, tailored drugs, and disposable drug dispensers available for everyone will secure a huge market similar to that of computers today.

The rapid expansion of the field of microfluidics seems to be driven in part by the possibility of integration. The domain of integrated analysis systems has been designated as μTAS (micro-total analysis systems), or also 'lab-on-a-chip' (LOC) systems. The area of μTAS has expanded rapidly in recent years. In its simplest sense, μTAS involves the miniaturisation of all functions found in chemical analysis, including sampling, removal of matrix interference, pumps, valves, and mixing and reaction chambers. μTAS not only enables a size reduction of the analytical system, but also improves its performance. One of the most exciting prospects of the μTAS concept is the suggestion that the entire chemical measurement laboratory could be miniaturized onto a device of a few square centimeters. Its portability, rapid assay times, and smaller sample requirements are encouraging the microanalysis industry, while conventional laboratory analysis is time consuming, tedious,

and requires expensive equipment and highly trained personnel. There have been some remarkable progresses in this domain and some lab-on-a-chip devices accomplishing a small number of functions have already been commercialized. Table 1.1 lists some companies who distribute different microfluidic products. Nevertheless, various challenges still remain to be faced to succeed in this field.

1.2 History and present of microfluidics

Microfluidics is an emerging technology. It is an exciting field in which to work, with simultaneous advances being made on many fronts.

Embryo: In the late 1970s, silicon technology was extended to machining mechanical microdevices [3] which later came to be known as microelectromechanical systems (MEMS).

Early stage: In the late 1980s the development of silicon microflow sensors, micropumps, and microvalves were developed and investigated. They dominated the early stage of microfluidics. The field has been seriously and rapidly developed since the introduction by Manz et al. at the 5th International Conference on Solid-State Sensors and Actuators (Transducers '89), which indicated that life sciences and chemistry are the main application fields of microfluidics [4]. This can be considered as a milestone of microfluidics. At that time, a number of microfluidic devices with integrated sensors and actuators were made in silicon. Microfluidics was a part of MEMS technology, which in turn used the established technologies and infrastructure of silicon microelectronics.

Development: In the mid 1990s, development has been shifted to the exploration of new actuating schemes for microfluidics, because of the limit of power in microscopic scale. Electrokinetic pumping, surface tension-driven flows, electromagnetic forces, and acoustic streaming are effects that usually have no impact at macroscopic length scales, but offer particular advantages over mechanical principles at the microscale. Meanwhile, microfabrication technology has developed and has been moving to plastic micromachining. Batch fabrication of plastic devices is possible with many replications and forming techniques. The master (stamp or mold) for replication can be fabricated with traditional silicon-based micromachining technologies.

Growing: From late 1990s to today, the application of microfluidics has extended in many fields, such as flow control, chemical analysis, biomedical diagnostics, and drug discovery. Constant innovation in the field of microfluidics and μTAS has enabled LOC technologies to successfully enter the mainstream commercial market.

Today, microfluidics is looking for further application fields beyond conventional ones. An apparent prove of the advancement of microfluidics is that the publication of microfluidics-related papers in international journals and conferences increased exponentially in recent

Table 1.1: Commercial microfluidic products

Company	Products	Location	Foundation year	Website
Microfluidics	Microfluidizer® fluid processors for emulsion, deagglomeration, dispersion and cell disruption	US	1984	www.microfluidicscorp.com
Bartels Mikrotechnik	microEngineering and microComponents (i.e. Bartels micropumps)	Germany	1996	www.bartels-mikrotechnik.de
Micronics	microFlow^{TM} System (the first integrated microfluidics workstation with low-pulse twist syringe pumps), Active lab cards , Access cards	USA	1996	www.micronics.net
Fluigent	Flow control in micro-channels and genetic testing in capillaries and chips	France	2000	www.fluigent.com
Syrris	Africa (a fully automated, flexible and easy-to-use microreactor flow system)	UK and USA	2001	www.syrris.com
Dolomite	Standard products (i.e. micropumps, Connectors, Microfluidic Chips, Membrane Device, Valves) and Custom products	UK	2005	www.dolomite-microfluidics.com
microLIQUID	Standard (Single microfluidic channel or Capillary Electrophoresis chips (CE chips), with or without integrated electrodes) and customized microfluidic products	Spain	2006	www.microliquid.com

years, as illustrated in Figure 1.1.

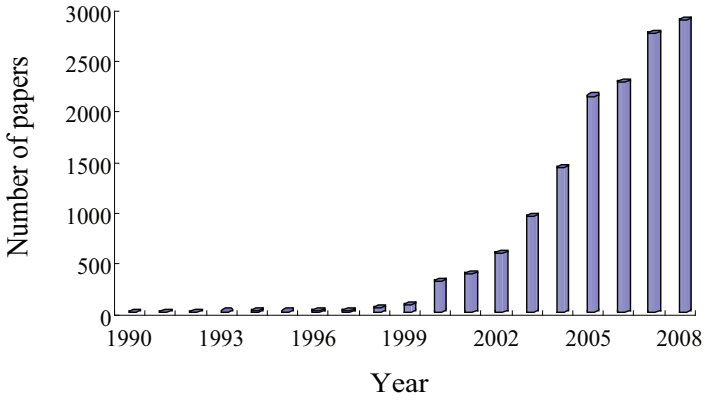

Figure 1.1: Publications of microfluidics-related papers in recent years (Plotted from Web of Science database.)

1.3 Physics at the micrometric scale

Since at the micrometric scales, something out of the ordinary have happened, e.g. capillary forces become dominant, while gravitational forces become negligible in miniaturized systems, several significant situations arise in microsystems where the macroscopic description must be amended, or even simply abandoned. So it is important to rationalize using physical laws in their more detailed form to ensure that the effect of miniaturization is significant within the range of dimensions on the order of ten or a hundred micrometers, which are the scales normally used in microsystems. Two important dimensionless parameters deduced from scaling laws in microfluidic systems are introduced.

- Peclet number, P, is the ratio of axial bulk flow to diffusion mass transport (effectively describing the relative importance of convective or diffusive transport, or change in flow rate). This can be used to judge the competition between the diffusion phenomena and hydrodynamic transport phenomena. In most common cases, convective transport is faster than diffusive transport, even though the length scales are small. In other words, the Peclet number is usually large.

$$P = Ul/D_m, \tag{1.1}$$

In the equation, U is the average axial flow rate, D_m is the molecular diffusivity, and l is the typical cross-sectional dimension of the microchannel. Common values of

these parameters are $U = 0.1 \sim 1$ cm s^{-1}, $l = 10^{-3} \sim 10^{-2}$ cm, and $D_m = 10^{-7} \sim 10^{-5}$ cm^2 s^{-1}. Therefore, $10 < P < 10^5$.

- Reynolds number, Re, represents the ratio of inertial forces to viscous forces. It characterizes the fluid flow as being laminar or turbulent. The Reynolds number is a particularly useful dimensionless parameter.

$$Re = Ul/\nu, \tag{1.2}$$

where U is the average flow rate and ν is the kinematic viscosity of the fluid. Physically, flows of common liquids at practical pressures in microfluidic channels (typical cross-sectional dimension, $l \sim 100$ μm) are characterized by low values of the Reynolds number Re. So the fluid flow is generally laminar. General strategies for controlling flow in microfluidic devices should not depend on inertial effects, because these only become important for $Re \geq 1$. The low Reynolds number "rule" for microfluidic systems applies well for most of the microfluidic systems of practical interest.

1.4 Materials

For the development of MEMS, glass, steel and silicon have been widely used to fabricate microelectronic devices. And some of the earliest work in fluidic microsystems did, in fact, use silicon and glass, but now these materials have largely been displaced by polymers. Particularly, silicon is expensive, and opaque to visible and ultraviolet light, so cannot be used with conventional optical methods of detection.

Use of poly(dimethysiloxane) (PDMS), poly-methyl methacrylate (PMMA), poly- tetrafluoroethylene (PTFE), commonly known as "Teflon", and quartz became common in the recent past [5–7]. But in many regards, much of the exploratory research in microfluidic systems was carried out with a polymer- PDMS (poly(dimethysiloxane)) (see Figure 1.2).

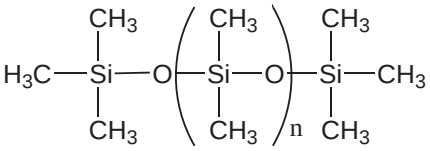

Figure 1.2: Chemical structure of PDMS

PDMS is one of the most actively developed polymers for microfluidics, as it reduces the time, complexity and cost of prototyping and manufacturing [8, 9]. PDMS has very good physical-chemical properties, including (1) high optical quality, transparent above

230 nm; (2) high electrical bulk resistivity; (3) good chemical stability; (4) support for electroosmotic flow (EOF) after plasma oxidation and (5) good adhesion to a variety of clean and flat substrates at low temperatures. PDMS microchannels can be fabricated by soft lithography within 24h and do not require specialized laboratories and equipment. And rapid prototyping of microchannel designs can easily be achieved. Replica moulds with feature sizes of 10 nm can be achieved through the use of suitable masters. The protocols of microfabrication of the mould and the PDMS microchannel are shown in the Appendix.

But whether the microfluidic devices that ultimately become widely used will use PDMS or one of the engineering polymers (such as polycarbonate or polyolefin) remains to be seen.

1.5 Fabrication technologies for microfluidics

In parallel to the development of microfluidic devices, microfabrication techniques have also evolved significantly. Some of the important fabrication techniques include lithography (soft and photolithography), lamination, injection molding, hot embossing, micromachining with laser, and electrochemical or ultrasonic technologies [10–13]. Among them, lithography is used most commonly.

1.5.1 Photolithography

Photolithography powered the advent of Micro Electro Mechanical Systems (MEMS), which are now starting to become more and more diverse in commercial products from mechanical to biomedical devices, helping to change the way people perceive the applicability of IC technology. The approach bottom-up (ascending, from the individual base elements until a complete top-level system) or top-down (descendant, breaking down a system to gain insight into its compositional sub-systems) are the choices to carry out according to the precise motive and usable machinery.

Photolithography is the process of transferring geometric shapes from a photomask to a light-sensitive chemical (photoresist, or simply "resist") on the surface of a silicon or glass, or any other flat surface wafer. A single iteration of photolithography combines several steps in sequence, which include wafer cleaning, barrier layer formation, photoresist application, soft baking, mask alignment, exposure and development, and hard-baking. Modern cleanrooms use automated, robotic wafer track systems to coordinate the process.

In the following, we describe the typical lithographic steps for a silicon wafer. In the first step, the wafers are chemically cleaned to remove particulate matter on the surface as well as any traces of organic, ionic, and metallic impurities. After cleaning, silicon dioxide, which serves as a barrier layer, is deposited on the surface of the wafer. After the formation of the SiO_2 layer, photoresist is applied to the surface of the wafer. High-speed centrifugal

whirling of silicon wafers is the standard method for applying photoresist coatings in IC manufacturing. This technique, known as "Spin Coating", produces a thin uniform layer of photoresist on the wafer surface.

There are two types of photoresists: positive and negative. The principle of the photoresist is as Figure 1.3. One very common negative photoresist is based on epoxy-based polymer whose common product name is SU8 photoresist. It was originally developed as a photoresist for microelectronics industry, to provide a high-resolution mask for fabrication of semiconductor devices. It is now mainly used in the fabrication of microfluidics and MEMS parts. Negative resists were popular in the early history of integrated circuit processing, but positive resist gradually became more widely used since they offer better process controllability for small geometry features.

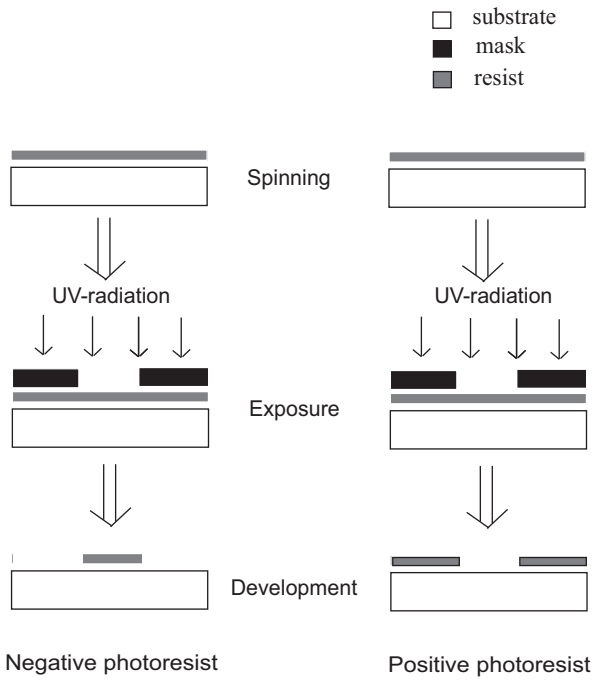

Figure 1.3: Principle of photoresist

Soft-baking is the step during which almost all of the solvents are removed from the photoresist coating. Soft-baking plays a very critical role in photo-imaging. The photoresist coatings become photosensitive, or imageable, only after softbaking.

Mask alignment is one of the most important steps in the photolithography process. A mask or "photomask" is a square glass plate with a patterned emulsion of metal film (e.g. chrome) on one side. The mask is aligned with the wafer, so that the pattern can be transferred onto the wafer surface. Each mask after the first one must be aligned to the previous pattern.

Once the mask has been accurately aligned with the pattern on the wafer's surface, the

photoresist is exposed through the pattern on the mask with a high intensity ultraviolet light. There are three primary exposure methods: contact, proximity, and projection. They are shown in the Figure 1.4.

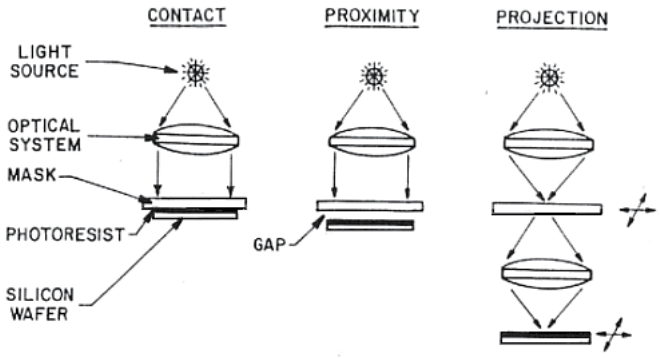

Figure 1.4: Three primary exposure methods

One of the last steps in the photolithographic process is development. A post-exposure bake is performed before developing, typically to help reduce standing wave phenomena caused by the destructive and constructive interference patterns of the incident light. The cross-linked photoresist is developed by immersing in a special developer; immersing time depends on the thickness of photoresist.

Hard-baking is the final step in the photolithographic process. This step is necessary in order to harden the photoresist and improve adhesion of the photoresist to the wafer surface.

Rapid prototyping

Rapid prototyping is a simplified method of photolithography. In this way, a transparency replaces a chrome mask, which can be 20-100 times more expensive and can take weeks compared to hours to obtain. The hallmark is the reduction in time and cost for a cycle of design, fabrication, and testing of new ideas compared to methods that use a chrome mask in the photolithographic step. The process of rapid prototyping is shown in Figure 1.5. The drawback is that the resolution of the transparency is lower ($> 20\mu m$) than that of a chrome mask ($\sim$ 500 nm). The channel or capillary diameter for most applications, however, ranges from 50 -100 μm, which is within the capacity of rapid prototyping. For devices that require features smaller than 20 μm, a chrome mask needs to be used.

1.5.2 Soft lithography

Soft lithography represents a non-photolithographic strategy based on self-assembly and replica molding for carrying out micro- and nano-fabrication. The term "soft" refers to

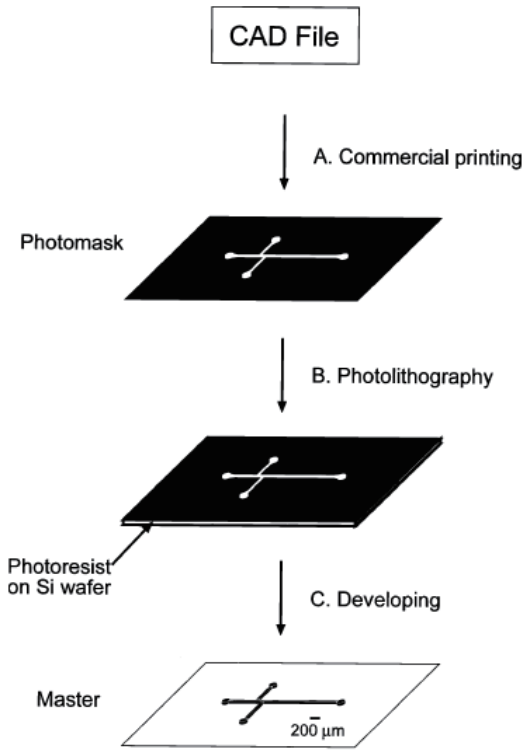

Figure 1.5: Scheme of rapid prototyping of microfluidic mold

an elastomeric stamp with patterned relief structures on its surface. Development of soft lithography expanded rapidly during the period 1995 to 2005 [14].

It has some unique advantages over other forms of lithography (such as photolithography and electron beam lithography). They include the followings:

- Lower cost than traditional photolithography in mass production
- Well-suited for applications in biotechnology
- Well-suited for applications in plastic electronics
- Well-suited for applications involving large or nonplanar (nonflat) surfaces
- More pattern-transferring methods than traditional lithography techniques (more "ink" options)
- Does not need a photo-reactive surface to create a nanostructure
- Smaller details than photolithography in laboratory settings ($\sim$30 nm vs $\sim$100 nm). The resolution depends on the mask used and can reach 6 nm [8].

Soft lithography and its derivative technologies represent a new (or more properly, freshly reexamined) approach to micropatterning. The techniques of soft lithography clearly complement those of photolithography and extend micropatterning into dimensions, materials, and geometries to which photolithography cannot, in practice, be applied.

Six such techniques have been developed: microcontact printing (μCP) [15], replica molding (REM) [16], microtransfer molding (μTM) [17], micromolding in capillaries (MIMIC) [18], solvent-assisted micromolding (SAMIM) [19], and phase-shift photolithography [20]. Among them, replica molding is primarily used to the fabrication of microfluidic devices.

The process of replica molding is illustrated in Figure 1.6.

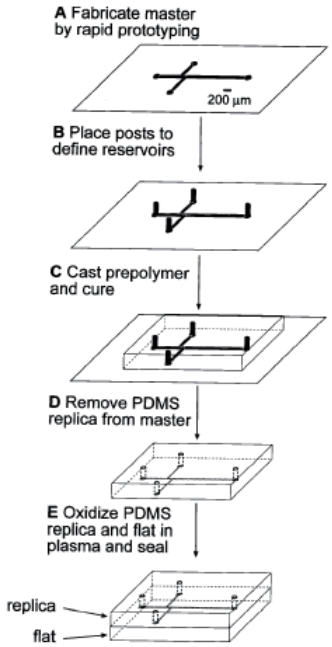

Figure 1.6: Scheme of replica molding of microfluidic devices in PDMS

Poly(dimethylsiloxane) (PDMS) elastomer (or silicone rubber) is used in most demonstrations because of its advantages which are described previously. There are different techniques to transfer the pattern on this elastomeric stamp: microcontact printing and replica micromolding [9]. In many applications, the elastomeric PDMS part can be used directly as a microfluidic device with microchannels on it.

1.5.3 Sealing

Molding provides a PDMS replica that contains three of the four walls necessary for enclosed channels. Sealing the replica to a flat surface provides the fourth wall. This flat material can be PDMS or other materials. There are two kinds of sealings: reversible and irreversible. Reversible sealing occurs because of van de Waals contact. This method is watertight and fast and occurs at room tempreture. It cannot withstand high pressures (> 5 psi). With this method, PDMS can be used numerous times without degradation.

Irreversible sealing occurs when exposing a PDMS replica to an air plasma or an oxygen plasma. The plasma can introduce silanol groups (Si-OH) at the expense of methyl groups (Si-CH_3) on PDMS surface. Then these silanol groups condense with appropriate groups (OH, COOH, ketone) on another surface when the two layers are brought into conformal contact. A covalent bond of Si-O-Si is formed in the case of PDMS and glass. This seal can withstand pressures of 30-50 psi. It is possible to seal PDMS irreversibly to the surfaces of a number of materials: PDMS, glass, Si, SiO_2, quartz, silicon nitride, polyethylene, polystyrene, and glassy carbon, while Saran, polyimide, poly(methylmethacrylate) and polycarbonate do not work [21].

Our approach to the fabrication of microfluidic devices is based primarily on the techniques of rapid prototyping and replica molding. Once a master is fabricated by rapid prototyping, the microchannels are formed in PDMS by replica molding. Then oxygen plasma treatment is commonly used to bond PDMS. PDMS can be irreversibly adhered to a number of materials such as glass, silicon, and quartz [21].

1.6 Components of microfluidics

In the "lab-on-a-chip" devices, people attempt to incorporate many necessary components and functionalities observed in a typical laboratory on the surface of a substrate. The major components of these devices consist of micropumps, microvalves, and micromixers etc., which are used to handle and control fluid flow on a chip.

1.6.1 Micromixers at Re $\ll 1$

Under typical operation conditions, flows in microchannels are laminar, the spontaneous fluctuations of velocity that tend to homogenize fluids in turbulent flows are absent. The streams mix only by diffusion across their common interface and so we address transverse diffusive transport in Poiseuille flow. In order to enhance the mixing, transverse flows must be generated. According to two strategies with which one can generate transverse flows, there are two kinds of micromixers:

- Active mixer: with active methods, transverse flows are generated by oscillatory (mechanical or electrical) within the channel. Yang et al. reported a micromixer using turbulences produced by valveless micropumps [22]. Woias et al. reported an active silicon micromixer whose key element is a silicon chip with a thin piezoelectrically actuated membrane [23]. Yasuda and Ichiki designed an ultrasonic mixer where the samples were introduced from the side wall [24]. Electrokinetically driven parallel and serial mixing was demonstrated by Jacobson et al., using a single voltage source and choosing the dimensions of the channels to be in the desired splitting of the sample [25].

- Passive mixer: with passive methods, transverse flows result from the interaction of externally driven flow (e.g. pressure-driven or electro-osmotic) with the fixed channel geometry. Liu et al. developed a three-dimensional serpentine microchannel as a passive micromixer [26]. Hong et al. presented a passive micromixer based on the Coanda effect [27]. Stroock et al. designed a staggered herringbone mixer that used a passive method for mixing streams of steady state flows in microchannels at low Reynolds number. The structure is as in Figure 1.7. The relationship between the channel length and the Peclet number was investigated, and it was found that mixing could be achieved when the channel length grew logarithmically with the Peclet number [28].

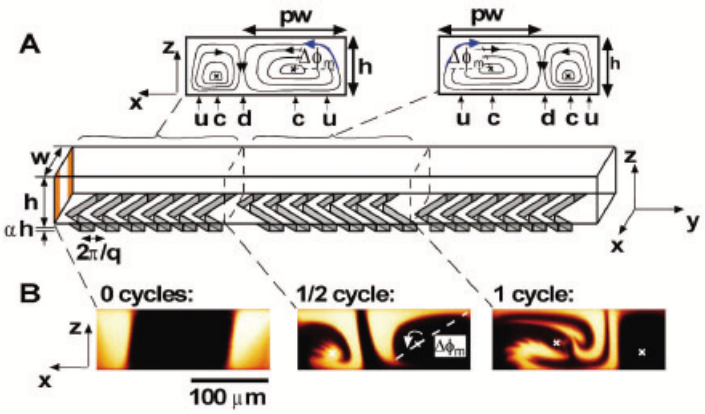

Figure 1.7: Micromixer created by Strooke et al. [28]. Staggered herringbone mixer (SHM). (A) Schematic diagram of one-and-a-half cycles of the SHM. (B) Confocal micrographs of vertical cross sections of a channel as in (A).

1.6.2 Micropump

Commercial syringe and peristaltic pumps are generally too bulky for incorporation into integrated or portable devices. Further development of integrated, inexpensive, miniatur-

ized and versatile micropumps is needed to facilitate the application of more completely integrated and portable flow devices. It is also important to simplify micropump fabrication so that pump designs providing a wide range of flow rates are accessible for a variety of research applications. Micropumps have been broadly classified into two distinct families without standard nomenclature: mechanical and nonmechanical [29] (also known as displacement and dynamic [30] and as reciprocating and continuous flow [23]).

Polydimethylsiloxane (PDMS) has become one of the most common microfluidic chip materials due to ease of fabrication and elastic properties that make PDMS well-suited for mechanical pumping and valving applications.

For nonmechanical pumps, there are many solutions. For example, Handique et al. developed a microchip-based pumping system that can generate pressure by controlling the volume of an air plug trapped in microchannel using resistive heating [31]. Prins at al. demonstrated controlled fluid motion in 3D structures with thousands of channels using the electrocapillary pressure by electrostatically controlling the channel-fluid interfacial tension [32]. McKnight et al. used multiple thin metal electrodes inside a microchannel to allow electroosmotic pumping of the fluid between separate pairs of electrodes, inducing hydraulic pumping between unconnected sections [33].

Many kinds of mechanical pumps are also designed.

1.6.3 Microvalves

The problem of controlling the movement of fluids has not yet received a definitive solution. One first control element is the valve. Microvalve is an important part of many fluidic operations where a fluid flow has to be controlled. The significance of applying MEMS in fluid control was already analyzed by Hou [34]. Nowadays, microvalves can be roughly classified into two groups: active microvalves, using mechanical and non-mechanical moving parts, as well as external systems, and passive microvalves, using mechanical and non-mechanical moving parts.

1.6.4 Flow control

Fluid movement in a microreactor requires low flow rates and minimal pulsation. Flow control is mainly achieved by pressure-driven or electroosmotic flow (EOF). The two flow profiles are depicted in Figure 1.8. Pressure-driven flow can be used for both aqueous and non-aqueous liquids. The flow depends on the viscosity of the fluid and the geometry of the channel. Pressure-driven flow exhibits a parabolic velocity profile and average velocity is proportional to the second power of transverse channel dimension. Syringe or piston pumps can be used to achieve pressure-driven flow within the device. Another approach

to pressure-driven flow is to fabricate micromechanical pumps within the devices using micromachining techniques.

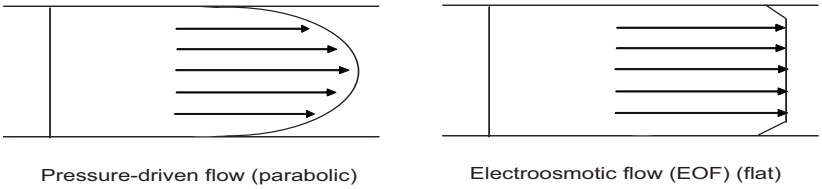

Figure 1.8: Flow profiles for pressure-driven flow and electroosmotic flow (EOF)

Electroosmotic flow is the bulk flow of a solution produced as a result of an electric field on counterions adjacent to the negatively charged channel wall. The ideal EOF in a narrow cylindrical channel should be characterized by a flat, i.e. pluglike velocity profile at distances from the surface that are of the order of the electric double-layer thickness. As a consequence, the average velocity of electroosmotic flow is roughly independent of the device size.

1.6.5 Detection methods

A comparison of several detection methods used in microfluic system is demonstrated in Table 1.2.

In most microfluidic applications so far, on-chip detection has relied on optical detection and, for sensitivity reasons, fluorescence (FL) detection. On-chip FL detection has typically been carried out with FL microscopy or laser-induced fluorescence (LIF) excitation and the data have been collected by charged coupled device (CCD) or photomultiplier tube (PMT).

A simple, inexpensive, and compact portable-assay system requires a small, inexpensive, stable, and durable light source as an excitation source. Light emitting diodes (LED) are excellent sources for this purpose. LEDs are exceptionally stable, provide high emission intensity. And a wide range of wavelengths from violet to near infrared is available. Furthermore, LEDs are small and cheap, provide long lifetime and can be operated with battery power, making them particularly attractive for portable systems. Recently, LEDs are being exploited to achieve absorption and fluorescence detection in microanalytical systems, providing excellent prospects for detector integration and miniaturization [72–76].

1.7 Introduction of fluorophore

The various energy levels involved in the absorption and emission of light by a fluorophore are classically presented by a Perrin-Jablonski energy diagram (see Figure 1.9).

Table 1.2: The comparison of detection methods

Method	Advantage	Disadvantage	Ref.
Fluorescence	High sensitivity amidst small separation channel dimensions	Optics required, derivatization of analytes needed for non-fluorescent analytes	[35–41]
EC	Inexpensive, sensitive and, small enough to fit onto a single chip	Strong electric field applied	[42–49]
Mass Spectrometry	Fast detection speed, detection the unknown analytes	Expensive, difficult to be integrated and miniaturized	[50–52]
CL and EL	No excitation light source required, inexpensive setup,easy to be miniaturized	Lack of versatile reagent systems	[53, 54]
Nonfluorescence Optical	Alternative and innovative compared with fluorescence	Highly specific and isolated analyses	[55–67]
NMR	Nondestructive, direct solution-based determination for unknown compounds	Expensive, no microcoils applied to samples with small amounts of analytes.	[68–71]

EC: Electrochemical; CL: Chemiluminescent; EL: Electroluminescence; NMR: Nuclear magnetic resonance.

This tutorial explores how electrons in fluorophores are excited from the ground state into higher electronic energy states and the events that occur as these excited molecules emit photons and fall back into lower energy states.

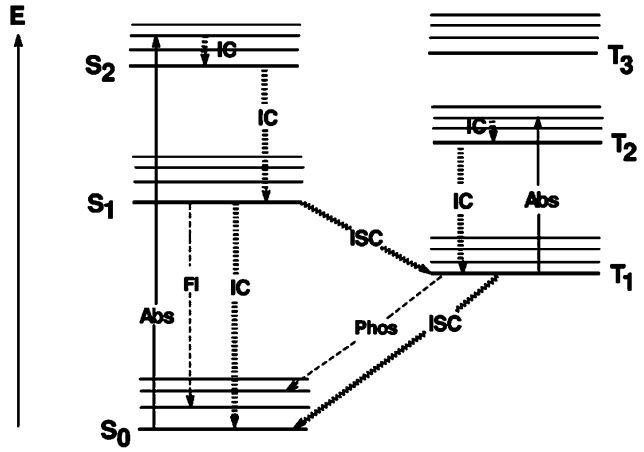

Figure 1.9: Perrin-Jablonski diagram. Abbreviations and acronyms: Abs: absorption, Fl: fluorescence, Phos: phosphorescence, IC: internal conversion, ISC: intersystem crossing.

In absorption and fluorescence spectroscopy, two important types of orbitals are considered: the Highest Occupied Molecular Orbitals (HOMO) and the Lowest Unoccupied Molecular Orbitals (LUMO). Both of them refer to the ground state of the molecule.

1.7.1 Absorption

In many cases, the absorbance of a sample follows the $Beer - Lambert$ Law.

$$A(\lambda) = log\frac{I_0}{I_t} = \epsilon(\lambda)lC \tag{1.3}$$

where A(λ) is the absorbance in the wavelength λ, $\epsilon(\lambda)$ is the molar absorption coefficient (commonly expressed in L mol^{-1} cm^{-1}), C is the concentration (in mol L^{-1}) of absorbing species and l is the absorption path length (thickness of the absorbing medium) (in cm).

According to the Born-Oppenheimer approximation, the motions of electrons are much more rapid than those of the nuclei (i.e. the molecular vibrations). Promotion of an electron to an antibonding molecular orbital upon excitation takes about 10^{-15} s, which is very quick compared to the characteristic time for molecular vibrations (10^{-10}-10^{-12} s). The Franck-Condon principle (see Figure 1.10) which comes from this approximation, describes that there is no concomitant displacement of the nuclei when the transition occurs.

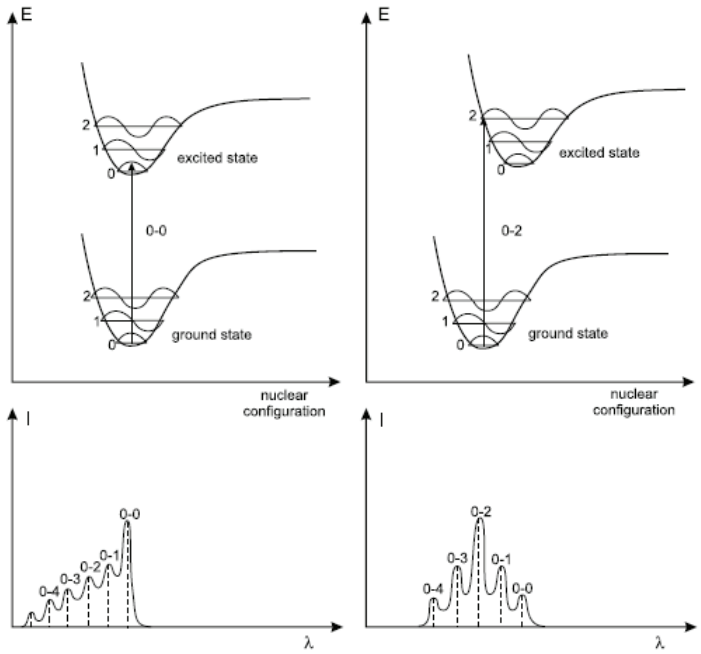

Figure 1.10: Top: Potential energy diagrams with vertical transitions (Franck-Condon principle). Bottom: shape of the absorption bands; the vertical broken lines represent the absorption lines that are observed for a vapor, whereas broadening of the spectra is expected in solution (solid line) [77].

1.7.2 Fluorescence

Emission of photons accompanying the $S_1 \rightarrow S_0$ relaxation is called fluorescence. In general, the differences between the vibrational levels are similar in the ground and excited states, so that the fluorescence spectrum often resembles the first absorption band ('mirror image' rule). The gap (expressed in wavenumbers) between the maximum of the first absorption band and the maximum of fluorescence is called the Stokes shift.

Considering a dilute solution of a fluorescent species, the time evolution of the concentration of excited molecules in absence of any quenching process is expressed by the following equation:

$$[A]_t = [A]_0 exp(-\frac{t}{\tau}) \qquad with\ \tau = \frac{1}{k_r + k_{nr}} \qquad where\ k_{nr} = k_{ic} + k_{isc} \tag{1.4}$$

where k_r, k_{nr}, k_{ic} and k_{isc} are respectively the rate constant for radiative deactivation, non-radiative deactivation, internal conversion and intersystem crossing.

For a steady-state fluorescence, the intensity is given by:

$$I_F = kl\epsilon(\lambda_{exc})I_0(\lambda_{exc})\Phi_F C \tag{1.5}$$

where k is the apparatus constant, $I_0(\lambda_{exc})$ is the intensity of the incident light, Φ_F is the fluorescence quantum yield, which is the number of emitted photons per absorbed photons, $\epsilon(\lambda_{exc})$ is the molar absorption coefficient in λ_{exc}, C is the concentration.

1.8 Fluorescent sensors for cations

Most of the fluorescent chemosensors for cations are composed of a cation recognition unit (ionophore) linked to a fluorogenic unit (fluorophore) and are called fluoroionophores [78, 79]. An effective fluorescence chemosensor must convert the event of cation recognition by the ionophore into an easily monitored and highly sensitive light signal from the fluorophore. They played an important role in detecting metal ions, like sodium, potassium, calcium and magnesium, or lithium in the clinical diagnose, even some trace metal ions, like lead, mercury and chromium in the environmental pollution. The detection principle is that when the metal ion can form the complex with ionophore, some photophysical property changes (e.g. color, λ_{em}, $\epsilon(\lambda_{exc})$ or I_F) will happen. One scheme of the principle of fluoroionophores is illustrated in Figure 1.11.

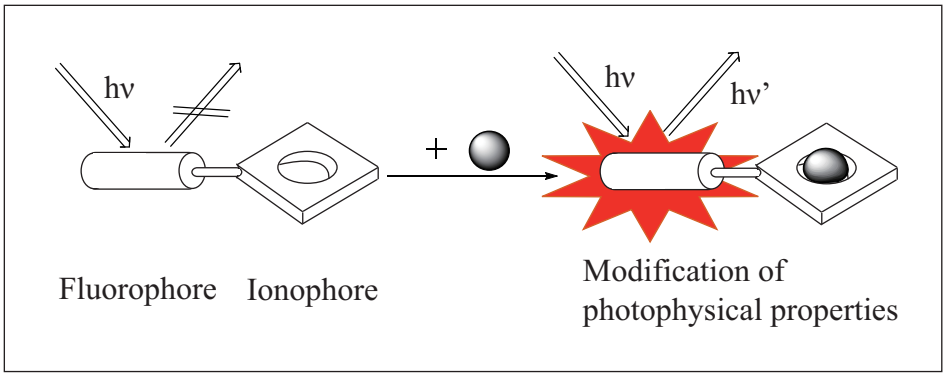

Figure 1.11: Principle of recognition of cation and the detection by the fluoionophores.

These changes are mainly due to changes of several photoinduced phenomena: photoinduced electron transfer, photoinduced charge transfer, photoinduced energy tranfer, excimers and exciplexes.

1.8.1 Photoinduced electron transfer

The fluoroionophores of this type are usually composed of a fluorophore linked to an electron donor by a spacer. The fluorophores are usually aromatic hydrocarbons such as benzene, naphthalene or, in most cases, anthracene (see Figure 1.12). The receptors employed in these probes are often polyaza , azaoxa or azathia or related compounds macrocyclic or open chain structures predominate. When a photon excites a molecule, an electron

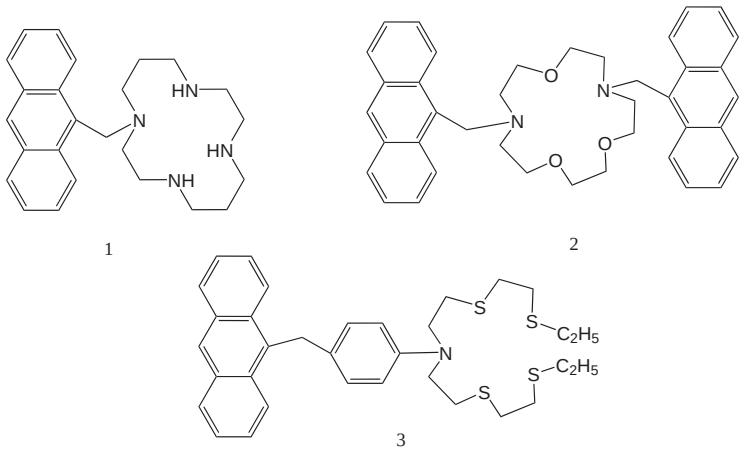

Figure 1.12: Some examples of Fluorophore-spacer-receptor sensors: (1)[80], (2)[81], (3)[82].

in a ground state orbital can be excited to a higher energy orbital (LUMO). This excited state leaves a vacancy in a ground state orbital (HOMO) that can be filled by an electron donor. Promotion of an electron from the HOMO to the LUMO of the fluorophore allows a fast electron transfer from the donor's HOMO to fluorophore's HOMO, thus quenching the fluorescence. In this case, the electron transfer acts just like an "ON-OFF" or "OFF-ON" switch. A scheme of this phenomenon is illustrated in Figure 1.13.

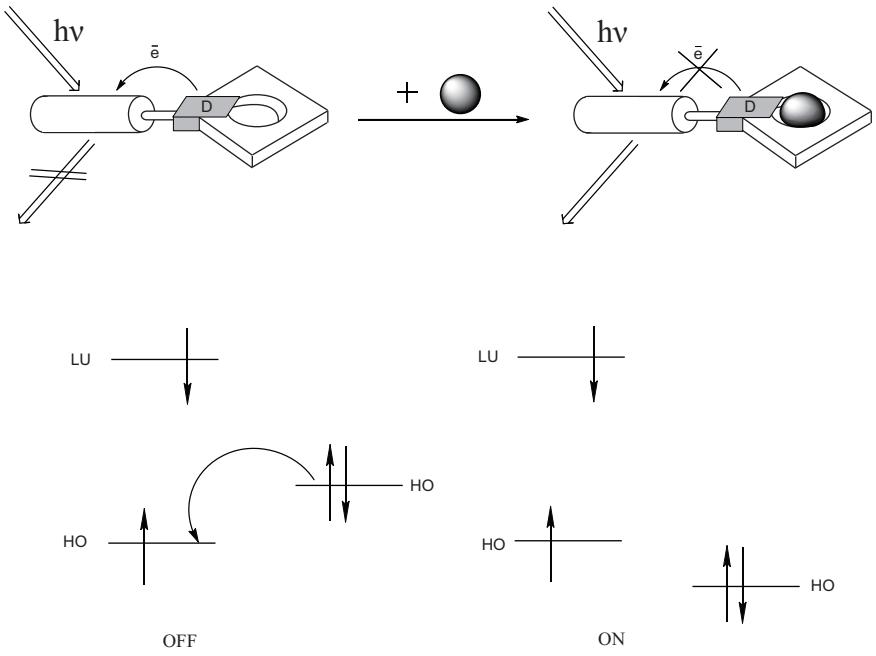

Figure 1.13: Mechanism of OFF-ON photoinduced electron transfer

Electron transfer (ET) in the excited state from the electron donating molecule to the fluorophore, which can then be influenced by metal ion coordination. The result is an emissive complex with virtually unchanged spectral characteristics. Although this concept of signal generation harbors the disadvantage that complexes of a certain probe with different cations cannot be spectrally distinguished, the complexation-induced fluorescence enhancement factors often exceed those of intrinsic probes by one or two orders of magnitude, i.e., the light is indeed switched "ON" at least for the great majority of fluorophore spacer donor systems for protons, alkali and alkaline-earth metal ions. But for some heavy metal ions, photoinduced electron transfer happens between fluorophore and metal ion. For example, a fluoroionophore based on calixarene **4** (Figure 1.14), can cause a fluorescent extinction when complexing with Hg^{2+}. The electron transfer occurs from fluorophore to complexed Hg^{2+}. Another example is a fluorescent molecular sensor for Hg^{2+} based on the phosphane sulfide derivative **5** (Figure 1.14). In terms of electron transfer between the excited fluorophore to the complexed mercury cation, a strong decrease of the fluorescence is observed upon mercury complexation.

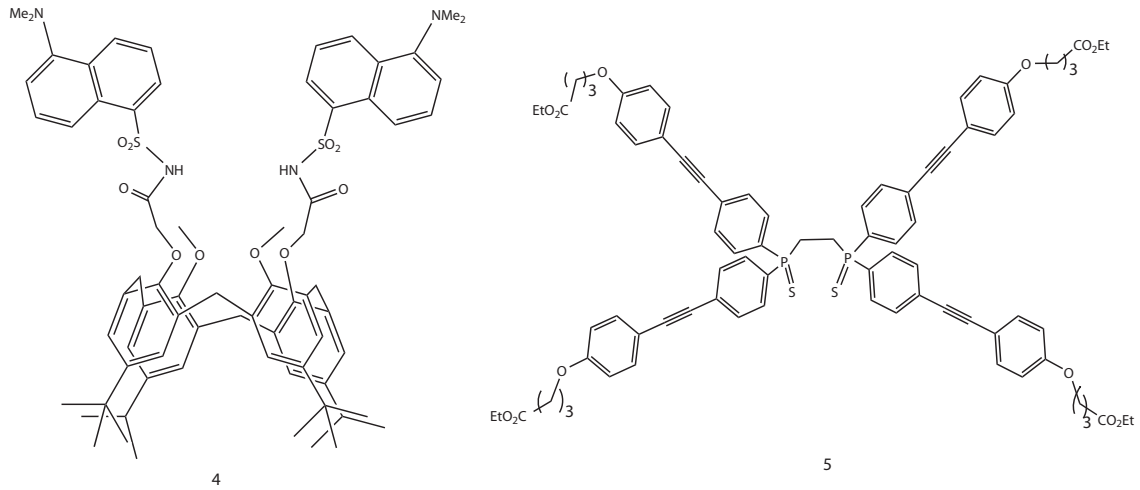

Figure 1.14: Examples of electron transfer between fluorophore and metal ion: (4) [83], (5) [84].

1.8.2 Photoinduced charge transfer

Photoinduced charge transfer is the fundamental process by which light energy is converted to potential energy associated with separation of electrical charge. For this type, the fluorophores always possess an electron donor conjugated with an electron acceptor, which is usually called intrinsic probes. Their construction plans usually combine an electron donating (D) and an electron accepting (A) fragment, separated by a vinyl, butadienyl, phenyl,

styryl or stilbenyl type of subunit, thus keeping donor and acceptor in π-conjugation. It is designed in a certain modular way, receptor and basic fluorophore share the same π electron system. For the majority of the sensor molecules, the receptor is situated in the donor part of the molecule and consequently binding of a positively charged ion reduces its electron donating capability. This receptor is closely connected to a macrocyclic molecular cage that will trap the metal ion. In absorption, hypsochromic shifts are found, roughly depending on the charge density of the cation. After excitation, the CT (charge transfer) process still proceeds but is less exergonic due to the cation-nitrogen atom interaction. Figure 1.15 shows some examples of intrinsic fluorescent sensors.

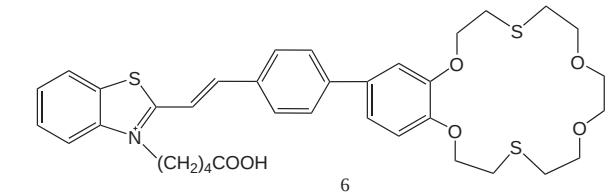

6

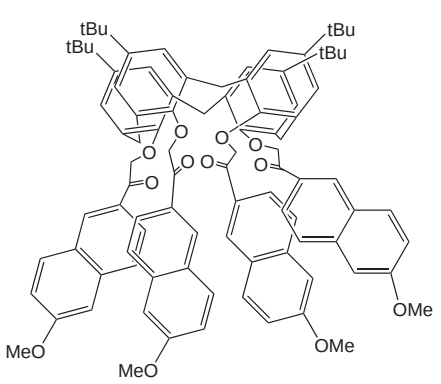

7

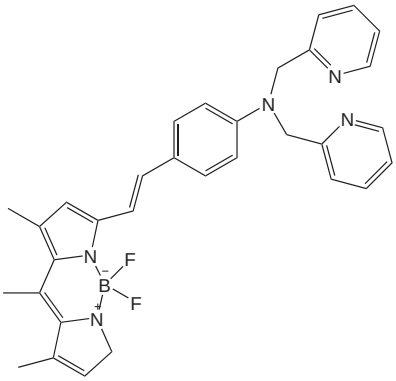

8

Figure 1.15: Some examples of intrinsic fluorescent probes of D-A type: (6) [85], (7) [86], (8) [87].

Charge Transfer character often identifies with solvatochromism. Solvatochromism is the ability of a chemical substance to change color due to a change in solvent polarity. Negative solvatochromism corresponds to hypsochromic shift, positive solvatochromism corresponds to bathochromic shift with increasing solvent polarity. Meanwhile, the interaction between the cations and the donor part or acceptor part of fluorophores are also able to modify their photophysical properties because of the effective photoinduced charge transfer. When the electron acceptor part interacts with the cation, the conjugation in the fluoionophore increases, the red shift of spectra (absorption and fluorescence) appears and the molar absorption coefficient enhances. On the contrary, when the electron donor part interacts with the cation, charge transfer reduces, the blue shift is observed (Figure 1.16).

This phenomenon can also be described in the term of dipolar interaction. The dipole moment of the dye molecule in its excited state is usually higher than its ground state. When the cation interacts with the acceptor (or donor), the excited state is more stable (or unstable) and the red (or blue) shift of the spectra is observed. Unlike electron transfer to induce a switch, this phenomenon induces just a spectral displacement.

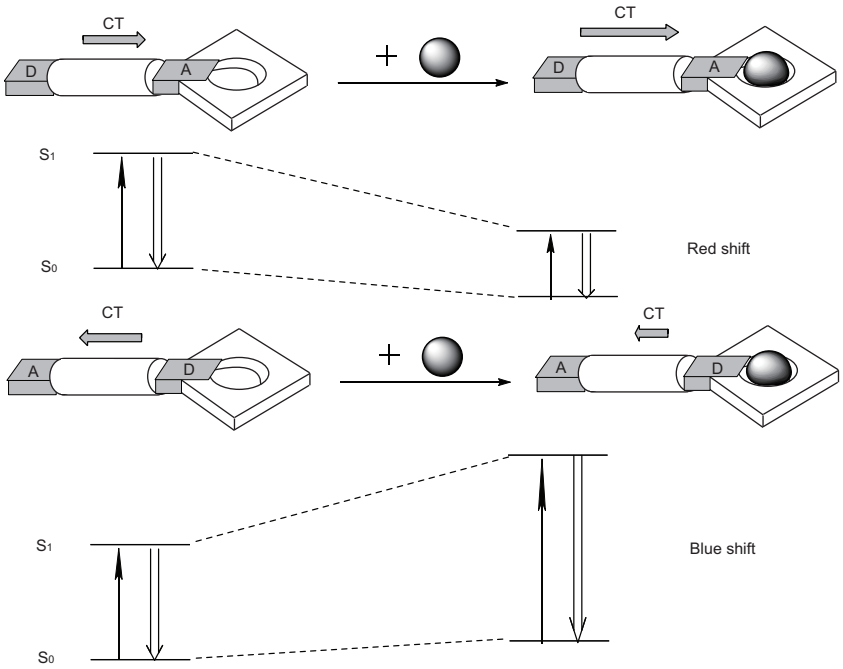

Figure 1.16: Mechanism of photoinduced charge transfer

1.8.3 Energy transfer

The energy transfer is analogous to a near field radio, because the radius of interaction is much smaller than the wavelength of light used. In this sense the excited molecule emits a virtual photon which is accepted by the receiving molecule. It is termed a non radiative transfer because the virtual photon only exists if it is accepted by the receiver, and therefore no radiation can be observed. The non-radiative excitation energy transfer happens between a fluorophore with energy donor and a fluorophore with energy acceptor. This requests an overlap between absorption spectrum of the acceptor and emission spectrum of the donor, making that the vibrating transitions of the donor has the same energy as the corresponding transitions of the acceptor.

Energy transfer can be dipole-induced (Förster or Coulombic, for the distances from 1 to 100 nm) or electron exchange-induced (Dexter, for the distances less than 0.6 - 0.8 nm). The details are shown in Figure 1.17.

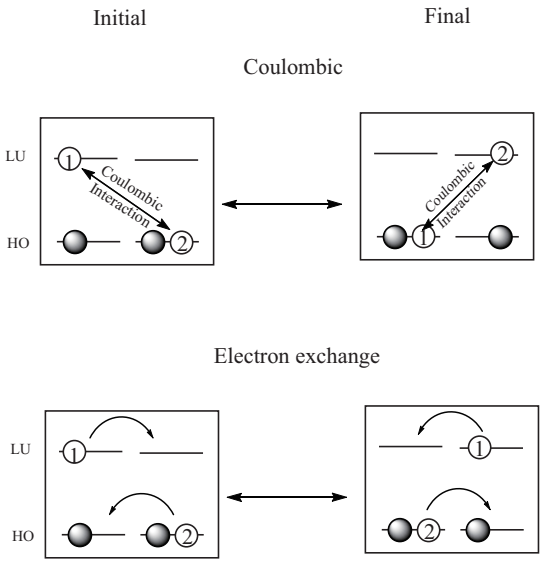

Figure 1.17: Comparison of the Coulombic and Exchange mechanism of electronic energy transfer

Several examples of energy transfer are shown in Figure 1.18.

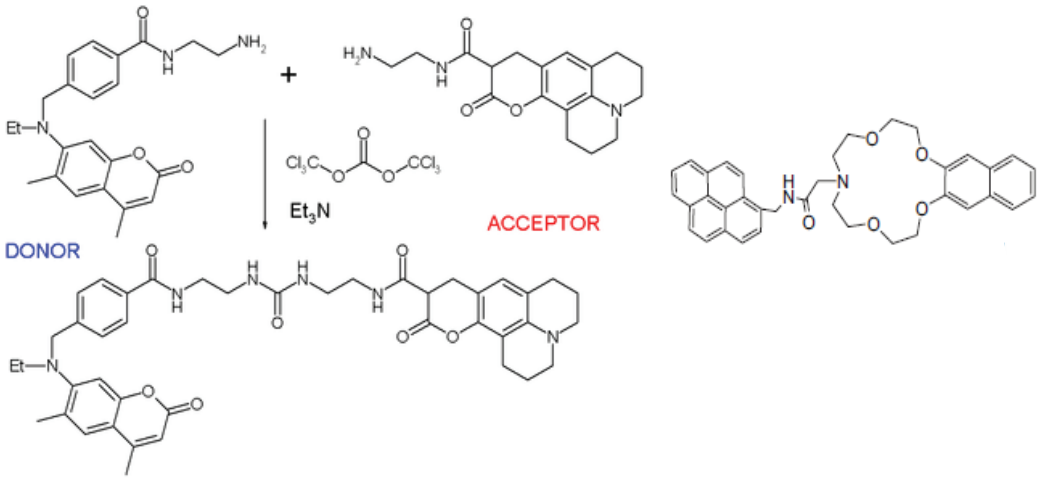

Figure 1.18: Examples of fluorescence probe with energy transfer: (9) [88], (10) [89].

1.8.4 Formation of excimers and exciplexes

Excimers are dimers in the excited state. They are formed by collision between an excited molecule and an identical unexcited molecule:

$$^1M^* +^1 M \rightleftharpoons^1 (MM)^*$$

The symbolic representation $(MM)^*$ shows that the excitation energy is delocalized over the two moieties. Exciplexes are excited complexes formed between an excited molecule and a different neutral molecule.

The formation of excimers and exciplexes are diffusion-controlled processes. The photophysical effects are thus detected at relatively high concentrations of the species so that a sufficient number of collisions can occur during the excited-state lifetime.

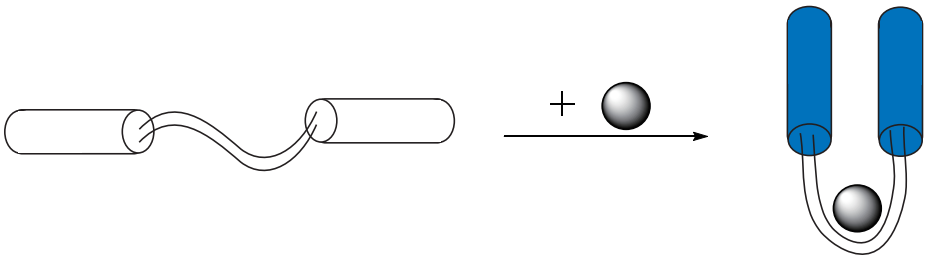

Figure 1.19: Principle of a fluorescent sensor by forming an excimer

When a fluoroionophore contains two fluorophores whose mutual distance is affected by cation complexation, recognition of this cation can be monitored by the monomer: excimer fluorescence-intensity ratio. Cation binding may favor or hinder excimer formation. In any case, such a ratiometric method allowing self-calibration measurement is of great interest for practical applications. The principle of a fluorescent sensor by forming an excimer is illustrated in Figure 1.19.

Many aromatic hydrocarbons such as naphthalene or pyrene can form excimers. Several examples are given in Figure 1.20.

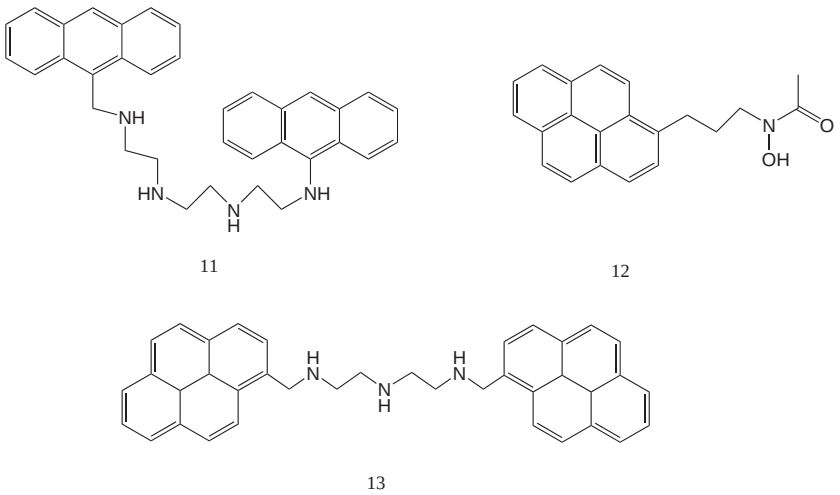

Figure 1.20: Some examples of excimers forming sensors: (11) [90], (12) [91], (13) [92].

1.9 Heavy metal ions in the environment

The contamination by heavy metals from various environmental sources including natural water is a great concern nowadays.

1.9.1 Lead ion

Toxic effect of lead ion

Environmental monitoring of heavy metals is of great importance for ecological assessments as well as for understanding the dissemination of pollutants [93]. Among them, lead is the most abundant and certainly the most toxic causing health problem. Lead is a cumulative general poison, infants, children up to 6 years of age, the fetus, and pregnant women being the most susceptible to adverse health effects. Its effects on the central nervous system can be particularly serious. It accumulates in the body and can cause lead poisoning. Lead is proved to be a carcinogenic agent and to cause disturbances to several organs. Even at low concentrations, when there are no outward symptoms, lead can damage the brain, kidneys, nervous system and red blood cells. Besides lead is toxic to both the central and peripheral nervous systems, inducing subencephalopathic neurological and behavioural effects. There is evidence from studies in humans that adverse neurotoxic effects other than cancer may occur at very low concentrations of lead and that a guideline value derived on this basis would also be protective for carcinogenic effects. All theses facts cause alarming concern in public health, demanding accurate analytical procedures for the quantification of these elements at trace levels.

Lead ion in drinking water

Lead ion has many origins, such as paint, petrol, pipes used for drinking water, soil erosion and industrial and agricultural processes etc.. Owing to the decreasing use of lead-containing additives in petrol and of lead-containing solder in the food processing industry, concentrations in air and food are declining, and intake from drinking-water constitutes a greater proportion of total intake. Lead is present in tap water to some extent as a result of its dissolution from natural sources but primarily from household plumbing systems in which the pipes, solder, fittings, or service connections to homes contain lead. The piping systems in distribution network and inside the networks of old buildings are still based on lead pipes. Lead was being considered to be a cheap and convenient material to convey water to the consumer's tap. Although situations varies widely from one country to another, several millions of installed lines are still in service in Western Europe and North America [94]. In France, about 10 million household networks (38%) are still equipped with lead pipes, the situation being worse in big cities as Paris were the proportion of lead-based

service lines reaches about 70% in 1995 [95]. In addition, corrosion of household brass and bronze plumbing fixtures such as pipe's jointing assemblies and faucets, tin-lead soldered joints, valves, and gaskets in water treatment plants or distribution mains were identified as other potential sources.

Table 1.3: Admissible maximal concentration of lead ion in drinking water

	Lead
Guided value of WHO	10 μg L^{-1} from 2003
Guided value of UE	10 μg L^{-1} for 2013
Admissible maximal concentration in France	25 μg L^{-1} from 2003
Admissible maximal concentration in China	10 μg L^{-1} from 2007

Recently, many measurements have been carried out to reduce lead's environmental levels, such as the ban on leaded gasoline and the progressive replacement of lead pipes in the public water supply, implement of a selective lead-uptake cartridge at the faucet. The use of lead piping is forbidden today. Relying on epidemiological studies, the World Health Organization had recommended in 1996 the guideline for drinking-water quality, which included a lead maximal value of 10 μg L^{-1} [96–98], other countries set their own regulations according to this guideline. Some details are shown in Table1.3. The Council of the European Communities approved in 1998 a directive (98/83/CE) related to the quality of consumption water. The European standard sets a target to reduce the quantity of lead in water to 10 μg L^{-1} by 2013, which will lead to the replacement of all existing lead piping in time.

1.9.2 Method for heavy metal ions detection

Commercial apparatus at lab

The major existing techniques for trace-metal analyses are spectroscopy (in particular, graphite furnace atomic absorption spectroscopy (GF-AAS) and inductively coupled plasma mass spectroscopy (ICP-MS)), neutron activation analysis (NAA), and voltammetry and chronopotentiometry.

Many methods of atomic spectrometry techniques are still most commonly carried out for the determination of trace metals using a preconcentration step prior their detection.

- Atomic absorption spectrometry
  - Flame atomic absorption spectrometry (FAAS): a very attractive technique for routine metal determinations, owing to its ease of operation, its low acquisition

and operating costs [99, 100]. Detection limit can attain some μg L^{-1}.

  - Graphite furnace atomic absorption spectrometry (GFAAS)[101]
  - Electrothermal atomic absorption spectrometry [102]

- Atomic emission spectrometry
  - Inductively coupled plasma optical emission spectrometry (ICPOES)
- Mass spectrometry
- Inductively coupled plasma mass spectrometry(ICP-MS) [103]

Currently, the amount of lead is measured using atomic absorption or emission spectroscopies, because of its excellent sensitivity (1ppb for lead ion) and selectivity, but they are only the apparatus of laboratory, not transportable and expensive (60000 $\sim$100000 Euros). Other methods using spectrophotometry, fluorimetry, chemiluminescence or electrochemistry are actually not so popular. The use of fluorescence will offer many advantages in terms of sensitivity, selectivity and low cost. In contrast to the variety of fluorescent molecular sensors developed for alkali and alkaline-earth cations, there are only few examples of fluoroionophores developed for heavy metal ions and particularly for lead.

Commercial portable apparatus

In the market, now we can find several kinds of commercial portable apparatus for the lead ion detection which use ASV (Anodic Stripping Voltammetry). Three of them are as follows:

- SA-1000 (Palintest): As in Figure 1.21A, this system is very sensitive with sensibility of 2 ppb, and the measurement is reliable and accurate. But it utilizes mercury electrode which is deleterious for the environment and human's health.
- Nanoband Explorer (Trace Detect Fondis Electronic): As in Figure 1.21B, the sensibility attains 0.1 ppb, and the analysis lasts only 3 minutes. But it is not so accurate and still expensive (9000$).
- PDV 6000 plus (Lab21 Environmental): As in Figure 1.21C, the function of this system is similar to Nanoband Explorer, with high sensitivity (0.1 ppb) but a little expensive(9000$).

As we stated in this chapter, there are very few portable apparatus for heavy metal ion detection. But in environmental monitoring, monitoring heavy metal ion *in situ* is very important and valuable. To accomplish this task, several factors have to be considered: high selectivity, high sensitivity, low cost, portable, etc...

A B C

Figure 1.21: Three commercial portable apparatus for lead ion detection

Microfluidic device in researching for heavy metal ions detection

Several approaches have been published for the separation and simultaneous determination of metal ions based on microfluidic devices [104–107]. For example, Jacobson et al. have demonstrated a successful separation of Zn, Cd, and Al with detection limits in the 10-100 ppb range using a capillary electrophoresis (CE) microchip [104]. Zhu et al. have successfully generated the mercury microelectrode by manipulating mercury microfluidics in a device. The detection on 1×10^{-7} mol L^{-1} Pb^{2+} or its mixture with 1×10^{-7} mol L^{-1} Cd^{2+} using the square wave stripping voltammetry was achieved [107]. Shaikh et al. have presented microfluidic lab-on-a-chip (LOC) systems based on a modular architecture. They used a DNAzyme-based biosensor to identify the presence of Pb^{2+} at a sensitivity of 500 nM in <1 nl of solution [106]. Chang et al. have developed a miniaturized lead sensor by combining a lead-specific DNAzyme with a microfabricated device containing a network of microfluidic channels. This device demonstrated a detection limit of 11 nM for lead ion [105].

1.10 Endocrine disrupting chemicals

Endocrine disrupting chemicals refer to a range of man-made chemicals, which are suspected of interfering with the endocrine systems of both humans and wildlife. Hormones, as the body's own chemical messengers between tissues and cells, regulate a multiplicity of processes. Female and male sex hormones (estrogens and androgens) play decisive roles in reproduction and the development of an organism. If a foreign chemical has the same effects as the body's own estrogens or androgens, it is defined as having estrogenic or androgenic activity. If a chemical inhibits the effects of the body's own sex hormones, however, its effect is described as anti-estrogenic or anti-androgenic. The threat of impairment of human reproductive function and the impact on health and reproduction of wildlife

as a result of exposure to endocrine-active substances in the diet and in the environment is a topic receiving increasing attention.

1.10.1 Classes and sources of EDCs

Which kind of man-made chemicals belong to endocrine disrupting chemicals? Various organisations have published lists of suspected endocrine-disrupters. For example, in order to establish a priority list of substances for further evaluation of their role in endocrine disruption, BKH Consulting Engineers (Delft, the Netherlands) under the commission of the European Commission by letter of 1 February 1999 has conducted a study on endocrine disruption focusing on man-made chemicals. The final report illustrated 564 substances in the existing lists and other sources of information; 146 substances of selection of highly persistent and/or "high production volume" (HPV) substances; 66 substances for preliminary evaluation of scientific evidence of ED-related effects; 60 substances for preliminary evaluation of exposure to humans and wildlife [108]. A more in depth investigation into such lists is conducting in order to ascertain and assess the reliability of the selection criteria used to establish the lists and to include information on the sources, uses of such chemicals and the pathways in human and wildlife exposure.

Although no intensive screening for endocrine disrupters has taken place to date, some of these chemicals have already been identified:

- Natural estrogens, such as 17β-estradiol, estrone and estriol, are effective even at very low concentrations.
- Synthetic estrogens, such as 17α-ethinylestradiol (EE2, the estrogenic compound used in oral contraceptives).
- Phyto- and myco-estrogens, such as isoflavone and other compounds, are synthesised by the plants themselves, or by fungi that infest the plants. Their effect is estrogenic, although some anti-estrogenic effects have also been described.
- Metabolites of alkylphenolpolyethoxylates (APEO: nonylphenol, octylphenol and further breakdown products) are currently used primarily as the active substances in industrial detergents, and are also to be found as additives in paints, pesticides and other products. They have estrogenic effect and are of particular significance in sewage contaminated rivers.
- Certain industrial chemicals used in plastics (bisphenols, especially bisphenol A) show estrogenic effects. Phthalates have so far been shown to have estrogenic effects in vitro, but their effect on whole organisms is not clear.

- Others: Various organochloropesticides, such as DDT and its breakdown products DDE, DDD, Lindane (γ-hexachlorcyclohexane) and kepone (chlordecone). Various chlorinated and hydroxylated biphenyls (PCB, OH-PCB) that are widespread due to their minimal breakdown, show estrogenic and anti-estrogenic effects. Various polychlorinated dibenzo-p-dioxins and furanes show anti-estrogenic effects. The fungicide vinclozoline has an anti-androgenic effect. Organotin compounds such as tributyltin (TBT) and triphenyltin (TPT), both of which are used in antifouling paints for ships, show an androgenic effect on various marine snail species, even at the very low concentrations of a few nanogrammes per litre. The use of these antifouling paints on small boats is now usually prohibited. However, organotin compounds are used today in antifoulings for large vessels, in agriculture (TPT, vegetable cultivation), in wood preservatives and in textile finishing.

1.10.2 Content of endocrine disrupters

Another concern is as to what level of EDCs can interfere with the endocrine homeostasis of humans and animals, and what effects on individuals or populations may result. Although the chemicals responsible for the disturbances of these endocrine disrupting chemicals should be identified with a combination of analytical chemistry and biological assay systems (Toxicity Identification and Evaluation, TIE), analytical chemistry is a powerful tool to screen the known substances in environmental samples (e.g. waste water, drinking water) first. So, reliable and sensitive analytical methods are needed to detect EDCs in the aquatic environment. Many analytical methods were reported for EDCs detection. For example, Grover et al. compared three analytical techniques (gas chromatography-mass spectrometry (GC-MS), gas chromatography-tandem mass spectrometry (GC-MS-MS) and liquid chromatography-tandem mass spectrometry (LC-MS-MS) for the measurement of three highly potent steroidal estrogens in the aquatic environment. Three techniques all appeared comparable, but that tandem-mass spectrometric techniques were able to detect at lower concentration levels of the three steroidal estrogens of interest [109]. A pilot study used biological (E-screen assay) and chemical (stir bar sorptive extraction-GC-MS) analyses to quantify estrogenic activity in several effluent water samples [110]. Hibberd et al. described an improved method for the extraction and analysis of seven endocrine disrupting chemicals with wide-ranging polarities from water and sediments using gas chromatography-tandem mass spectrometry (GC-MS/MS) [111]. Zhao et al. developed an analytical method for phenolic endocrine disrupting chemicals and acidic pharmaceuticals in river water using gas chromatography mass spectrometry (GC-MS) coupled with negative chemical ionization (NCI) technique [112]. In a word, Gas chromatography-mass spectrometry (GC-MS), High pressure liquid chromatography (HPLC)-mass spectrometry

(GC-MS) and their derivations are the most popular and effective methods for EDCs detection in nowadays.

However, it is still unclear whether the presence of environmental pollutants could lead to actual exposure of the human population to such an extent that human reproductive function could be adversely affected. The research about EDCs is still working on and has a long way to go.

1.11 Conclusion

The appearance of miniaturized devices accommodate the demand of portable apparatus. Miniaturization is currently an important trend in environmental monitoring due to its potential to reduce cost, provide portability, and increase analysis speed. Comparing with other commercial bulk apparatus (e.g. AAS), the advantage of microfluidic device is evident. Meanwhile, for the detection system, optical detection methods display their advantages especially non toxic quality over mercury electrode for heavy metal ion detection. The variety of fluoroionophores have been designed for cation recognition, progress still needs to be made regarding the selectivity towards a given cation in a specific range of concentration which can be very different according to the application. On the other hand, for some endocrine disrupting chemicals, electrochemical detection shows high sensitivity. In this thesis, the two detection methods coupled with miniaturized analysis system will both be used for different applications.

Chapter 2

Fluorimetric microfluidic device for Pb^{2+} sensing

2.1 Introduction

Microfluidics, which means the manipulation of fluids in channels with dimensions of tens of micrometers, has emerged as a distinct new field. The first applications of microfluidic technologies have been in analysis, for which they offer a number of useful capabilities: the ability to use very small quantities of samples and reagents, and to carry out separations and detections with high resolution and sensitivity, low cost, short times for analysis, and small footprints for the analytical devices [113].

Analytical techniques based on fluorescence detection are very popular because of their high sensitivity and selectivity, together with the advantages of spatial and temporal resolution, and the possibility of remote sensing using optical fibers.

When an analyte is fluorescent, direct fluorimetric detection is possible by means of a spectrofluorimeter operating at appropriate excitation and observation wavelengths. This is the case for aromatic hydrocarbons (e.g. in crude oils), proteins (e.g. in blood serum, in cow milk), some drugs (e.g. morphine), chlorophylls, etc.. Numerous fields of applications have been reported: analysis of air and water pollutants, oils, foods, drugs; monitoring of industrial processes; monitoring of species of clinical relevance; criminology; etc..

However, most ions and molecules are not fluorescent, formation of a fluorescent complex is the basis of most methods of ion and molecule recognition. This chapter is an example of fluorimetric microfluidic device's application in trace heavy metal ion sensing. In our work, we will build a lead sensor based on both microfluidic and fluorimetric detection.

2.2 Fluoroionophores for lead ion sensing

The allowable concentrations are 10 μg L^{-1} for Pb^{2+} set by the World Health Organization (WHO) for drinking water quality. Accordingly, the European Union reduced the allowable concentration values for Pb^{2+} for water pollutants to 10 μg L^{-1} for 2013. Many fluoroionophores are studied for lead ion determination. Kavallieratos et al. has reported an

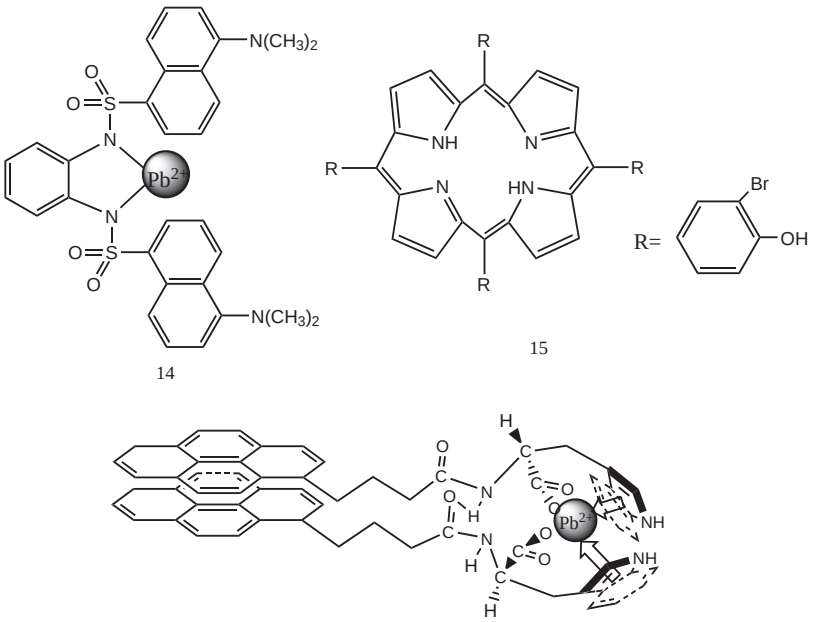

Figure 2.1: Some fluorescent sensors for lead ion detection

efficient and selective ion-exchange extraction of Pb^{2+} from water into 1,2-dichloroethane with concurrent fluorescence quenching using as an ion-exchanger, the sulfonamide fluorophore **14** (Figure 2.1). Bozkurt et al. [114] studied a fluorescent-based sensor for Pb^{2+} using 5,10,15,20-tetra-(3-bromo-4-hydroxyphenyl) porphyrin (TBHPP) **15** (Figure 2.1). Ma et al. [115] reported a fluoroionophore sensor, N-[4(1-pyrene)-butyroyl]-L-tryptophan (PLT) **16** (Figure 2.1) which can distinguish Pb^{2+} from other 12 metal ions, but the sensitivity was very low, the detection limit was just 0.15 μM in aqueous solution. Guo et al. [116] used a fluorescent ligand 2-hydroxy-1-naphthaldehydene-8-aminoquinoline(HNAAQ) for lead detection. Because of a coplanar effect and the degree of molecular conjugation, the fluorescent intensity of the complex was obviously increased in presence of lead ion. But the selectivity of this sensor was not satisfying. Its selectivity was also very poor. Saito et al.[117] employed an aromatic polyaminocarboxylate, 1-(4-aminobenzyl) -ethylenediamine-N,N,N',N'-tetraacetic acid (abbreviated as ABEDTA) as a fluorescent agent to detect Pb^{2+} and Cd^{2+}. Co-existing ion Zn^{2+} interfered their detection.

Dansyl-appended probe, derivatives of (5-N,N-dimethylaminonaphthalene-1-sulfonyl)-acetylamide (DANS1) is one class of intrinsic probes which have good charge transfer in the excited state in numerous systems. Concerning their photophysical properties, DANS1 is very sensitive to the polarity of its environment, which can cause important Stokes shift. So most of these probes display cation-induced shifts in absorption and emission, reminiscent of D-A type probes. The fluorescence intensity changes, which are found upon heavy and transition metal ion complexation, are rather similar to most fluorescent ligands. Calix-DANS4 **17** (see Figure 2.2 left), a derivative of Dansyl, developed in our lab by Metivier et al. [118], has shown good sensitivity and selectivity for Pb^{2+}.

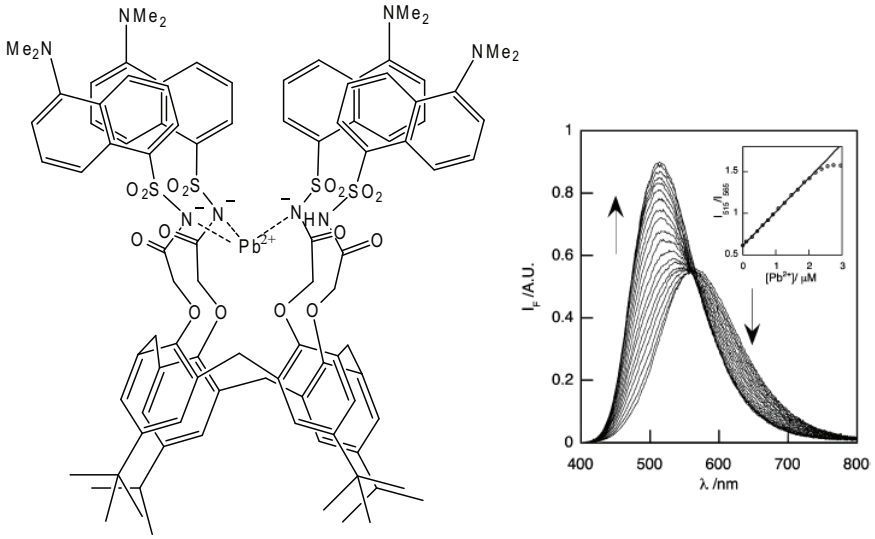

Figure 2.2: Left: The structure of Calix-DANS4 and its binding with Pb^{2+}. Right: Fluorescence spectra of Calix-DANS4 in the presence of increasing Pb^{2+}.

They have shown that it was not absolutely soluble in water, but in a partially aqueous solution CH_3CN/H_20 (60:40 v/v). This solvent mixture was chosen to facilitate solvation of the fluoroionophore and the metal ions. Interaction mechanism was explained to be the complexation of Pb^{2+} with three nitrogen in the dansylamide group of Calix-DANS4. This complexation was very sensitive to pH. It has been shown that the fluorophore can have three acido basic forms (acid form, neutral form and basic form, see Chapter 4, Figure 4.3): the acid form corresponded to the protonation of the amino group, whereas the basic form was due to the deprotonation of the carboxysulfonamide group. A pH[1]5.2 has been chosen to perform complexation measurements in order to have the highest ratio of the fluorophore in the neutral form. The fluorescence spectra of Calix-DANS4 in the presence of increasing

[1]All the pHs in this manuscript are real pHs, not measured pHs. The relationship between real pH and measured pH in the solution of CH_3CN/H_20 (60:40 v/v) is explained in Appendix A.4.6.

concentration of Pb^{2+} in this condition were shown in Figure 2.2 right. The blue shift was rationalized by the deprotonation of the sulfonamide group upon cation binding.

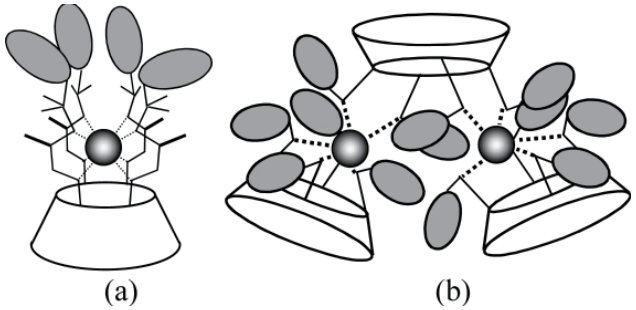

Figure 2.3: The binding models of the complexation of Calix-DANS4 and lead ion (a) ML complex; (b) M_2L_3 complex

Table 2.1: Summary of several fluoroionophores for lead ion sensing

Fluoionophore	Detection limit	Selectivity	Ref.
HNAAQ	8.3×10^{-8} mol L^{-1}	Fe^{3+}, Al^{3+}, Mg^{2+}, Ni^{2+} and Cr^{3+} were allowed only 20 folds.	[116]
TBHPP	4×10^{-8} mol L^{-1}	Cd^{2+}, Zn^{2+}, Zr(IV), Mn^{2+}, Ni^{2+}, Cu^{2+}, Co^{2+} showed obvious interfering effect when excess 5×10^{-5} mol L^{-1}	[114]
PLT	1.5×10^{-7} mol L^{-1}	Good selectivity over 12 other metal ions	[115]
ABEDTA	1.5×10^{-8} mol L^{-1*}	100 to 1000 fold coexisting ions do not interfere, except Zn^{2+}	[117]
Calix-DANS4	1.9×10^{-8} mol L^{-1}	Allow more than 1000 fold for Na^{+}, K^{+}, Hg^{2+} and Cu^{2+}, but abundant Ca^{2+} and Cd^{2+} interfere the detection	[83]

* as a precolumn derivatizing agent in HPLC.

The formation of two different complexes were proposed (see Figure 2.3): a 2:3 complex (M_2L_3) and a 1:1 complex (ML) with Pb^{2+} were successively formed with the following stability constants: $logK_{23} = 33.5 \pm 1.5, logK_{11} = 10.0 \pm 0.5$.

$$2M + 3L \rightleftarrows M_2L_3 \qquad K_{23}$$

$$M + L \rightleftarrows ML \qquad K_{11}$$

The selectivity towards Pb^{2+} with respect to the other cations was found to be higher than 1000, but the interference of Ca^{2+}, Cd^{2+} should not be neglected as the stability constants of their 1:1 complex were compatible (log $K_{Ca^{2+}}$ = 7.23, log $K_{Cd^{2+}}$ = 7.3) with that of Pb^{2+}. The detection limit was unprecedented (4 μg L^{-1}) and compatible with the level defined by WHO.

A summary of the detection limit and selectivity of these fluoroionophores are presented in Table 2.1. Calix-DANS4 demonstrated relative high sensitivity and selectivity comparing with others.

2.3 Choice of an efficient fluorescent molecular sensor

Since the miniaturization of the system requires the use of a low-cost LED (Light-emitting diode), we are limited in the choice of the excitation wavelength. For our microfluidic detection system, the efficient fluorescent sensor should satisfy primarily one requirement, that is it can be excited in the near UV, because of our care to use a commercial LED source, emitting in this wavelength range. The best compromise in term of cost and performance is to use a 365 nm LED. As described above, Calix-DANS4 was a good candidate of fluorescence sensor for lead ion, which had excellent sensitivity and selectivity. And it fitted for our requirements (λ_{ex}=350 nm). We chose it for our lead ion detection study.

Because of the shift to lower wavelengths of the absorption spectra upon lead complexation (see Figure 2.4a), a decrease of the absorbance upon lead complexation is observed at 365 nm. We also chose to optimize the pH of the solution in order to increase the amplitude of the response. We tried several pHs, the best compromise in term of variation of the fluorescence intensity and efficiency of the binding was pH 3.2. In order to have a higher change of the fluorescence intensity, we have chosen to observe the fluorescence at a high wavelength where there is a decrease of the fluorescence (with a high-pass filter at 515 nm). In this condition, the fluorescence signals mainly decreased when increasing the concentration of Pb^{2+}. At pH 3.2, fluorescence spectra of Calix-DANS4 when increasing the concentration of lead ion are shown in Figure 2.4b.

The stability of the complex was then examined in this condition. Analysis (using SPECFIT Global Analysis software) of the emission spectra on gradual addition between 3.2×10^{-7} mol L^{-1} and 2.7×10^{-5} mol L^{-1} of lead thiocyanate revealed the formation of two complexes of 2:3 and 1:1 (metal : ligand) stoichiometry with the constants of $logK_{23} = 23.6 \pm 0.1, logK_{11} = 6.23 \pm 0.05$, which was smaller than the values that Metivier obtained at pH 5.2. It indicates that the complexation at pH 3.2 is less stable than at pH 5.2. That's

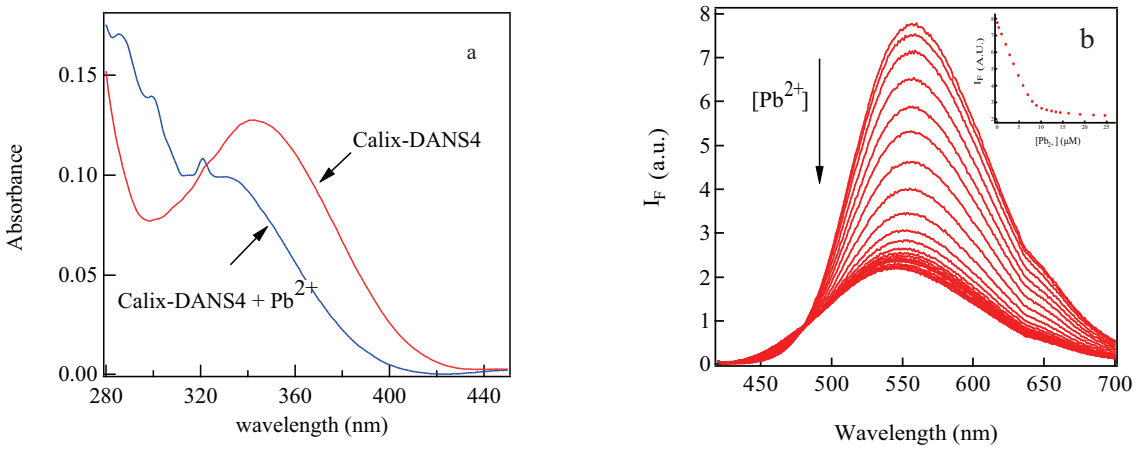

Figure 2.4: (a) UV-Visible spectra and (b) fluorescence spectra of Calix-DANS4 and its complex with Pb^{2+} when increasing the concentration of Pb^{2+}. All are in a milieu CH_3CN/H_20 (60:40 v/v), pH 3.2, [Calix-DANS4]= 5.6×10^{-6} mol L^{-1}, λ_{exc}=365 nm

because there are more protonated forms of Calix-DANS4 at pH 3.2, which are less efficient for the interaction with lead ion.

2.3.1 Effect of fluoroionophore concentration

The concentration of fluorescent sensor is a major factor which governs the experimental response. The effect of concentration of fluoroionophore to cation titration was mentioned by Valeur [77]. The Eq.2.1 demonstrated the relationship between the fluorescent intensity and ratio of c_M/c_L for a complex ML 1:1.

$$Y = Y_0 + \frac{Y_{lim} - Y_0}{2}\{1 + \frac{c_M}{c_L} + \frac{1}{Kc_L} - [(1 + \frac{c_M}{c_L} + \frac{1}{K_s c_L})^2 - 4\frac{c_M}{c_L}]^{1/2}\} \qquad (2.1)$$

where Y_0 is the photophysical parameter observed (absorbance, fluorescence...) of the free ligand, it is proportional to the concentration c_L; Y_{lim} is the limiting value in the presence of an excess of cation such that the ligand is fully complexed; Y is the photophysical parameter observed (absorbance, fluorescence...) after addition of a given amount of cation at a concentration c_M. K is the complexation constant. Figure 2.5 shows the variations of $(Y - Y_0)/Y_0$ versus c_M/c_L for $Y_{lim} = 2Y_0$, representing the spectrofluorimetric titration curves for this kind of complex ML.

If c_L is too large, the detection sensitivity, which is related to the ratio of the concentration of Pb^{2+} to the concentration of fluorescent sensor, is too small. Inversely, if it is too weak, the ratio of signal to noise (S/N) is too small.

So there is an optimal ligand concentration to be determined, not too low in order to keep an acceptable S/N ratio, and not too high in order to save a good sensitivity.

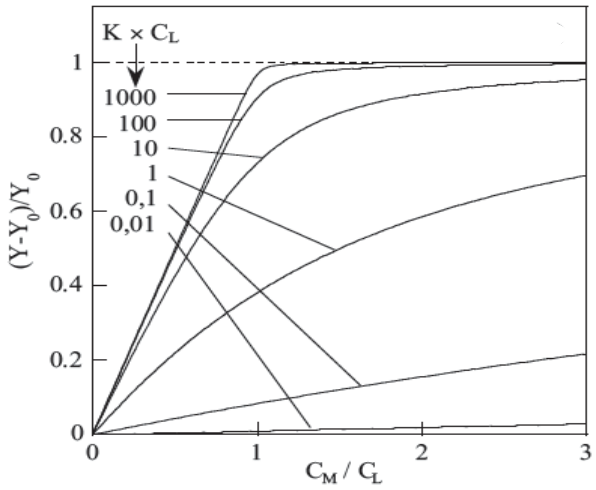

Figure 2.5: Spectrofluorimetric titration curves for a complex 1:1.

Our later measurements will prove that the concentration of fluoroionophore does affect the titration curve. A microchip with a particular design has a particular sensitivity and some suitable concentration range for cation detection.

2.4 Fluorimetric microfluidic device performance

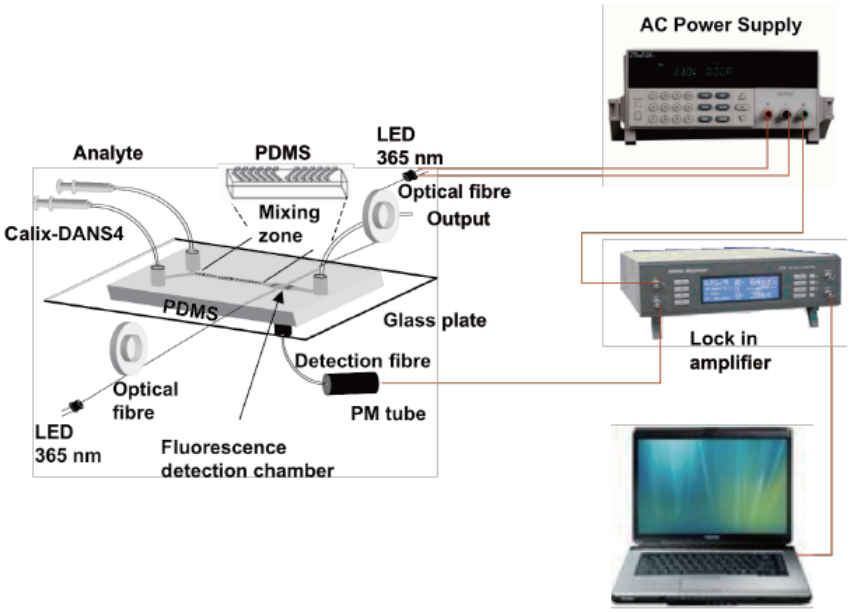

Figure 2.6: Schematic microfluidic system

The scheme of the experimental set-up of our microfluidic device is shown in Figure 2.6.

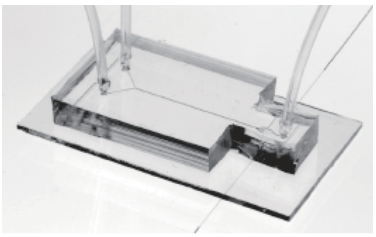

Figure 2.7: Photograph of the microchip with connected fibres and tubings

A microchip which included a Y-shape microchannel (see Figure 2.7) was employed in our work. Microfabrication procedures were used to prepare the microfluidic chip using molded PDMS and glass coverslip as described in Appendix A.1. Two inlet tubes enabled introduction of both analyte and fluorescent molecular sensor solutions via syringes mounted on two commercial syringe pumps (Harvard type PHD 2000). Mixing of the solutions was achieved in the microchannel (200 μm wide, 100 μm high) via a passive mixer analogous to that described by Stroock et al. [28] (see Figure 1.7), with ridges 200 μm wide and 25 μm high. The efficiency of mixing was assessed by use of a fluorescent dye and confocal microscopy in our lab [98]. A 365 nm UV LED (UVLED 365-10, 1.4 mW) was used as excitation source, the power supply of which, modulated with a square signal (77 Hz) enabled lock-in amplifier detection of fluorescence. A lock-in amplifier uses phase-sensitive detection, in which the modulated analytical signal is compared with reference signals at given frequency, then only the component of the input signal at the reference signal is amplified, and all other frequencies, e.g. noise are filterd out, so it can greatly improve the signal-to-noise ratio. The light beam from this LED was focused into 100 μm optical fiber (SiO_2 for the core, doped SiO_2 for the shell, 100/110/125) and then directed into the PDMS microchannel. The optical fiber was embedded in the PDMS matrix, at a distance of 70 μm from the fluidic microchannel. The fluorescence emission of the dye was collected by a bundle of seven optical fibers (core diameter 400 μm, external diameter 440 μm) and focussed through a high-pass filter (OG515) ($\lambda_c > 515$ nm) at the entrance of a PM tube (Hamamatsu R928). The electrical signal from the PM tube was amplified with a current-voltage converter with gain varying from 10^4 to 10^9, in steps. The voltage signal was routed to a lock-in amplifier (Signal Recovery 7265 DSP) and acquired by a PC computer via a RS232 bus; it was at the millivolt level and far from a signal-to-noise ratio of one. The 515-nm high-pass filter in the detection system blocks the scattered excitation beam and allows only fluorescence emission higher than 515 nm to be detected. Since the fluorescence signal is weak, suppressing the scattered excitation beam is a key issue. The

use of a lock-in amplifier also contributes to improve the S/N ratio.

A photo of our set-up is illustrated below (Figure 2.8), which includes the main part of the set-up (LED, microfluidic chip, exciting and recovery optical fibers) in a black box to prevent natural light.

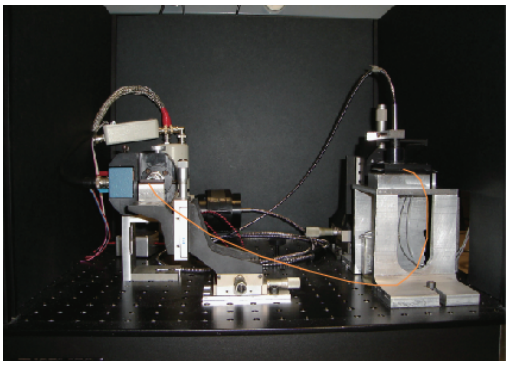

Figure 2.8: Photograph of fluorimetric microfluidic device

2.4.1 SEM images for characterizing the SU8 mold

The molds of PDMS chip in our research which are obtained from rapid prototyping are all SU8 negative photoresist on Si wafer. The structure of the mold was characterized by Scanning Electron Microscope (SEM). SEM images of our Y-type mold are shown in Figure 2.9.

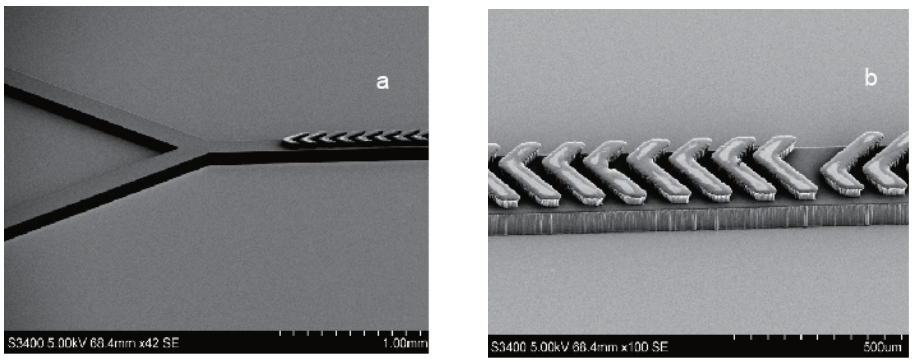

Figure 2.9: SEM images of the SU8 mold (a) microchannel, (b)staggered herringbone mixer.

Well defined structures of microchannel and staggered herringbone mixer are observed. These images show high resolution for these $\sim 100\mu$m structures. These molds can be used hundreds of times. It is a very economic choice for chip making.

2.5 Device design and performance

In order to get better sensitivity, several microchips were designed and their performances are demonstrated as follows. All these chips have a passive mixer and the same dimension (200 μm wide, 100 μm high) for the microchannel.

2.5.1 Choice of the microchip

Microchip I

Firstly, we carried out the lead ion detection in a simple Y-shape microchip I (see Figure 2.10.).

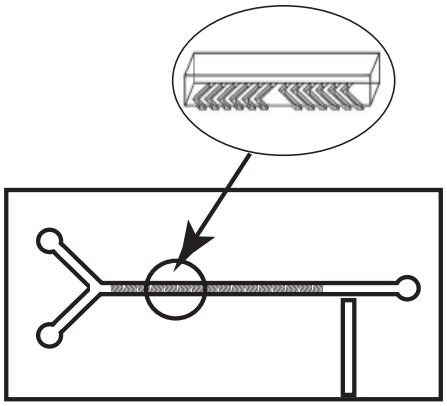

Figure 2.10: Y-shape microchip I

For this chip, there are only a straight mixing channel and one exciting optical fiber. A solution of Calix-DANS4 $(1 \times 10^{-5}$ mol $L^{-1})$ in CH_3CN/H_20 (60:40 v/v) (pH=3.2) was introduced in one channel at a flow rate of 0.5 mL h^{-1} and meanwhile solutions of lead ions at concentration between 1×10^{-7} mol L^{-1} and 3×10^{-5} mol L^{-1} in CH_3CN/H_20 (60:40 v/v) (pH=3.2) were introduced into the second channel at the same flow rate. Calix-DANS4 was excited at 365 nm and fluorescence was collected after using a 515 nm band-pass filter. The Calix-DANS4 fluorescence response to increasing concentrations of lead ion are depicted in Figure 2.11a. And Figure 2.11b shows the calibration plot, i.e. the plot of fluorescence intensity versus lead concentration (in the input solution).

This experiment clearly showed the capability to detect lead ion in 10^{-6} mol L^{-1} range. As mentioned previously, the calibration curve was non linear, and depended on the concentration of ligand. The detection limit, defined as the concentration at which the signal differs from the reference signal by 3σ (standard deviation, σ=0.0002 V) was found to be 5×10^{-7} mol L^{-1}.

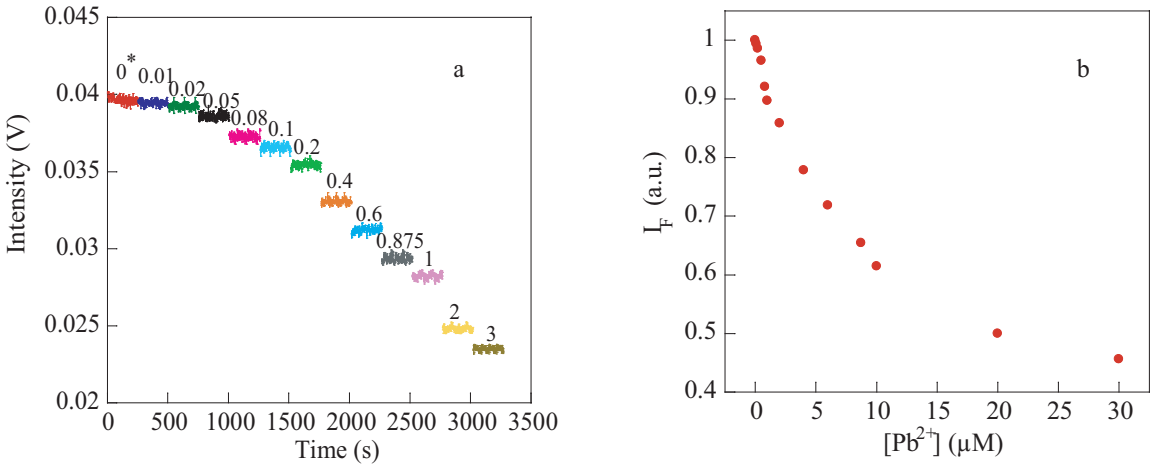

Figure 2.11: (a)Variations in fluorescence intensity measured at the end of microfluidic channel for different lead concentration added in one channel of microchip I. The numbers on the signals represent [Pb^{2+}]/[Calix-DANS4]. (b) Plot of fluorescence intensity versus lead concentration introduced in the analyte channel. Composition of the analyte solution: Lead thiocyanate at the desired concentration in 60:40 (v/v) Acetonitrile/H_2O. Composition of the fluorescent solution: Calix-DANS4 (10^{-5} mol L^{-1}) in 60:40 (v/v) Acetonitrile/H_2O. Flow rate is 0.5 ml h^{-1}.

With this chip, the titration curves under two concentrations of Calix-DANS4 were obtained in order to test the effect of concentration of ligand. Our measurements proved that the concentration of fluoroionophore does affect the titration curve (see Figure 2.12), (a) shows that when a larger concentration is applied, more decline in the calibration curve appears, while (b) tells us with weaker concentration we can get higher sensitivity.

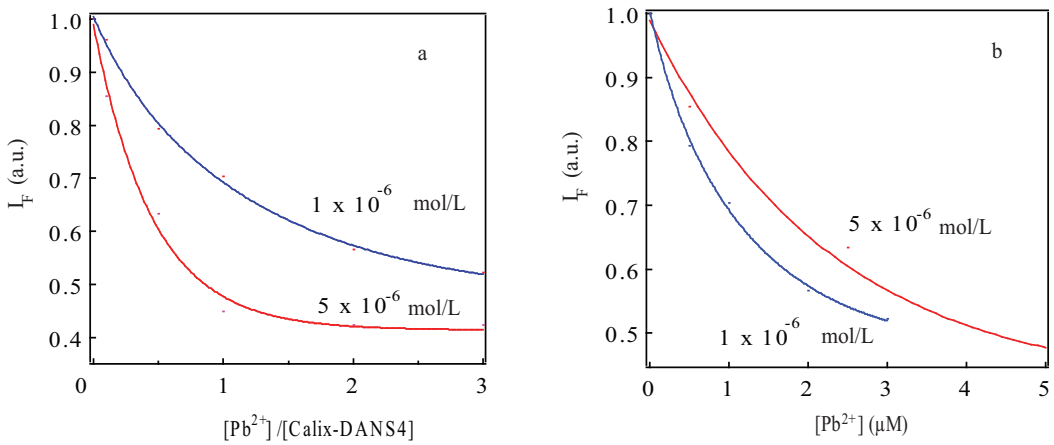

Figure 2.12: Effect of the concentration of Calix-DANS4 for titration curves. The values beside the curves represent the concentration of Calix-DANS4. Other conditions are as in Figure 2.4.

Microchip II

Then, in order to enhance the fluorescence intensity and increase the detection sensitivity, we improved our microchip by adding a bend to enlarge the detection zone (see Figure 2.13).

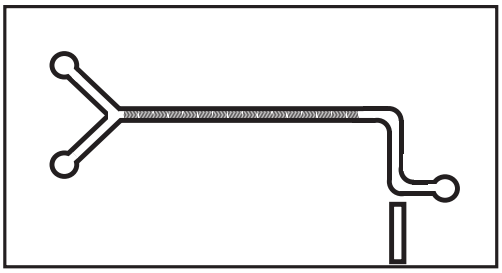

Figure 2.13: Microchip II

The experimental conditions were just as for microchip I. The Calix-DANS4 fluorescence response to increasing concentrations of lead ion are depicted in Figure 2.14a. And Figure 2.14b shows the calibration plot, i.e. the plot of fluorescence intensity versus lead concentration (in the input solution).

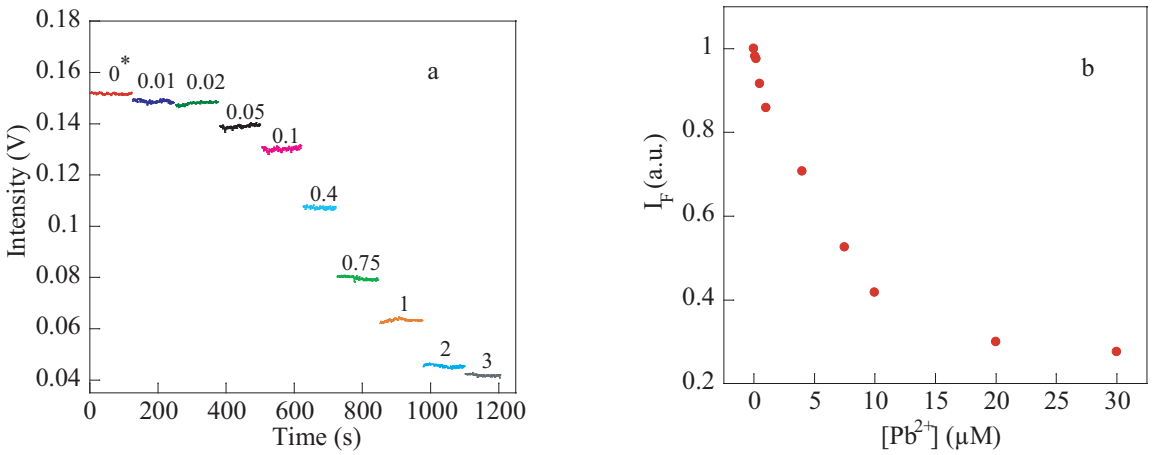

Figure 2.14: (a)Variations in fluorescence intensity measured at the end of microfluidic channel for different lead concentration added in one channel of Microchip II. The numbers on the signals represent [Pb^{2+}]/[Calix-DANS4]. (b) Plot of fluorescence intensity against lead concentration introduced in the analyte channel. Composition of the analyte solution: Lead thiocyanate at the desired concentration in 60:40 (v/v) Acetonitrile/H_2O. Composition of the fluorescent solution: Calix-DANS4 (10^{-5} mol L^{-1}) in 60:40 (v/v) Acetonitrile/H_2O. Flow rate is 0.5 ml h^{-1}.

This improvement has increased the fluorescence intensity by a factor of 3 and thus decreased the detection limit which was found to be 1×10^{-7} mol L^{-1} in this bend microchip.

Microchip III

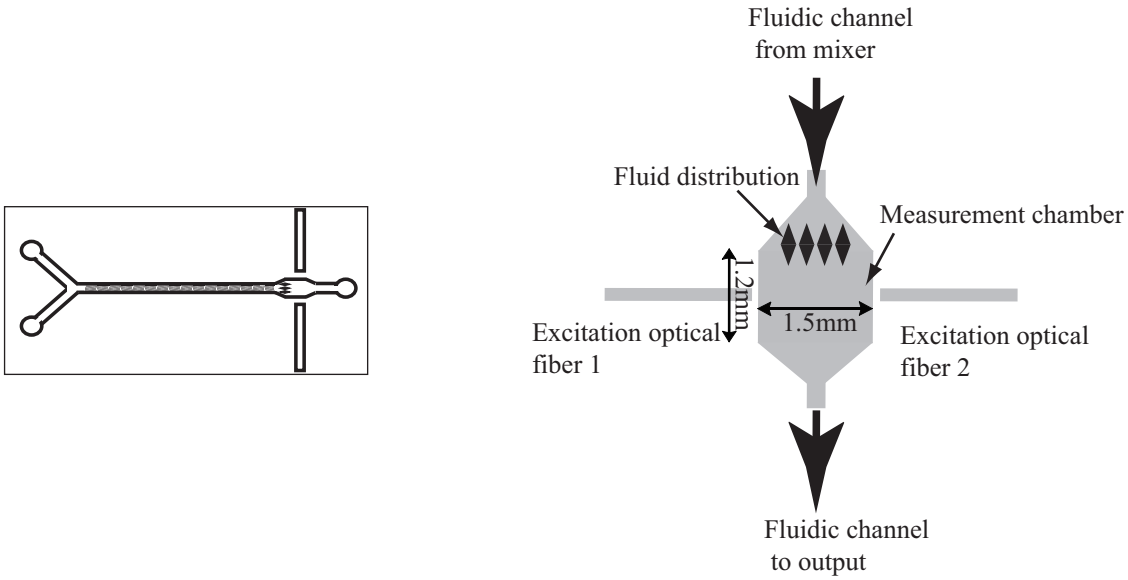

Figure 2.15: Microchip III (left) and detection chamber (right)

In order to increase more the sensitivity, a new detection chamber has been designed in microchip III (as in Figure 2.15). Dual-optical fibers, each excited by a LED, were used in both sides of the chamber.

Meanwhile the distribution of fluid in this new detection chamber was simulated with a commercial modeling software COMSOL MULTIPHYSICS 3.4, as illustrated in Figure 2.16. The comparison of velocity profiles in the detection chamber with and without diamand-shape pillars showed that the fluid was distributed more uniformly in the detection chamber which had four diamand-shape pillars. So it can eliminate the fluctuation of the signal.

The concentration of Calix-DANS4 could be decreased to $1\times\ 10^{-6}$ mol L^{-1}, other experimental conditions were just as for microchip III. Let us remember that lower concentration of fluoroionophores allow to detect low concentration of heavy metal ions (see Figure 2.12). Furthermore, taking into account the extinction coefficient of Calix-DANS4 which was lower than 15000 $M^{-1}cm^{-1}$ at 365 nm, and the concentration of Calix-DANS4, the optical density of the fluorescent dye at the excitation wavelength inside the irradiation chamber has been estimated to be lower than 0.001, which ensured a homogeneous excitation across the chamber.

A calibration plot for determination of lead in this microfluidic device was then conducted. The Calix-DANS4 fluorescence response to increasing concentrations of lead ion is depicted in Figure 2.17a. And Figure 2.17b shows the calibration plot, i.e. the plot of fluorescence intensity versus lead concentration (in the input solution).

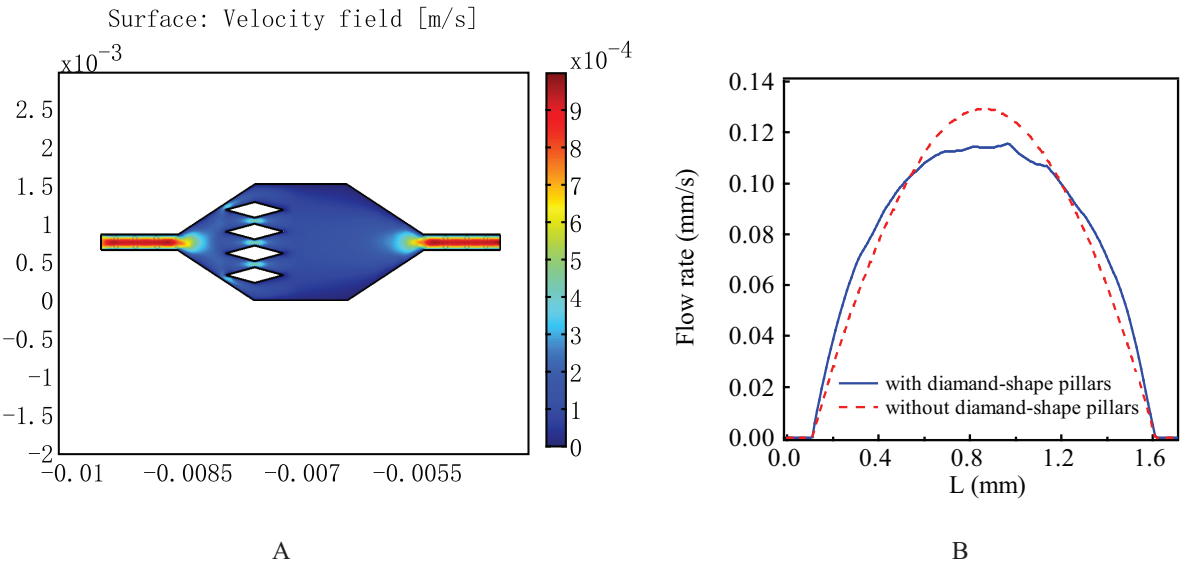

Figure 2.16: (A)Fluid velocity distribution simulation in detection chamber by Comsol. Flow rate is 0.5 ml h^{-1}. The colors indicates different velocities. (B)The velocity profiles in the detection chambers with and without diamand-shape pillars.

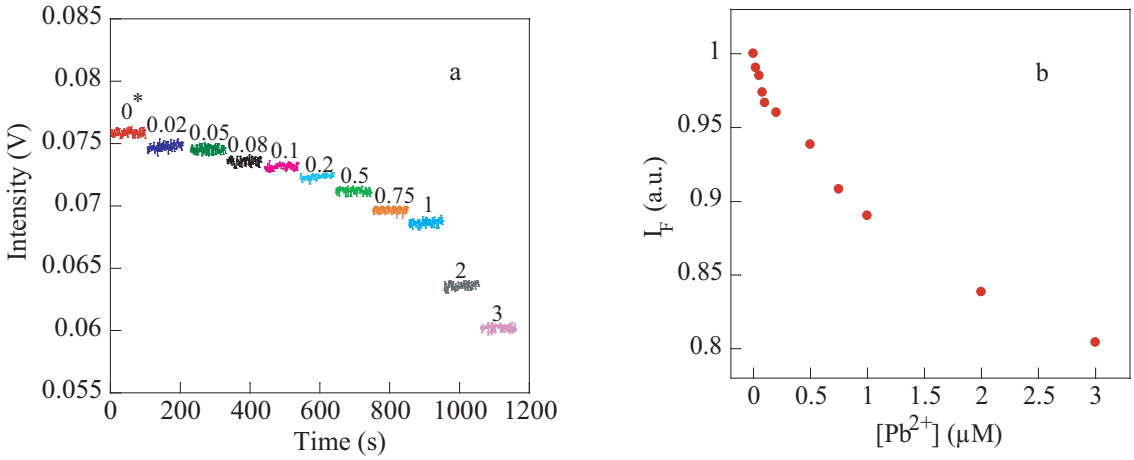

Figure 2.17: (a)Variations in fluorescence intensity measured at the end of microfluidic channel for different lead concentration added in one channel of Microchip III. The numbers on the signals represent [Pb^{2+}]/[Calix-DANS4]. (b) Calibration curve of the microchip response upon lead addition. Composition of the analyte solution: Lead thiocyanate at the desired concentration in 60:40 (v/v) Acetonitrile/H_2O. Composition of the fluorescent solution: Calix-DANS4 (10^{-6} mol L^{-1}) in 60:40 (v/v) Acetonitrile/H_2O. Flow rate is 0.5 ml h^{-1}.

This improvement has greatly increased the fluorescence intensity and thus decreased the detection limit which was found to be 5×10^{-8} mol L^{-1} in this detection chamber.

2.5.2 Microchip IV

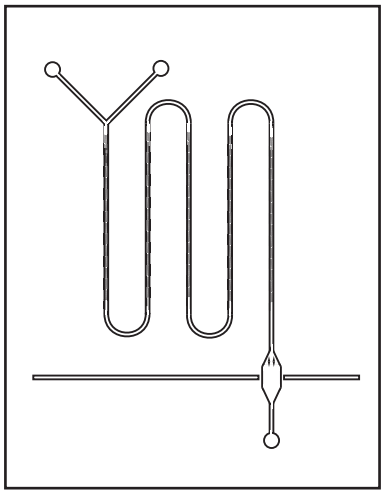

Figure 2.18: Scheme of Microchip IV.

Microchip IV is a new designed microchip with longer microchannel compared with other three chips (Figure 2.18). It was designed to improve the complexation reaction between Calix-DANS4 and lead ion when studying this reaction in microfluidic device in Chapter 4. More details will be described in Chapter 4. Here, we just arrange its quantitative measurements with others together. The detection limit in microchip IV has been tested (from Figure 2.19a). A detailed titration curve for very low lead concentrations in microchip IV is shown in Figure 2.19b.

The detection limit was determined from Figure 2.19, which was 2.5×10^{-8} mol L^{-1} (i.e. 5.2 μg L^{-1}) for a flow rate of 0.25 ml h^{-1}. This detection limit is twice lower than for Microchip III. So we still improved the sensibility of our device by a factor of two.

Conclusion

From these results, we can conclude that the design of the optical chamber in which the fluorescence was measured and dual-exciting in Microchip III greatly increased the sensitivity. So this microchip was chosen to conduct our lead ion detection later (unless otherwise specified). And the concentration of Calix-DANS4 was chosen to be 1×10^{-6} mol L^{-1} in order to get more sensitivity in microchip III. The detection limit, defined as the concentration at which the signal is equal to the blank signal plus (minus) 3σ (N=5), was found to be 5×10^{-8} mol L^{-1} (i.e. 10 ppb, which corresponds to 26 ppb in the initial water solution, taking into account the addition of acetonitrile) for Microchip III. It is noteworthy that this value is nearby the maximum allowed quantity of lead in drinking water since

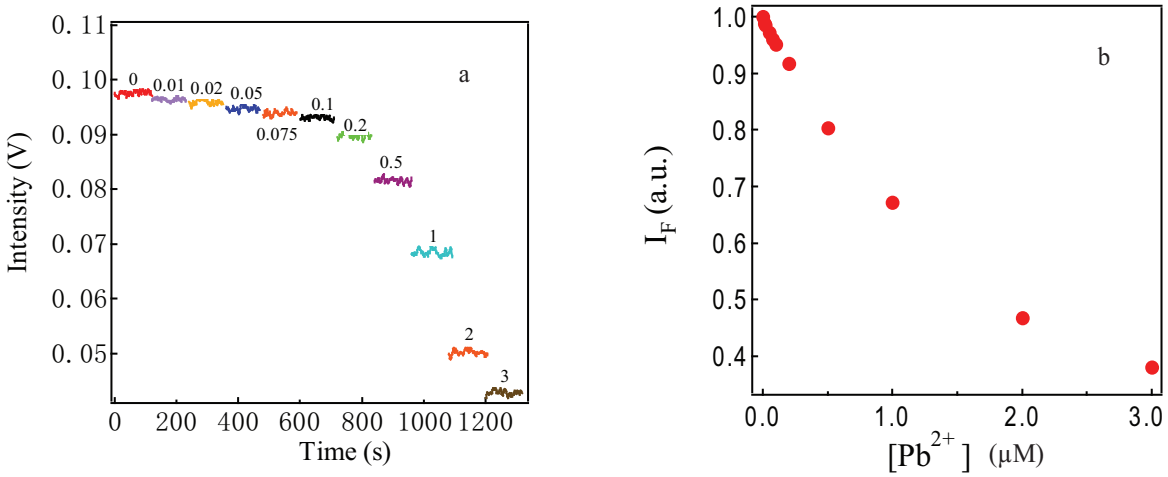

Figure 2.19: (a)Variations in fluorescence intensity measured at the end of microfluidic channel for different lead concentration added in one channel of Microchip IV. The numbers on the signals represent [Pb^{2+}]/[Calix-DANS4]. (b) Calibration curve of the microchip response upon lead addition. Composition of the analyte solution: Lead thiocyanate at the desired concentration in 60:40 (v/v) Acetonitrile/H_2O. Composition of the fluorescent solution: Calix-DANS4 (10^{-6} mol L^{-1}) in 60:40 (v/v) Acetonitrile/H_2O. Flow rate is 0.25 ml h^{-1}.

2003 (10 ppb). With Microchip IV, which is longer than Microchip III, we still decreased the detection limit to 5 ppb, which is lower than the European norm for 2013.

2.5.3 Reproducibility

The stability and reversibility of the fluorescence signal of Calix-DANS4 in the microchannel were verified by introducing alternately pure solvent (CH_3CN/H_2O 60:40 v/v at pH 3.2) and Calix-DANS4 solution. The reproducibility is demonstrated in Figure 2.20, (a) for 1×10^{-5} mol L^{-1} Calix-DANS4 in Microchip I , (b) for 1×10^{-6} mol L^{-1} Calix-DANS4 in Microchip III. The signal level only varies by 0.1% for each microchip. It is also interesting to note that the signal over noise ratio is very good (S/N >50).

2.5.4 Influence of Calcium

Métivier et al have shown that the co-existing calcium ion can form a compatible complex with Calix-DANS4, with a stability constant of log $K_{Ca^{2+}}$ = 7.23 for 1:1 complex [118]. Also as we know, concentration of calcium in surface water is about 10^{-3} mol L^{-1} for a slightly hard water. Despite the high selectivity of calix-DANS4 to lead determination demonstrated in cuvette experiments, we checked the interference of calcium ions in our microfluidic set-up.

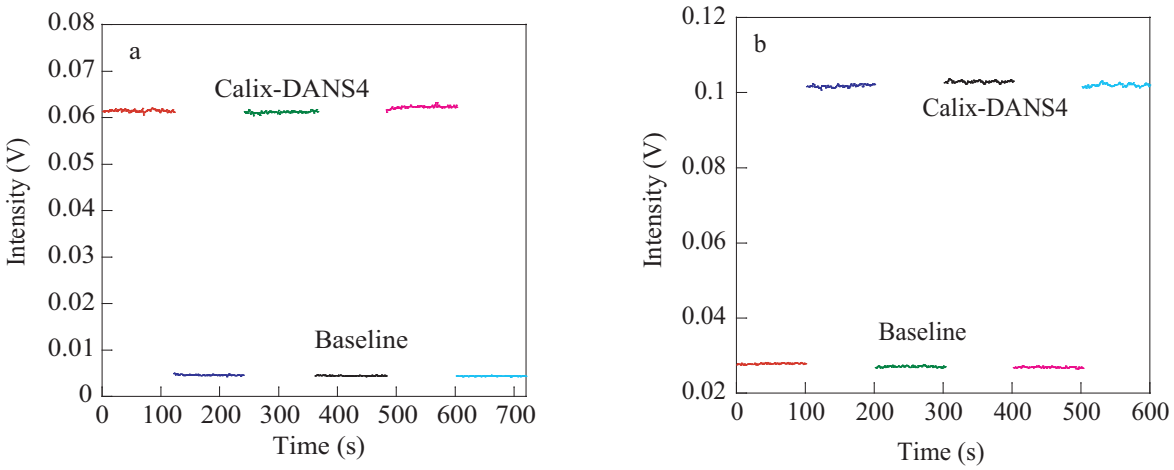

Figure 2.20: Reproducibility tests (a)[Calix-DANS4] is 1×10^{-5} *mol* L^{-1} *in Microchip I. (b) [Calix-DANS4] is* 1×10^{-6} *mol* L^{-1} *in Microchip III. Flow rate is 0.5 ml* h^{-1}.

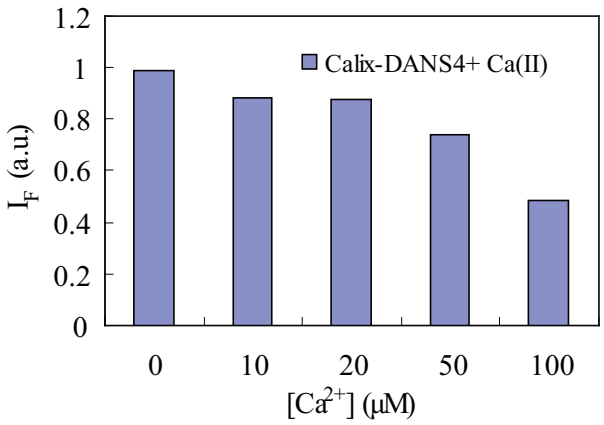

Figure 2.21: Interference of calcium ion in Microchip I. The concentration of Calix-DANS4 is fixed to 1×10^{-5}*mol* L^{-1}*. Flow rate is 0.5 ml* h^{-1}.

Then, the interference of calcium ion was checked in more concentrated calcium solution. Two concentrations of Calix-DANS4 ligand were used. Firstly, the concentration of Calix-DANS4 was fixed to 10^{-5} mol L^{-1}, and we used the microchip I (Figure 2.10). In this microchip, we determined the minimum concentration of Ca^{2+} that affected the detection of lead ion (see Figure 2.21). A series concentrations from 10^{-5} mol L^{-1} to 10^{-3} mol L^{-1} of Ca^{2+} was introduced into the microchannel. When $[Ca^{2+}]$ was above 10^{-5} mol L^{-1}, it affected the fluorescence signal. We found that the fluorescence declined 20% when $[Ca^{2+}]$ was 5×10^{-4} mol L^{-1}.

Secondly, with a concentration of 10^{-6} mol L^{-1} Calix-DANS4, we determined the limit concentration which could interfere with lead ion detection. We fixed the concentration of lead ion to 10^{-6} mol L^{-1}, which resulted in an obvious fluorescence quenching, then

introduced different concentrations of calcium. The results are as in Figure 2.22: when [Ca^{2+}] is above 10^{-4} mol L^{-1}, it has an interference effect.

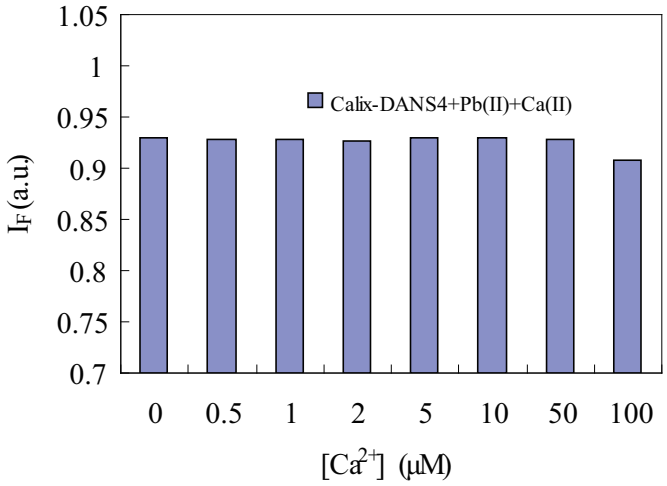

Figure 2.22: Interference of calcium ion in Microchip III. The concentrations of Calix-DANS4 and lead ion are fixed to 1×10^{-6} *mol* L^{-1}*. Flow rate is 0.5 ml* h^{-1}*.*

For practical use in the assay of lead in surface water, we have to take care of interferences with other ions, mainly calcium which is abundant in waters with a high hydrotimetric degree. We found that the fluorescence of Calix-DANS4 (10^{-6} mol L^{-1}) in the presence of lead ions (10^{-6} mol L^{-1}) did not change for calcium concentrations below 10^{-4} mol L^{-1}. However, a slight decrease was observed for higher calcium concentrations which showed that positive interference with calcium ion may occur in the determination of small traces of lead in surface water rich in calcium.

2.6 Sample analysis

Water samples containing a given concentration of lead were made by putting water (Millipore 18 MΩ) in contact with a piece of lead for 2 min and 30 min, respectively, then each was diluted 100 times by deionized water to get Sample 1 and Sample 2. The lead concentrations of these two samples were measured by two different methods, first fluorimetric titration in our microfluidic device and second anodic stripping voltammetry (ASV) (See Appendix A.4.3).

The microfluidic device, as described previously, was used to determine these two samples. Microchip III was applied in these determinations. A calibration curve was obtained (see Figure 2.17b) at first, and the samples were tested in the same conditions. (Solvent: 60:40 (v/v) Acetonitrile/H_2O, [Calix-DANS4]= 10^{-6} mol L^{-1}, pH 3.2, flow rate: 0.5 ml

h^{-1}.) Then comparing the signals of samples and the calibration curve, we could get the concentration of lead ion in the samples. Each sample was tested five times with RSD of less than 10%.

A calibration curve with known lead thiocyanate solutions at pH 2 was drawn by the ASV method, and a detection limit of 5×10^{-9} mol L^{-1} was determined for this method. The concentrations of lead ion in samples were determined according to the calibration curve, with RSD about 5%. The results are gathered in Table 2.2. Good correlation is obtained with the two methods.

Table 2.2: Determination of the lead content in two water samples, by fluorimetric titration and by ASV, n=3

	Microfluidic device (mol L^{-1})	ASV (mol L^{-1})
Sample 1	$(3.45 \pm 0.32) \times 10^{-8}$	$(3.86 \pm 0.23) \times 10^{-8}$
Sample 2	$(1.15 \pm 0.10) \times 10^{-7}$	$(1.07 \pm 0.06) \times 10^{-7}$

2.7 Conclusion

In conclusion, we have demonstrated the feasibility of incorporating a Pb^{2+} selective fluorescent molecular sensor in a microfluidic device and its application for the detection of lead in water. This device is made of PDMS polymer with the bottom of the main channel structured in order to make a passive mixer. The fluorescent molecular sensor is flowed inside the microchannel and the water to be analysed is incorporated in another one. The mixture is excited with a 365 nm LED. At first the pH has been optimized in order to obtain the highest variation upon lead complexation in the microchip system. At pH 3.2 a calibration plot relating the decrease of the fluorescence intensity towards the lead concentration has been obtained with a 2.5×10^{-8} mol L^{-1} (i.e. 5.2 μg L^{-1}) detection limit. Furthermore, this system can be regenerated by injection of mixture solvent in the microchip.

However, considering the real application for lead ion detection in surface water, the devices described above still need to be improved because of their limited sensitivity and influence of calcium ion. Chapter 3 will introduce an improved microfluidic system and this system will be applied to the lead ion detection in tap water.

Chapter 3

Detection of Pb^{2+} in tap water based on solid phase extraction

3.1 Introduction

There are many quantitative testing methods for toxic heavy metal ions, e.g. Pb^{2+}, Hg^{2+}, Cd^{2+} in matrix samples; however, because of the high setting up costs and high running costs of sophisticated instrumental methods, such as atomic absorption spectrometry (AAS) and inductively coupled plasma mass spectrometry (ICP-MS), considerable interest has been focused on the development of low cost and portable apparatus. On the other hand, even with these selective and sensitive analytical techniques, there is a crucial need for the preconcentration of trace elements before their analysis due to their frequent low concentration in numerous samples (especially water samples).

Reliable, low cost, quick analytical techniques that permit real time sampling of Pb^{2+} are important in the fields of environmental monitoring, clinical toxicology, waste water treatment, and industrial monitoring. The development and fabrication of microfluidic systems for analyzing chemical and biological samples has increased dramatically in the past decade.

Our aim is to develop an economical microfluidic device for heavy metal ions detection in real time. Our system developed in Chapter 2 has demonstrated its potential in real time heavy metal ion detection. In order to apply to environmental monitoring, a micro-column solid phase extraction will be added before fluorimetric microfluidic lead detection.

Sample preconcentration is a crucial step in the development of multifunctional integrated microfluidic devices. The most important is that it enables purification of samples and detection of trace or low-abundance species. This is of particular importance in the field of clinical diagnostics, forensics, environmental monitoring, and biodefense applications.

This chapter demonstrates the combination of a commercial amino-functionalized sil-

ica gel based solid phase extraction with a fluorimetric microfluidic device. The methods for adapting this real time lead ion detection in tap water to the microfluidic device are explored, an optimal protocol is identified, and the method validation including calibration curve, limit of detection, accuracy, and precision are determined.

3.2 Preconcentration

Lead usually exists in unpolluted natural waters at levels below 1 μg L^{-1}, difficulties still lie in its analysis because of both its low abundance levels in the samples and the high complexity of the sample matrices, even with modern sensitive instrumentation such as GFAAS or ICP-MS, so preconcentration and/or separation steps are often necessary [119, 120]. Among the available methods for concentrating specific metal species from water, solid phase extraction has been shown to be promising for determination of trace elements in view of an enhanced sensitivity, the efficient removal of matrix, the high sample throughput.

Various sample preconcentration techniques including solvent extraction, coprecipitation, cloud point extraction [121], ion-exchange, solid phase extraction and electroanalytical techniques [122] have been used for the enrichment and separation of heavy metals at trace levels in various environmental samples around the world. Solid phase extraction is an attractive separation preconcentration technique for heavy metal ions with some important advantages: simplicity, flexibility, economic, rapid, higher enrichment factors, absence of emulsion, low cost because of lower consumption of reagents, more importantly environment friendly. Various solid phase extraction materials have been successfully used for the preconcentration and separation of heavy metal ions at trace levels [123]. For example, MCI GEL CHP 20Y polymeric resin as a sorbent in a solid phase extraction column was used to extract nickel, silver, cobalt, copper, cadmium and lead ions in the aide of a spectrophotometric reagent 2-(2-Quinolinil-azo)-4-methyl-1,3-dihydroxidobenzene (QAMDHB) [124]. A mini-column packed with sulfur as a new solid phase extractor has been developed for simultaneous preconcentration of lead and cadmium in water samples prior to flame atomic absorption spectrometric determinations [125]. Octadecyl-bonded silica membrane disks modified with 1,8-dihydroxy-2,7-bis(prop-1'-enyl)-9,10-anthraquinone were applied for extraction and determination of trace amounts of lead(II) ions in water samples [126]. Tsogas et al. suggested that cation exchange resin should be preferable for the extraction and preconcentration of Cd^{2+} and Sn^{4+} while solid phase extraction (SPE) offers better results for Pb^{2+}, after comparing three popular preconcentration methods: cation exchange resin, physical absorption onto activated carbon and hydrophobic extraction of metal chelates on C18 cartridges. The limit detection for Pb^{2+} was about 0.1 μg ml^{-1} [127].

3.2.1 Solid Phase Extraction

Solid-phase extraction (SPE) for liquid samples became a widely used laboratory technique following the introduction in the 1970s of disposable sorbent cartridges containing porous particles sized to allow sample processing by gentle suction.

The development of solid phase extraction brought alternative sampling formats from cartridge to disk. Disk technology has gained acceptance for processing both large sample volumes and small volumes, but otherwise cartridge devices are still dominant. A typical solid-phase extraction cartridge consists of a short column containing a sorbent with a nominal particle size of 50-60 μm, packed between porous metal or plastic frits.

Four distinct steps are distinguished for sample processing in solid-phase extraction.

1. Condition: the sorbent is conditioned with solvent to improve the reproducibility of analyte retention and to reduce the carry through of sorbent impurities at the elution stage.

2. Sample processing (Adsorption): Sample passes through the sampling device at a controlled flow-rate. The solid is then "loaded" with the analyte of interest.

3. Rinse: After sample processing, the sorbent is rinsed with a weak solvent to displace undesired matrix components from the sorbent without displacing the analytes.

4. Elution: The analytes of interest are eluted from the sorbent in a small volume of strong solvent for subsequent determination.

Poole et al. have extensively reported the main experimental variables that influence analyte recovery by SPE [128]. For conditioning stage, washing step is highly recommended when determining trace elements and conditioning solvent should be similar to that of the sample. In loading stage, sample volume, sample flow-rate, sample pH and sample matrix should be well optimized. While for elution procedure, nature of solvent, solvent pH, solvent flow-rate and solvent volume are all important for efficient elution.

Silica gel based sorbents present the advantages of mechanical, thermal and chemical stability under various conditions. They frequently offer a high selectivity towards a given metal ion. They can be used as a very successful adsorbing agent, as it does not swell or strain, has good mechanical strength and can undergo heat treatment. In addition, chelating agents can be easily loaded on silica gel with high stability, or be bound chemically to the support, affording a higher stability. Retention on silica gel is highly dependent on sample pH values over 7.5-8, as under acidic conditions silanol groups are protonated and ion-exchange capacity of the silica gel is greatly reduced or even reduced to zero at low pHs. The modification of silica gel surface can greatly improve the selectivity. There are two

Table 3.1: Classification of cations and their binding ability with functional group atoms

	Hard cations	Borderline cations	Soft cations
Cations	**Ca**$^{2+}$,Mg^{2+},Na^{+} and other alkaline and alkaline-earth metals	Fe^{2+},Co^{2+},Ni^{2+}, Cu^{2+},Zn^{2+},**Pb**$^{2+}$,Mn^{2+}	Ag^{+},Cd^{2+},Hg^{2+}
Binding capacity	O>N>S, only hard oxygen ligands	(O,O)<(O,N) <(N,N)<(N,S)	O<N<S

approaches for loading the surface with specific organic compounds, chemical immobilization (chemical bond formed between the silica gel surface groups and those of the organic compound) and physical adsorption (organic compound adsorbed on the silanol groups of the silica gel surface). And the sorbents are called functionalized sorbent and impregnated or loaded sorbent.

For trace heavy metal ions, using functionalized sorbent is the common and efficient SPE method. There are several functional group atoms for chelating trace elements. The most frequently used atoms are nitrogen (e.g. amines, azo groups, amides, nitriles), oxygen (e.g. carboxylic, hydroxyl, phenolic, ether, carbonyl, phosphoryl groups) and sulfur (e.g. thiols, thiocarbamates, thioethers). The inorganic cations may be divided into three groups: hard cations, soft cations and borderline cations in the middle. "Hard cations" mean that they have a low polarizability, "soft cations" mean that they are relatively easy to polarize. The chaleting ability of each groups with different functionalized ligands are listed in Table 3.1.

As highlighted in Table 3.1, Pb^{2+} is our aimed cation, which is a borderline cation. It can be strongly bound with the sorbent containing (N,S) or (N,N). While Ca^{2+}, as the major interferent for Pb^{2+} detection in water sample, is a hard cation, can be strongly bound with the sorbent containing oxygen ligands. So it is possible to selectively extract Pb^{2+} instead of Ca^{2+} or other cations using N or S functionalised silica gel sorbents.

3.3 Experimental part: Solid phase extraction for lead ion in water

3.3.1 Principle

In our study, 3-aminopropyl functionalized silica gel which was purchased from Sigma-Aldrich was used as the sorbent for lead ion. Various samples of aminopropyl-functionalized silica gel (APS) are always prepared by grafting an organosilane precursor 3-aminopropyl-

triethoxysilane (APTES) onto the surface of silica gel. The basic principle of this SPE relies on selective complexation of lead ion by 3-aminopropyl functionalized silica gel (APS), as illustrated in Figure 3.1. The chelating efficiency of this silica gel sorbent much depends on the sample pH, because of the properties of functionalized amino ligand.

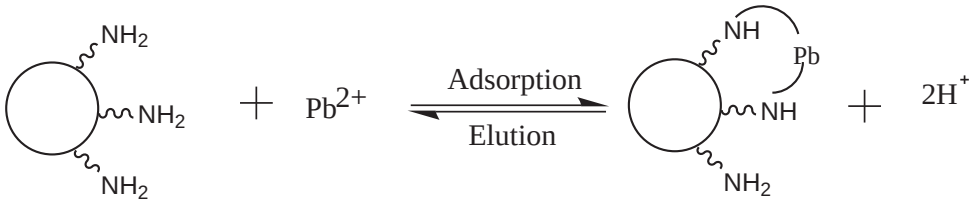

Figure 3.1: Solid phase extraction principle for APS

3.3.2 Procedure

Batch method

The batch procedure was carried out in a plastic flask. 2mg APS was added in 10 mL lead thiocyanate solution and reacted with agitation. The sorbent was separated by centrifugation. The supernatant fluid was collected for residual lead ion determination by Anodic Stripping Voltammetry (ASV) (The principle of ASV is explained in Appendix A.4.3).

Column method

The column procedures were carried out in a home-made mini-column (described below), which acted as a knotted reactor (KR). It consisted of a polytetrafluoroethylene (PTFE) tube properly knotted, which can be applied as a sorbent surface (Figure 3.2). The determination of $[Pb^{2+}]$ was realized by Anodic Stripping Voltammetry (ASV) also.

Reagents and solutions

All reagents were of analytical-grade unless otherwise stated. Standard lead ion solution of 10^{-3} mol L^{-1} was prepared with lead thiocyanate dissolved in Millopore water (18 MΩ). Working solutions were prepared by appropriate dilution of the stock standard solutions with Millipore water (18 MΩ).

Real samples of tap water (or other water source) were filtrated through Millipore TYPE HA filters (pore size, 0.45μm). Commercial 3-aminopropyl functionalized silica gel (Sigma-Aldrich) were used for lead ion extraction. Perchloric acid ($HClO_4$) 0.01 mol L^{-1} was used for the elution of metal complexes from silica gel.

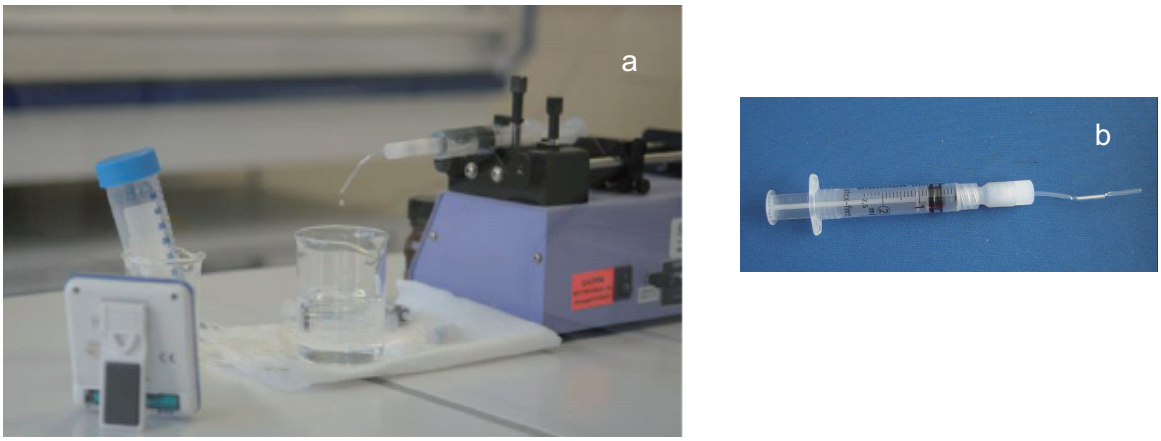

Figure 3.2: (a)Photograph of solid phase extraction process, (b)Photograph of mini-column for lead ion extraction

The pH of the working solutions and real samples was monitored with a standard pH meter (Radiometer PHM 210) and maintained to the desired pH values by drop-wise addition of diluted $HClO_4$ or NaOH.

Manufacture of the PTFE mini-column

The mini-column as shown in Figure 3.2b, at the output of a plastic syringe was a home-made plastic column. A capillary of Polytetrafluoroethylene (PTFE) (Rotilabo-Fep-Schlauch ID 0,8mm) was screwed on one side to prevent the silica gel beads out but let circulate the fluids. From the other side, the slurry of silica gel was introduced with a syringe until about 10 mm long. And then the outlet of the capillary was screwed in the same way. No frits or glass wools were needed at either end to block the silica gel. The weight of this 10 mm long silica gel was about 4∼5 mg. The mini-column was freshly made for each use. Before each use, in order to prevent the loss of sorbent, several milliliters of water were passed through this mini-column at the flow rate of real operation until the length of sorbent in the column becomes constant. The loss of sorbent for each measurement was less than 2%.

3.4 Solid phase extraction features

3.4.1 Adsorption isotherm

The adsorption isotherms were determined using the batch experiments at room temperature. Aqueous solutions of heavy metal ions were shaken with the modified silica gel.

The metal ions in the supernatant were determined by ASV and the adsorbed amount q of heavy metal was calculated using Eq.3.1 as follows:

$$q = \frac{V(C_0 - C)}{m} \tag{3.1}$$

where C_0 is the initial concentration of heavy metal ions (in mol L^{-1}), C the equilibrium concentration of heavy metal ions (in mol L^{-1}), V the volume of heavy metal ions solutions, m the mass of the modified silica gel (in g) and q is amount of heavy metal ions adsorbed per gram of modified silica gel. Adsorption isotherm is often described by the Langmuir equation Eq.3.2:

$$\frac{C_{eq}}{q} = \frac{C_{eq}}{q_m} + \frac{1}{b \times q_m} \tag{3.2}$$

where b is the Langmuir constant, q_m a constant representing adsorption capacity, also known as monolayer coverage of the surface, and is a constant related to b, C_{eq} is adsorbate concentration in the solution at equilibrium.

In order to determine the adsorption capacity q_m, firstly, several samples with same quantity of APS (2mg) in the presence of 10 ml lead ion at 5×10^{-4} mol L^{-1} but reacting for different times (5, 10, 15, 20, 25, 30, 60 min) were tested. The result is shown in Figure 3.3A. In this condition, the complete retention occurs after 25 min and sorption quantity in this test is calculated to be 4.55×10^{-4} mol g^{-1}.

Secondly, the adsorption isotherm was determined by testing a series of lead thiocyanate solutions from 1×10^{-5} mol L^{-1} to 5×10^{-4} mol L^{-1} with 2 mg APS after a retention time of 40 min. Figure 3.3B clearly displays a maximum sorption quantity of 4.7×10^{-4} mol g^{-1} for APS, which matches the result in Figure 3.3A.

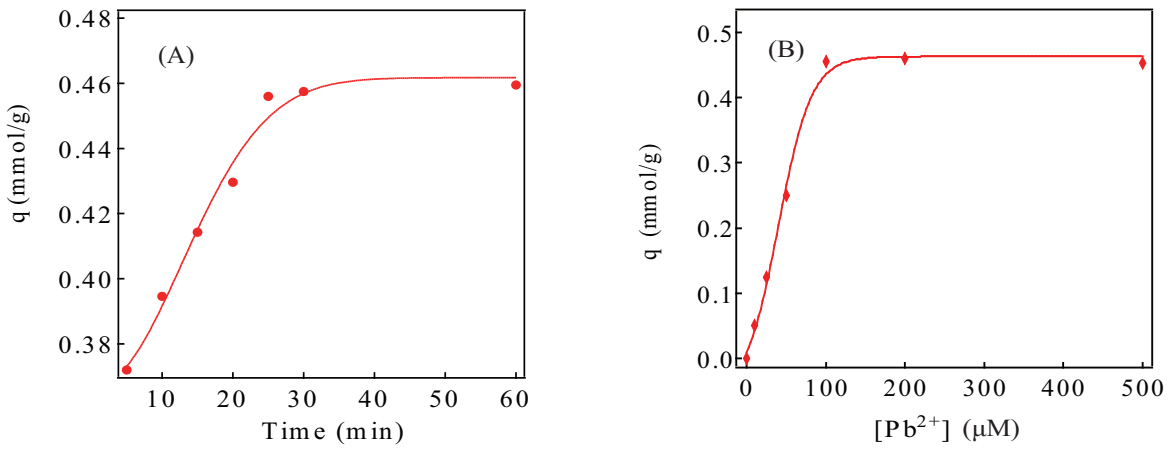

Figure 3.3: (A)Effect of adsorptiong time; (B) The adsorption capacity measurements of 2mg APS at neutral pH.

3.4.2 Column procedure

Effect of pH on sorption

Careful optimization of the pH should be carried out, because it is of prime importance for efficient retention of the trace element on the sorbent. Its influence strongly depends on the nature of the sorbent used, and here it is commercial 3-aminopropyl functionalized silica gel. Several pH values, which were adjusted with NaOH and $HClO_4$ were tested for the effective lead ion extraction from water. As we can see in Figure 3.4, in different pH conditions, 3-aminopropyl functionalized silica gel has a structure which depends on the protonation or deprotonation of the amino group. pH is the most important factor for the sorption of lead ion with this silica gel.

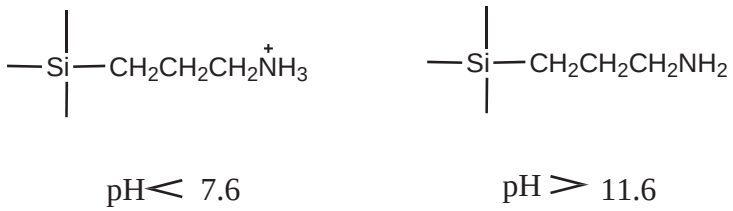

Figure 3.4: Functionalized silica gel (APS) at different pHs

Also the precipitation of metal ion should be considered. The metal cations, e.g. lead ion, can precipitate in aqueous solution according the equilibrium below:

$$M^{2+} + 2OH^- \rightleftarrows M(OH)_{2(s)} \qquad K_{sp} = [M^{2+}][OH^-]^2 \tag{3.3}$$

where K_{sp} is the solubility product constant. Meanwhile, it is able to form other complexes with n OH^-, according the equilibrium below:

$$M^{2+} + nOH^- \rightleftarrows M(OH)_n^{2-n} \qquad \beta_n = \frac{[M(OH)_n^{2-n}]}{[M^{2+}][OH^-]^n} \tag{3.4}$$

where β_n is the formation constant of hydroxide complexes. The solubility product constant and three formation constants for lead ion are as follows (Table 3.2):

Table 3.2: Solubility product constant and hydroxide complex formation constant for lead ion

Cation	-log(K_s)	log(β_1)	log(β_2)	log(β_3)
Pb^{2+}	16.09	6.2	10.3	13.3

According to the solubility product constant and hydroxide complex formation constants, Figure 3.5 can illustrate the precipitate area of lead ion.

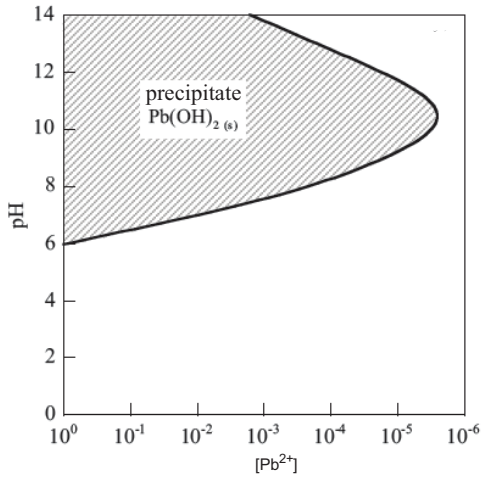

Figure 3.5: Precipitate region of lead ion in aqueous solution [129]

Finally three pHs (8, 9, 10) were studied for lead ion extraction (1×10^{-6} mol L^{-1}), using 0.5 ml 10^{-2} mol L^{-1} $HClO_4$ as the elution solution with a flow rate of 0.5 ml min^{-1}. Higher pHs can cause instability of silica gel sorbent. Best retention was obtained at pH 10 with about 95% retention.

Table 3.3: Extraction efficiency in different pHs

	pH 8	pH 9	pH 10
Efficiency (%)	-*	70	95

* - means there is little lead ion found.

Influence of flow rate during the sorption process

The sample flow-rate should be optimized to ensure quantitative retention along with minimization of the time required for sample processing. As a rule, cartridges and columns require lower maximum flow-rates than disks ranging typically from 0.5 to 5 ml min^{-1} in SPE procedure which was described by Poole et al. [128]. Considering the less firm quality of our home-made mini-column, the flow rate of sorption was studied in the range of 1 ml $min^{-1} \sim 2.5$ ml min^{-1} maintaining 0.5 ml min^{-1} for elution step. The diagram of retention quantity vs. flow-rate is desplayed in Figure 3.6.

From this diagram, we can see that the flow-rate in this range has not much influence on the sorption. We chose 2 ml min^{-1} as our flow-rate for sample loading process in the

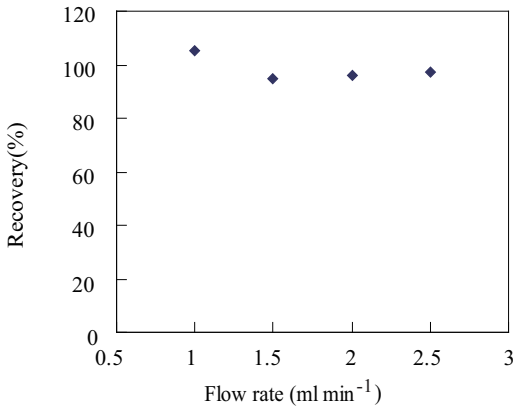

Figure 3.6: Effect of flow rate on the adsorption of lead ion in the mini-column. (25ml 2×10^{-8} *mol* L^{-1} *Pb*$^{2+}$*, pH 10.)*

later operations.

Elution

The nature of the elution solvent is of prime importance for efficiency elution of target species. As reported in many studies, strong acid is always used for lead ion elution from silica gel sorbent [130–132]. In our study, considering the final determination in our microfluidic device, perchloric acid was chosen as the elution, because of its use in the fluorimetric titration of Pb^{2+} by Calix-DANS4 (see Chapter 2). Several concentrations were studied, and the results showed that when [$HClO_4$] reduced to 10^{-2} mol L^{-1}, it can have the same elution efficiency as at lower pHs. The volume of elution was maintained to 0.5 mL, which was appropriate for the detection in microfluidic device later. And we have verified through ASV detection that Pb^{2+} was completely eluted with 0.5 mL of 10^{-2} mol L^{-1} $HClO_4$, after analysing the second and the third 0.5 ml elution solutions and checking that no Pb^{2+} ion was detected in these last two steps (see Table 3.4). The flow rate for elution was 0.5 ml min^{-1}, Pb^{2+} can be eluted in 1 min.

Table 3.4: Elution volume determination

Volume (ml)	1^{er} 0.5	2^{nd} 0.5	3^{rd} 0.5
Recovery %	95	0	0

In the optimized conditions described above, lead ion speciation and preconcentration procedure are shown in Figure 3.7. 50 ml water sample was passed at a fitted flow rate through our micro-column which was filled with about 4 mg of silica beads APS (3-

aminopropyl functionalized silica gel). A pH value of 10 was maintained during the sorption process by addition of solid sodium hydroxide in the water sample to be analysed. After it was completed, vacuum was introduced to drive away the rest sample. Then silica was washed with 5 ml Millipore water and vacuum was introduced again. Finally, lead ion was eluted with 0.5 ml of 0.01 mol L^{-1} $HClO_4$ at a flow rate of 0.5 ml min^{-1}. A 100 fold preconcentration was achieved by this procedure.

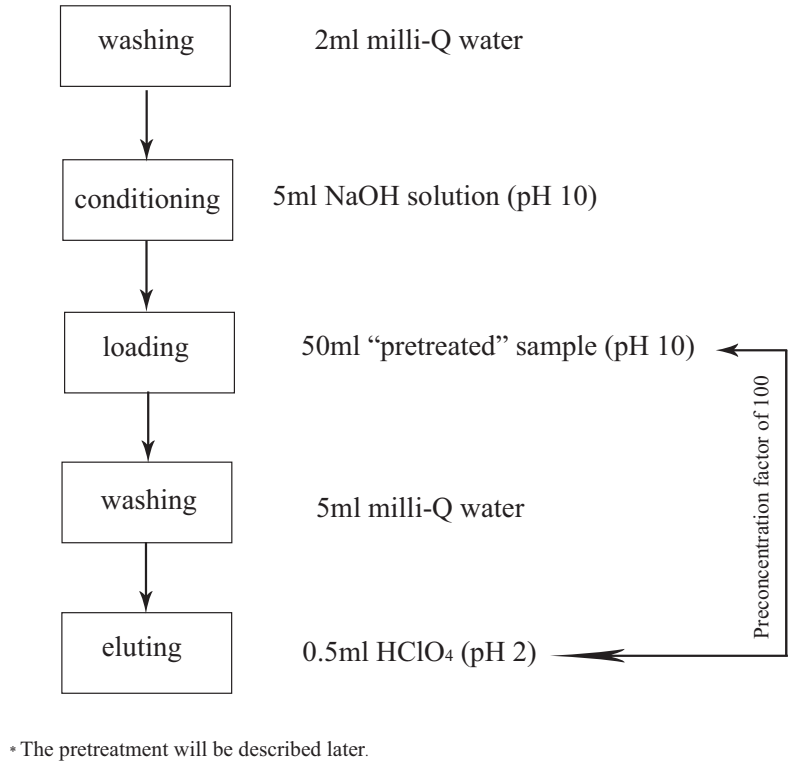

Figure 3.7: SPE preconcentration diagram

Sorption capacity and reproducibility

Although we have studied the sorption capacity of this sorbent in batch method, which was about 4.7×10^{-4} mol g^{-1}, the study in mini-column is still done to verify the complete retention in column method. The concentration of Pb^{2+} in tap water is always very weak, the maximal value set by EU is below 10 μg L^{-1} (i.e. 4.8×10^{-8} mol L^{-1}) for 2013. The maximum concentration value which can be detected in our method is also limited by optimal pH for Pb^{2+} adsorption to prevent precipitation. So our detectable concentration is below 1×10^{-7}mol L^{-1}.

The sorption study was carried out by passing successively volumes of 4×10^{-8} mol L^{-1} solution through the mini-columns containing about 4 mg functionalised silica gel (APS)

under the selected optimum conditions. The result of the recovery of Pb^{2+} was measured by ASV method (Figure 3.8), suggesting that lead ion can be well extracted by APS especially when exceeding 20 ml.

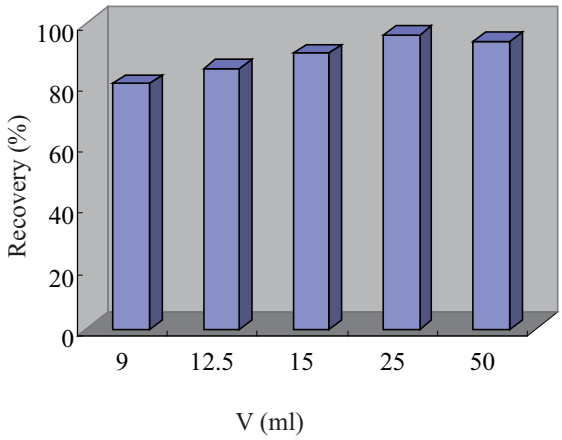

Figure 3.8: Sorption study after successive adsorption of several Pb^{2+} solutions with the concentration of 4×10^{-8} mol L^{-1}

Interference of calcium

In the assay of lead ion in drinking or surface water, calcium is generally the major interferent cation, whose concentration is about 1×10^{-3} mol L^{-1} for a slightly hard water. The interference of calcium for the extraction of lead ion in this micro-column was tested with [Ca^{2+}] of 1×10^{-3} mol L^{-1}.

Titration method for calcium with EDTA was applied to test the interference effect, using calcone as indicator. The same procedure as described in Figure 3.7 was applied: we collected the discharged solutions at the output of the loading step and titrated [Ca^{2+}] using EDTA. The results are shown in Table 3.5. It can be seen that more than 90% of calcium ions do not adsorb on the silica beads. It could be one of powerful proofs to believe its non-interfering effect.

Table 3.5: [Ca^{2+}]in the discharged solution

	[Ca^{2+}]$_{in}$ (mol L^{-1})	[Ca^{2+}]$_{out}$ (mol L^{-1})
S1	1×10^{-3}	$(0.91 \pm 0.02) \times 10^{-3}$
S2	1×10^{-3}	$(0.94 \pm 0.01) \times 10^{-3}$

In the optimized conditions for the procedure of solid phase extraction, we got a 100

fold preconcentration, and the final solution we obtained for the immediate detection in microfluidic device was 0.5 ml recovery lead ion solution which included nearly 1×10^{-2} mol L^{-1} $HClO_4$. Another advantage of using this SPE was the elimination of potentially interfering calcium ions during the sorption process.

3.5 Fluorimetric detection of lead ion in the microfluidic device

3.5.1 Effect of pH and concentration for fluorescence sensor

Fluoroionophores are always protic species, so the complexation of metal ions is very sensitive to pH. Their inert responses to the operative pH are of extreme importance [133]. Because of the low pH of the elution, we studied the quenching of fluorescence when increasing the concentration of lead ion at lower pHs. Besides pH 3.2, two other pHs were tested, pH 2.4 and pH 2.9. The concentration of Calix-DANS4 was maintained at 1×10^{-6} mol L^{-1}.

First, we measured the fluorescence quenching in a quartz cuvette by using a standard fluorimeter (FluoroMax; Jobin Yvon) and obtained three calibration curves, as showed in Figure 3.9. Then, we applied these three pHs in our microfluidic device. The device we used in this chapter was always microchip III as described in Figure 2.15 of chapter 2. At pH 2.4 and pH 2.9, we cannot see much changes in the fluorescence quenching. It indicated that we cannot decrease pH at a value lower than 3.2.

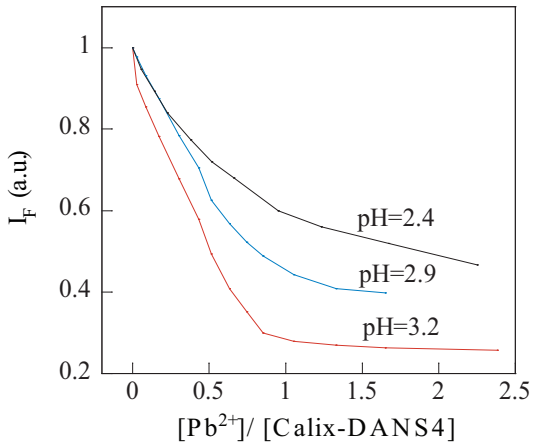

Figure 3.9: Spectrofluorimetric titration curves for lead ion at different pHs in quartz cells. Experiments performed in quartz cells. [Calix-DANS4]=5×10^{-7} mol L^{-1} in the final solution.

For the concentration of the fluorescent molecule, in this chapter, 2 μM has fulfilled our

need, because of a 100 fold preconcentration.

3.5.2 Effect of buffer solution

Because the elution is performed in a more acidic condition (pH=2), pH has to be adjusted by a buffer solution. To change from pH 2 to pH 3.2, base should be added in the final elution solution and then for the detection in microfluidic device. If using strong inorganic base, such as NaOH or KOH, a considerable amount of cations compared to the lead ion in water has to be added. They may interfere with the trace lead ion detection. Then organic buffers caught our attention. Considering the pKa of the buffer and our desired pH value, we chose 3-chloropyridine (pKa 2.84) as the buffer in our microfluidic system, other than $HClO_4$ only. We tested the effect of this buffer for the determination of lead ion in

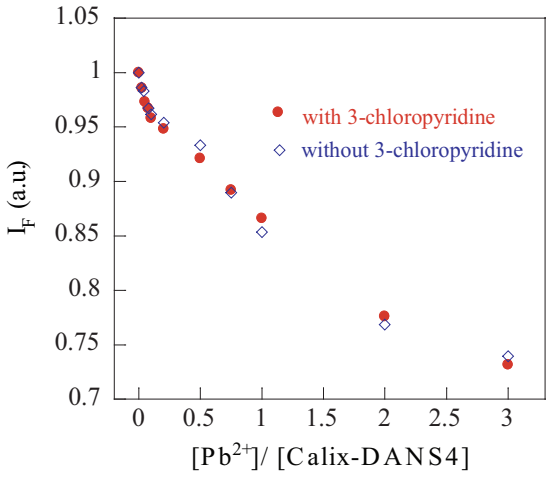

Figure 3.10: Spectrofluorimetric titration curves in microfluidic system with or without 3-chloropyridine buffer in Microchip III. ([Calix-DANS4]=$2 \times 10^{-6} mol\ L^{-1}$, pH=3.2)

Microchip III. The two curves are shown in Figure 3.10. The two curves are very similar. So it appears that 3-chloropyridine is a good buffer for our detection system. The optimum conditions for the microfluidic detection system are [Calix-DANS4]= 2×10^{-6}mol L^{-1}, in a 3-chloropyridine buffer solution (pH 3.2). Others are as the optimal conditions in Chapter 2.

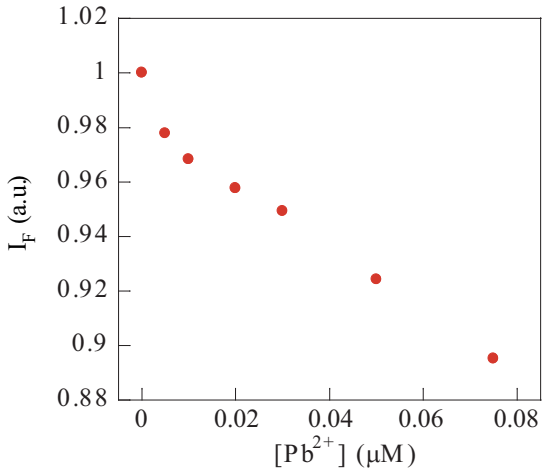

Figure 3.11: Calibration curve for the SPE/Microfluidic system. ([Calix-DANS4]=2 × 10^{-6}mol L^{-1}) in 3-chloropyridine buffer. Flow rate is 0.5 ml h^{-1}.

3.6 Conbination of SPE and microfluidic device for the determination of lead in tap water

3.6.1 Sample pretreatment

The tap water was collected in our lab. Firstly, the water sample was filtered through 0.45 μm Millipore Filter (type HA). The filtered samples were then acidified to pH 1.6 with nitric acid, and then resultant samples were stored at $4\,^{\circ}\mathrm{C}$ in plastic bottles. The non oxydized samples were also tested to simplify the detection process, the pollution of silica beads was observed immediately because of the adsorption of microorganisms on the sorbent.

3.6.2 Calibration curve

Blanks consisting of standard aqueous solutions containing 0, 1, 2, 4, 8, 12 μg L^{-1} of lead in Millipore water were each carried through the preconcentration procedure, and run by fluorimetric microfluidic detection. The calibration curve is shown in Figure 3.11, abscissa is the concentration in the real samples before preconcentration. The detection limit in this calibration curve is 2 μg L^{-1} (i.e. 2 ppb) in water sample (not in the detection solution).

3.6.3 Method application in the analysis of real samples

The results from the analysis of real samples are gathered in Table 3.6. As we can observe, with the method described above, the lead ion in the tap water in Cachan (France) is below our detection limit. Thus several known amounts of lead ion were added in samples of tap water from Cachan and tested respectively.

Table 3.6: Lead ion in tap water

Analyte	Added (μ g L^{-1})	Found$_{(\mu TAS)}$(μ g L^{-1})	Found$_{(AAS)}$ (μ g L^{-1})
Pb^{2+}	0	-	-
	4.14	3.9$\pm$ 0.4	4.05$\pm$ 0.4
	7.25	6.85 $\pm$ 0.25	6.74 $\pm$ 0.04
	8.29	7.6 $\pm$ 0.35	7.87$\pm$ 0.08

The results are listed in Table 3.6. The RSD of our method is less than 10%.

3.6.4 Comparison with results obtained by Atomic Absorption Spectrometry

In order to evaluate the accuracy of the proposed method, Atomic Absorption Spectrometry (AAS) (see Appendix A.4.7) was used. First the calibration curve was obtained with a series of lead ion solutions 0, 1, 2, 4, 8, 12 μg L^{-1}, as in Figure 3.12. Then several tap water samples in Cachan added with the same known amounts of lead as before were induced with this method.

The results are in Table 3.6. The results from both methods μTAS and ASV only differ by less than 5% and show a good correlation for the determination of lead ion in tap water samples. Our method has a potential application because of its sensitivity, possible miniaturization and low-cost.

3.7 Conclusion

Our SPE based microfluidic system has demonstrated effective lead ion detection. The detection limit attained 2 μg L^{-1}, which was only one fifth of European maximum admissible value in drinking water for 2013. This limit can still be improved by a factor of 2 by using Microchip IV (see section 2.5.2). And this is a basis for an integrated SPE-microfluidic detection system (CNRS patent, No. 08/06954 of 11/12/2008).

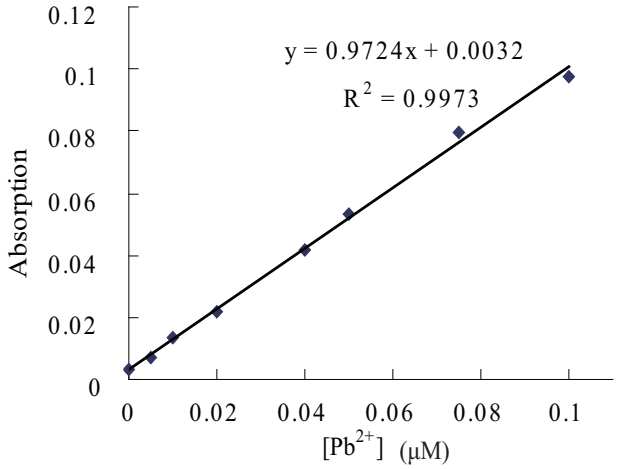

Figure 3.12: Calibration curve for lead ion detection with AAS (n=3).

In conclusion, several advantages were emerged in this microanalysis system. This method can give precise lead ion detection in water, which have been proved by AAS. Its low detection limit is adapted to the application for trace heavy metal ion determination. Although the necessary volume of water sample which costs nearly nothing was significant in the SPE procedure, the consumption of other reactants were tiny, such as several mg APS for solid phase extraction and several μg Calix-DANS4 for fluorescence detection. In addition, the detection can be achieved during about 30 min including the preconcentration step. And the microfluidic chip can be reused hundreds of times which greatly reduced the cost also.

Based on the above observations, a preliminary assessment of the pollution status of Cachan tap water was undertaken. The results suggest that no significant lead ion pollution issue is raised with regards to the presence of lead ion examined. Although these data are not adequate to infer final conclusions regarding the pollution burden of the examined ecosystems, they enable a first interpretation of water quality and aid the design of an appropriate monitoring and sampling protocol.

Chapter 4

Chemical reaction performance in the microfluidic device: mixing, transit and chemical kinetics

4.1 Introduction

Microfluidic devices face presently a tremendous interest, especially for the development of lab-on-a-chip systems. One of the primary challenges for such applications is the ability to perform as a chemical reactor.

When performing chemical reactions in continuous flow microreactors, the most important things is to understand the mixing process, transit process and reaction kinetics. First, we have to know whether the reactants have been completely mixed in the course of their transit. Because of the particular laminar flow in microfluidic device, a mixer is often needed to get ideal mixing. Then we want the chemical reaction under study to be at equilibrium at the detection point, the kinetics of this reaction and the transport process in the microfluidic device will determine the state of the reaction. In other words, the study of chemical reactions in continuous-flow microfluidic system relies on complete mixing and reaching of equilibrium state during transit.

In previous chapters, we have described Y-type fluorimetric microfluidic systems resorting to staggered herringbone mixer for lead ion detection, which depended on the complexation of fluorophore (Calix-DANS4) and lead ion. In this chapter, we will investigate in detail three aspects of this complexation reaction under study in the continuous flow microfluidic systems: mixing, transit and chemical kinetics.

Mixing study will be based on the use of a very fast reaction in the microfluidic device. The transit time can be adjusted by varying the form or length of the microfluidic channel, while chemical kinetics study relies on another conventional method, stopped-flow. The

mixing step can easily be achieved down to 1 s with classical means, and down to a few milliseconds in conventional stopped-flow devices, where the mixing occurs via turbulence. Finally, the results obtained in the microfluidic devices will be simulated with the help of the reaction rate parameters determined by stopped-flow.

4.1.1 Basic ideas on chemical kinetics

Assuming a reaction of type:

$$aA + bB \longrightarrow cC \tag{4.1}$$

is carried out, we define different quantities to characterize it. The coefficients a, b, c before the reactants A and B and the product C, are known as the stoichiometric coefficients.

In practice, in the case when the chemical reaction obeys a simple rate law, we can express the rate of reaction in the form:

$$v = k[A]^{\alpha}[B]^{\beta} \tag{4.2}$$

where k, α and β are coefficients that are independent of time. The exponent α represents the order of the reaction for the reactant A, and β represents the order of the reaction for the reactant B. Where α = a, β = b then the order is said to be equal to the molecularity. This situation is mainly encountered for elementary reactions. The unit of k depends on the order of the reaction. The simplest case, but not necessarily the most frequent, is the first-order reaction, which is written:

$$v = k[A] \qquad with\, k\, in\, s^{-1} \tag{4.3}$$

Considering the most frequent case , the second-order reaction, the rate of reaction is written:

$$v = k[A][B] \qquad with\, k\, in\, M^{-1}s^{-1} \tag{4.4}$$

4.1.2 Chemical reaction in a microfluidic system

Microfluidic systems operate at low flow rate and small cross-sectional dimensions, and therefore at low Re (Re < 100). As mentioned previously, the mixing relies on only diffusion and cannot complete spontaneously in microfluidic channel at low Re which causes the laminar flow phenomena. Thus the temporal resolution is strongly limited by the mixing time of the reactants in microfluidic system. Moreover, in a continuous flow microfluidic device, transit time and reaction time are also important as well as mixing time.

Damköhler numbers

The Damköhler numbers (Da) are dimensionless numbers used in chemical engineering to relate chemical reaction timescale to other phenomena occurring in a system. In the microfluidic device, two Damköhler numbers can be defined.

$Da_{(m)}$ relates chemical reaction time to mixing time, it can be described by the following expression:

$$Da_{(m)} = \tau_C/\tau_M \tag{4.5}$$

where τ_C is the characteristic time of the chemical reaction, and τ_M is the mixing time (which can be controlled by the hydrodynamics or the diffusion).

According to $Da_{(m)}$, there exists two cases:
- High $Da_{(m)}$: in this case, the kinetics are much slower than the mixing. After this mixing time has passed, the concentration field homogenizes itself, and the preceding equations are considerably simplified. For a reaction of type 4.1, with second-order kinetics, we thus have:

$$\frac{dC_A}{dt} \approx -kC_AC_B \tag{4.6}$$

This type of regime is used in measurements of chemical kinetics.

- Low $Da_{(m)}$: in this case, the situation is more complex. The system develops fronts of reaction that are progressively mixed to form a homogeneous ensemble. The regime of evolution towards the completely homogenized situation is complex.

$Da_{(t)}$ relates chemical reaction time to transit time, it can be described by the following expression:

$$Da_{(t)} = \tau_C/\tau_T \tag{4.7}$$

where τ_C is the characteristic time of the chemical reaction, and τ_T is the transit time (which can be controlled by varying the geometry of the microchannel).

According to $Da_{(t)}$, there also exists two cases:
- High $Da_{(t)}$: in this case, at the end of the transit, the reaction is not finished. If a reaction occurs in this condition, the application of the reaction has some kind of limitation.

- Low $Da_{(t)}$: in this case, the reaction is completely finished at the output of the microchannel. It can have perfect performance and applications.

4.2 Experimental part

The Y-type microchannel (type Microchip III Figure 4.1) was taken for the first kinetic studies.

The microfluidic measurements here are all performed as follows: the reactants (A and B) are injected into two arms of the microchannel, then mixed with the aid of staggered

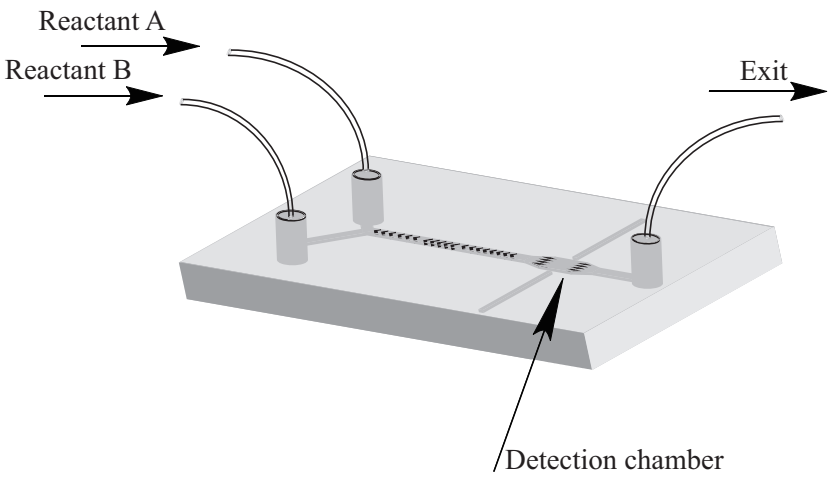

Figure 4.1: Y-type microchannel like Microchip III

herringbone mixer which relies on turbulence to achieve fast mixing times, and the concentrations of the products/reactants are measured at a fixed position downstream by the fluorescence detection method.

With respect to the experiment of mixing, mixing inside refers to two reactants injected separately into two inlets. Mixing outside means equal volume of two reactants mixed before injecting, then the same mixture is injected into both inlets of the Y-type microchannel.

4.3 Mixing performance

4.3.1 Mixing efficiency in microchip I

The mixing performance in a 2 cm long Y-type microchip containing a staggered herringbone mixer, the same as Microchip I in chapter 2, has been determined previously by Destandau et al.[98]. Figure 4.2 illustrated the fluorescence intensity analysis by confocal microscopy in order to examine the mixing efficiency. Two identical liquids (H_2O/acetonitrile, $10/90$ v/v) containing perchloric acid at a concentration of 10^{-4} mol L^{-1}, with one labelled by Calix-bodipy (a fluorescent dye used in a previous work for the selective detection of potassium), were introduced at the inlets of the channel at a flow rate of 0.5 mL h^{-1}. Calix-bodipy was excited at 493 nm and its fluorescence was collected above 515 nm.

It was apparent that concentration homogeneity was achieved by use of the staggered herringbone whereas a clear interface between the two liquids was observed when they flow side-by-side without external perturbation. This observation indicated that at least at 1.5 cm beyond the injection zone, the mixing was finished.

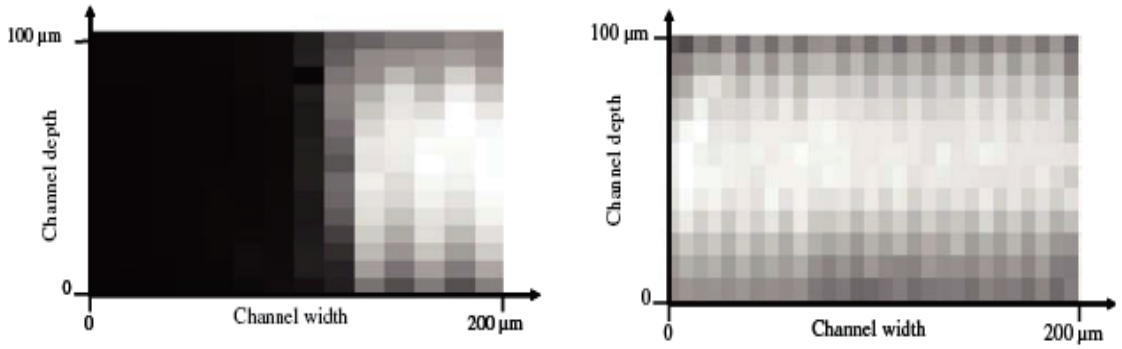

Figure 4.2: Fluorescence intensity analysis by confocal microscopy. [98] Left: Cross section of the channel, near the injection zone. Right: Cross section of the channel 1.5 cm beyond the injection zone.

4.3.2 Mixing efficiency in Microchip III

In order to further test the reaction performance of our system, which has been successfully used for the determination of lead ion in tap water, we checked the mixing efficiency of our microdevice. The device was as mentioned in chapter 3, microchip III, also shown in Figure 4.1.

Model reaction

A fast model reaction of DANS1, which is also the fluorophore in Calix-DANS4, as in Figure 4.3, was chosen for this test.

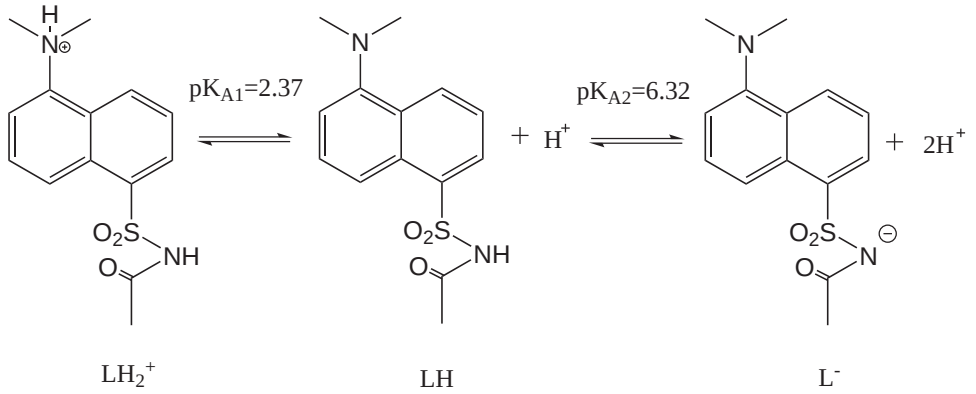

Figure 4.3: Fast model reaction of DANS1.

At different pHs, the fluorescence changes a lot. Two solutions with different pHs have different fluorescence intensities. When both solutions with different pHs meet together, the

reaction of proton exchange occurs. This proton exchange reaction is known to be very fast, with a rate constant probably near the diffusion limit (5×10^9 L mol^{-1}s^{-1}). If the mixing is not complete in the microchannel, the fluorescence will vary a lot and fluctuate when compared with the complete mixing experiment in which the solutes are mixed outside.

Firstly, we studied the steady-state fluorescence of DANS1. Two solutions of DANS1 with different pHs (1.0 and 3.8) were prepared, the absorbance and fluorescence spectra of these two solutions and their mixture (1:1) were studied in the quartz cells. An equilibrium of $LH^+_2 \rightleftharpoons LH$ occurs in this condition. The results are as in Figure 4.4.

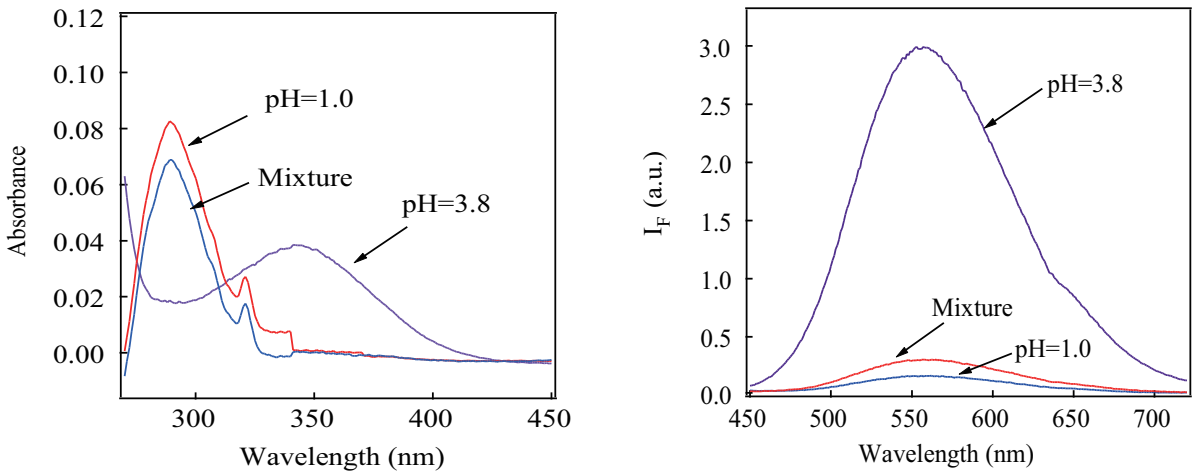

Figure 4.4: Absorbance (left) and fluorescence (right) spectra of DANS1 (λ_{ex}=365 nm) in solvent CH_3CN/H_20=60/40 at different pHs. [DANS1]=10^{-5}mol L^{-1} in each solution.

In the mixture, the recording signal is nearby the signal of solution at pH=1, because the final pH is also nearby pH=1.

Mixing in microfluidic channel

In order to understand the mixing efficiency of this fast model reaction, mixing inside and outside the microchip were tested and compared. The signals under different flow rates were also recorded, other conditions were as for Calix-DANS4 (λ_{ex}=365 nm, a 515 nm band-pass filter for fluorescence). If the mixing was complete in the channel, the two series of signals of mixing outside and inside at the same flow rate should overlap.

And the results (Figure 4.5) of our test well demonstrate that the two series overlap. So we conclude that mixing is complete in microchip III.

4.4 Reaction performance

When considering the reaction in our microchips, the three chips which were mentioned in chapter 2 were examined again. Comparing their titration curves of Pb^{2+} by Calix-

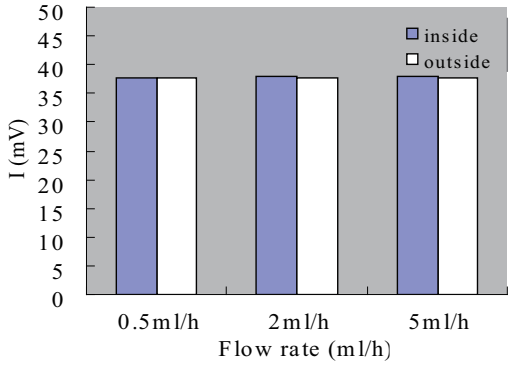

Figure 4.5: Comparing mixing inside and outside the microchip. [DANS1]=10^{-5} mol L^{-1}. (λ_{ex}=365 nm, a 515 nm band-pass filter for fluorescence)

DANS4, there was something important which needed to be elucidated (Figure 4.6).

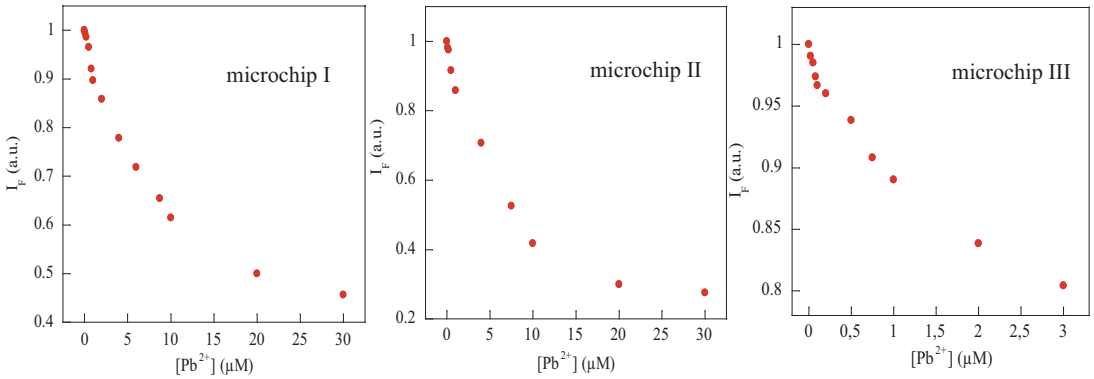

Figure 4.6: Comparing the titration curves of three microchips. [Calix-DANS4]=10^{-5}M in microchip I and II; [Calix-DANS4]=10^{-6}M in microchip III; flow rate for all three microchips is 0.5 ml h^{-1}.

As we can see, in the microchip I, the fluorescence signals of fluorophore decrease about 60% when [Pb^{2+}] is three times higher than [Calix-DANS4]. In microchip II, the signals decrease about 70%, while in microchip III, the signals decrease only about 20%. For Microchip III, although the concentration of Calix-DANS4 is just 10% of that in Microchip I and II, the quenching of fluorescence is much less than in Microchip I and II. The differences observed in Figure 4.6 may be the result of both a change in concentration and a change in the length of the microchannel, inducing a change in the transit time.

In other words, we are wondering if the reaction in the microfluidic channel is complete. In order to put into evidence the influence of the kinetics, another test was performed. The reaction of fluorophore and lead ion was carried out inside and outside the microchips respectively under the same conditions. The inside and outside reaction titration curves

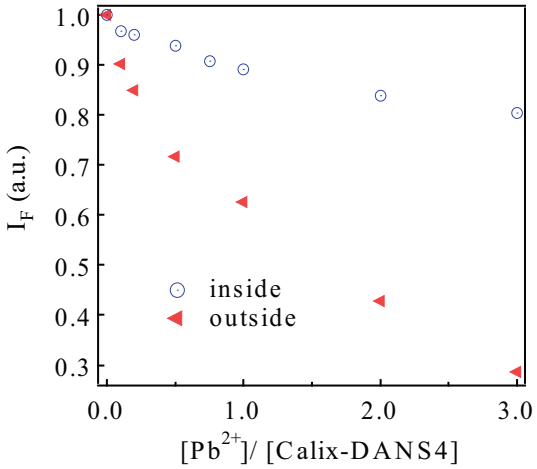

Figure 4.7: The titration curves of the reaction inside and outside the microchip III. [Calix-DANS4]=10^{-6} M. Flow rate: 0.5 ml h^{-1}.

in microchip III were plotted on Figure 4.7. The big difference between the two titration curves indicates that this reaction is not finished when it is carried out in the microchips. Referring to the Damköhler number, in our microchips, mixing has finished, but the reaction not, so we have a high $Da_{(m)}$, and also a high $Da_{(t)}$. It indicates that it may be a slow reaction and that the increase of the transit time may improve this reaction in our chips.

4.5 Influence of transit time

4.5.1 Transit time in microchip III

As explained above, mixing of the reactants in our chips is satisfied. But the reaction seems not to be complete. Another factor, transit time, also has to be considered and compared with the reaction time.

The microchip III which has a width of 0.2 mm and a height of 0.1 mm is used in this study. Its top view is schematized as follows (Figure 4.8):

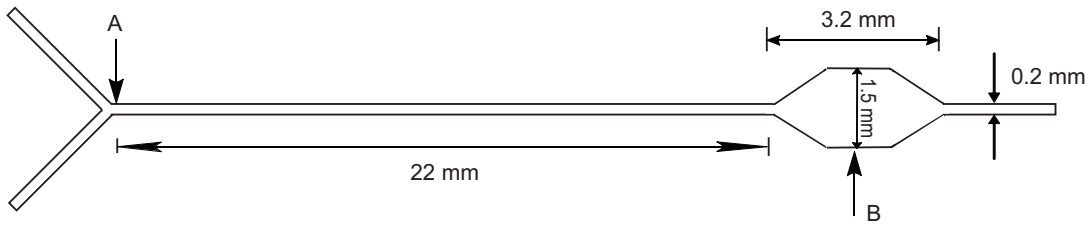

Figure 4.8: The dimensions of microchip III

And then the transit time in this chip can be calculated with equation 4.8:

$$t_{transit} = \frac{V}{\nu} \tag{4.8}$$

in which V is the volume of microchip from the meeting point A of the two solutions to the detection optical fiber (point B), ν is the flow rate. In this calculation, the herringbone structure of the passive mixer has not been taken into account.

When applying the flow rate of 0.5 ml h^{-1}, the transit time in this chip can be calculated and has been found equal to 4.43 s. So a transit time of 4.43 s in microchip III is not sufficient for the reaction to be complete.

The mixing, reaction and transit processes in microchip III have been studied. And it shows that the reaction is not complete while the mixing is complete. In order to get a better yield, several methods have been tried, such as slowing down the flow rate and/or lengthening the microchannel.

4.5.2 Effect of flow rate in microchip III

The flow rates of 3 ml h^{-1}, 0.5 ml h^{-1} and 0.25 ml h^{-1} in microchip III have been studied. Three calibration curves obtained for the same solutions which correspond to three flow rates are shown in Figure 4.9, and compared with the calibration curve in which mixing is performed outside at a flow rate of 0.5 ml h^{-1}.

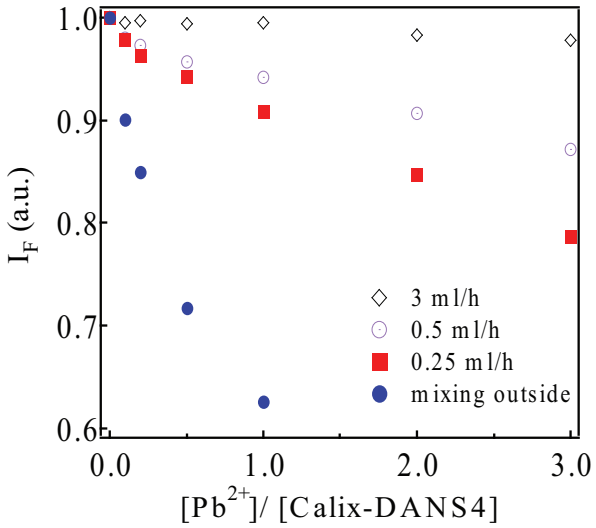

Figure 4.9: Titration curves under different flow rates on the determination of lead ion with microchip III. [Calix-DANS4]=10^{-6} M.

Faster the flow rate is, fewer the complexation is. With 3 ml h^{-1}, there is little complexation. In order to observe a complete reaction, the flow-rate should be decreased towards a

very low value. But when the flow rate is below 0.25 ml h^{-1}, there are more fluctuations in the fluorescence signals. So, with our set-up, this flow rate is the lowest one.

But comparing the titration curve of mixing outside, the reaction is still not finished with a flow rate of 0.25 ml h^{-1}. So we decided to increase the length of our microreactor.

4.5.3 New design of microchip IV

A new design of microchip IV which included a lengthened microchannel was developed. As shown in Figure 4.10, the microchannel was 5 times longer than that in microchip III. A staggered herringbone structure was present on all the length of the microchannel.

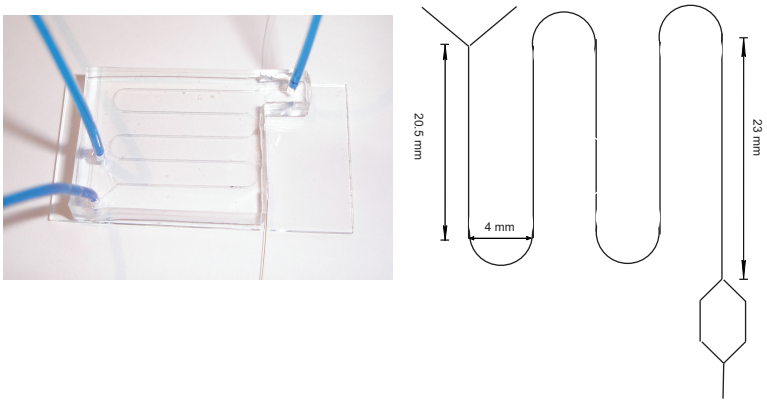

Figure 4.10: Left: Photograph of microchip IV. Right: Schematic dimensions of microchip IV.

Transit time

To calculate the transit time, a scheme of the dimension of microchip IV is illustrated in Figure 4.10right.

The transit time in this microchip was calculated as before, and determined to be 40 ± 1 s for a flow rate of 0.25 ml h^{-1} and 20 ± 1 s for a flow rate of 0.5 ml h^{-1}.

Titration curves under different flow rates

The measurement of titration curve in microchip IV was performed under the same conditions as in microchip III. The titration curves which included both mixing inside and outside the microchip were obtained under two different flow rates (0.5 ml h^{-1} and 0.25 ml h^{-1}). Figure 4.11 shows that the flow rate still affected the titration curve. And the distance between two curves of mixing inside and outside the microchannel told us that the reaction in microchip IV even with a flow rate of 0.25 ml h^{-1} is still not complete. However, the gap between both curves is considerably reduced, compared with microchip III.

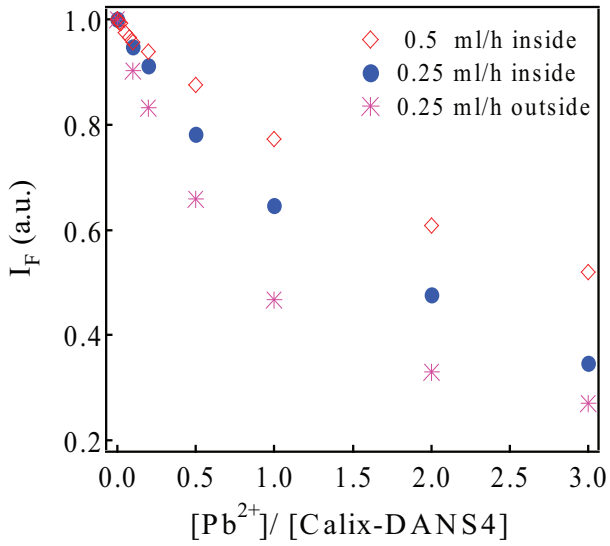

Figure 4.11: Titration curves when mixing inside the microchip IV under two flow rates and mixing outside the microchip IV with a flow rate of 0.25 ml h^{-1}. [Calix-DANS4]=1×10^{-6}mol L^{-1} before mixing. Other conditions are as in Figure 2.11.

4.6 Complexation equilibrium constant

Equilibrium constant for the complexation reaction of lead ion and Calix-DANS4 can be determined from the titration curves [129] with the SPECFIT^{TM} software. In order to get a reference equilibrium constant, the fluorescence spectra when increasing lead ion were conducted with a conventional spectrofluorimeter at the same working conditions as in microchip IV. The spectra and titration curve are presented in Figure 4.12.

With the titration curves, the equilibrium constants were calculated. In this analysis, it was shown that the consideration of a 1:1 complex was enough to adequately fit the results. Equilibrium constants are given in Table 4.1.

The complexation constant obtained from calibration curve in Microchip IV was lower than the one which was obtained from spectrophotometric measurements. It further proved that the complexation was not complete in our microchips. Comparing the values obtained in Chapter 2 for [Calix-DANS4]=5.6×10^{-6} mol L^{-1} ($(logK_{23} = 23.6 \pm 0.1, logK_{11} = 6.23 \pm 0.05)$), the disappearance of the constant for complex M_2L_3 is because the concentration of ligand is so weak that the software does not account the tiny existence of this species.

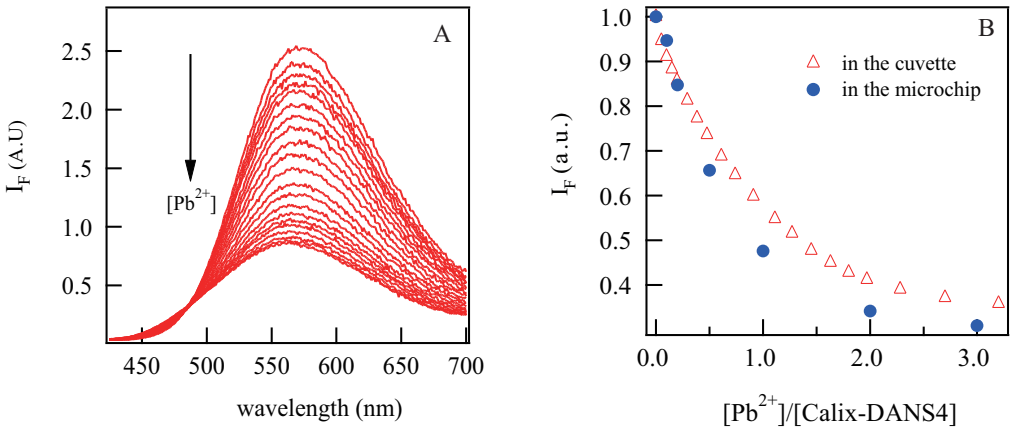

Figure 4.12: (A)Spectra of Calix-DANS4 and its complex with Pb^{2+} when increasing the concentration of Pb^{2+}. (B)Titration curves in the cuvette and in the microchip IV with mixing outside. [Calix-DANS4]=1×10^{-6}mol L^{-1} before mixing. Flow rate= 0.25 ml h^{-1}. Other conditions are as in Figure 2.11.

Table 4.1: The complexation equilibrium constant of the complex of Calix-DANS4 and lead ion in bulk and microfluidic system at pH 3.2, [Calix-DANS4]=5×10^{-7} M in the final solution.

	cuvette[1]	microchip IV[2]
[Calix-DANS4]	5×10^{-7}mol L^{-1}	5×10^{-7}mol L^{-1}
ML	6.82±0.03	6.20±0.05

[1] values obtained from the fluorescence spectra in Figure 4.12A.

[2] values obtained from the titration curve with a flow rate of 0.25 ml h^{-1} in microchip IV in Figure 2.19.

4.7 Complexation kinetics analysis

In order to further prove our hypothesis of the incompleteness of the complexation between our fluoroionophore and metal ion in our microchips, another method, stopped-flow technique, was applied to get rate constants of this reaction.

4.7.1 Introduction of Stopped-flow

Perhaps the most frequently used technique to study the kinetics of fast reactions in solution is stopped-flow.

A schematic diagram of stopped-flow apparatus is shown below (Figure 4.13). In a

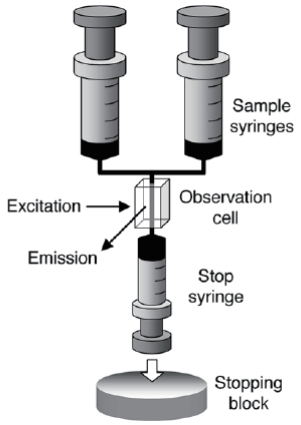

Figure 4.13: Schematic of the stopped-flow apparatus.

stopped-flow apparatus, syringes containing two sample solutions of reactant A and B are compressed, forcing the mixing of the reactants and their entry into an observation cell. Reactant A and B are supposed to reach an equilibrium as follows:

$$A + B \underset{k_{-1}}{\overset{k_1}{\rightleftharpoons}} AB$$

The contents of the observation cell, consisting of the previous reaction solutions, are forced out and passed into the stop syringe, whose plunger hits the stopping block, terminating the mixing process. The progress of the reaction is monitored in the observation cell using excitation light and emission measured at right angles to the excitation beam.

The reaction is monitored by recording fluorescence changes in the observation cell upon formation of products. By fitting the spectroscopic data to simple exponential equations, quantitative information about the extent of binding, from the fluorescence amplitudes, and the observed rate of the approach to binding equilibrium (k_{obs}) is obtained. The dependence of k_{obs} on reactant concentrations for a simple one-step binding mechanism allows determination of kinetic constants k_1 and k_{-1}, from which the apparent equilibrium constant (K) can be calculated ($K = k_1/k_{-1}$). The dependence of the observed fluorescence change amplitude on reactant concentration provides an independent measure of the K value.

4.7.2 Kinetics measurements

Stopped-flow experiments were carried out with a HITECH Scientific -Kinet Asyst apparatus at $20\,^{\circ}\mathrm{C}$. Excitation wavelength for Calix-DANS4 and lead ion complex was 365 nm (with a xenon high pressure lamp, 709 W), while fluorescence was measured above 455 nm. Stray light below 360 nm was removed with a high-pass filter inserted before the photomultiplier tube.

4.7.3 Data analysis

The data were analyzed by linear and nonlinear least squares regressions and all uncertainties were twice the standard deviations. All the observed kinetics were pure monoexponentials (for high [Pb^{2+}]) or biexponentials (for low [Pb^{2+}]) and were dealt with as relaxation modes. All experimental conditions were set so as to allow the use of the methods and techniques of chemical relaxation.

To study this reaction mechanism, it is necessary to assume that the equilibrium of the deprotonation reaction of Calix-DANS4 occurs quickly with respect to the complexation reaction. This is a quasi-first-order reaction.

Then the complexation of Calix-DANS4 and lead ion at pH 3.2 is in a very simple way like below:

$$\mathrm{M} + \mathrm{L} \underset{k_{-1}}{\overset{k_1}{\rightleftharpoons}} \mathrm{ML}$$

The kinetics equation for the disappearance of metal ion M is written as follows:

$$\frac{d[M]}{dt} = -k_1[M][L] + k_{-1}[ML] \tag{4.9}$$

Let define x as

$$x = [M] - [M]_e = [L] - [L]_e = [ML]_e - [ML]$$

where the index e refers to the equilibrium condition. Then it comes

$$\frac{dx}{dt} = -k_1(x + [M]_e)(x + [L]_e) + k_{-1}([ML]_e - x) \tag{4.10}$$

In the equilibrium state, relation 4.11 comes

$$k_1[M]_e[L]_e = k_{-1}[ML]_e \tag{4.11}$$

If [M] $\gg$ [L], x^2 is negligible in Eq. 4.10 (This is the necessary condition for chemical relaxation.). After considering the equilibrium state in Eq. 4.11, it comes:

$$\frac{dx}{dt} = -k_1 x([M]_e + [L]_e) - k_{-1}x \tag{4.12}$$

The integration of this differential equation gives:

$$x = x_0 \quad exp(-(k_1([M]_e + [L]_e) + k_{-1})t) \tag{4.13}$$

where x_0 is the the value at t=0.

This mono-exponential has one relaxation time constant τ, which is

$$\frac{1}{\tau} = k_1([M]_e + [L]_e) + k_{-1} \tag{4.14}$$

As mentioned above, we consider here only when [M] » [L], so $[M]_e$ +$[L]_e \approx [M]_e \approx$ [M] (initial concentration).

And Eq. 4.14 can be simplified as:

$$\frac{1}{\tau} = k_1[M] + k_{-1} \tag{4.15}$$

Plotting $\frac{1}{\tau}$ versus [M] gives a straight line with slope k_1 and intercept k_{-1}.

4.7.4 Kinetics of complex formation

The kinetics study of complex formation between Calix-DANS4 and Pb^{2+} was carried out at the same conditions as in Microchip IV (pH 3.2, CH_3CN/H_2O = 60/40). The solutions of ligand (Calix-DANS4) (5×10^{-7} mol L^{-1} in the mixture) were mixed with much more concentrated metal ion Pb^{2+} (from 5×10^{-6} mol L^{-1} to 1.3×10^{-5} mol L^{-1}) solutions in the stopped-flow detection cell. The kinetics processes related to the interaction of Calix-DANS4 with lead ion were acquired by fluorescence emission at $\lambda > 455$ nm for the kinetic runs. Two kinetics processes were detected, but the first one was too weak to be analyzed. This may be related to the deprotonation of Calix-DANS4. In our study, this process was neglected. The second one appeared as an exponential decrease of fluorescence, and took place in about 20 s for a $10c_0$ (c_0 was the concentration of Calix-DANS4) (see Figure 4.14).

At fixed pH 3.2 and constant c_0 (concentration of Calix-DANS4), and with c_1 ([Pb^{2+}]) $\geq 10c_0$, there is a linear relationship between the experimental reciprocal relaxation times τ^{-1} and c_1 (Figure 4.15), in agreement with Eq. 4.15. From this fitting, the experimental results match this quasi first order reaction mechanism in the condition of [M]$\gg$ [L]. And k_1 is $(9.4 \pm 0.4) \times 10^4$ M^{-1} s^{-1} obtained from Figure 4.15. As k_{-1} from Figure 4.15 has a too high uncertainty, we calculated its value from equilibrium constant $K = k_1/k_{-1}$. At pH 3.2, K for $M + L \rightleftarrows ML$ is $10^{6.82}$, which was obtained with software SPECFIT (Table 4.1). So, we got a k_{-1} of 0.014 s^{-1}.

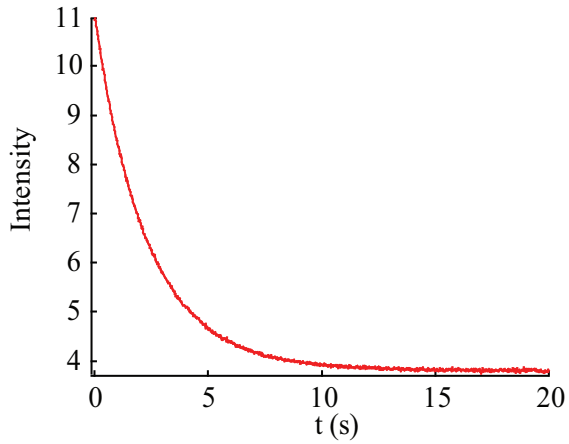

Figure 4.14: Variation of the fluorescence with time between a solution of Calix-DANS4 and a solution of $Pb(SCN)_2$ after rapid mixing for pH 3.2, and $[Pb^{2+}]$ = 5 μM with [Calix-DANS4] = 0.5 μM.

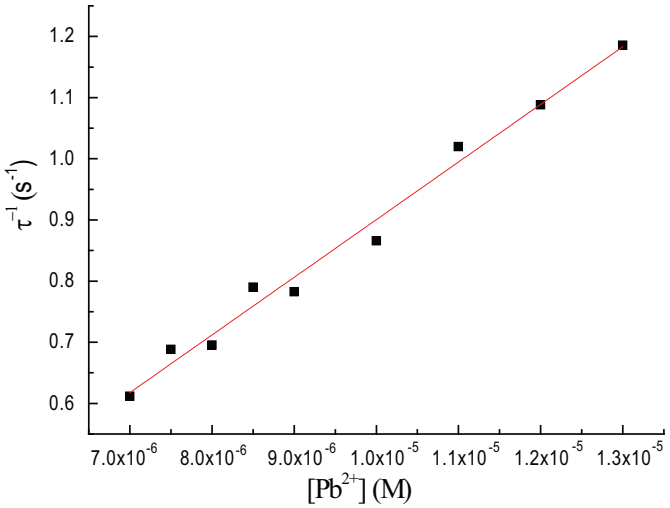

Figure 4.15: τ^{-1} against $[Pb^{2+}]$ at pH 3.2. Intercept, -0.04 ± 0.04 s^{-1}; slope, $(9.4 \pm 0.4) \times 10^4$ M^{-1} s^{-1}; r =0.9964.

4.7.5 Simulation of kinetics of the complexation reaction

The software tool Chemical Kinetics Simulator (CKS) program which is developed by chemists at IBM's Almaden Research Center is used here to simulate the chemical kinetics of the complexation reaction between Calix-DANS4 and lead ion. The simplest reaction model $M + L \rightleftarrows ML$ was applied for this simulation. The k_1 and k_{-1} were the results obtained from stopped-flow experiment and SPECFIT calculation ($k_1 = (9.4 \pm 0.4) \times 10^4$ M^{-1} s^{-1}, k_{-1}=0.014 s^{-1}). The decay of ligand concentration versus reaction time for a series concentrations were plotted in Figure 4.16.

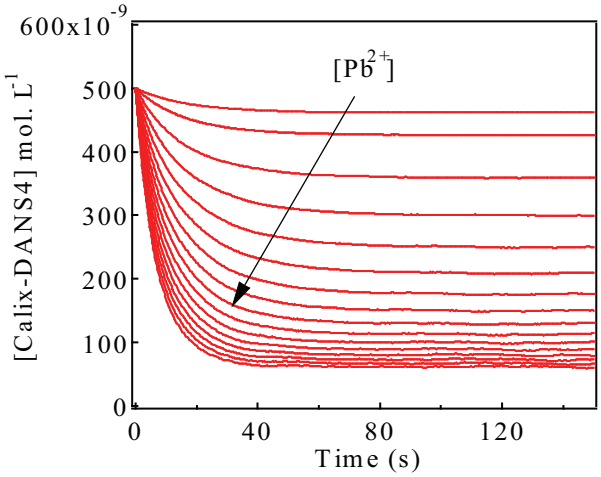

Figure 4.16: Decay of ligand concentration versus reaction time calculated by CKS. [Pb^{2+} is increased between 5×10^{-8} M and 1.5×10^{-6} M]

The comparison between simulation curve and stopped-flow experimental curve was made from one curve in Figure 4.16 and one curve from stopped-flow measurement at the same concentration of ligand (Figure 4.17).

Figure 4.17 has well demonstrated the coherence of computational results from Chemical Kinetics Simulator and experimental results from stopped-flow. The time scale of this complexation reaction in the same conditions as in Microchip IV even when [Pb^{2+}]/[Calix-DANS4]=3 is about 40 s, while for other smaller concentrations, the reaction times are much longer than 40 s. That indicates this reaction has not finished in our chips. And this kind of simulation can be useful to check the validity of our previous results.

So for the unfinished complexation in our chips, we can also simulate them with this software. Two performances in two chips, one with flow rate of 0.5 ml h^{-1} in Microchip III and the other with flow rate 0.25 ml h^{-1} in Microchip IV were appraised. They are corresponding to transit times of 4.4 s and 40 s respectively. So the theoretical (simulation) curves were obtained from CKS at the condition of reaction times of 4.4 s and 40 s respectively, which were calculated from Figure 4.16. By plotting the I_F/I_0 versus

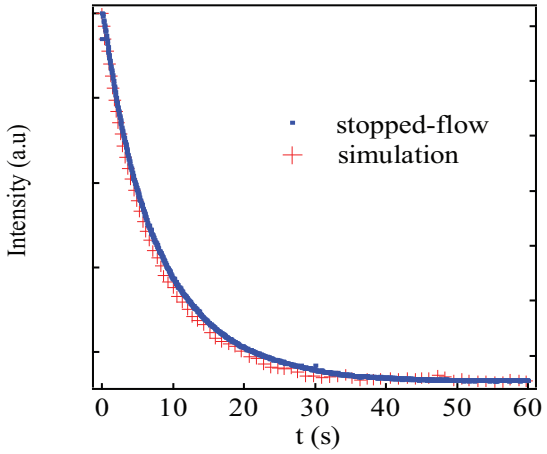

Figure 4.17: Dots: Simulation of chemical kinetics of Calix-DANS4 and lead ion complexation. [Calix-DANS4]= 0.5 μM, [Pb^{2+}]= 1.5 μM, other conditions are as in Figure 4.14. Cross: Experimental curve of stopped-flow in this condition.

[Pb^{2+}]/[Calix-DANS4], experimental curves and simulation curves are depicted in Figure 4.18.

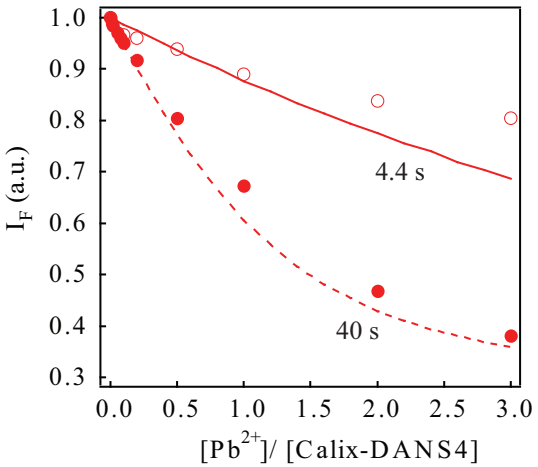

Figure 4.18: Comparison between calculated and experimental calibration curves in two different conditions: ○ Microchip III, flow rate 0.5 ml h^{-1} (transit time 4.4 s); ● Microchip IV 0.25 ml h^{-1} (transit time 40 s). Full line: calculated curve at t= 4.4 s; dashed line: calculated curve at t=40 s. [Calix-DANS4]=5×10^{-7} M in the mixture.

This graph shows a rather good agreement between calculated and experimental curves. Comparing two series of curves, Microchip IV has more similarity with the simulation curve than Microchip III has. The state of almost superposition shows that in Microchip IV the complexation between Calix-DANS4 and lead ion is upcoming complete. The departures of two series between the simulation curve and experimental curve are all because the

mixing times in the microchips have not been taken into account for the reaction time. For a shorter transit time, like 4.4 s in Microchip III, this uncertainty is more important than for a longer transit time, like 40 s in Microchip IV. So a larger departure appears for shorter transit time.

4.8 Effect of the PDMS-glass surface of the microchannel

The last factor for the reaction in microfluidic device, which is the effect of the walls of the microfluidic device, has been evaluated. We have seen previously that the fluorescence of Calix-DANS4 and its lead complexes is very sensitive to pH. Besides, the walls of the microchannel has acido-basic properties; furthermore, they can be polluted by lead deposited during previous assays. In order to determine the influence of the walls, we compared calibration curves obtained by conventional measurements of fluorescence intensity in cell with those obtained in Microchip IV from solutions mixed before flowing into the microchip. The fluorescence spectra obtained in the quartz cell were shown in Figure 4.12A and the calibration curves obtained by both methods were depicted in Figure 4.12B. Although both curves are nearby each other, the curve obtained in the microchip is slightly lower, which could be a consequence of desorption of lead ions previously adsorbed on the walls of this very long channel.

4.9 Conclusion

This chapter has studied the details of the complexation between Calix-DANS4 and lead ion at the same conditions as that we applied in the previous applications (in chapter 2 and chapter 3). The reaction mechanism was analyzed by a relaxation method; chemical kinetics of the complexation was measured by stopped-flow technique; association equilibrium constant was calculated by a software SPECFIT. From these data, its kinetic constants were obtained with a k_1 of $(9.4 \pm 0.4) \times 10^4$ M^{-1} s^{-1} and k_{-1} of 0.014 s^{-1}. All the results show that this complexation cannot be finished at the end of our microchannels, in which the transit times are always shorter than the reaction time. The computer simulation with a software CKS further attested our experimental results.

Chapter 5

Optofluidic sensor based on microcavity laser

5.1 Introduction and motivation

The recently established field of optofluidics combines microphotonics with microfluidics for the complementary aims of using optics for sensing in microfluidic lab-on-a-chip devices and of using microfluidics to tune optical devices. Optofluidic integration holds much promise for highly sensitive integrated sensors.

Due to the unique properties of fluids, such integration provides a new way for dynamic manipulation of optical properties and shows many potential applications [134, 135]. The most exciting optofluidic applications is to realize sensors. A wide variety of optical methods have been used for biochemical sensing, such as absorbance [136, 137], fluorescence [138], Raman-scattering, refraction [139], or surface plasmon resonance [140] measurements. By contrast, photonic microresonators can produce more compact sensors with a reasonably high sensitivity that does not directly depend on the device footprint. Resonant optical structures dramatically increase, beyond their physical length, the effective length of interaction between the fluid and the optical field that is trapped and built up inside the resonator [141, 142].

Particularly, several optofluidic sensors based on optical microcavities have been developed in recent years [143]. Armani et al. have displayed a D_2O sensor in aqueous environments. They have monitored unprecedented low concentration levels of D_2O in water (0.0001%) using microtoroids, because resonators immersed in H_2O have lower quality factors than those immersed in D_2O due to the difference in optical absorption [144]. Silicon microdisks have enabled the detection of fluid index variations down to 10^{-4} for 10 femtoliters surrounding fluid volume [145]. Polystyrene microrings have enabled the detection of glucose concentrations of 0.1% (w/w) as well as the specific binding of biomolecules with

low-mass coverage on their surfaces [146]. A glucose sensor has been exploited by combining a microring and a waveguide comprising partially reflecting elements. The slope in their transmission spectrum is significantly steeper than for the single microcavity response [147]. Boyd et al. have demonstrated a photonic device based on a high-resolution, whispering-gallery-mode disk resonator that can be used for the detection of biological pathogens [94].

But as we can see from the number of papers, optofluidic applications usually focused on the sensing of biomolecules in fluidics. Rare applications are performed in environmental monitoring, such as metal ion sensing.

Here, we will present the principle of an integrated microphotonic device which could serve as an effective and miniaturized metal ion sensor through modifying the refractive index of dye doped polymer microcavity laser. The aim of our research is to find a suitable material for microcavity laser metal ion sensor.

5.2 Strategy for effective metal ion sensor based on microcavity laser

5.2.1 Optical microresonators

Optical microresonators used for sensing biological molecules or chemical molecules represent an emerging technology which is now intensively studied and developed. The principle involved in these sensors is based on the detection of the change in environment close to the sensor surfaces using an optical evanescent wave.

Generally, there are two major optical microresonators: 1) passive microresonators, e.g. which are based on the modification of linear optical properties, the material involved in the process lacking of any nonlinear or laser properties; 2) active laser microresonators, such as laser dyes or semiconductor quantum dots.

One example of passive resonators is microring resonator with integrated waveguide coupling, from Xu et al. [148], as shown in Figure 5.1a. It included a waveguide in close proximity to provide selective evanescent coupling in particular directions. Continuous-wave light (dominant electric field parallel to the plane of the substrate) from a tunable laser was coupled to the waveguide adjacent to the ring, and the output spectrum of the waveguide was measured. Figure 5.1b shows a typical spectrum of the relative transmission through the modulator.

A microcavity laser microresonator in the form of stadium made of a polymer matrix doped with visible laser dyes with a high fluorescence Stokes shift was developed by Lebental et al., which was a good example of active microresonator [149]. A typical stadium-shape microcavity laser which was made of PMMA doped with a laser dye (DCM) and its

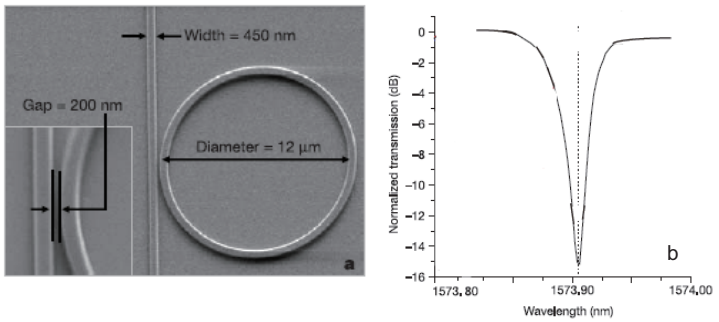

Figure 5.1: Example of passive resonator [148].

spectrum are shown in Figure 5.2. This is the basis of our later study.

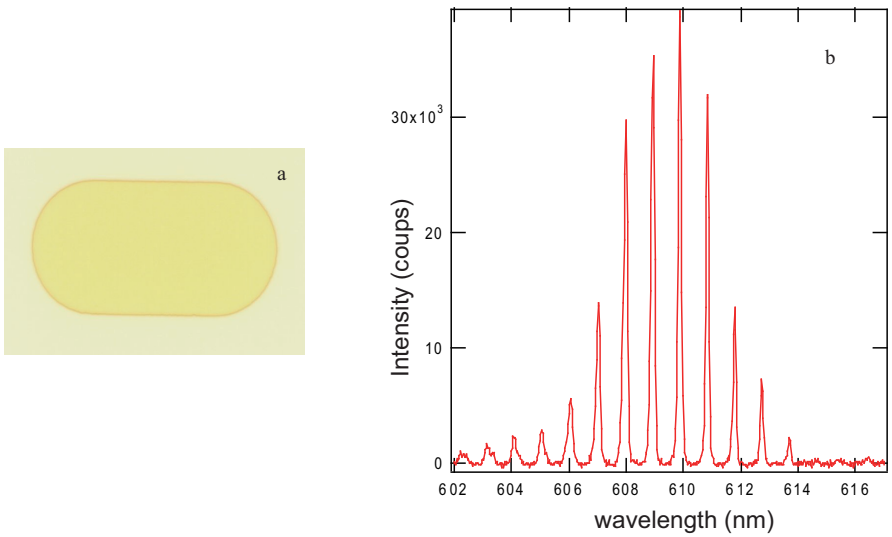

Figure 5.2: (a) Stadium shaped microcavity laser, (b) Experimental spectrum of a stadium-shaped PMMA/DCM microcavity laser. [149]

5.2.2 Microcavity laser

High-sensitive optical devices such as optical sensors, polymeric optical fibers, photonic crystals, micro-lasers, with an optical microcavity as a main element used for gain and controlled conversion of electromagnetic radiation, have been well developed recently.

Micro-laser cavities are of particular interest as sensors for chemical or biological applications. Dielectric microcavities were used as laser resonators, providing the gain is large enough to overcome the cavity losses.

As a rule, such cavities are manufactured in the form of optically transparent dielectric objects. Usually, dielectric microcavities are quasi two-dimensional objects whose thickness is of the order of the wavelength but with much larger plane dimensions. Several cavities with different boundary geometries have been investigated, such as Fabry-Perot resonator, polygonal cavities (square and pentagon), circular cavities and stadium-shaped cavities (Figure 5.3). Their lasing spectra consist mainly of almost equidistant peaks and the distance between peaks reveals the length of a quantized periodic orbit as seen in Figure 5.2b [149].

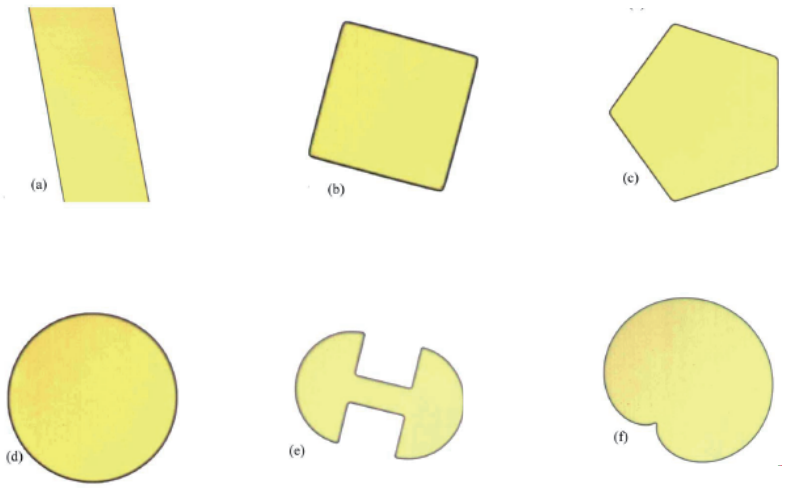

Figure 5.3: Optical microscope photographs of some organic micro-lasers: (a)stripe (used as Fabry-Perot resonator), (b)square, (c)pentagon, (d)disk, (e)quasistadium, and (f)cardioid. Typical dimentsion: 100 μm. [150]

The principle of their functioning is based on resonance excitation of morphology-dependent resonances (MDRs) in a microcavity. A special subfamily of cavity MDRs known as whispering gallery modes (WGMs) are charaterized by ultrahigh quality factor Q, (which defined as $Q = \lambda/\Delta\lambda$, λ is the resonant frequency, $\Delta\lambda$ is the resonance linewidth)(Q $> 10^5$), narrow spectral width, sufficiently long lifetime (nanoseconds), and high degree of optical field localization near the cavity surface also. Vollmer et al. demostrated WGMs in several different resonators in microfluidic devices [151] (Figure 5.4).

When light is incident at a planar interface from a high refractive index n_1 to a low refractive index n_2 medium, it can be completely reflected, provided the angle of incidence exceeds the critical angle, $\theta c = \arcsin(n_2/n_1)$. This total internal reflection can be used to

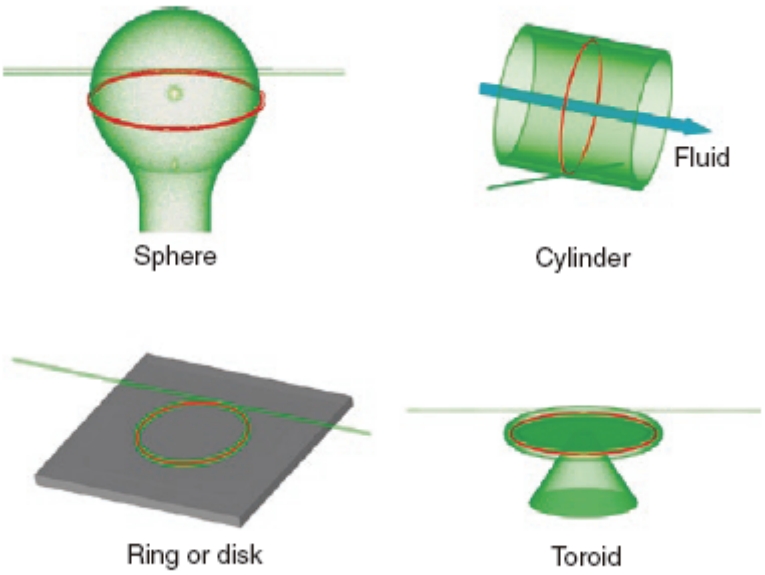

Figure 5.4: WGM resonator geometries. The WGM is highlighted in red, blue indicates microfluidic flow. [151]

form extremely efficient reflectors in a microcavity, not dependent on the metal or multilayer properties. Because the light skims around the inside of such a high refractive index bowl, it resembles the whispering-gallery acoustic modes first noticed by Lord Rayleigh in Saint Paul's Cathedral in London.

WGMs have attracted much attention due to potential applications in photonics, quantum electrodynamics (QED), atom optics and telecommunications. Such applications in technological and scientific fields are e.g. the realization of microlasers, narrow filters, optical switching, ultrafine sensing, displacement measurements, high resolution spectroscopy, Raman sources and studies of nonlinear optical effects.

5.2.3 Principle of metal ion sensing with microcavity laser

Sensing methods

The sensing principle is based on the spectral shift of the optical response of micro-disk or microrings, induced by the change of refractive index of the microresonator or of its environment or surface state. For a passive resonator, when coupled to an adjacent waveguide, this response can easily be transferred and detected. This architecture combines three attractive features: high sensitivity related to the underlying physical process, improvement

of integration using waveguides coupled to the microsensor, and insertion of the component inside a microfluidic circuit. Spectral method and intensity variation method are two major methods for microsensor.

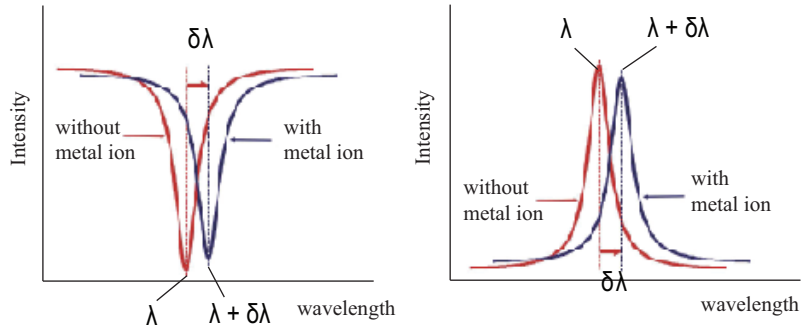

Figure 5.5: Spectral method for the influence of the target molecules on the spectrum and principle of detection : (a): passive resonator; (b): active resonator.

The spectral method consists of measuring the spectral shift $\delta\lambda$ of the resonant peak. Figure 5.5a shows the shift in a passive resonator, Figure 5.5b is the principle for an active resonator. Another optical interrogation method is the intensity variation method in which we measure the change of the output intensity due to the signature of target molecules at a fixed and stable wavelength of the optical input signal.

Metal ion sensing

The organic "guest-host" material used for microcavity laser is composed of one polymer (PMMA or diblock copolymer) for the passive host and a laser dye for the active guest. The formation of this system in bulk is as in Figure 5.6.

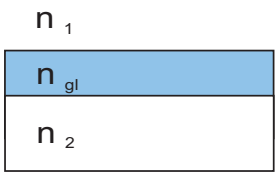

Figure 5.6: Formation of organic micro-laser cavity. From top to bottom, the layers are air (n_1 =1), a polymer doped with a laser dye (DCM) (n_{gl}), and SiO_2 layer (n_2= 1.46).

One considers electromagnetic fields as propagating inside an infinite dielectric slab (gain layer) with refractive index n_{gl} surrounded by medias with refractive indices n_1 and n_2 smaller than n_{gl}. The gain layer is made of a polymer (PMMA or block copolyer) doped with a laser dye (DCM) and sandwiched between the air and a SiO_2 layer.

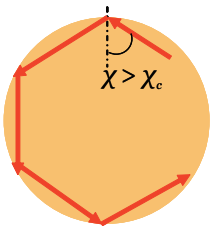

Figure 5.7: Disk-like active microcavities

Figure 5.7 depicts a light wave circumnavigating a microdisk of radius R and returning in phase. The resonance condition is

$$m\lambda_r/n = 2\pi R \tag{5.1}$$

where n is the orbital refractive index of the disk, R is the disk radius and m is the integer number of orbital wavelengths $\lambda_s = \lambda_r/n$. Based on this resonance condition, the sensitivity of the resonance wavelength to changes in radius ΔR or refractive index Δn is :

$$\Delta\lambda_r/\lambda_r = \Delta R/R + \Delta n/n \tag{5.2}$$

Increases in the radius or refractive index lead to a red shift in the WGM. With only the radius enlarged, an orbit having the same number of wavelengths must have its wavelength increased in proportion to the increase in radius: $\Delta\lambda_r/\lambda_r = \Delta R/R$. This simple idea was the basis for earlier thoughts on reactive WGM biochemical sensing.

Microresonator effective-index changes are detected through the monitoring of the resonance-wavelength shift or the intensity variation at a fixed wavelength; narrower resonance linewidths (proportional to 1/Q) thus improve the sensor resolution by reducing the smallest detectable shift in the resonance.

When the metal ions react with the polymer, the refractive index of host-guest system will change. Then a shift of laser emission occurs. The relationship between wavelength shift and the concentration of metal ion will be discovered. This is the basis of metal ions' detection.

5.3 Host-Guest microcavity laser system

5.3.1 Photophysical properties of laser dye molecules

Laser dyes are complex organic molecules containing conjugated double bonds (i.e. alternating single and double carbon bonds, =C-C=C-) or aromatic molecules. The large molecular size and the relatively free moving π-electrons in the conjugated double bonds

give rise to a large transition dipole moments of dye molecules (or equivalently, oscillator strengths). The complex molecular structure also leads to many vibrational and rotational levels within a single electronic state. Therefore, laser dyes often have strong and wide absorption bands in the UV and visible region. The emission spectra of dye molecules are Stokes-shifted to longer wavelength and form almost mirror images of the absorption bands due to the so-called Frank-Condon principle (Svelto 1998). This is a rather fortunate feature because the laser emission will generally not be strongly absorbed by the dye itself.

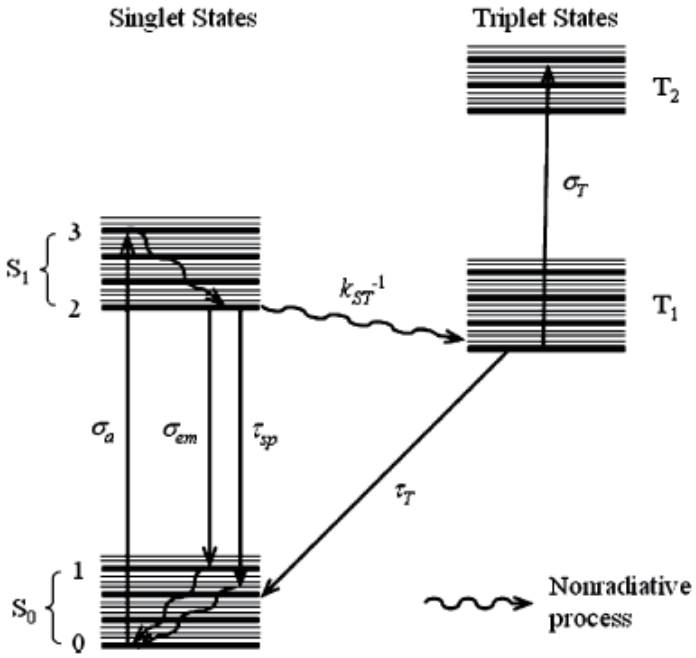

Figure 5.8: Typical energy levels of a dye molecule.

In the following, we will briefly discuss the energy levels and the transition processes involved in laser operation. Schafer et al. have presented more complete discussions of the photophysical and photochemical properties of laser dyes including the environmental effects [152]. It is important to realize that the dye laser is a classical four-level system (if one neglects the triplet states) where the four energy levels are marked 0-3 in Figure 5.8. Under optical excitation, dye molecules are pumped from the bottom of the ground state S_0 (ground level 0) to some vibrational-rotational sublevels in the first singlet state S_1 (intermediate pump level 3). The dye molecules in level 3 quickly relax to the bottom of S_1 (upper laser level 2). This nonradiative decay process happens on the time scale of a few picoseconds or less. The energy lost in this process contributes to the heating of the solvent.

From the upper laser level 2, dye molecules can undergo either spontaneous emission or stimulated emission to some vibrational-rotational sublevels in S_0 (lower laser level 1). The nonradiative decay time from the lower laser level 1 to the bottom of the ground state S_0 (ground level 0) is also a few picoseconds. Due to the extremely fast nonradiative decay processes, the populations of the lower laser level n_1 and the intermediate pump level n_3 are negligibly small. Therefore, dye lasers can reach threshold at very small population inversions, with typical n_2/n of only 0.01 or less [153].

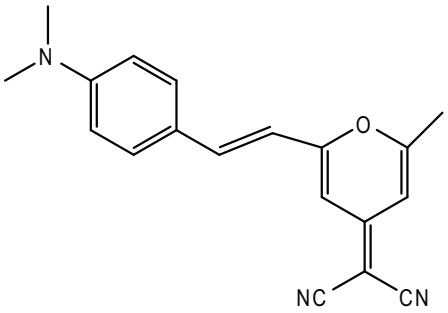

Figure 5.9: Chemical structure of DCM.

4-dicyanomethylene-2-methyl-6-(4-dimethylaminostyryl)- 4H-pyran (DCM) (see Figure 5.9) is a laser dye with a fluorescence spectrum centered around 600 nm. Besides relatively low cost availability, the main assets of DCM are a good fluorescence quantum yield and large Stokes shift (∼100 nm) which prevents from reabsorption of the emitted light. Its absorption and fluorescence spectra in ethanol are illustrated in Figure 5.10. Several typical absorption and fluorescence spectra of DCM in different solid matrices will be presented afterwards.

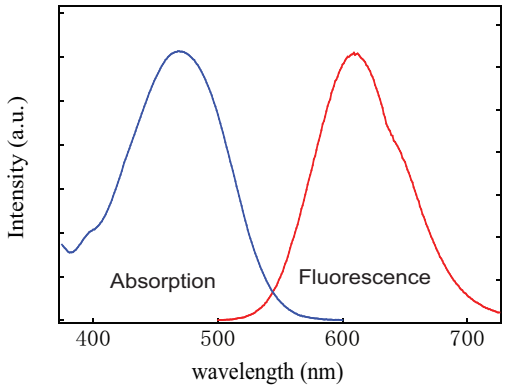

Figure 5.10: Absorption and fluorescence spectra in ethanol solution.

Lebental et al. have gone deep into the study of this laser dye in their polymer microcavity laser [150]. They showed that 5 wt% of DCM in polymer host can lead to a good

microcavity laser emission. So in our following study, 5 wt% of DCM compared to the polymer was kept.

5.3.2 Requirements for a good host material in microcavity laser

PMMA has been used as a passive host in microcavity laser in the previous work of Lebental [149]. The stadium-shaped microcavity laser of the host-guest system was realized by photolithography and O_2 plasma Reactive Ion Etching (RIE). Although stadium-shaped resonators are fully chaotic, these microcavities appear to be high efficient microlasers with resonator quality factors greater than 6000.

But for an effective optofluidic metal ion sensor, the effective selectivity and high sensitivity for metal ions are the most important. Some requirements for a good optofluidic sensor material are as follows: 1) Can make films with good optical quality; 2) Must accomodate both a laser dye (DCM or rhodamine ...) and an organic cryptand or ligand, without release of these compounds in water; 3) Must be swollen by water, in order to trap and concentrate heavy metal ions; 4) Must be easily processable into microcavities by conventional methods available in clean rooms (UV lithography, plasma etching ...). Taking into account these requirements, PMMA alone is not suitable for our purpose. Our final goal is to choose a highly selective polymer or to modify the surface of a well-known polymer for metal ion sensing.

5.4 Apparatus for characterization

5.4.1 Atomic Force Microscopy

The principle of Atomic Force Microscopy is depicted in Appendix A.4.4. AFM was performed on VEECO (Thermo microscope), in tapping mode to obtain height images and phase images, using Silicon Nitride cantilevers. All images were obtained using a scan rate of 2 Hz, unless otherwise noted.

5.4.2 Ellipsometry

The principle of ellipsometry is depicted in Appendix A.4.5. The dependance of n_{gl} is determined with the GES 5 SOPRA ellipsometer from a regression with the Winelli II software.

5.4.3 Others

The UV-Vis absorption and fluorescence of as cast thin film with "host-guest" system was measured by a Uvikon 943 and Fluoromax (HORIBA Jobin Yvon).

The thickness of thin films was primarily measured by a profilometer (Veeco DekTak 150 surface profiler).

5.5 Host polymer study: PS-b-P2VP, PS-b-P4VP

Considering the requirements for a good optofluidic ion sensor, diblock copolymer has been attracted much attention. Diblock copolymer materials spontaneously form patterns through a minimization of free energy - a process known as $microphase\ separation$ [154]. The immiscibility of the two chemically distinct "blocks" that comprise each polymer molecule drives the system toward a minimum interaction volume, while the covalent bond between these blocks simultaneously limits the maximum distance by which the two blocks can separate. The resulting equilibrium patterns have molecular-scale dimensions determined by the intrinsic polymer properties of the degree of polymerization (N) (proportional to the polymer molecular weight), the weight ratio of the constituent blocks, and the Flory -Huggins parameter (χ), which characterizes the interaction strength of the blocks. The morphologies of block copolymers usually contain spheres, hexagonally packed cylinders, lamellae, bicontinuous and perforated layers, as described by Förster et al [155] (Figure 5.11).

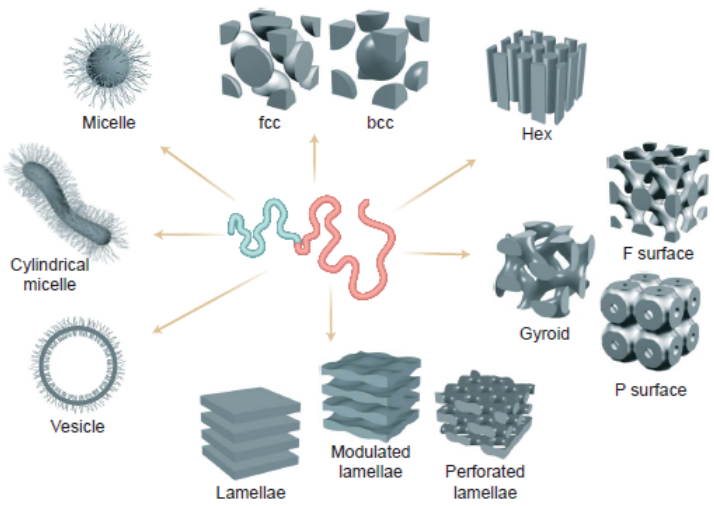

Figure 5.11: Schematic diagram of five different ordered microstructures[155]

The self-assembly of block copolymers (BCPs) into highly ordered morphologies pro-

vide the microphase separation structures over large scales. Generally, the part which can contain laser dye molecular (hydrophobic) can be well separated from the part which will interact with metal ion (hydrophilic). Thus, diblock copolymers are of great interest as a metal ion sensor based on microcavity laser in microfluidic channel. Furthermore, the "size" of the microstructures may cause some light scattering in optical measurements. However, the size of the micelles is often less than 100 nm, which is smaller than the visible wavelength. In this study, we focus our attention on several diblock copolyers, such as PS-b-P2VP, PS-b-P4VP, PS-b-PAA. Atomic force microscopy, ellipsometry and profilometry are main methods for characterizing the surface morphology and refractive index.

5.5.1 Materials and Methods

Poly(styrene-b-4-vinyl pyridine)(PS-b-P4VP) (Mn = 22500-b-29000 , PDI = 1.2), Poly (methyl methacrylate-b-2-hydroxyethyl methacrylate) (PMMA-b-PHEMA) (Mn = 17000-b-17500, PDI = 1.2) were purchased from Polymer Source. Inc. (Canada) and used as received. Organic solvents employed for the photophysical measurements and polymer film making (3-pentanone, 1,4-dioxane, toluene, cyclohexanone, tetrahydrofurane, ethanol, methanol) were in spectrophotometric purity superior 99% and purchased from Aldrich, Sigma or Merck.

DCM was purchased from Exciton.

The structures of polymers are shown in Figure 5.12.

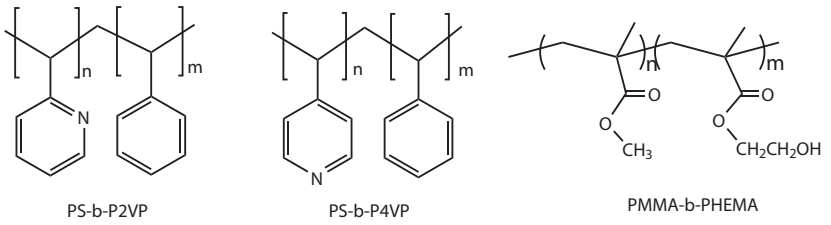

Figure 5.12: Structures of polymers and dye

PS-b-P2VP, PS-b-P4VP were used as a matrix for microcavity laser. PMMA-b-PHEMA was used as a surface modification polymer on PMMA surface.

5.5.2 Solution preparation

To prepare the block copolymer thin films, 6 wt% block copolymer (compared to the solvent) was dissolved in a good solvent or mixture solvent. 6 wt% of Poly(styrene-b-2-vinyl pyridine) (PS-b-P2VP) solution was prepared with a mixture of toluene and THF (50:50) (spectroscopic grade, 99% from Sigma- Aldrich Co) and stirred all the night without

heating. 6 wt% of Poly(styrene-b-4-vinyl pyridine) (PS-b-P4VP) solution was prepared with 3-pentanone (spectro grade, 99% from Sigma- Aldrich Co) and stirred and equilibrated at least 1 day without heating.

All the solutions were added with 5 wt% of DCM compared to the polymer when making the films of Polymer-Dye system.

5.5.3 Preliminary study of the sensibility of copolymer films to water and metal ions

Film fabrication

All the films were prepared as follows: solutions were deposited onto the substrate and spin-casting was performed on a Spin Coater (Karl Suss Model CT62). The substrates were spun at 1000 r.p.m. with acceleration of 1000 r.p.m. s^{-1} for 25 seconds. Films were then allowed to dry in the oven for 2 hours at $100\,^{\circ}\mathrm{C}$.

Water treatment and metal ion solution treatment

In order to test the influence of water on the microcavity materials, the thin films made by spin-coating were immersed in water for 1 h and dried by nitrogen stream. AFM and ellipsometry measurements were actualized to characterize the morphology and refractive index changes after this treatment.

The sensibilities of microcavity materials to metal ions were tested by immersing the thin films into the metal ion solution. The thin films were immersed in 10^{-3} M $HClO_4$, 0.1 M NaCl, 0.1 M $Cd(AC)_2$ or 0.1 M $ZnCl_2$ solutions for 1 h, respectively. They were rinsed by Millipore water (18 MΩ) and dried by nitrogen stream.

5.6 PS-b-P2VP

Poly(styrene-b-2-vinyl pyridine)(PS-b-P2VP) (Mn = 22 000-b-26 000) was synthesized by others in our lab. The rationale for using this system is that block copolymers composed of polystyrene (PS), a hydrophobic block, and poly(2-vinyl pyridine) (PVP), a hydrophilic block, form microphase separation [156, 157]. Another very important aspect of this system is that the nitrogen atom in the pyridine ring can be used for functionalization or interactions with different compounds because of its nucleophilic character [158, 159] or coordination bonding [160, 161]. This characteristic makes this specific BCP can be used as a model to test microcavity laser as possible metal ion sensor. In our study, making the thin film with optical quality is critical for a metal ion sensor based on microcavity laser.

5.6.1 UV-Vis absorption and fluorescence of DCM laser dye

The photophysical properties of organic laser dyes are sensitively affected by matrix materials when they are incorporated as dopants. The absorption and emission spectra of a gain medium studied in this thesis were measured from thin solid films of a dye-doped polymer.

The thin films for UV-Vis and fluorescence study were casted on glass slides (1 mm thickness microscope slide) from 6 wt% polymer solution which contains 5% (weight ratio to the polymer matrix) DCM laser dye. The spectra of DCM in PS-b-P2VP matrix are shown below (Figure 5.13). These spectra are similar with those obtained from solutions of DCM (Figure 5.10).

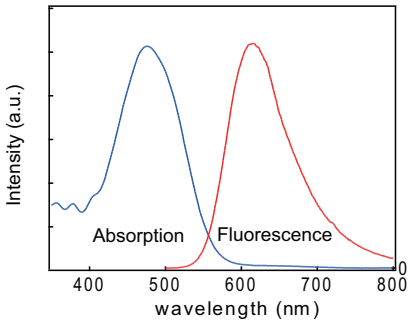

Figure 5.13: UV-Vis absorbance and fluorescence of 5 wt%DCM in PS-b-P2VP matrix.

5.6.2 AFM characteristics

Pure block copolymer thin films are casted on silicon wafer (Microchem.) for morphology study. PS-b-P2VP thin films (ca. 1 μm in thickness) were spin-coated from a 6 wt% of toluene and THF (50:50 v:v) mixture solution followed by annealing at $100\,^{\circ}\mathrm{C}$ for 2 h. AFM height image (Figure 5.14A) shows mixed structures with most of the cylindrical microdomains parallel to the surface.

Furthermore, the influence of water and the incorporation of a small amount of Zn^{2+} solution were studied by immersing the PS-b-P2VP thin film into water or 0.1 M $ZnCl_2$ solution respectively for 30 min. The thin films were dried with nitrogen gas before AFM and Ellipsometry measurements. The changes of morphologies of this diblock copolymer are demonstrated by AFM phase images (Figure 5.14).

As we can see in AFM height images, both water treatment film and Zn^{2+} treatment film changed the morphology of this BCP. The increase of roughness for the thin film indicated that the film can be swollen in water and may have some interaction with Zn^{2+} ion.

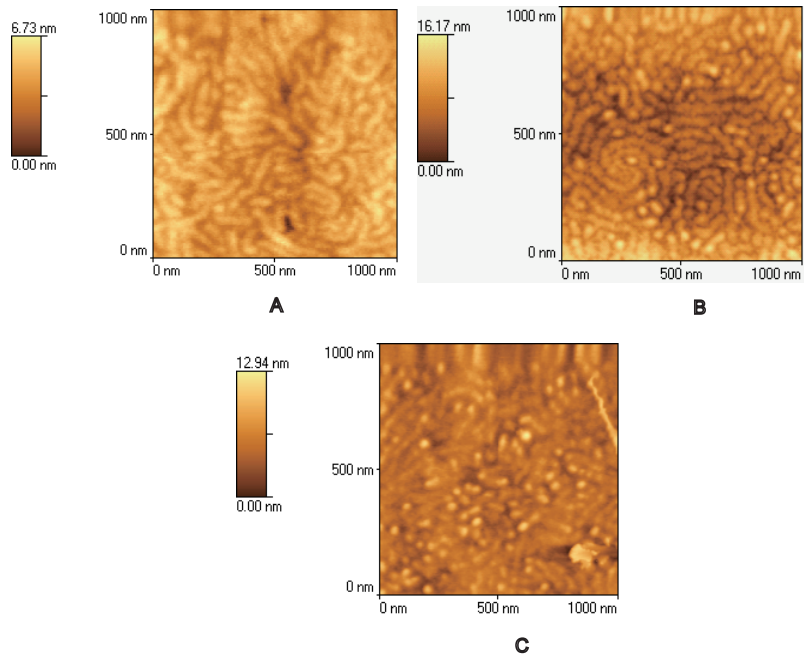

Figure 5.14: AFM height images of several PS-b-P2VP thin films: (A) original, (B) water treatment, (C) 0.1 M $ZnCl_2$ treatment.

5.6.3 Ellipsometry measurements

Ellipsometry was used to characterize the refractive index and thickness of spin-coated thin film of block copolymers on silicon wafers. The film thickness of 6 wt% of PS-b-P2VP casting from THF/Toluene (50/50) was about 0.63 μm, while that of PS-b-P2VP/DCM was about 0.43 μm.

Refractive index of PS-b-P2VP/DCM

The optical changes were investigated by ellipsometry. Laser dye doped BCP thin films were prepared for ellipsometry study, the protocol was just as that for BCP thin film, except 5 wt% DCM was added in the solution. 12 measurements in different spots on the same film are illustrated in Figure 5.15, with the average refractive index of 1.5798 (633nm) and STD of 0.292%.

The stability of refractive index was tested by measuring at the same spot for 10 times continuously. Figure 5.16 displays that the refractive index is very stable with a STD only 0.0135%. So the variations observed in Figure 5.15 come from some film inhomogeneity.

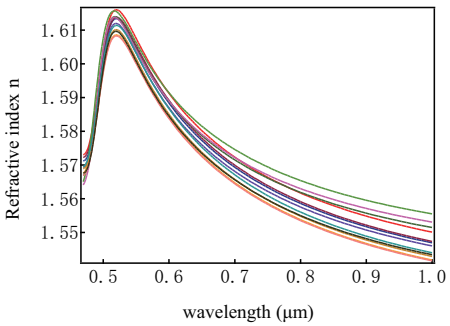

Figure 5.15: Refractive index distribution in one thin film of PS-b-P2VP/DCM versus the wavelength inferred from ellipsometric measurements.

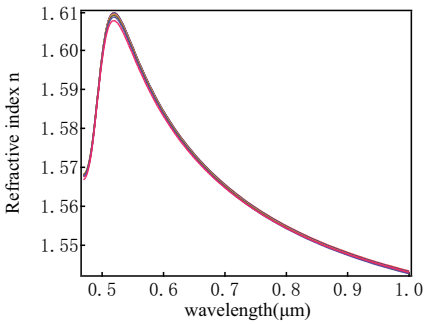

Figure 5.16: Refractive index stability of PS-b-P2VP/DCM

Water and metal ion solution treatments

The thin film of PS-b-P2VP alone was immersed in water for 1 h and measured after drying by nitrogen to withdraw water adsorbed on the surface to test water influence. A comparison of refractive index between original film and water treatment film is shown in Figure 5.17. The measurements displayed a decrease of refractive index after water treatment.

0.1 M $ZnCl_2$ solution was applied to test the coordination of Zn^{2+} and pyridine in PS-b-P2VP. Figure 5.18 shows refractive index change after Zn^{2+} treatment. A decrease of refractive index is also observed after treatment with a Zn^{2+} solution ($ZnCl_2$ 0.1 M). This may be explained if we suppose that there is no strong interaction between Zn^{2+} and PS-b-P2VP.

The refractive index changes and thickness changes after water treatment and 0.1 M $ZnCl_2$ solution treatment are summarized in Table 5.1.

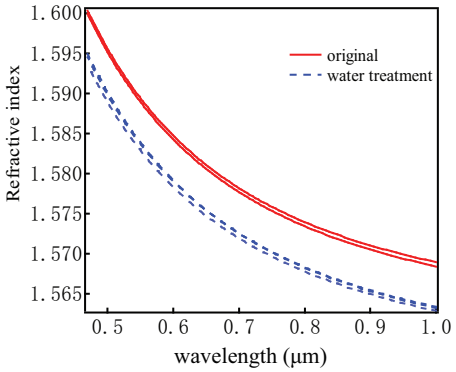

Figure 5.17: Refractive index change of PS-b-P2VP after water treatment.

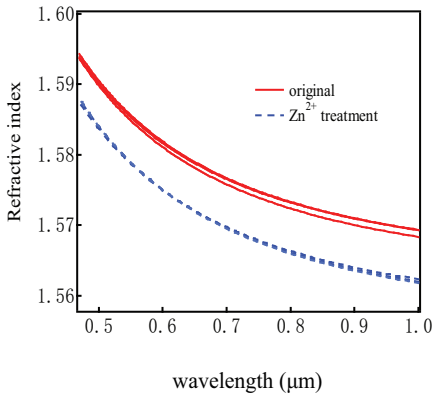

Figure 5.18: Refractive index change of PS-b-P2VP after 0.1 M Zn^{2+} treatment.

Table 5.1: The refractive index changes of PS-b-P2VP

	Original	Δ n (Water)	Δ n (0.1 M $ZnCl_2$)
n	1.580	-0.003	-0.007

5.7 PS-b-P4VP

As shown in Figure 5.12, the only difference between PS-b-P4VP (Poly(styrene-b-4-vinyl pyridine)) and PS-b-P2VP (Poly(styrene-b-2-vinyl pyridine)) is the position of the nitrogen atom in the pyridine ring. But P4VP is more polar than P2VP, because nitrogen, the electronegative element in P4VP, is in a better position to interact with a polar solvent. The larger chemical dissimilarity between PS and P4VP blocks causes the formation of PS-b-P4VP spherical micelles in 3-pentanone. Moreover, the nitrogen in P4VP is easier spatially to coordinate with metal ions.

5.7.1 UV-Vis absorption and Fluorescence

The thin films for UV-Vis and fluorescence study were casted on glass slides (1 μm thickness microscope slide). The spectra of DCM in PS-b-P4VP matrix are showed below (Figure 5.19). Once again, they are similar with those of DCM in a solvent like ethanol (Figure 5.10) .

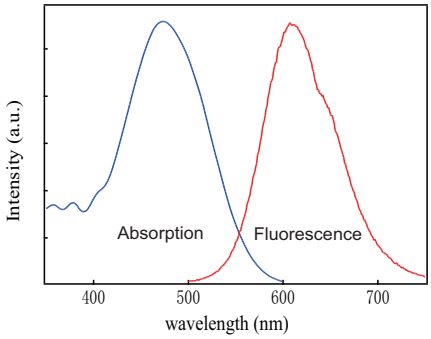

Figure 5.19: UV-Vis absorbance and fluorescence of 5 wt% DCM in PS-b-P4VP matrix.

5.7.2 AFM characterization

PS-b-P4VP

The microphase-separated structures of PS-b-P4VP (Poly(styrene-b-4-vinyl pyridine)) as-cast films and the effects of water, acid and several cations were investigated by AFM, as shown in Figure 5.20. It is worth noting that when 3-pentanone is used as a solvent, PS-b-P4VP forms a micelle solution. AFM image indicates that periodically ordered surface micelles were detected on the PS-b-P4VP film surface casted from 3-pentanone solution. The diblock copolymer forms hexagonal arrays of spherical micelles consisting of a P4VP core surrounded by a PS corona with diameter of $\sim$ 50 nm. Water treatment sample induces not so much change about the surface morphology, while the film treated by 0.1 M Zn^{2+} solution totally changed this morphology. We assume that it is the result of the interaction between Zn^{2+} and nitrogen in pyridine ring. The coordination can shrink the P4VP core, and make a flatter and porous surface.

The 3D AFM images (Figure 5.21) have further developed the effect of Zn^{2+} on the morphology of diblock copolymer: the original bumps due to the core of the micelles are replaced by holes when Zn^{2+} ions are present. This is a consequence of the complexation of Zn^{2+} ions by the pyridine groups, which leads to a packing and volume reduction of the pyridine micelle.

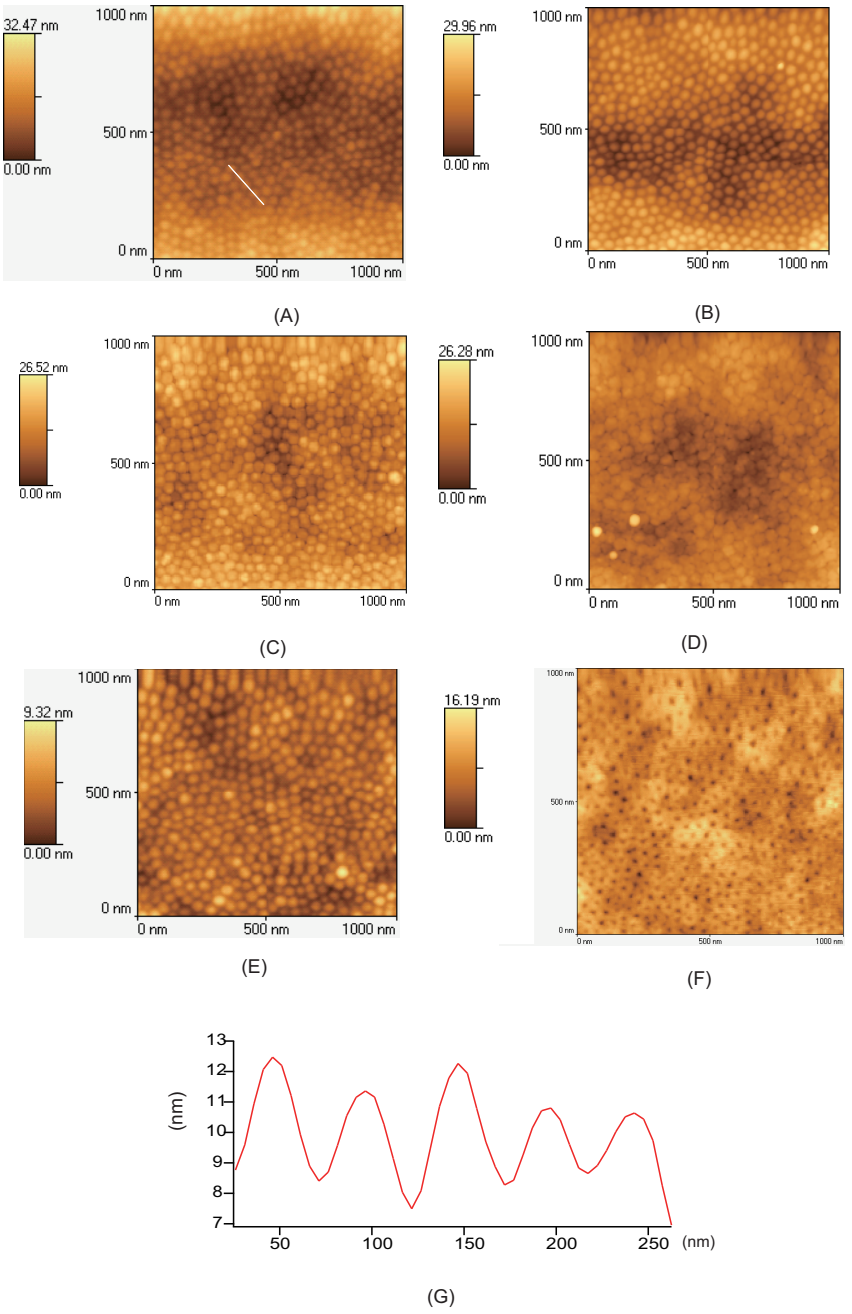

Figure 5.20: AFM height images of several PS-b-P4VP thin films: (A)original (average diameter D=50 nm), (B)water treatment, (C)10^{-3}M $HClO_4$ treatment, (D)0.1 M NaCl treatment, (E)0.1 M $Cd(AC)_2$ treatment, (F)0.1 M $ZnCl_2$ treatment, (G)line profile for AFM height image A.(1×1 μm scan size).

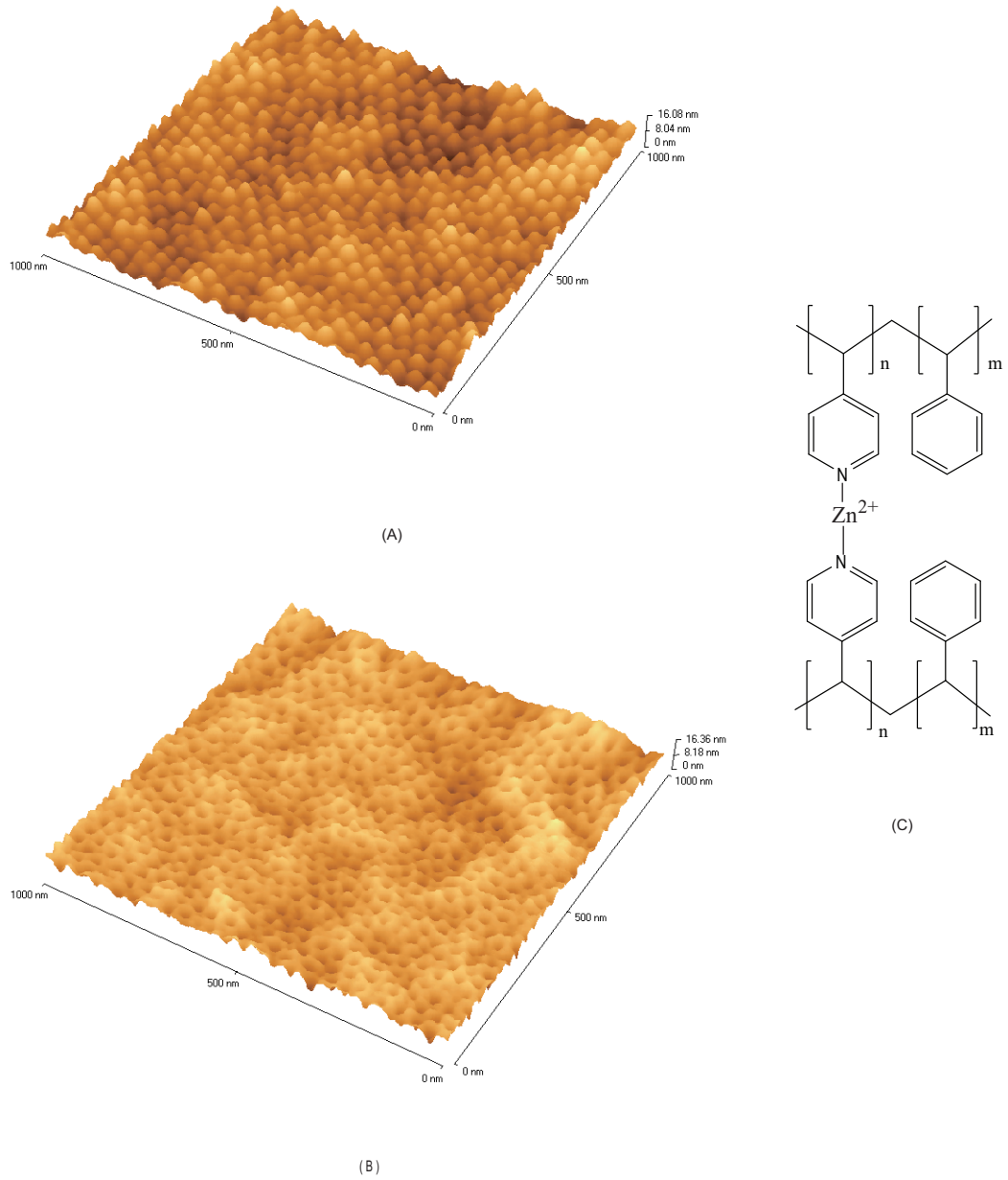

Figure 5.21: AFM 3D images of PS-b-P4VP thin films: (A) original, (B) 0.1 M $ZnCl_2$ treatment, (C) Structure of the complex between PS-b-P4VP and Zn^{2+}.

Morphology of PS-b-P4VP in different solvents

In order to get a better optical surface, thin PS-b-P4VP films were prepared from different solvent mixtures. Figure 5.22 shows AFM images of PS-b-P4VP in two solvent mixtures, 3-pentanone/toluene=50/50 (v/v) and 3-pentanone/cyclohexanone=50/50 (v/v). Both can give better optical surface than 3-pentanone alone. And micelles also form in 3-pentanone/toluene=50/50 (v/v) as in 3-pentanone alone. So in the following microcavity laser study, 3-pentanone/toluene=50/50 (v/v) was chosen.

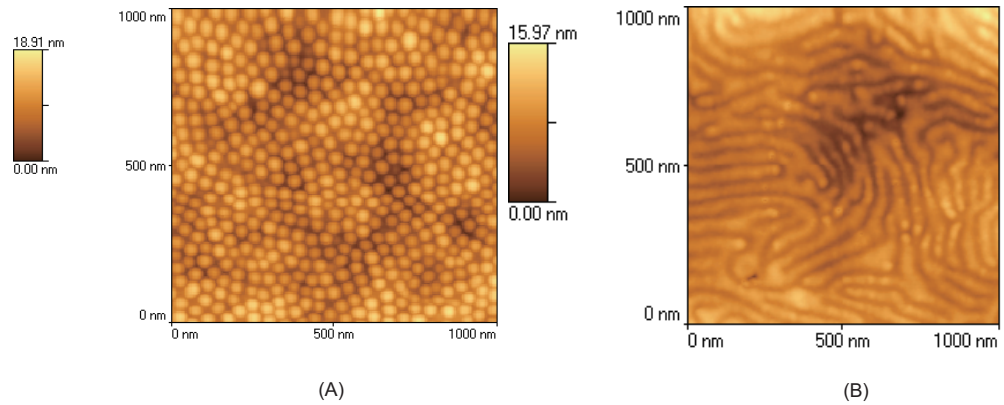

Figure 5.22: AFM images of as-cast PS-b-P4VP thin films in different solvents: (A)3-pentanone/toluene=50/50, (B)3-pentanone/cyclohexanone=50/50.

5.7.3 Ellipsometry characterization

Ellipsometry was used to characterize the refractive index and thickness of spin-coated thin film of block copolymers. The film thickness of 6 wt% of PS-b-P4VP casting from pure 3-pentanone was about 0.43 μm, while that of PS-b-P4VP/DCM was about 0.42 μm.

Ellipsometric mearsurements of PS-b-P4VP/DCM

The refractive index of as-cast PS-b-P4VP/DCM was measured by ellipsometry. Results obtained from 12 different spots in one wafer are illustrated in Figure 5.23, with the average refractive index of 1.5693 (633nm) and STD of 0.1775%.

The refractive index of as-cast PS-b-P4VP/DCM was measured temporally by ellipsometry to verify its optical stability. 10 measurements were applied in the same spot continuously, the results were illustrated in Figure 5.24 with a STD only 0.0316%. The larger variations in Figure 5.23 come from film inhomogeneity.

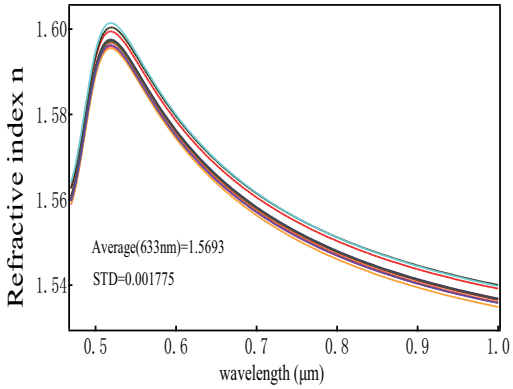

Figure 5.23: Refractive index of PS-b-P4VP/DCM as-cast thin film measured by ellipsometry.

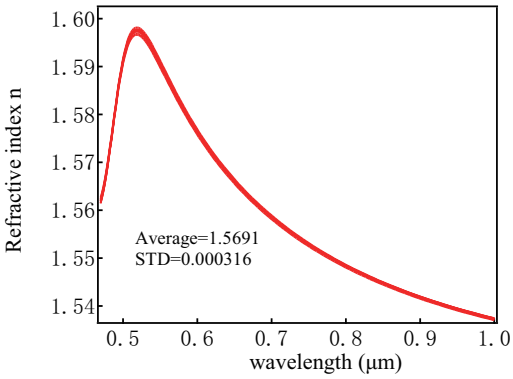

Figure 5.24: Optical stability of PS-b-P4VP/DCM as-cast thin film.

Refractive index change after water treatment

The thin film was immersed in water for 1 h and measured after drying by nitrogen to test water influence. A comparison of refractive index between original film and water treatment film is shown in Figure 5.25. The measurements displays a decrease of refractive index after water treatment.

Refractive index change after Zn^{2+} solution treatment

0.1 M $ZnCl_2$ solution was applied to test the coordination of Zn^{2+} and pyridine in PS-b-P4VP. Figure 5.26 shows refractive index changes after Zn^{2+} treatment.

An increase of refractive index was observed after treatment with a Zn^{2+} solution ($ZnCl_2$ 0.1 M). This may be explained if we suppose that there is strong interaction between Zn^{2+} and PS-b-P4VP. The increase of density of the film due to adsorption of Zn^{2+} ion may be at the origin of the this increase.

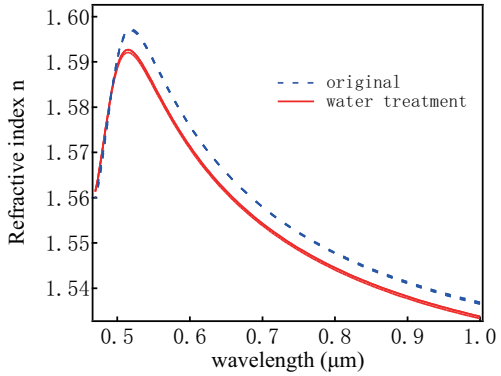

Figure 5.25: Refractive index change of PS-b-P4VP/DCM after water treatment.

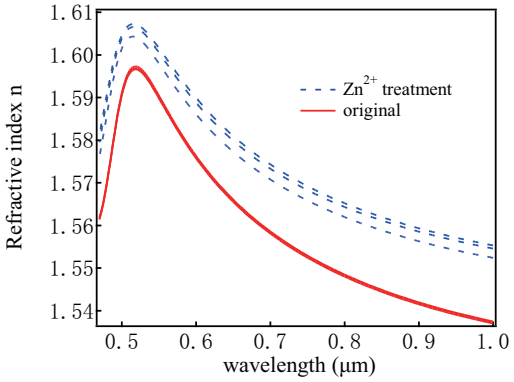

Figure 5.26: Refractive index change of PS-b-P4VP/DCM after 0.1 M Zn^{2+} treatment.

The refractive index changes after water treatment and 0.1 M $ZnCl_2$ solution treatment are summarized in Table 5.2.

Table 5.2: The refractive index changes of PS-b-P4VP/DCM

	Original	Δ n (Water treatment)	Δ n (0.1 M $ZnCl_2$ treatment)
n	1.569	-0.005	0.013

The large difference of refractive index and morphology among original thin films, water treatment and $ZnCl_2$ solution treatment shows that this material may introduce a spectral shift in a microcavity laser. More studies were carried out on this material. Finally, in the following studies, this polymer was chosen for microcavity laser preparation.

5.7.4 Amplified Spontaneous Emission (ASE) test

The diblock copolymer PS-b-P4VP has shown a patterned morphology and stable optical quality. And treatment by water or metal ion had a strong effect. Our coworkers Lebental et al. have first attempted to test the ASE (Amplifier Spontaneous Emission) for this new host-guest microcavity laser systems. The principle of ASE is presented in Appendix A.4.8. Taking into account of the signal intensity, the thin film must have a reasonable thickness and a good optical surface. We adjusted the concentration of diblock polymer PS-b-P4VP solution to 80 mg ml^{-1} in 3-pentanone/toluene (v/v=50/50), but DCM was kept in 5 wt% in the polymer. The ASE spectrum of this system is shown in Figure 5.27. It is worthy to note that the mid-height of this spectrum is smaller than that of the fluorescence spectrum of DCM (see Figure 5.10). Strong red ASE was observed, even with naked eyes. Then microcavity laser was successfully realized with this host-guest system.

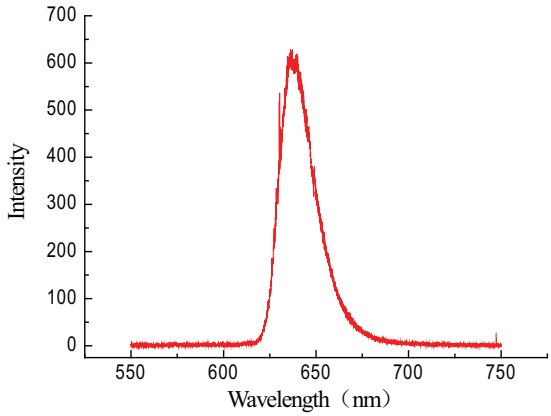

Figure 5.27: ASE spectrum of PS-b-P4VP/DCM thin layer.

5.8 Design and fabrication of optofluidic device for metal ion sensing

An optofluidic sensor based on microcavity laser is illustrated in Figure 5.28. The mirocavity is made of a diblock polymer matrix (PS-b-P4VP) containing a laser dye (DCM). Figure 5.29 shows the experimental set-up of the optofluidic sensor based on the microcavity laser.

The optofluidic channel was composed of a Si/SiO_2 substrate which supported the microcavity laser and a PDMS cover which allowed to be drilled with an entrance and an exit for fluid flow. The fluid flow was controlled by a syringe pump.

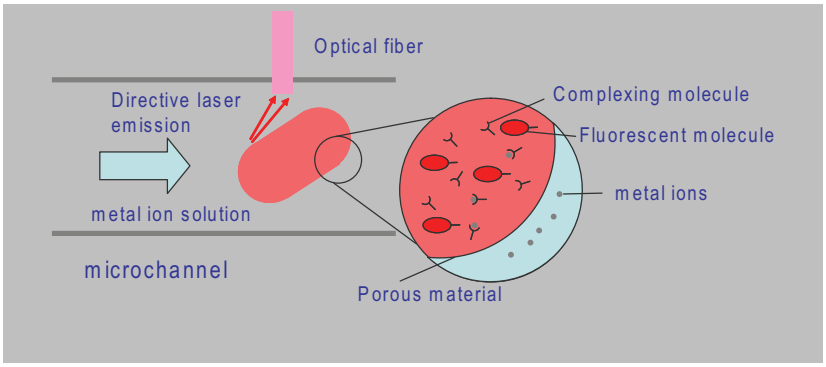

Figure 5.28: Scheme of an optofluidic sensor

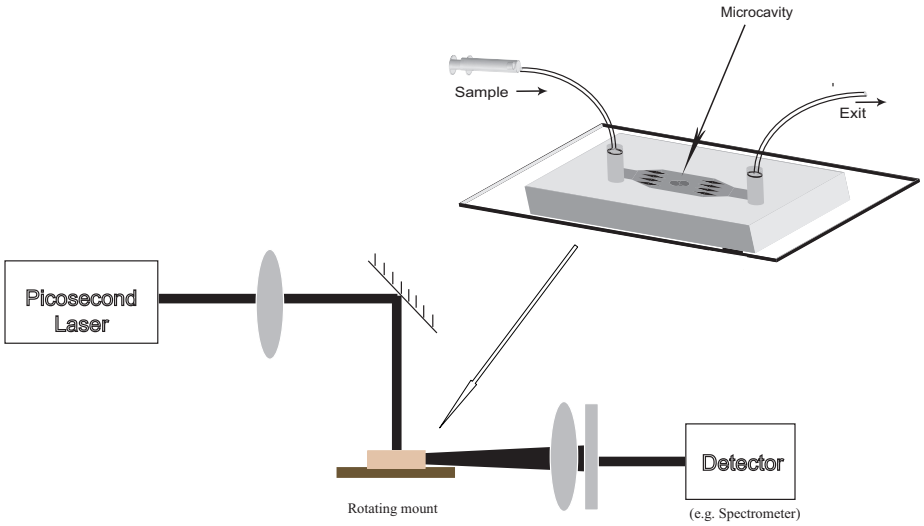

Figure 5.29: Schematic illustration of optofluidic sensor based on a microcavity laser

5.8.1 First demonstration of the optofluidic sensor

This first demonstration was made in collaboration with Sergey LOZENKO from LPQM (ENS CACHAN). In this optofluidic device, water and zinc ion solution were used as samples. A typical experimental laser emission spectra of PS-b-P4VP/DCM system in optofluidic channel was obtained from an octagon microcavity, as in Figure 5.30. When water was passed through a octoganal microcavity laser, a new spectrum was observed with no large spectral shift ($\Delta\lambda$= 0.007 nm) (Figure 5.31). Then water was replaced by 0.1 mol L^{-1} $ZnCl_2$ solution passing through microfluidic channel. An apparent shift of 0.12 nm was observed (Figure 5.32).

As this is only a preliminary experiment for an optofluidic sensor, there are still many studies to be done to better understand the behavior of these microcavities and to build a highly selective optofluidic metal ion sensor.

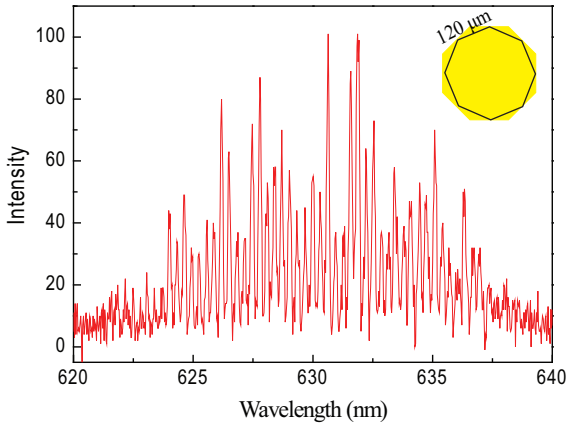

Figure 5.30: Laser emission of an octogonal microcavity laser made of PS-b-P4VP/DCM inside the microfluidic channel.

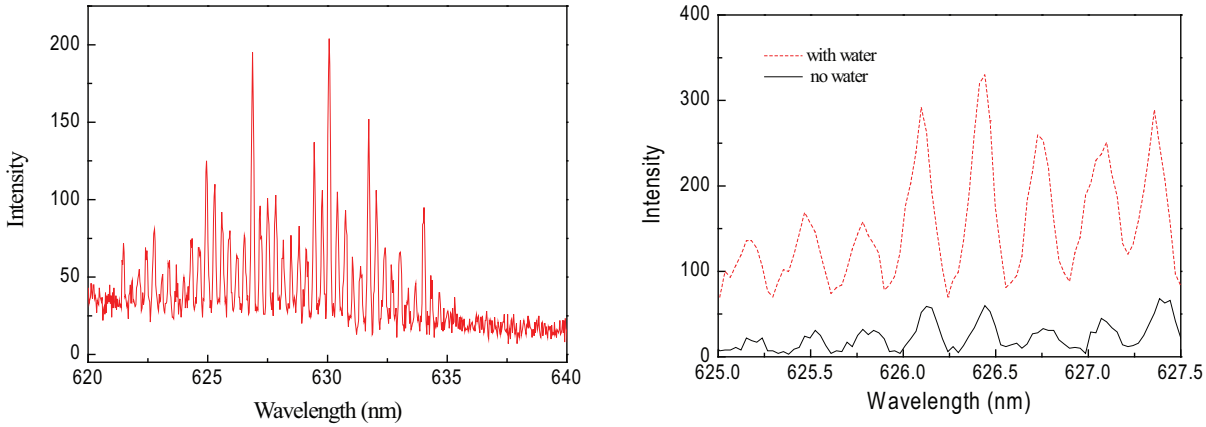

Figure 5.31: Left: Laser emission of an octogonal microcavity laser inside the microfluidic channel after water treatment. Right: an overlap image of spectra before and after water treatment. (Dashed line is after water treatment, full line is before.)

5.9 Surface modification of PMMA

Another strategy is being developed for microcavity lasing materials. Instead of using diblock copolymers, we directly modify the surface of PMMA which has been extensively used as a convenient matrix for microlaser.

The presentation below is one approach of the modification of PMMA surface. PMMA has been successfully used as a microcavity laser matrix. As the host-guest system PMMA-DCM is suitable for laser action, we attempted to functionalize the surface of PMMA with a specific ligand to act as an optofluidic metal ion sensor. In order to keep this good lasing system, one modification strategy is to form a monolayer of ligand for metal ion sensing

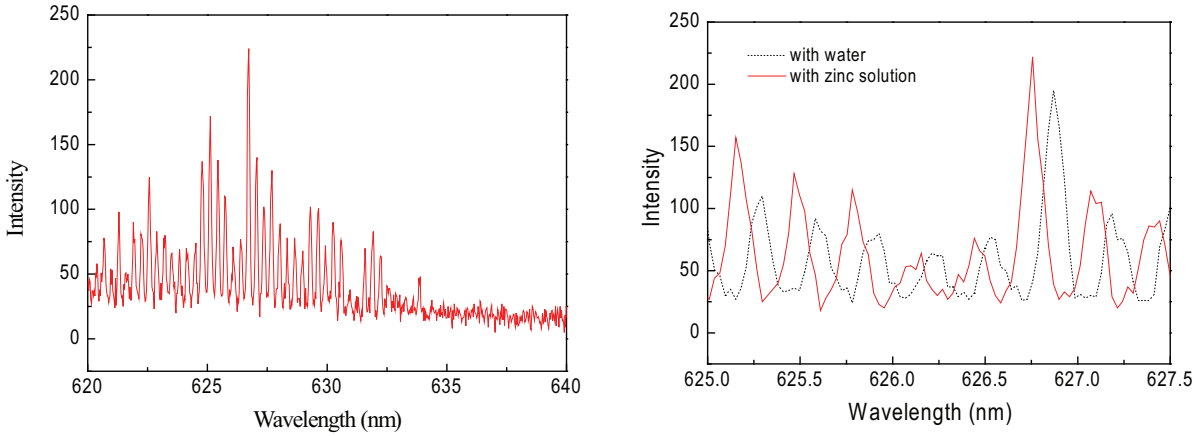

Figure 5.32: Left: Laser emission of an octogonal microcavity laser inside the microfluidic channel after $ZnCl_2$ solution treatment. Right: an overlap image of spectra before and after zinc ion solution treatment. (Full line is after zinc ion treatment, dashed line is just after water treatment.)

on the PMMA surface. Amphiphilic block copolymer is a good choice to form this kind of monolayer.

5.9.1 PMMA-b-PHEMA micelle solution preparation

PMMA-b-PHEMA is an amphiphilic block copolymer, which can yield a micellar solution when dissolved in a selective solvent, which dissolves one component and does not dissolve the other. Yin et al.[162] have studied three solvents for micellar solution preparation and film making. Methanol was a selective solvent of the PHEMA sequence, thus micelles with PMMA as core and PHEMA as corona were formed. External PHEMA is propitious to further graft special ligand for metal ion recognition. In our study, 0.5 wt% solution of PMMA-b-PHEMA in methanol was made for the following use, unless otherwise specified.

5.9.2 Surface modification of PMMA

The surface modification of PMMA by PMMA-b-PHEMA monolayer was performed with a homemade dip-coater. The PMMA thin film was previously made on Si-wafers with the same process as all other block copolymer films. Then PMMA thin films were dipped into the 0.5 wt% solution of methanol with a velocity of 40 mm min^{-1}, subsequently pulled out of the solution with a velocity of 5 mm min^{-1}, and then exposed to air for drying. The distinct regular 2-D hexagonal lattice of PMMA-b-PHEMA sphere structure was observed in the AFM image (Figure 5.33).

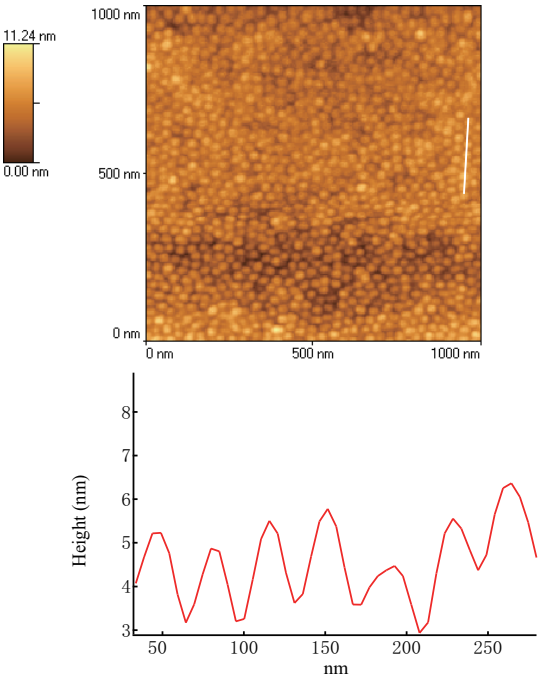

Figure 5.33: AFM height image of PMMA-b-PHEMA thin film dip-coated from 0.5 wt% methanol solution on PMMA surface.

It has been well-known that the free surface of BC film tends to cover itself with a component having relatively low surface tension to minimize the surface energy [162]. Thus on PMMA surface, the PMMA core of PMMA-b-PHEMA micelles tend to attach with PMMA surface to form a well-organized monofilm. A scheme of this attachment is as follows (Figure 5.34):

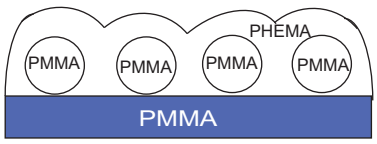

Figure 5.34: Schematic drawing of the side views of thin films of PMMA-b-PHEMA adsorbed onto PMMA thin film from methanol micellar solution.

Self-assembled monolayers (SAMs) have successfully been used to demonstrate that the molecular recognition process is feasible at the monolayer solution interface. The advantages of SAMs for surface confined sensing are fast response times, ease and reproducibility of synthesis, and the introduction of additional chelating effects from the preorganization of the surface platform.

5.9.3 Microcavity laser measurement after modification

Laser spectrum before modification

A rectangle microcavity which is composed of PMMA and 5% DCM (see Figure 5.35) was chosen here to test the effect of this PMMA-b-PHEMA modification. The laser spectrum of this microcavity laser before treatment was illustrated in Figure 5.35. The microcavity was fabricated as described by Lebental et al. [149].

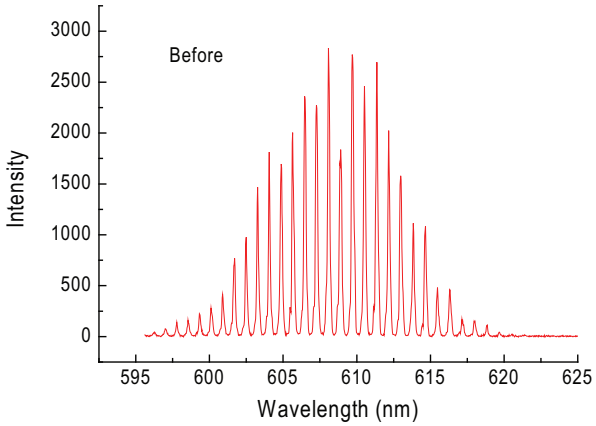

Figure 5.35: Typical laser spectrum of PMMA/DCM system in the rectangle plane before PMMA-b-PHEMA solution treatment.

Dip-coating of PMMA-b-PHEMA on PMMA/DCM surface

Considering the solubility of DCM in pure methanol, we adjusted the solvent of PMMA-b-PHEMA with a certain amount of water. Several ratios were tested, methanol/H_2O= 80/20, 70/30, 60/40, 50/50. These solutions were used for making dip-coating thin films of PMMA-b-PHEMA on PMMA/DCM thin film. AFM images showed that all of them can make a self-assembly layer on PMMA/DCM thin film (see Figure 5.36), and DCM did not dissolve in the solvent during dip-coating period. But the surfaces of (C) and (D) seemed to be more regular. Solutions containing more methanol evaporated more rapidly. An optimal composition of the solvent was fount to be MeOH/H_2O =70/30 (v/v).

Laser spectrum after modification

The microcavity whose laser spectrum has been recorded was modified by a monolayer of PMMA-b-PHEMA as described above with dip-coating method. The laser spectrum of this rectangle was also recorded as in Figure 5.37 after this modification. Comparing both spectra of the same microcavity before and after modification, we can see that laser signal

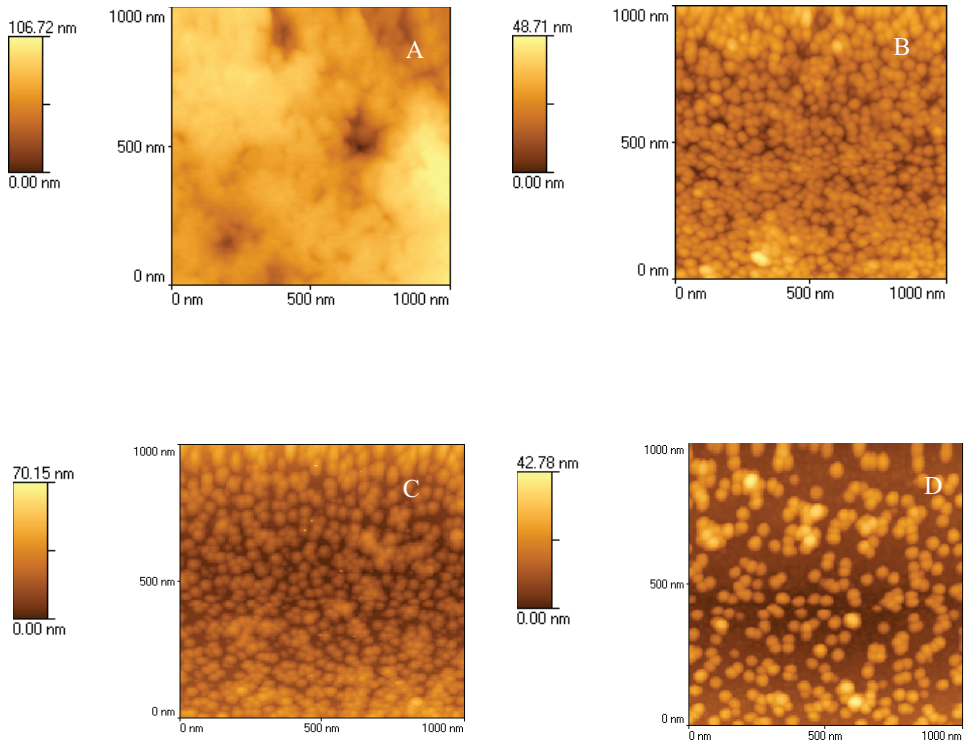

Figure 5.36: AFM height images of PMMA-b-PHEMA self-assembly layer dip-coated from different solutions. (A)MeOH/H_2O= 50/50, (B)MeOH/H_2O= 60/40, (C)MeOH/H_2O= 70/30, (D)MeOH/H_2O= 80/20.

is still maintained. Although the intensity has greatly decreased (only about 20%), it is comparable with that of optofluidic sensor made of PS-b-P4VP/DCM.

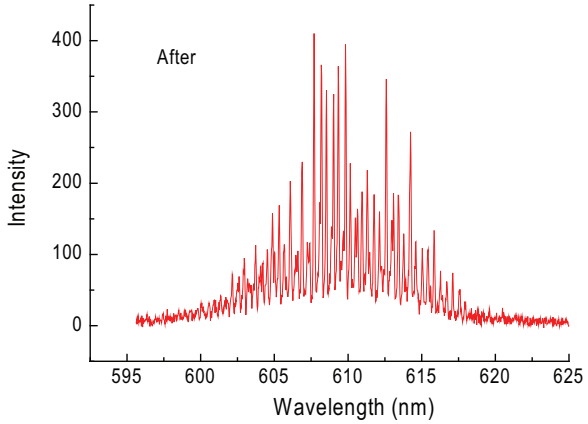

Figure 5.37: Typical laser spectrum of PMMA/DCM system in the rectangle plane after PMMA-b-PHEMA solution treatment.

5.10 Conclusion

In summary, we have proposed an optofluidic sensor for metal ion based on microcavity laser. The diblock copolymer materials have shown their capability as microcavity laser host. The morphologies and optical properties (such as refractive index) of two diblock materials (PS-b-P2VP and PS-b-P4VP) have been studied before testing their laser effect and sensing function. PS-b-P4VP seems to have more potential as an optofluidic sensor materials since it has obvious microphase separation structures and shows preliminary sensing ability towards zinc ion in water solution. However, the performance of our first optofluidic sensor still have some major defects, such as the effect of photobleaching and a lack of selectivity for metal ion sensing.

In addition, the direct modification of PMMA/DCM microcavity laser by a diblock copolymer (PMMA-b-PHEMA) has been tried. Its laser spectrum could be partially kept after this modification. More studies have to be done to realize an optofluidic sensor. The further step will be the chemical functionnalization of this surface monolayer with a ligand chosen to be specific of the heavy metal ion of interest. Work has already been done to synthesize these ligands (Djibril Faye, Ph-D thesis).

Part III

Detection of EDCs in miniaturized capillary electrophoresis

Chapter 6

Miniaturized capillary electrophoresis

6.1 Introduction

In the area of micro total analysis system (μ-TAS), particular attention has been paid to capillary electrophoresis microchips over the past several years, due to its advantages over conventional analysis methods, such as rapid separation, high separation efficiency, design flexibility, reagent economy, automation, and its potential portability and disposability [163, 164]. Fifteen years ago, Harrison etc. [165] demonstrated the principles of micromachining a miniaturized capillary electrophoresis based chemical analysis system on a chip (μ-CE). Now, capillary electrophoresis has been developing to a new miniaturized age.

Electrochemical detection (ED) possesses several advantages such as extremely low cost, low-power requirement, high selectivity, remarkable sensitivity, inherent miniaturization, high compatibility, advanced micromachining and micro-fabrication technologies. Among electrochemical techniques, amperometric detection has been the most widely employed method for μ-CE, since first reported in 1998 by Wolley et al. [166].

The combination of capillary electrophoresis with electrochemical detection (ED) has been successfully applied in chemical and biological fields, such as clinical diagnostics, environmental monitoring, and biological assays [167, 168].

Because of the potential global scope of the Endocrine Disrupting Chemical (EDC) problem, the possibility of serious problems in humans and wildlife, and the persistence of some suspected EDCs in the environment, research on EDCs is a high priority for human being. We choose EDCs in waste water as our research object.

However, sometimes an enhancement of the CE sensitivity and selectivity by using more specific detection systems or by on/ off-line sample preconcentration is necessary. Solid-Phase Extraction preconcentration is a good choice in this case.

Micellar electrokinetic chromatography (MEKC) is a well-known capillary electrophoretic method for the analysis of neutral compounds of low molecular weight. Samples are sepa-

rated by differential partitioning between a pseudo-stationary micellar phase and an aqueous mobile phase. The solution used in this mode contains a surfactant at a concentration that is greater than the critical micelle concentration (CMC). Above this concentration, surfactant monomers are in equilibrium with micelles. Sodium dodecyl sulfate (SDS) is the most commonly used surfactant in MEKC applications.

A miniaturized MEKC with amperometric detection has been developed to determine five EDCs in several water samples in our study, and solid-phase extraction method was used to extract the target EDCs.

6.2 Principle of capillary electrophoresis

In capillary electrophoresis, a sample is separated into its components as it migrates through a capillary under the driving force of an electric field.

6.2.1 Driving force

Generally, electroosmosis is a prominent mechanism for controlling fluid flow, requiring surface charges. The diagram of electro-osmotic flow (EOF) is demonstrated in Figure 6.1. The double layer formed closest to the surface is termed the "Inner Helmholtz or Stern Layer" and is essentially static. A more diffusion layer formed at some distance from the Stern Layer is termed the "Outer Helmholtz Plane" (OHP). The charge on the inner wall of the capillary causes the flow of electrolyte from the anode (where the sample is applied) to the cathode (where the sample is analyzed). The flow of electrolyte through the capillary is called electro-osmotic flow (EOF), and it drives positively charged, neutral, and negatively charged analytes through the capillary to the detector [169, 170]. The electroosmotic velocity is

$$\nu_{eof} = \epsilon\zeta E/4\pi\eta, \tag{6.1}$$

ϵ is the dieletric constant of the fluid, η is the fluid viscosity, E is the applied field strength, and ζ is the zeta potential of the surface [171]. The electroosmotic mobility (μ_{eof}) is the electroosmotic velocity normalized by the applied field:

$$\mu_{eof} = \nu_{eof}/E, \tag{6.2}$$

A second force, electrophoresis, which drives cations toward the cathode and anions toward the anode, enhances EOF for cations and opposes EOF for anions, resulting in their further separation. Electrophoretic mobility (μ) of a charged molecular species can be approximated from the Debye-Huckel-Henry theory

$$\mu = q/6\pi\eta r \tag{6.3}$$

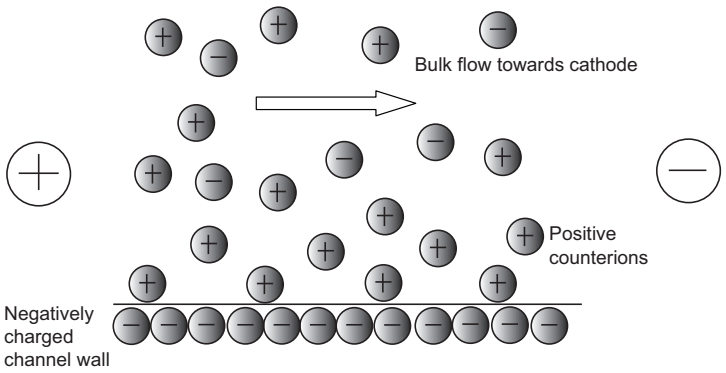

Figure 6.1: Schematic representation of electroosmotic flow(EOF)

where q is the charge of the particle, η is the viscosity of the buffer, and r is the Stokes' radius of the particle. It is evident that a small, highly charged particle will have a high mobility, while a large, minimally-charged species will have a low mobility.

6.2.2 Separation principle

The principle of electrophoresis refers to the migration of charged electrical species when dissolved, or suspended, in an electrolyte through which an electric current is passed. Cations migrate toward the negatively charged electrode (cathode) and anions are attracted towards the positively charged electrode (anode). Therefore, separation by electrophoresis relies on differences in the speed of migration (migration velocity) of ions or solutes. Ion migration velocity can be expressed as: $\nu = \mu$ E where ν is ion migration velocity (m s^{-1}), μ is electrophoretic mobility ($m^2V^{-1}s^{-1}$) and E is electric field strength (V m^{-1}).

From Eq. 6.3 it can be seen that the migration rates depend on charge-to-size ratio. A smaller ion will migrate faster than a larger ion with the same charge. An ion with a higher charge will migrate faster than one with a lower charge, if they are the same size. Electrophoretic mobility is probably the most important concept to understand in electrophoresis. This is because electrophoretic mobility is a characteristic property for any given ion or solute and will always be constant. It is the defining factor that decides migration velocities. Different types of ions or solutes have various migration velocities at the same electric field strength. From difference in electrophoretic mobility, it is possible to separate mixtures of various ions and solutes by using electrophoresis.

The EOF or "bulk flow" acts as a pumping mechanism to propel all molecules (cationic, neutral and anionic) toward the detector with separation ultimately being determined by differences in the electrophoretic migration of the individual analytes. As EOF is pH-dependent and can be quite strong, adjusting the pH of the electrolyte can control the balance between the EOF and the force associated with electrophoresis. At pH above 5, the

silanol groups on the inner wall of the silica capillary are ionized, giving the wall a negative charge and resulting in an EOF. At pH below 5, the capillary wall loses its charge, causing the EOF to disappear and making electrophoresis the dominant force.

6.2.3 The modes of CE

Capillary electrophoresis has several separation modes, such as Capillary Zone Electrophoresis (CZE), Capillary Gel Electrophoresis (CGE), Capillary Isoelectric Focusing (CIEF), Isotachophoresis (ITP), Micellar Electrokinetic Capillary Chromatography (MECC OR MEKC), Electrokinetic Chromatography (EKC), Micro Emulsion Electrokinetic Chromatography (MEEKC), Affinity Capillary Electrophoresis (ACE),Chiral CE, Non-Aqueous Capillary Electrophoresis (NACE), Capillary Electrochromatography (CEC).

Among them, CZE is used the most frequently, it is also known as free-solution CE (FSCE); it is the simplest form of CE. The principle of CZE can be seen in Figure 6.2 [172]. The separation mechanism is based on differences in the charge-to-mass ratio of each individual analyte. Fundamental to CZE are homogeneity of the buffer solution and constant field strength throughout the length of the capillary. The separation relies principally on the pH controlled dissociation of acidic groups on the solute or the protonation of basic functions on the solute.

We adopted another mode - Micellar Electrokinetic Capillary Chromatography (MECC or MEKC), which was named by Terabe et al. [173] in 1984. It is a mode of electrokinetic chromatography in which surfactants are added to the buffer solution at concentrations that form micelles. The separation principle of MEKC is based on a differential partition of the analytes between the micelle and the solvent. This principle can be employed with charged or neutral solutes and may involve stationary or mobile micelles. MEKC has great utility in separating mixtures that contain both ionic and neutral species, and has become valuable in the separation of very hydrophobic pharmaceuticals from their very polar metabolites [174].

6.3 Endocrine-Disrupting Chemicals

EDCs are residual chemicals that can cause harmful effects on human and wildlife via interactions with the endocrine system. EDCs have been shown to have a profound influence on the reproduction of some species and their offspring as well, for example, the occurrence of reproductive and developmental disruptions in snails, fishes, piscivorous birds, alligators, and sea mammals [175–184]. Effects on human health have been linked to reduced sperm counts in human males experiencing occupational exposure to these chemicals [185, 186]. Various reports suggest possible involvement of EDCs in lower sperm counts,

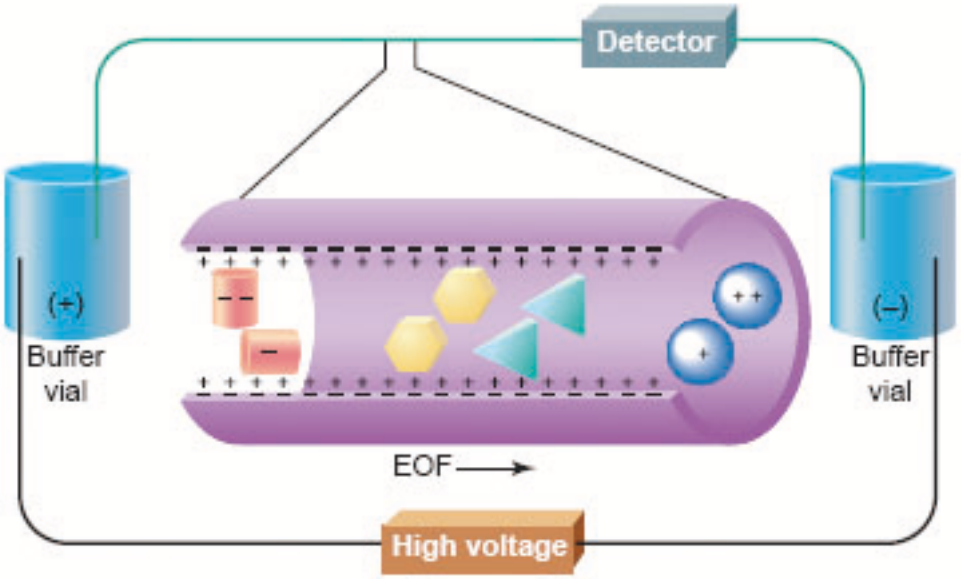

Figure 6.2: CZE separation in a CE system: An open-ended capillary extends between two buffer reservoirs, across which a high voltage is applied. This voltage causes analytes to migrate from the site of sample application at the cathode (+) buffer through a detector to the anode (-). The EOF that results from wall-pumping drives the separation of analytes. Electrophoresis speeds the migration of anions through the capillary [172].

undescended testicles, early puberty, and thyroid dysfunction [187–190]. Aware of the problem, the European Union (EU) has set a "priority list of substances for further evaluation of their role in endocrine disruption" [191] and indicates the need to assess the levels and effects of EDCs. The list of substances reported to cause endocrine disruption is diverse including both natural and synthetic chemicals. Among them, the natural estrogens estrone (E1), 17α-estradiol (αE2), and 17β-estradiol (βE2) and the exogenous EE2, the active ingredient in oral contraceptive pills, possess the highest estrogenicity. Apart from these steroids, alkylphenols such as 4-tert-butylphenol and the technical isomer mixture of 4-n-nonylphenol, both breakdown products of nonionic surfactants, and bisphenol A, a widely used monomer for epoxy resins and polycarbonates, show estrogenic potentials of 4 and more orders of magnitude lower than βE2[192]. Therefore, they are considered as

xenoestrogens. But also representatives of the groups of PCBs, polychlorophenols (like 2.4-dichlorophenol), dioxins, phytoestrogens, pesticides, preservatives, antioxidants or phthalic esters contribute to the daily exogenous burden of humans and wildlife with hormonally active agents [193–196]. In our environment, sewage treatment works (STWs) permanently receive a complex mixture of industrial, domestic and agricultural wastewater containing a lot of synthetic and natural chemical compounds [197–200]. The low level of these contaminants in wastewater effluents is still a major concern for the receiving environment and downstream users because EDCs exert physiological effects at very low concentrations. A number of researchers reported that conventional wastewater treatment efficiencies for degrading EDCs varied significantly throughout the year and that some EDCs were always present in effluent samples [197, 201, 202].

6.4 Methodology

6.4.1 Solid-Phase Extraction

Different techniques exist for extracting targeted contaminants from environmental matrices. The most common techniques are liquid-liquid extraction [203], steam distillation [204], solid-phase extraction [205, 206], solid- phase micro-extraction [207], immunoextraction [208], Soxhlet extraction [209], ultrasonication [210], microwave extraction system [211, 212], pressurized liquid extraction [213] and supercritical fluid extraction [214].

Enrichment of the analytes should contribute to the sensitivity and selectivity of the method and is often performed by solid phase extraction (SPE), which can discriminate between the target compounds and the matrix components to a degree that depends on the selectivity of the solid phase.

6.4.2 MEKC-ED

For the determination of EDCs, many techniques have been reported, including radioimmunoassay [215], enzyme-linked immunosorbent assay (ELISA) [216], liquid chromatography and hyphenated gas chromatography [217, 218], plus fluorescence and UV detection [219] and mass spectrometry with particle beams [220], electrospray and atmospheric pressure chemical ionization [221]. As an alternative methodology, capillary electrophoresis (CE) often possesses higher resolution, greater peak efficiency and shorter analytical time comparing with LC approach, so CE is a suitable method to determine numerous analytes to which GC and LC cannot be achieved ideally. Therefore, CE is often used in the analyses of many environmental pollutants such as polycyclic aromatic hydrocarbons (PAHs) [173, 222], alkylbenzenes [223], chlorophenols [224, 225] and alkylphenols [226]. Since

most of these compounds are electrically neutral and migrate at the velocity equal to the electroosmotic flow (EOF), it is difficult to separate them under normal conditions using common CE method. Micellar electrokinetic chromatography (MEKC), using sodium dodecyl sulfate (SDS) as the running buffer additive, is used to separate neutral compounds on the basis of their distribution into the micelles. And for the first time amperometric detection was employed for detecting these EDCs.

In this study, SPE as a preconcentration technique followed by MEKC/ED as the separation and determination method was developed for analyzing five EDCs in sewage.

6.5 Experimental

6.5.1 Reagents, Chemicals, and Sewage

2,4-dichlorophenol (DCP), 4-tert-butylphenol (BP), bisphenol A (BPA), 17α-ethynyl estradiol (EE2) and 4-n-nonylphenol (NP) were purchased from Sigma (St Louis, MO, USA). Their molecular structures are shown in Figure 6.3. SDS was purchased from Shanghai Reagent Factory (Shanghai, China), and they were all used as received. Acetonitrile, methanol, ethanol, dichlomethane were all of HPLC grade quality (Shanghai Reagent Factory, Shanghai, China). Stock solutions of five analytes (1.00×10^{-3} g mL^{-1} each) were prepared in anhydrous ethanol (AR grade), stored in the dark at $4\,^{\circ}C$, and were diluted to the desired concentration with the running buffer (H_3BO_3-$Na_2B_4O_7$). Before use, all solutions were sonicated and filtered through 0.22 μm nylon filters. All experiments were performed at room temperature. A sewage influent sample was collected randomly from Tian Shan Municipal Sewage Treatment Plant, Shanghai, China.

6.5.2 Analytical Equipment and Methods

A lab-made miniaturized MEKC system was used in this work (as Figure 6.4). The principles and details of the lab-built miniaturized MEKC-AD system were reported previously [227]. A direct current power supply (Shanghai Institute of Applied Physics, Chinese Academy of Sciences, Shanghai, China) provided a voltage between the ends of the capillary. The inlet end of the capillary was held at a positive potential and the outlet end of capillary was maintained at ground. The separations were proceeded in a 14 cm length of 25 μm i.d. fused-silica capillary (Polymicro Technologies, Phoenix, AZ, USA). After being coated with insulated varnish film, the carbon lead available in market with 300 μm diameter can be directly used as the disk working electrode (Figure 6.4a). Before use, the disk surface of carbon electrode was polished with emery sand paper, sonicated in deionized water, and then positioned carefully opposite to the capillary outlet through the guiding

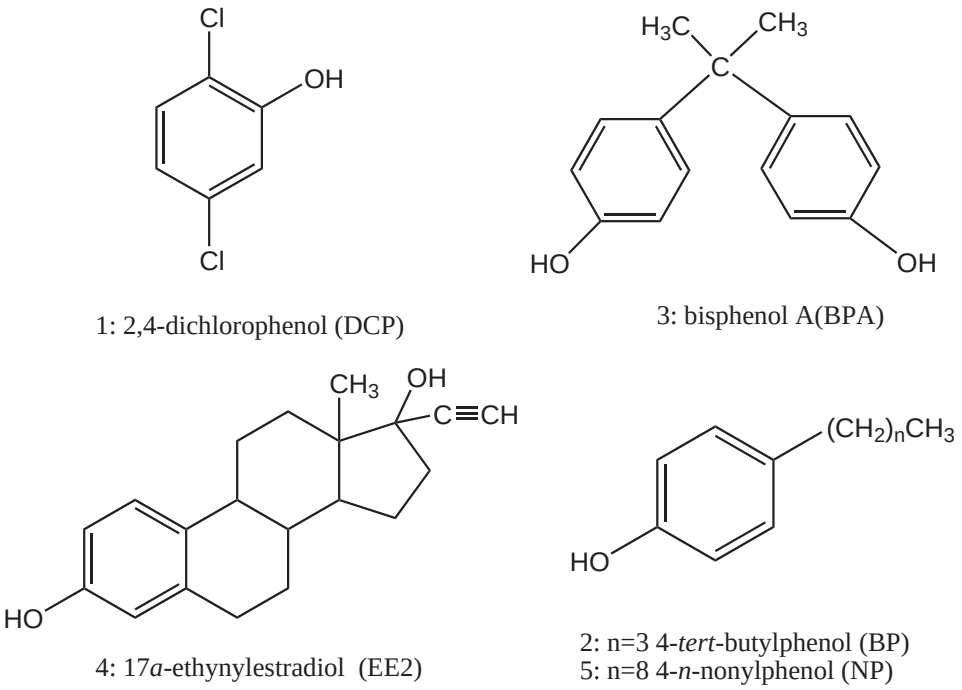

Figure 6.3: Molecular structures of (1) DCP, (2) BP, (3) BPA, (4) EE2, and (5) NP

metal tube (Figure 6.4i) which was fabricated for the alignment of the working electrode and capillary. The other end of carbon electrode was connected to copper lead by soldering tin used as connecting line to the detector. A three-electrode electrochemical cell consisting of a lab-made 300 μm diameter carbon disc working electrode (Figure 6.4a), a platinum auxiliary electrode (Figure 6.4b) and a Ag/AgCl reference electrode (Figure 6.4c), was used in combination with a BAS LC-4C amperometric detector (Bioanalytical Systems Inc., West Lafayette, IN, USA). The electropherograms were recorded using a chart recorder (Shanghai Da Hua Instrumental Factory, China). The whole system was assembled in an air-conditioned room at $25\,^{\circ}\mathrm{C}$ in order to minimize the variation of running buffer viscosity, which is important for the good reproducibility of the experimental results.

6.5.3 Extraction of sewage sample

Optimization of the SPE extraction of DCP, BP, BPA, EE2 and NP from the real samples using C_{18} cartridge was performed as published [228]. The cartridges (0.2 g HLB, Waters) were conditioned successively with 5 mL of methanol, 5 mL of methanol/water (50:50, v/v), and then 5 mL of water. Then water samples (0.2 l of sewage, 0.5 l of river water) were filtered through a $0.45\,\mu$m cellulose acetate membrane filter, and passed through the cartridge at a flow-rate 5 mL min^{-1}. After the sample was passed through the cartridge, the vacuum was reduced. The retained compounds were eluted with 10 mL of a

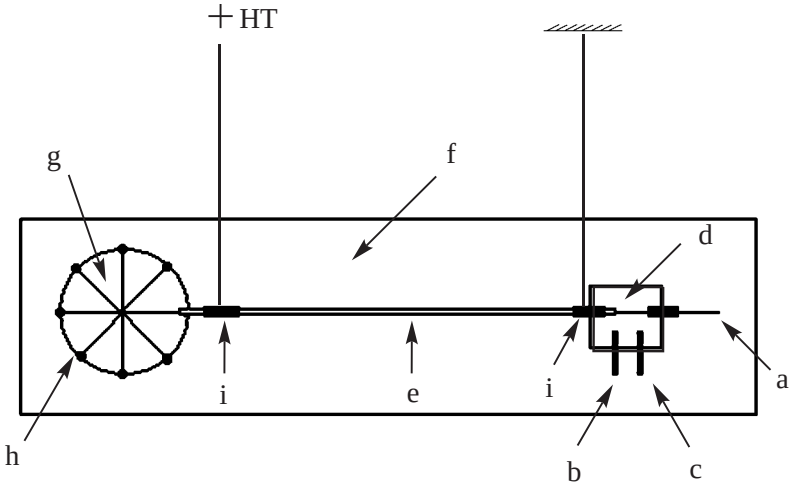

Figure 6.4: Top view of the schematic diagram of the miniaturized MEKC-AD system. (a)carbon working electrode; (b)Ag/AgCl reference electrode; (c)Pt auxiliary electrode; (d)detection cell; (e)capillary; (f)plexiglass plate; (g)rotating sampling disk; (h)plastic cuvette containing sample solution or running buffer; (i)guiding metal tube.

dichloromethane: methanol (50:50, v/v) solution. In a thermostatic bath (Shanghai Mei Yingpu Instrument Manufacturing Co., Ltd., China) set at $40\,^{\circ}\mathrm{C}$, the extracts were, then, evaporated to dryness under a gentle nitrogen stream. The residues were dissolved in 100 μL of water: acetonitrile (50:50, v/v) solution. They were electrokinetically injected to the MEKC-AD system for analysis. All sample solutions were stored in a $4\,^{\circ}\mathrm{C}$ refrigerator.

6.5.4 MEKC optimum conditions

Effect of running buffer

In this work, a borate buffer (pH 7.4) with additive SDS was used in a MEKC mode for the determination of EDCs in sewage. Effects of pH, concentration of running buffer and SDS were studied. The running buffer pH did not much affect the separation of these EDCs, therefore, a running buffer with low concentration (20 mmol L^{-1} pH 7.4 (H_3BO_3-$Na_2B_4O_7$) buffer) was selected. According to a work published by Masatoki Katayama et al. [229], SDS can improve the separation of BPA and alkylphenols. The typical electropherograms of before and after adding SDS are as in Figure 6.5 and Figure **??**. In this work SDS ranging from 10-100 mmol L^{-1} was added to the running buffer for testing. It was found when SDS was below 15 mmol L^{-1}, BP cannot be separated from DCP. As higher concentration of SDS may cause larger background current and longer analysis time, finally 15 mmol L^{-1} SDS was selected as running buffer additive for better separation.

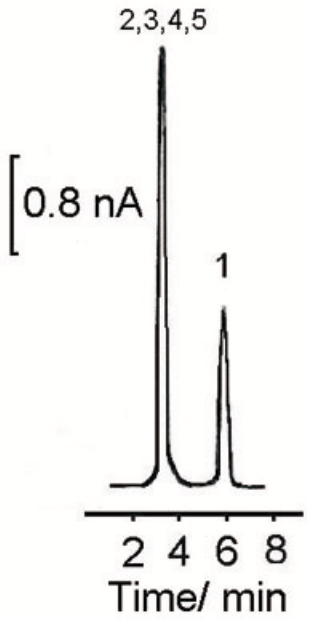

Figure 6.5: Electropherogram of five EDCs without adding SDS. Fused-silica capillary: 25 μm i.d. $\times$ 14 cm; working electrode: 300 μm diameter carbon disc electrode; running buffer: 20 mmol L^{-1} (pH 7.4); separation voltage: 1.15 kV; injection time: 8 s (at 1.15 kV); the concentrations of five analytes:2.0×10^{-5} *g mL^{-1} each, and the labels of anlytes 1-5 were the same as in Figure6.3.*

Effect of the potential applied to the working electrode

In amperometric detection, the potential applied to the working electrode directly affects the sensitivity, detection limit and stability of this method. Therefore, hydrodynamic voltammetry experiment was investigated to obtain optimum detection. As shown in Figure 6.6, the peak current increases rapidly when the applied potential exceeds +800 mV for all five EDCs. However, when the applied potential is greater than +1000 mV (vs Ag/AgCl), although the peak currents of the analytes still slightly increase, both the baseline noise and the background current increase substantially, which is a big disadvantage for sensitive and stable detection. Therefore, the potential applied to the working electrode is maintained at +1000 mV (*vs* Ag/AgCl), where the background current is not too high and the signal-to-noise (S/N= 3) ratio is the highest.

Effect of separation voltage and injection time

For a given capillary length, the separation voltage determines the electric field strength, which affects both the velocity of electroosmotic flow (EOF) and the migration velocity of the analytes, which in turn determines the apparent migration velocity of the analytes. In

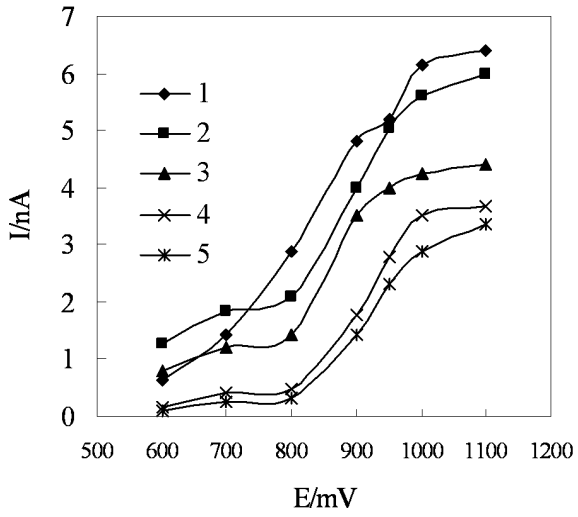

Figure 6.6: Hydrodynamic voltammograms (HDV) of five EDCs in miniaturized MEKC. Fused-silica capillary: 25 μm i.d. × 14 cm; working electrode: 300 μm diameter carbon disc electrode; running buffer: 20 mmol L^{-1} (pH 7.4) with 15 mmol L^{-1} SDS; separation voltage: 1.15 kV; injection time: 8 s (at 1.15 kV); the concentrations of five analytes: 2.0×10^{-5} *g mL^{-1} each, and the labels of anlytes 1-5 were the same as in Figure 6.3.*

this work, because of using short capillary, the applied voltage was also low. When it was higher than 1.15 kV, EE2 and NP cannot be well separated. So a separation voltage of 1.15 kV was finally selected. The injection time determining the amount of sampling affected both peak current and peak shape. The effect of injection time on peak current was studied by varying injection time from 2 to 10 s at 1.15 kV(see Figure 6.7). The peak current increased with increasing injection time. When the injection time was longer than 8 s, peak current nearly leveled off and peak broadening became more severe. In this experiment, 8 s (1.15 kV) was selected as the optimum injection time.

Through the experiments above, the optimum conditions for these five EDCs have been decided. The applied potential to the working electrode was selected at +1000 mV (*vs* Ag/AgCl), and the injection time was 8 s (1.15 kV), and all five analytes can be well separated within 12 min at the separation voltage of 1.15 kV in a 20 mmol L^{-1} borat running buffer (pH 7.4) containing 15 mmol L^{-1} SDS. Figure 6.7a shows the typical electropherogram for a standard mixture solution of five analytes in the optimum conditions, from which we can see that a good separation can be achieved within 12 min. In the running buffer without SDS at pH 7.4, the separation of five EDCs was not achieved, because these compounds are nearly electrically neutral species at this pH, and their apparent migration velocities are

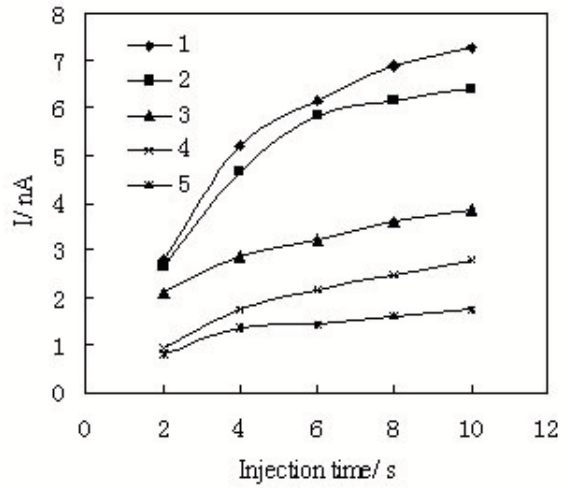

Figure 6.7: Effect of injection time. Fused-silica capillary: 25 μm i.d. × 14 cm; working electrode: 300 μm diameter carbon disc electrode; running buffer: 20 mmol L^{-1} (pH 7.4) with 15 mmol L^{-1} SDS; potential on working electrode: 1000 mV; separation voltage: 1.15 kV; the concentrations of five analytes: 2.0×10^{-5} *g mL^{-1} each, and the labels of anlytes 1-5 were the same as in Figure 6.3*

similar from one another (about the same as EOF) .

6.6 Method Validation

The method was validated by the following set of parameters: linearity, sensitivity, reproducibility, precision, accuracy, stability and robustness. To determine the linearity of DCP, BP, BPA, EE2 and NP, a series of the standard mixture solutions with concentrations ranging from 5.0×10^{-6} to 1.0×10^{-4} g mL^{-1} were tested. The peak current versus concentration of five EDCs were subjected to regression analysis to calculate the calibration equation and correlation coefficient. The results of regression analysis on calibration curves are summarized in Table 6.1. Sensitivity was evaluated by determining the limit of detection (LOD). LOD was defined as the lowest concentration with a signal-to-noise ratio of at least 3. The results were also reported in Table 6.1. The reproducibility of the peak current and migration time of five environmental endocrine-disrupting chemicals were estimated by making repetitive injections of a standard mixture solution (2.0×10^{-5} g mL^{-1}) under the selected optimum conditions (n=7). Their injection-to-injection repeatability in peak current and migration time was obtained with RSD of 1.8%, 2.8% (DCP), 2.6%, 2.0% (BP), 3.5%, 2.5% (BPA), 4.4%, 2.3% (EE2), and 4.8%, 3.7% (NP), respectively. Such high

stability was attributed to the use of extremely small sample volumes that resulted in a negligible accumulation of reaction products at the working electrode surface. Furthermore, the extraction efficiency of SPE was 93.0%. To further evaluate the precision and accuracy of the method the recovery experiments under the optimum conditions were also conducted with campus river sample (n=3). Recovery was determined by adding known and appropriate volumes of the working standard solution to previously analyzed aqueous sample. The assay result was 97.5% (BP), and the R.S.D was 3.6%. The results indicate the method is accurate enough for the simultaneous determination of the above analytes. As the separation capillary employed in our experiments was purchased from Polymicro Technologies (Phoenix, AZ, USA), which possessed much better stability and reproducibility than those of self-made chip channels, the analytical results were almost intact within 200 injections without significant migration time shift. The home-made working electrode could provide satisfactory performance within a month. Furthermore, all stock solutions were stored in a $4\,^{\circ}\mathrm{C}$ refrigerator, and were re-prepared after 4 days. Therefore, the proposed miniaturized MEKC-AD system could provide sufficient stability to complete the entire experiment satisfactorily. The robustness/ruggedness of an analytical procedure is a measure of its capacity to remain unaffected by small, but deliberate variations in method parameters and provides an indication of its reliability during normal usage. In this regard, relevant robustness test was conducted, and it was found that a good efficiency of the analyte peak and migration time was always obtained within variations of 10% of the optimum value of the electrophoretic parameters such as pH, concentration of running buffer solution and SDS, as well as the separation voltage and working electrode potential.

Table 6.1: The results of regression analysis on calibration curves and the detection limits[a]

Compound	Regression equation[b]	Correlation coefficient	Linear range (10^{-4} g mL^{-1})	Detection limit[c] (10^{-6} g mL^{-1})
DCP	$y = 1.21 \times 10^5 x + 0.22$	0.9991	$0.05 - 1.0$	1.6
BP	$y = 7.97 \times 10^4 x + 0.65$	0.9926	$0.05 - 1.0$	1.2
BPA	$y = 8.47 \times 10^4 x + 0.20$	0.9990	$0.05 - 1.0$	3.5
EE2	$y = 6.20 \times 10^4 x - 0.12$	0.9951	$0.05 - 1.0$	3.9
NP	$y = 4.46 \times 10^4 x - 0.10$	0.9974	$0.05 - 1.0$	4.0

[a] Working conditions were the same as in Figure 6.6.

[b] Here the y and x were the peak current (nA) and concentration of the analytes (g mL^{-1}), respectively.

[c] The detection limits corresponding to concentrations were based on signal-to-noise ratio of 3.

Table 6.2: The results of EDCs in real samples[a]

Compound	Sewage (μg mL^{-1})	River water (μg mL^{-1})	Tap water (μg mL^{-1})
DCP	2.42	N.D	N.D
BP	1.18	1.38×10^{-2}	N.D
BPA	32.73	N.D	N.D
EE	N.D[b]	N.D	N.D
NP	N.D	N.D	N.D

[a] Working conditions were the same as in Figure 6.6.

[b] Not detected.

6.7 Analysis of Environmental Samples

After validation, the method, including SPE and miniaturized MEKC-AD was applied to the analysis of target EDCs in real samples. A typical electropherogram of sewage influent sample was shown in Figure 6.7b. Separation was accomplished within 12 min. By comparing the migration time of each analyte with those of standards (Figure 6.7a), and using standard addition method, quantification of target EDCs in these samples have been achieved; the results are listed in Table 6.2. It shows that DCP, BP and BPA exist at μg L^{-1} level in the selected sample, while EE2 and NP are not detected. The results for other two samples were listed as well in Table 6.2.

6.8 Conclusion

In this work, we extended the scope of the application of a new lab-made miniaturized MEKC-AD system. It was successfully employed for the determination of several EDCs in environmental water samples, providing a new method to monitor the level of EDCs. Advantages of this method include shorter analysis time, lower cost, less power supply and solvent consumption. The use of HLB cartridge SPE has proven to give high extraction yield of EDCs, and thus to obtain high enrichment factor when dealing with real water samples.

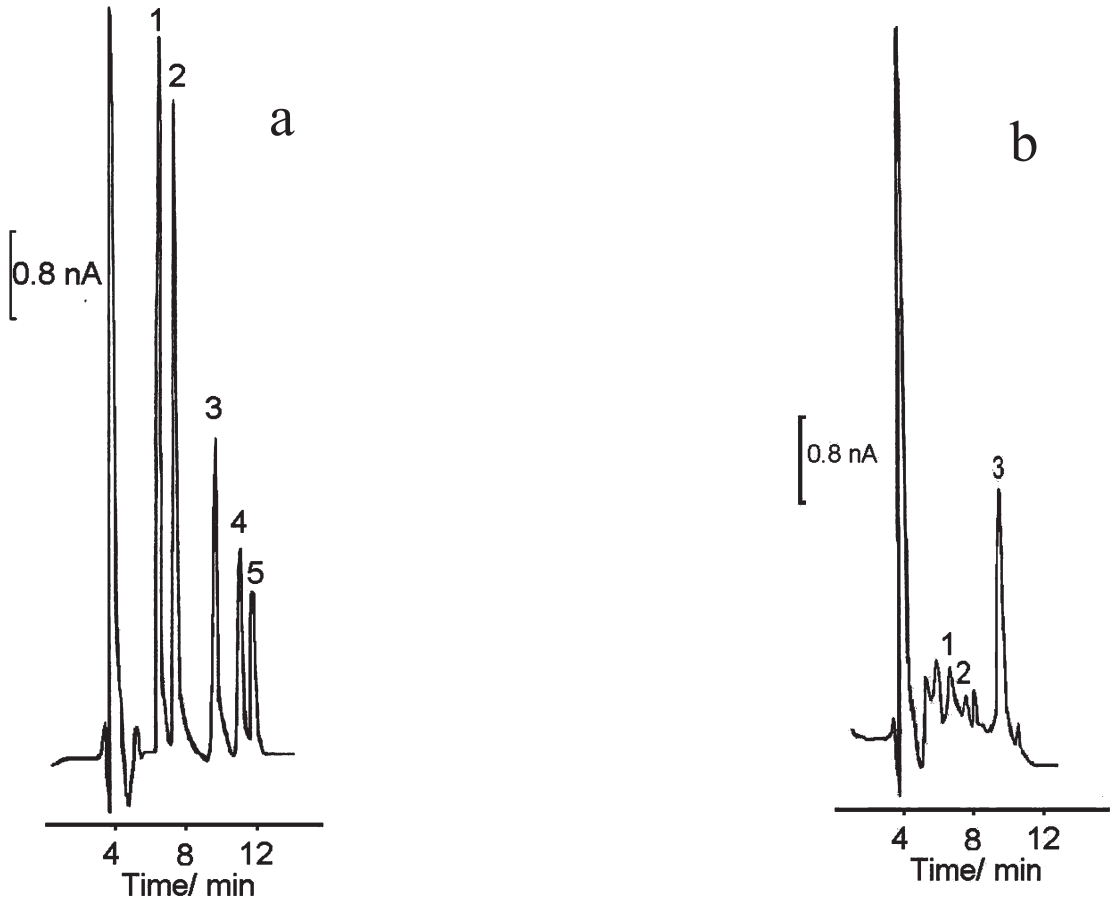

Figure 6.8: Typical electropherograms of the standard mixture solution (a, 2.0×10^{-5} g mL^{-1} each) and sewage sample (b). Experimental conditions and the labels of anlytes 1-5 were the same as in Figure 6.6.

Part IV

Conclusion

Chapter 7

Conclusion and Perspectives

7.1 Conclusion

The work presented in this thesis aimed to deal with some environmental problems with the aid of microanalysis systems. The attention to the harm of trace heavy metal ions, mainly lead ion, and endocrine disrupting chemicals (EDCs) in environmental water has been paid more and more. The great development conditions of miniaturized analysis system during the recent years provided an alternative method to the detection of the environmental pollutants (e.g. trace heavy metal and EDCs).

Three microanalysis systems have been developed in this thesis. One was flow injection microfluidic system based on fluorescence detection to detect lead ion in tap water. In order to achieve the detection of lead ion, a fluoroionophore called Calix-DANS4 was used. The complexation between this fluoroionophore and lead ion was studied experimentally and theoretically. The titration curves obtained with our microfluidic devices have shown excellent sensitivity, e.g. 5×10^{-8} mol L^{-1} (i.e. 10.3 μg L^{-1}) for our Microchip III and 2.5×10^{-8} mol L^{-1} (5.2 μg L^{-1}) for our longer Microchip IV, these values being nearby or inferior to the guideline of WHO for lead ion in drinking water (10 μg L^{-1}). The selectivity to other co-existing ions was also satisfactory. The coupling between a solid phase extraction process (SPE) and the previous flow injection microfluidic system has successfully been applied for trace lead ion detection in tap water in Cachan, France. The solid phase extraction was based on a functionalized silica gel (APS) in pH 10. This method has been validated by CNRS, France. Although, the comparison of the titration curves between the mixing inside and outside the microchannel demonstrated that the reaction in our microchips was not finished, the simulation by a software Chemical Kinetics Simulator (CKS) has demonstrated that the titration curves obtained from our microchips were workable. In order to do this simulation, the stopped-flow measurements provided us the chemical kinetics of this complexation. SPECFIT^{TM} Software was used to calculate the

stability equilibrium constants for this complexation.

The second system was an optofluidic sensor based on a microcavity laser. Microcavity laser has been previously studied in-depth by our colleagues. In this thesis, we were seeking a good microcavity laser material which can substitute popular PMMA and can serve as a selective chemical sensor. Diblock copolymer was finally chosen because of its microphase separation, which can accommodate laser dye and metal ion in two different phases. In order to know the sensing ability, the morphologies and refractive index changes of two diblock copolymers (PS-b-P2VP and PS-b-P4VP) after water and metal ion solution treatment were studied. The results showed that PS-b-P4VP had remarkable change with regard to both morphology and refractive index when treated with zinc ion . It was a good candidate as a chemical sensor. The preliminary design of an optofluidic sensor was made of PS-b-P4VP microcavity and PDMS cover. Its performance showed no evident shift with water treatment, but considerable blue shift with zinc ion solution treatment.

The third one was miniaturized capillary electrophoresis based on electrochemical detection. Five environmental endocrine disrupting chemicals (EDCs): 2,4-dichlorophenol (DCP), 4-tert-butylphenol (BP), bisphenol A (BPA), 17 α-ethynylestradiol (EE2) and 4-n-nonylphenol (NP), were monitored for the first time by our miniaturized micellar electrokinetic chromatography (MEKC) with amperometric detection (AD) coupled with a solid-phase extraction. The five EDCs were well separated under the optimum conditions within 12 min. This method was successfully applied for the determination of these five EDCs in sewage influent sample.

7.2 Perspectives

Some of the issues covered in this thesis are worthy of further investigations.

In the lead ion detection area in chapter 2 and 3, our interesting work in the future is to integrate all these elements in the aim of a lab-on-a-chip portable apparatus based on our flow injection microfluidic device. Otherwise, some other fluoroionophores will be developed and investigated as well, not only for lead ion, but other heavy metal ions, such as mercury, cadmium. Since these heavy metals are harmful at trace level as lead ion, our microfluidic device can also be employed in these applications.

As for the study of optofluidic sensor for heavy metal ion in Chapter 5, the first result has demonstrated that metal ion solution fluid can cause some spectral shift in the microcavity laser spectra, but how to improve the selectivity and sensitivity of the sensor is the most important. The research for a good material to fabricate microcavity laser is crucial. Taking benefit of the special microphase separation of diblock copolymers, one effective method to create a selective chemical sensor is to functionalize the hydrophilic part in diblock copolymer with a ligand which can bind the metal ion selectively. Other diblock

copolymers instead of PS-b-P2VP and PS-b-P4VP will be studied in the point of view of chemical functionalization, such as Polystyrene-b-Polyacrylic acid (PS-b-PAA), since PAA can be functionalized more easily. On the other hand, surface modification of PMMA with PMMA-b-PHEMA can be continued based on the work in the end of Chapter 5. Further modification on monolayer of PMMA-b-PHEMA should be easily made by a specific ligand for heavy metal ion. Once a microcavity laser is sensitive and selective for one specific ion, it will not be far from an effective optofluidic chemical sensor.

In the area of endocrine disrupting chemicals (EDCs), although the identification of potential EDCs and the assessment of the risk caused by individual chemicals or by combinations of chemicals are still under study, developing sensitive and portable detection devices should always be paid attention. That will provide more useful information for the administrative to make the regulations. The next step based on our capillary electrophoresis with electrochemical detection is also to realize the simultaneous separation and detection for several EDCs in a integrated lab-on-a-chip device. It will be a powerful tool to replace the bulk equipments used so far.

Appendix A

Experimental part

A.1 Protocol for the fabrication of microchips for lead ion detection

A.1.1 Materials and equipments

Materials: SU8 photoresist (MicroChem, Newton, MA) , SU8 photoresist developer (MicroChem), Acetone, Isopropyl alcohol, Sylgard 184 Silicone Kit (Dow Corning, Midland, MI), Silicon (Si) wafer. Mold release : hexamethyldisilazane.

Equipment: UV mask aligner (Karl S$\ddot{u}$ss MJB 3), Photoresist spinner (Karl S$\ddot{u}$ss Model CT62), Oven or hot plate.

A.1.2 Fabrication of bilayered microchannel mold

The primary resin used is the negative photoresist SU8 (GM 1070, Gersteltec, Switzerland). The structure of SU8 is as Figure A.1.

The main steps of our process are: mask manufacture, spin-coating of the SU8 resin on a silicon wafer, soft bake, UV exposure, post-exposure bake, development, rinsing and drying. Our protocol is optimized for definition of two layers (75 μm microchannel + 25 μm staggered herringbone mixer) SU8 structures on a silicon wafer [230].

Mask manufacture

The masks of the microfluidic devices (in our case Y-type microchannel (Layer 1)and staggered herringbone mixer(SHM)(Layer 2).) are designed with Adobe Illustrator®. Although glass or quartz masks are used for fabrication of devices with small features, a transparency (much cheaper) can be used as a mask for devices with relatively large feature

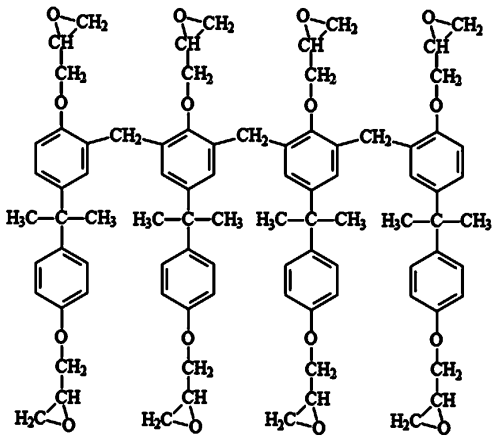

Figure A.1: The chemical structure of SU-8

sizes (>50 μm). The mask design is simply printed with a high-resolution printer on a regular transparency sheet.

Spin-coating for the first layer

Center the wafer on the photoresist spinner chuck and apply approximately 1 ml of SU8 photoresist per inch of substrate diameter. To spread the resist, ramp the speed to 2800 r.p.m. at an acceleration of 300 r.p.m. s^{-1} and hold for 30 s. The thickness of the microstructure depends on the formulation of SU8 and the final spin speed. The appropriate thickness can be determined using the manufacturer's data sheets for process guidelines. The final thickness of about 75 μm is obtained.

Soft bake

To evaporate the solvent and harden the photoresist, the wafer must be soft-baked. To avoid cracking the resist, baking is performed as a two-step process at $65\,^{\circ}\mathrm{C}$ and $95\,^{\circ}\mathrm{C}$. Bake times are determined by the thickness of the SU8 film. For our 75μm thick layer, place the wafer on a $65\,^{\circ}\mathrm{C}$ hot-plate for 1 min, followed by 8 min on a $95\,^{\circ}\mathrm{C}$ hot-plate. Allow the wafer to cool down to room temperature.

Exposure

Transparency of Layer 1 was stuck on a glass plate as a photomask. Place the photomask on the mask holder of the UV mask aligner (transparency side down). Place the wafer on the chuck of the mask aligner and bring the wafer into contact with the photomask. For 75μm

thick layer, the negatively-patterned photoresist is obtained through the UV exposure with aligner (Karl Suss MA6, Germany) for 45 s, where the power of 8 mW/cm^2 is applied with wavelength of 365 nm (i-line).

Post bake

After exposure, the SU8 which has been exposed to UV light is cross-linked by performing a two-step contact bake process. Bake times are determined by the thickness of the SU8 film. For our 75 μm thick microchannel, place the wafer on a $65\,^{\circ}\mathrm{C}$ hot-plate for 1 min, followed by 12 min on a $95\,^{\circ}\mathrm{C}$ hot-plate. Allow the wafer to cool to room temperature.

Spin coating for the second layer

To fabricate the second layer of the staggered herringbone mixer, coat first layer with an additional layer of photoresist. Choose an SU8 formulation based on the height of the desired feature. Spin speed and soft bake times will vary based on SU8 formulation and film thickness. For our 25 μm SHM, spread the SU8 2025 resist at 600 r.p.m. at an acceleration of 300 r.p.m. s^{-1} for 5 s, and then ramp to a final speed of 3,000 r.p.m. at an acceleration of 3000 r.p.m. s^{-1} and hold for 25 s.

Soft bake

For a 75 μm thick microchannel plus a 25 μm SHM, place the wafer on a $65\,^{\circ}\mathrm{C}$ hot-plate for 3 min followed by 9 min on a $95\,^{\circ}\mathrm{C}$ hot-plate. Allow the wafer to cool to room temperature.

Exposure

Using the UV mask aligner, align the alignment markers on the Layer 2 photomask to the alignment marks on the wafer from Layer 1. For 25 μm thick layer 2, the SHM structure is obtained through the UV exposure with aligner (Karl Suss MA6, Germany) for 25 s, where the power of 8 mW/cm^2 is applied with wavelength of 365 nm (i-line).

Post bake

Perform a post-exposure bake (for a 25 μm thick SHM, $65\,^{\circ}\mathrm{C}$ for 1 min followed by $95\,^{\circ}\mathrm{C}$) for 7 min. Allow the wafer to cool to room temperature.

Development

Develop the cross-linked SU8 by immersing in SU8 developer. Approximate developing times are based on SU8 film thickness. For a 75 μm thickness layer plus a 25 μm

thickness SHM, SU8 is developed for 14 min. Allow additional development time for each layer of features. Rinse the wafer with isopropyl alcohol. Dry with nitrogen. Check the microchannel dimensions using a microscope and profilometer.

A.1.3 Replica of PDMS chip and embedded optical fiber

To produce a replica, the most common PDMS elastomers, Sylgard®184 from Dow Corning®, was used. Sylgard is a two part resin system containing vinyl groups (part A) and hydrosiloxane groups (part B) shown in Figure A.2 below. Two components were mixed in the volume ratio of 10:1 (A:B), and poured on the wafer mold.

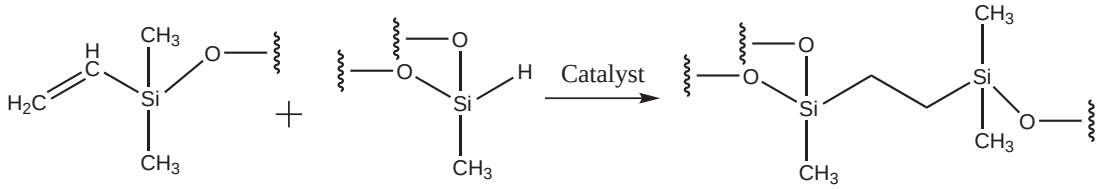

Figure A.2: PDMS crosslinking

Mixing the two resin components together leads to a cross-linked network of dimethyl siloxane groups. Because this material is flexible, it can be unmolded (peeled off) from the SU-8 master, leaving the master intact and ready to produce another device.

After bubbles are eliminated at 100 torr for 30 min evacuation, the PDMS is cured at $75\,^{\circ}\mathrm{C}$ for 2 h. The PDMS replica is peeled off from the master, and then the replica and glass coverslip (Marienfeld Micro Slides, Germany) are activated by O_2 plasma (HARRICK PLASMA CLEANER/ STERILIZER (PDC-001) for 20 s and sealed each other. A soft bake of the microdevice is then made at $75\,^{\circ}\mathrm{C}$ for 5 min.

Centimeter lengths of multi-mode optical fiber (corning, USA) were prepared, stripped of their protective plastic layers, by immersion in H_2SO_4 solution at $100\,^{\circ}\mathrm{C}$. The multi-mode optical fibers were inserted into the embedded optical-fiber channels until their front ends made contact with the thin walls between the fiber channels and the sample channel [231].

A.2 Protocol for the determination of stability constants of the complex of fluoroionophore and metal ion

The stability constants of metal ion complex had been determined by spectrophotometric measurement. The fluorescent spectra were registered by progressively increasing the

concentration of metal ion in a ligand solution with concentration of C_0. The concentration of ligand was kept unchanged in C_0, when adding the metal ion. The ionic force is not fixed by an external salt to prevent an additional complex between the salt and the ligand. When the excitation of fluorescence is situated out of the isosbestic point, the fluorescence spectra are systematically corrected by the evolution of absorbance (except special mention). As a consequence, the variation of fluorescence intensity are independent of the variation of absorbance.

The thermodynamical constants were determined by using the Specfit Global Analysis System V3.0 for 32-bit Windows system, which provided the complexation constants with a good accuracy. SPECFIT is a tool for fitting complex models of emission lines, absorption lines, and continua to 1-dimensional spectra. This software uses singular value decomposition and non-linear regression modeling by the Levenberg-Marquardt method [232, 233].

A.3 Reagents for lead ion detection

Lead thiocyanate ($Pb(SCN)_2$ 99.5%) is purchased from Aldrich, calcium perchlorate ($Ca(ClO)_4$ 99%) is purchased from Alfa Aesar. Perchloric acid ($HClO_4$ 99.999% diluted to 70% in water), sodium hydroxide (NaOH 97%) are purchased from Aldrich and employed for the buffer solutions. 3-chloropyridine (99%) is purchased from Aldrich. Water is always distilled and then deionized by a Milli-Q-plus machine (18 MΩ). Acetonitrile is of spectrophotometric grade and purchased from Aldrich.

A.4 Instrumental measurement

A.4.1 UV-Visible absorption spectroscopy and Steady-state fluorescence spectroscopy

Hellma quartz cells (3.0×1.0 cm^2) were used for the fluorescence and UV measurements.

The UV measurements were carried out in Uvikon 943, the spectra ranges from 190 to 900 nm, the precision is 0.1 nm.

Emission spectra were carried out in two kinds of Jobin-Yvon spectrofluorimeters, linked with a computer under Windows XP system and DATAMax V.1.03 software of Galactic Industries Corporation & Instruments S.A.:
- SPEX 1681 Fluorolog spectrofluorimeter: It is equipped with double monochromators (excitation and emission), which are made of 1200 groves mm^{-1} (the dispersion is 3.77

nm mm^{-1}) and are corrected for the photomultiplier response. A 450 W xenon arc lamp was used as the light source. And the spectral range is from 200 to 900 nm. The pass bands of excitation and emission monochromators are adjusted individually by the slits from 0.5 to 5.0 mm. The excitation and emission beam can be polarized independently. - FluoroMax-3 : The light source in this case was a Xenon arc lamp (150 W). The spectral range ranged from 200 to 900 nm. The band pass of the monochromator of excitation and emission were adjusted separately by computer (0,5 to 10 nm).

A.4.2 Photolithography

The instrument used for exposure in the photolithography is a Karl Suss MJB 3 Mask Aligner and shown in Figure A.3. It was designed for high resolution photolithography

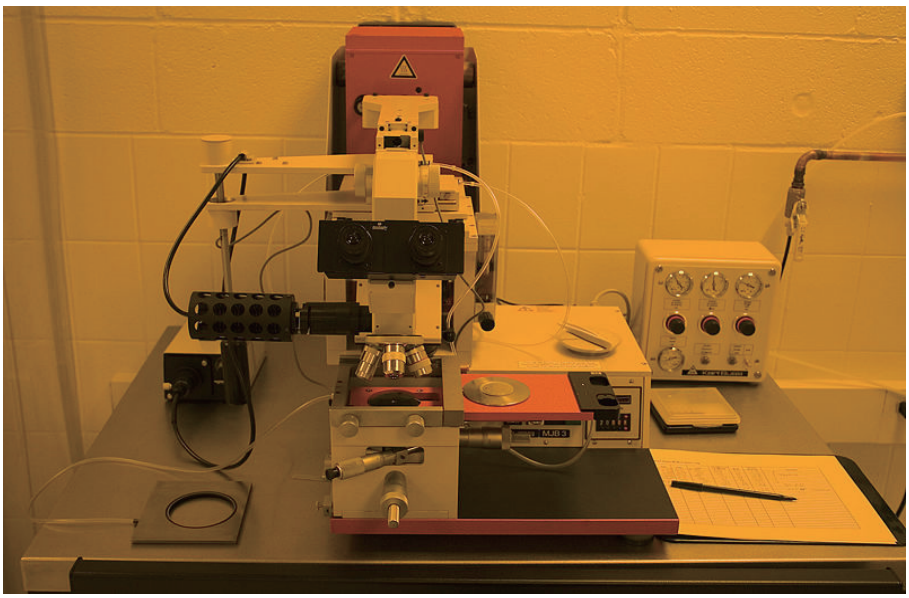

Figure A.3: Karl Süss MJB 3 contact mask aligner for photolithography.

in the lab. The alignment was operated manually in the aid of a single objective optical microscope. It can provide Ultraviolet (UV) exposure at 365 nm, 405 nm. Vacuum, hard, and soft contact modes were available.

A.4.3 Anodic stripping voltammetry (ASV)

The concentration of lead ion in the filtrates was quantified by ASV analysis, using a TraceLab 50 polarograph from Radiometer Analytical (Lyon, France) with a hanging mercury drop electrode module (MDE 150). The samples were pre-purged for 300 s with N_2(g) to remove dissolved oxygen. A -0.5 V potential was used for the electrodeposition

step of 300 s with stirring, followed by a 10 s homogenization period without stirring. Metal stripping was then carried out in the range of -0.5 V to -0.3 V [234].

TraceLab 50 consists of the POL150 Polarographic Analyser and MDE150 Polarographic Stand controlled by TraceMaster 5 Software, see Figure A.4.

Figure A.4: TraceLab 50 system

A three-electrodes system was used in the Anodic stripping voltammetry procedure. Reference electrode was Ag/AgCl-reference system with ceramic diaphragm type D, diameter=1mm. Reference system was Ag/AgCl(c(KCl)=3mol/L), supplied in a holder filled with c(KCl)=3mol/L as standard. Auxiliary electrode was Pt electrode, which serves merely to carry the current flowing through the cell. Working electrode was a hanging mercury drop electrode (HMDE), in which mercury was forced through a glass capillary until a drop forms at the capillary tip and the entire voltage sweep performed on this single stationary drop, in general with preceding enrichment (stripping voltammetry).

ASV can be used to determine all metals which can be soluble in mercury with the formation of amalgams or which can be deposited electrolytically at carbon or noble metal electrodes. The steps in an ASV determination are shown in Figure A.5

Section **a** is the accumulation time, in which the analyte is deposited at the working electrode at a constant potential and with the sample solution being stirred continuously. As deposition is always incomplete, the working conditions must be strictly controlled if reproducible measurements are to be achieved. These include the accumulation time, accumulation potential, the shape, size and arrangement of the stirrer, the stirring speed (rotation), the sample volume and the surface area of the electrode (surface of the mercury drop or film). Section **b** is the rest period. During this period the sample solution is no longer stirred, this means that the cathodic current drops because of lack of convection. As small amounts of the analyte are deposited even from an unstirred solution, this period must also be controlled. Several seconds pass before the solution comes to a standstill and the de-

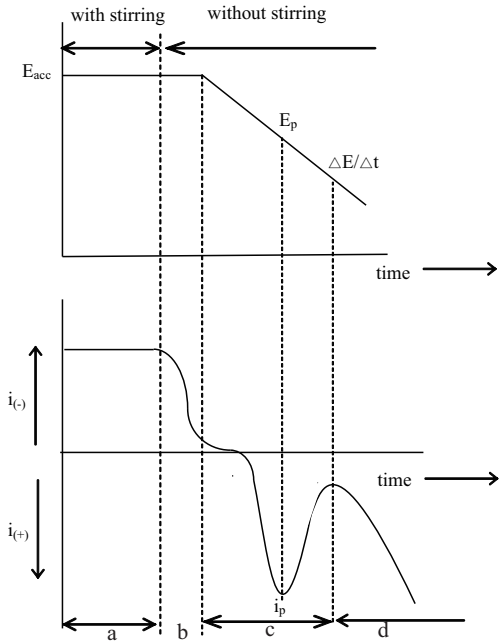

Figure A.5: Method steps and current-potential curve for determinations by anodic stripping voltammetry, $\mathbf{E}_{acc}$*=Accumulation potential;*Δ**E/**Δ**t=** *Potential scan rate;* $\mathbf{E}_p$ *Peak potential;* $\mathbf{i}_p$ *Current peak;* **a***: Accumulation time;* **b***: Rest period;* **c***: Determination step;* **d***: Anodic dissolution of the electrode mercury.*

posited metal is well distributed in the mercury drop. This is why the rest period is defined as being 5 s to a maximum of 30 s. In a mercury film the distribution process is completed after only a few seconds. Section **c** is defined by the potential scan rate (ΔE/Δt=const.), which is the rate at which the anodic stripping voltammogram is recorded. The measuring signal is the peak current i_p, which in Section **d** changes into the anodic current for the dissolution of the mercury electrode.

The amount of cathodically accumulated metal in amalgam:

$$C_{Me^{\circ}(Hg)} = \frac{i_{acc}.t_{acc}}{V_{Hg}.n.F} \tag{A.1}$$

$C_{Me\circ(Hg)}$: Concentration of metal (accumulated analyte) in the analgam
i_{acc}: Electrolysis current during the accumulation
t_{acc}: Accumulation time
n: Electron transfer during reduction of analyte
F: Faraday constant
V_{Hg}: Volume of the hanging mercury drop.

According to Equation A.1, the ***accumulation***, i.e. the amount of metal cathodically deposited or the concentration of the metal in the amalgam, depends on the electrolysis

current, the accumulation duration and the volume of the mercury drop or mercury film.

The electrolysis current i_{acc} is determined by the transport of analyte and the potential at which accumulation takes place. For high accumulation rates the solution should be stirred and the accumulation potential should be in the diffusion current range.The direct current polarograms or the half wave or peak potentials can be used as guidelines for this. As a rule of thumb it can be said that the accumulation potential should be about 200-400 mV more negative than the polarographic half-wave potential.

The transport of the analyte to the electrode surfaces takes place by diffusion and is supported by convection if the solution is stirred during accumulation. This means that the electrolysis current i_{acc} not only depends on the diffusion conditions, but also on the hydrodynamic conditions which are based on laminar or turbulent flow(at high stirring speeds or when working with a rotating electrode.) At a constant stirring speed, the amount of metal deposited at the cathode is proportional to both the accumulation time and the analyte concentration in the sample solution.

The accumulation time depends on the concentration of the analyte in the sample solution and must be chosen in a way that the measuring signal remains linear throughout as large a concentration range as possible. Deposition is never fully complete; at voltammetric working electrodes this could in any case only be achieved with very small samples volumes ($<$0.1mL) and long electrolysis times. Under normal working conditions with 5 to 20 ml sample solution and about 1 min accumulation at a mercury drop with a surface area of a few mm^2, only a few tenths of a percent are deposited.

In ASV the ***determination*** is based on the anodic dissolution of the accumulated analyte. This process is followed voltammetrically and produces a current peak which, when the HMDE is used, is proportional to the potential scan rate and the square of the radius of the mercury drop.

Peak current in an anodic stripping voltammogram using a HMDE:

$$i_p = k.n^{3/2}.D^{1/2}_{Me^{\circ}(Hg)}.v^{1/2}.r^2.t_{acc} \tag{A.2}$$

i_p: Peak current
k: constant
n: Electron transfer during oxidation of the analyte
$D_{Me^{\circ}(Hg)}$: Diffusion coefficient of the metal deposited in the amalgam
v: Scan rate
r: Radius of mercury drop
t_{acc}: Accumulation time

A.4.4 Atomic force microscopy

In this thesis, AFM was performed on VEECO (Thermo microscope), in tapping mode to obtain height images and phase images, using Silicon Nitride cantilevers and $2 * 2$ μm scanner tube. The resolution of this AFM in z direction is about 1 nm. The principle scheme of AFM is very simple (Figure A.6).

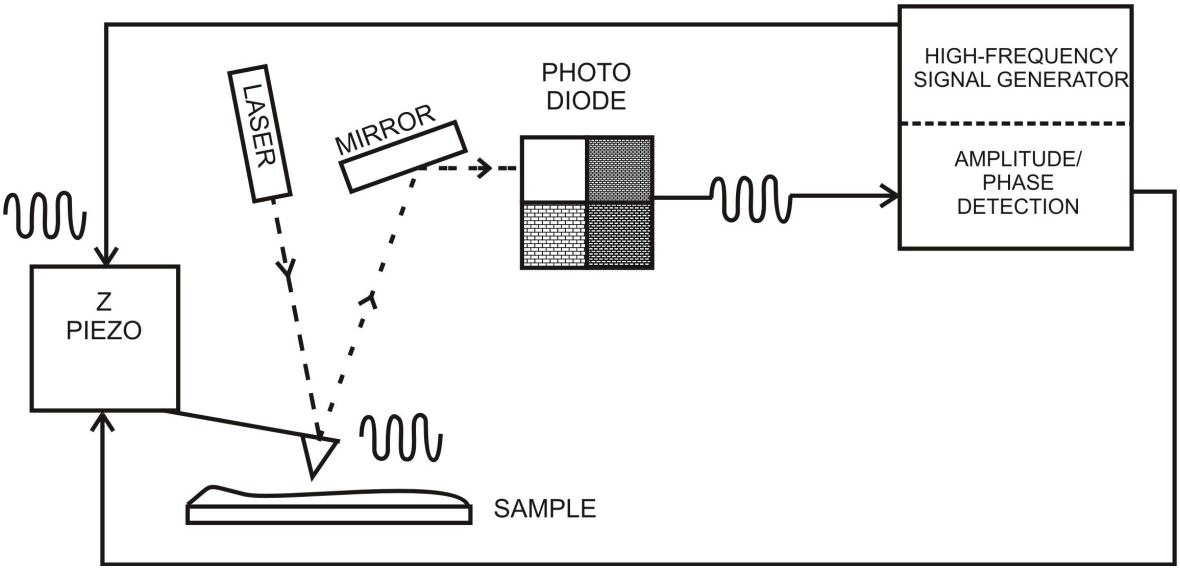

Figure A.6: Block diagram for atomic force microscope

A very sharp tip is scanned over a surface with feedback mechanisms that enable the piezo-electric scanners to maintain the tip at a constant force (to obtain topography information), or height (to obtain force information) above the sample surface. The cantilever is typically silicon or silicon nitride with a tip radius of curvature of the order of nanometers. When the tip is brought into proximity to a sample surface, forces between the tip and the sample lead to a deflection of the cantilever according to Hooke's law, $F = -kx$.

An optical detection system was applied in AFM in which the tip is attached to the underside of a reflective cantilever. Typically, the deflection is measured using a laser spot reflected from the top surface of the cantilever into an array of photodiodes. A feedback mechanism is employed to adjust the tip-to-sample distance to maintain a constant force between the tip and the sample. Traditionally, the sample is mounted on a piezoelectric tube, that can move the sample in the z direction for maintaining a constant force, and the x and y directions for scanning the sample. The resulting map of the area z = f(x,y) represents the topography of the sample.

There are three imaging modes: contact mode, non-contact mode, and intermittent contact or tapping mode, used to produce topographic images of sample surfaces. Tapping mode was applied in our polymer thin film research. When the oscillating cantilever ap-

proaches the surface and the tip starts to interact with it, the amplitude of oscillation linearly decreases and is maintained constant at a certain value by the feedback loop of the microscope. The images provided insight into the shape and size of the structures of polymers. It also provided quantitative information as to the breadth of the size distribution of the polymers. The AFM was used in tapping mode instead of contact mode, so that the probe tip would not shear the micelles. In tapping mode, the probe tip oscillates up and down at high frequency and periodically contacts the sample, which decreases the friction between the tip and the sample. The amplitude of the probe deflection depends on interactions with the sample. A feedback loop with the photodetector and the piezoelectric transducer, which is attached to the probe, maintains an average applied force. The fluctuations in amplitude are translated into data about the height of the sample. In tapping mode, one can attain x-y resolution of 1-2 nm. Tapping mode was also employed to determine phase information for the polymer thin films.

A.4.5 Ellipsometry

Ellipsometry is an optical technique that uses polarized light to probe the dielectric properties of a sample. The name "ellipsometry" stems from the fact that the most general state of polarization is elliptic. It is mainly used in semiconductor research and fabrication to determine properties of layer stacks of thin films and the interfaces between the layers. The most common application of ellipsometry is the analysis of very thin films.

The optical constants define how light interacts with a material. Optical absorption and refractive index of thin film can be measured at the same time by spectroscopic ellipsometry technique. The complex refractive index is a representation of the optical constants of a material, it is represented by Eq A.3.

$$\tilde{n} = n + ik \tag{A.3}$$

The real part or refractive index n, defines the phase velocity of light in material:

$$\nu = \frac{c}{n} \tag{A.4}$$

where ν is the speed of light in the material and c is the speed of light in vacuum. The imaginary part or extinction coefficient, k, determines how fast the amplitude of the wave decreases. The extinction coefficient is directly related to the absorption of a material and is related to the absorption coefficient by:

$$\alpha = \frac{4\pi k}{\lambda} \tag{A.5}$$

where α is the absorption coefficient and λ is the wavelength of light.

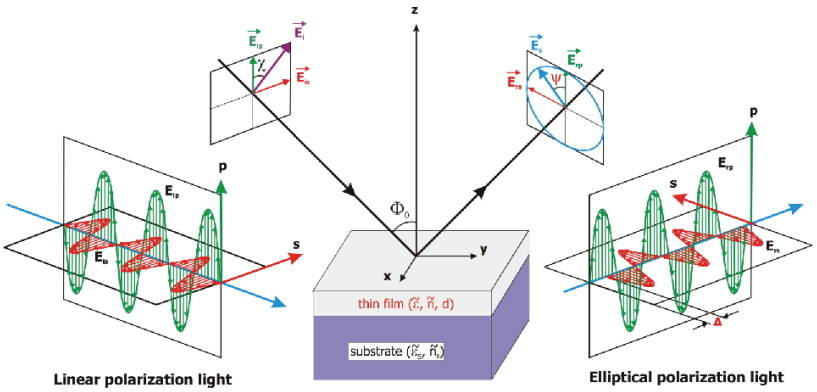

Figure A.7: Principle of ellipsometric technique

In this technique we measure the ratio of reflectivities between polarized optical waves parallel to incidence plane (Ep) and polarized waves perpendicular (Es) to incidence plane (Figure A.7). The coefficient of reflection of the thin film for polarizations which are parallel to incidence plane can be written as

$$r_p = \frac{E_{rp}}{E_{ip}} = |r_p| exp(j\delta_p) \tag{A.6}$$

where $|r_p|$ and δ_p are magnitude and phase of r_p respectively. And the coefficient of reflection of the thin film for polarizations which are perpendicular to incidence plane can be written as

$$r_s = \frac{E_{rs}}{E_{is}} = |r_s| exp(j\delta_s) \tag{A.7}$$

where $|r_s|$ and δ_s are magnitude and phase of r_s, respectively.

In practice, the measured quantity is the ratio of these two coefficients of reflection:

$$\frac{r_p}{r_s} = \tan(\Psi) e^{j\Delta} \tag{A.8}$$

where $\tan(\Psi)$=$|\frac{r_p}{r_s}|$ and Δ is the phase difference introduced by reflection.

A typical setup of an ellipsometry experiment is sketched in Figure A.8.

In this thesis, we used the spectroscopic ellipsometer GES 5 of SOPRA. The two parameters $\tan(\Psi)$ and cos(Δ) in function of wavelength are measured by using a scanning spectrometer and/or in function of incidence angle by changing the angular position of ellipsometer arms. These measurements are automatically carried out and controlled by computer. Then we made a curve fitting calculation from a physical model of thin film properties for these two experimental measured parameters. Hence, we can deduce from this fitting and/or simulation calculation the thickness and the complex optical index (which contains two parts: the real part represents the refractive index and the imaginary part represents the optical absorption) of the thin film sample [235].

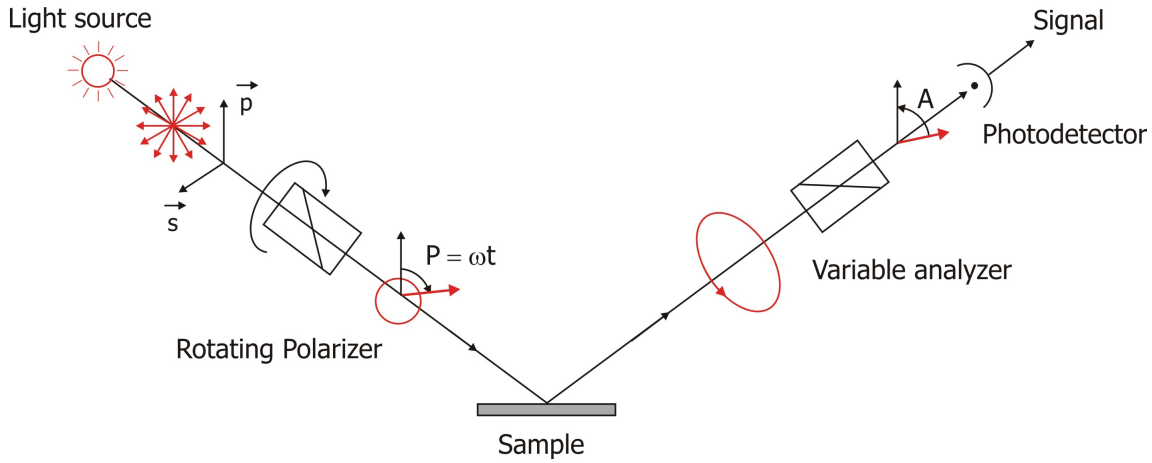

Figure A.8: Ellipsometry set-up diagram

A.4.6 pH meter

All pH measurement were carried out with a PHM 210 (Radiometer) pH-meter equipped with a Red Rod pHc 2401 (Radiometer) Ag/AgCl combined glass electrode filled with a saturated KCl solution. The electrode was calibrated with commercial buffers (pH=4.0, 7.0) purchased from Acros.

pH value in non-aqueous milieu

According to Rémi Métivier's thesis [129], we have to correct the pH value measured by pH meter with the general equation below in a non-aqueous solution:

$$pH^s = a + pH_{measured} + b[H^+]_{measured} \tag{A.9}$$

The relationship between the real pH^s of the solution and the $pH_{measured}$ is determined by measuring the pH in a CH_3CN/H_2O (6:4 v/v) solution when varying the quantity of $HClO_4$. The result is as follow:

$$pH^s = 0.23 + pH_{measured} \tag{A.10}$$

A.4.7 Atomic absorption spectrometer (AAS)

A HITACHI Z-8270 atomic absorption spectrometer (mode stop gas flow) with Zeeman Polarisation effect and Smith-Hieftje background correction was used for lead determination. All Standards for calibration were prepared by dilution of l000 mg/L stock lead solution (Aldrich) in 5% nitric acid. The injections of 20 μ1 of the sample or standard were automatically made into the furnace. 283.3 nm wavelengths were tested for lead determination. Peak heights of the emission were measured for determination.

A.4.8 Amplified spontaneous emission (ASE)

Amplified spontaneous emission (ASE) or superluminescence is light produced by spontaneous emission, that has been optically amplified by the process of stimulated emission in a gain medium. ASE is produced when a laser gain medium is pumped to produce a population inversion. If there is a feedback of the ASE by an optical cavity, it may produce laser operation if the lasing threhold is reached.

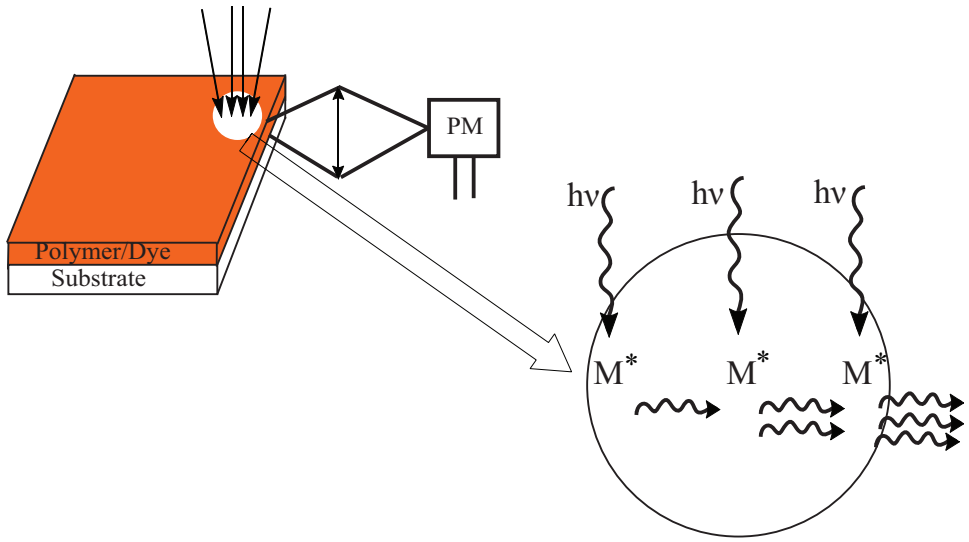

Figure A.9: Scheme of ASE set-up

The scheme of an ASE experiment is shown in Figure A.9. A cw Nd/YAG laser at 532 nm is focussed on the edge of the film of host/guest (polymer/laser dye) system which is casted on the substrate of a silicon plate covered by a thin film of silica. The emission is observed through the edge of the film. The polymer layer acts as an optical waveguide in which spontaneous emission produced by excitation of the dye molecules is amplified by a process of stimulated emission during the propagation of the beam in the waveguide.

Bibliography

[1] K. Schwab, J. Arlett, J.Worlock, and M. Roukes. Thermal conductance through discrete quantum channels. Physica E, 9:60–68, 2001.

[2] K. Schwab, E. Henriksen, J.Worlock, and M. Roukes. Measurement of the quantum of thermal conductance. Nature, 404:974–977, 2000.

[3] K. E. Petersen. Silicon as mechanical material. Proceedings of the IEEE, 70(5):420–457, 1982.

[4] A. Manz, N. Graber, and H.M. Widmer. Miniaturised total chemical analysis systems: a novel concept for chemical sensing. Sensors and Actuators B, 1:244–248, 1990.

[5] D. Ross, T.J. Johnson, and L.E. Locascio. Imaging of electroosmotic flow in plastic microchannels. Analytical chemistry, 73:2509–2515, 2001.

[6] S.L.R. Barker, D. Ross, M.J. Tarlov, M. Gaitan, and L.E. Locascio. Control of flow direction in microfluidic devices with polyelectrolyte multilayers. Analytical chemistry, 72:5925–5929, 2000.

[7] R.F. Ismagilov, D. Rosmarin, P.J.A Kenis, D.T. Chiu, W. Zhang, H.A. Stone, and G.M. Whitesides. Pressure-driven laminar flow in tangential microchannels: an elastomeric microfluidic switch. Analytical chemistry, 73:4682–4687, 2001.

[8] Y. Xia and G.M. Whitesides. Soft lithography. Angewandte Chemie International Edition., 37:551–575, 1998.

[9] Y. Xia and G.M. Whitesides. Soft lithography. Annual Review of Materials Research, 28:153–184, 1998.

[10] B.H. Weigl, R.L. Bardell, and C.R. Cabrera. Lab-on-a-chip for drug development. Advanced Drug Delivery Reviews, 55(3):349–377, 2003.

[11] H. Becker and L.E. Locascio. Polymer microfluidic devices. Talanta, 56(2):267–287, 2002.

[12] T. Chovan and A. Guttman. Microfabricated devices in biotechnology and biochemical processing. Trends in Biotechnology, 20(3):116–122, 2002.

[13] W. Ehrfeld. Electrochemistry and microsystems. Electrochimica Acta, 48:2857–2868, 2003.

[14] J.A. Rogers and R.G. Nuzzo. Recent progress in soft lithography. Materials today, 8(2):50–56, 2005.

[15] A. Kumar and G.M. Whitesides. Features of gold having micrometer to centimeter dimensions can be formed through a combination of stamping with an elastomeric stamp and an alkanethiol 'ink' followed by chemical etching. Applied Physics Letters, 63(14):2002–2004, 1993.

[16] Y. Xia, E. Kim, X.M. Zhao, J.A. Rogers, M. Prentiss, and G.M. Whitesides. Complex optical surfaces formed by replica molding against elastomeric masters. Science, 273(5273):347–349, 1996.

[17] X.M. Zhao, Y. Xia, and G.M. Whitesides. Fabrication of three-dimensional microstructures: Microtransfer molding. Advanced Materials, 8:837–840, 1996.

[18] E. Kim, Y. Xia, and G.M. Whitesides. Polymer microstructures formed by moulding in capillaries. Nature, 376:581–584, 1995.

[19] E. Kim, Y. Xia, X.M. Zhao, and G.M. Whitesides. Solvent-assisted microcontact molding: A convenient method for fabricating three-dimensional structures on surfaces of polymers. Advanced Materials, 9:651–654, 1997.

[20] J.A. Rogers, K.E. Paul, R.J. Jackman, and G.M. Whitesides. Using an elastomeric phase mask for sub-100 nm photolithography in the optical near field. Applied Physics Letters, 70(20):2658–2660, 1997.

[21] D.C. Duffy, J.C. McDonald, O.J.A. Schueller, and G.M. Whitesides. Rapid prototyping of microfluidic systems in poly(dimethylsiloxane). Analytical Chemistry, 70:4974–4984, 1998.

[22] Kluwer Academic Publishers, editor. In proceedings of Micro Total Analysis Systems 1998, Dordrecht, The Netherlands, 1998.

[23] P.Woias. Micropumps' past, progress and future prospects. Journal Sensors and Actuators B: Chemical, 105(1):28–38, 2005.

[24] K. Yasuda and M. Ichiki. In Transducers'99, pages 128–129, Sendai, Japan, June 7-10 1999.

[25] S.C. Jacobson, T.E. McKnight, and J.M. Ramsey. Microfluidic devices for electrokinetically driven parallel and serial mixing. Analytical chemistry, 71:4455–4459, 1999.

[26] R.H. Liu, K.V. sharp, M.G. Olsen, M.A. Stremler, J.G. Santiago, R.J. Adrian, H. Aref, and D.J. Beebe. In Transducers'99, pages 730–733, Sendai, Japan, June 7-10 1999.

[27] J.W. Hong, K. Hosokawa, T. Fujii, M. Seki, and I Endo. Microfabricated polymer chip for capillary gel electrophoresis. Biotechnology Progress, 17(5):958–962, 2001.

[28] A.D. Stroock, S. K. W. Dertinger, A. Ajdari, I. Mezic, H. A. Stone, and G. M. Whitesides. Chaotic mixer for microchannels. Science, 295:647–651, 2002.

[29] N.T. Nguyen, X. Huang, and T.K. Chuan. Mems-micropumps: a review. Journal of Fluids Engineering(ASME Transactions), 124(2):384–392, 2002.

[30] D.J. Laser and J.G. Santiago. A review of micropumps. Journal of Micromechanics and Microengineering, 14(6):35–64, 2004.

[31] K. Handique, D.T. Burke, C.H. Mastrangelo, and M.A. Burns. On-chip thermopneumatic pressure for discrete drop pumping. Analytical Chemistry, 73:1831–1838, 2001.

[32] M.W.J. Prins, W.J.J. Welters, and J.W. Weekamp. Fluid control in multichannel structures by electrocapillary pressure. Science, 291:277–280, 2001.

[33] T.E. McKnight, C.T. Culbertson, S.C. Jacobson, and J.M. Ramsey. Electroosmotically induced hydraulic pumping with integrated electrodes on microfluidic devices. Analytical Chemistry, 73(16):4045–4049, 2001.

[34] C.M. Hou and Y.C. Tai. Mems and its applications for flow control. Journal of Fluid Engineering, 118(3):437–447, 1996.

[35] T. Vilkner, D. Janasek, and A. Manz. Micro total analysis systems. recent developments. Analytical Chemistry, 76(12):3373–3386, 2004.

[36] J.H. Qin, Y.S. Fung, D.R. Zhu, and B.C. Lin. Native fluorescence detection of flavin derivatives by microchip capillary electrophoresis with laser-induced fluorescence intensified charge-coupled device detection. Journal of Chromatography A, 1027:223–229, 2004.

[37] V. Namasivayam, R.S. Lin, B. Johnson, S. Brahmasandra, Z. Razzacki, D.T. Burke, and M.A. Burns. Advances in on-chip photodetection for applications in miniaturized genetic analysis systems. Journal of Micromechanics and Microengineering, 14(1):81–90, 2004.

[38] J.C. Roulet, R. Volkel, H.P. Herzig, E. Verpoorte, N.F. de Rooij, and R. Dandliker. Performance of an integrated microoptical system for fluorescence detection in microfluidic systems. Analytical Chemistry, 74(14):3400–3407, 2002.

[39] J.C. Sanders, Z.L. Huang, and J.P. Landers. Acousto-optical deflection-based whole channel scanning for microchip isoelectric focusing with laser-induced fluorescence detection. Lab on a Chip, 1:167–172, 2001.

[40] P.S. Dittrich and P. Schwille. Spatial two-photon fluorescence cross-correlation spectroscopy for controlling molecular transport in microfluidic structures. Analytical Chemistry, 74(17):4472–4479, 2002.

[41] J.P. Shelby and D.T. Chiu. Mapping fast flows over micrometer-length scales using flow-tagging velocimetry and single-molecule detection. Analytical Chemistry, 75(6):1387–1392, 2003.

[42] C.D. Garcia and C.S. Henry. Direct determination of carbohydrates, amino acids, and antibiotics by microchip electrophoresis with pulsed amperometric detection. Analytical Chemistry, 75(18):4778–4783, 2003.

[43] N.E. Hebert, B. Snyder, R.L. McCreery, W.G. Kuhr, and S.A. Brazill. Performance of pyrolyzed photoresist carbon films in a microchip capillary electrophoresis device with sinusoidal voltammetric detection. Analytical Chemistry, 75(16):4265–4271, 2003.

[44] C.C. Wu, R.G. Wu, J.G. Huang, Y.C. Lin, and H.C. Chang. Three-electrode electrochemical detector and platinum film decoupler integrated with a capillary electrophoresis microchip for amperometric detection. Analytical Chemistry, 75(4):947–952, 2003.

[45] O. Klett and L. Nyholm. Separation high voltage field driven on-chip amperometric detection in capillary electrophoresis. Analytical Chemistry, 75(6):1245–1250, 2003.

[46] M. Galloway, W. Stryjewski, A. Henry, S.M. Ford, S. Llopis, R.L. McCarley, and S.A. Soper. Contact conductivity detection in poly(methyl methacylate)-based microfluidic devices for analysis of mono- and polyanionic molecules. Analytical Chemistry, 74:2407–2415, 2002.

[47] J. Wang, G. Chen, and A. Muck. Movable contactless-conductivity detector for microchip capillary electrophoresis. Analytical Chemistry, 75(17):4475–4479, 2003.

[48] F. Laugere, R.M. Guijt, J. Bastemeijer, G. van der Steen, A. Berthold, E. Baltussen, P. Sarro, G. W. K. van Dedem, M. Vellekoop, and A. Bossche. On-chip contactless four-electrode conductivity detection for capillary electrophoresis devices. Analytical Chemistry, 75(2):306–312, 2003.

[49] J. Huller, M.T. Pham, and S. Howitz. Thin layer copper ise for fluidic microsystem. Sensors and Actuators B, 91:17–20, 2003.

[50] S. Benetton, J. Kameoka, A.M. Tan, T. Wachs, H. Craighead, and J.D. Henion. Chip-based p450 drug metabolism coupled to electrospray ionization-mass spectrometry detection. Analytical Chemistry, 75(23):6430–6436, 2003.

[51] N. Sillon and R. Baptist. Micromachined mass spectrometer. Sensors and Actuators B, 83:129–137, 2002.

[52] J.A. Diaz, A.E.M. Vargas, F.C. Diaz, J.P. Squire, V. Jacobson, G. McCaskill, H. Rohrs, and R. Chhatwal. Test of a miniature double-focusing mass spectrometer for real-time plasma monitoring. TrAC Trends in Analytical Chemistry, 21(8):515–525, 2002.

[53] B.F. Liu, M. Ozaki, Y. Utsumi, T. Hattori, and S. Terabe. Chemiluminescence detection for a microchip capillary electrophoresis system fabricated in poly(dimethylsiloxane). Analytical Chemistry, 75(1):36–41, 2003.

[54] W. Zhan, J. Alvarez, L. Sun, and R.M. Crooks. A multichannel microfluidic sensor that detects anodic redox reactions indirectly using anodic electrogenerated chemiluminescence. Analytical Chemistry, 75(6):1233–1238, 2003.

[55] P.D.I. Fletcher, S.J. Haswell, and X.L. Zhang. Monitoring of chemical reactions within microreactors using an inverted raman microscopic spectrometer. Electrophoresis, 24(18):3239–3245, 2003.

[56] M. Palumbo, C. Pearson, J. Nagel, and M.C. Petty. A single chip multi-channel surface plasmon resonance imaging system. Sensors and Actuators B, 90:264–270, 2003.

[57] M.P. Duggan, T. McCreedy, and J.W. Aylott. A non-invasive analysis method for on-chip spectrophotometric detection using liquid-core waveguiding within a 3d architecture. Analyst, 128(11):1336–1340, 2003.

[58] A. Hibara, M. Nonaka, M. Tokeshi, and T. Kitamori. Spectroscopic analysis of liquid / liquid interfaces in multiphase microflows. Journal of the American Chemical Society, 125(49):14954–14955, 2003.

[59] N. Pamme, R. Koyama, and A. Manz. Counting and sizing of particles and particle agglomerates in a microfluidic device using laser light scattering: application to a particle-enhanced immunoassay. Lab on a Chip, 3:187–192, 2003.

[60] C.D. Costin and R.E. Synovec. A microscale-molecular weight sensor: Probing molecular diffusion between adjacent laminar flows by refractive index gradient detection. Analytical Chemistry, 74(17):4558–4565, 2002.

[61] M.L. Adams, M. Enzelberger, S. Quake, and A. Scherer. Microfluidic integration on detector arrays for absorption and fluorescence micro-spectrometers. Sensors and Actuators A, 104:25–31, 2003.

[62] E. Tamaki, K. Sato, M. Tokeshi, M. Aihara, and T. Kitamori. Single-cell analysis by a scanning thermal lens microscope with a microchip: Direct monitoring of cytochrome c distribution during apoptosis process. Analytical Chemistry, 74(7):1560–1564, 2002.

[63] Y. Mizukami, D. Rajniak, A. Rajniak, and M. Nishimura. A novel microchip for capillary electrophoresis with acrylic microchannel fabricated on photosensor array. Sensors and Actuators B, 81:202–209, 2002.

[64] S.L. Firebaugh, K.F. Jensen, and M.A. Schmidt. Miniaturization and integration of photoacoustic detection. Journal of Applied Physics, 92(3):1555–1563, 2002.

[65] G. Jenkins and A. Manz. A miniaturized glow discharge applied for optical emission detection in aqueous analytes. Journal of Micromechanics and Microengineering, 12(5):N19–N22, 2002.

[66] T. Nakagama, T. Maeda, K. Uchiyama, and T. Hobo. Monitoring nano-flow rate of water by atomic emission detection using helium radio-frequency plasma. Analyst, 128(6):543–546, 2003.

[67] J.W. Chung, C.P. Grigoropoulos, and R. Greif. Infrared thermal velocimetry in mems-based fluidic devices. Journal of Microelectromechanical Systems,, 12:365–372, 2003.

[68] C. Massin, F. Vincent, A. Homsy, and K. Ehrmann. Planar microcoil-based microfluidic nmr probes. Journal of Magnetic Resonance, 164(2):242–255, 2003.

[69] B. Sorli, J.F. Chateaux, M. Pitaval, and H. Chahboune. Micro-spectrometer for nmr: analysis of small quantities in vitro. Measurement Science and Technology, 15:877–880, 2004.

[70] J.H. Walton, de J.S. Ropp, M.V. Shutov, and A. G. Goloshevsky. A micromachined double-tuned nmr microprobe. Analytical Chemistry, 75(19):5030–5036, 2003.

[71] H. Wensink, F. Benito-Lopez, D. C. Hermes, and W. Verboom. Measuring reaction kinetics in a lab-on-a-chip by microcoil nmr. Lab on a Chip, 5:280–284, 2005.

[72] M.A.Burns, B.N. Johnson, S.N. Brahmasandra, K.Handique, J.R. Webster, M. Krishnan, T.S. Sammarco, P.M. Man, D. Jones, D. Heldsinger, C.H.Mastrangelo, and D.T. Burke. An integrated nanoliter dna analysis device. Science, 282:484–487, 1998.

[73] J.R. Webster, M.A.Burns, D.T. Burke, and C.H.Mastrangelo. Monolithic capillary electrophoresis device with integrated fluorescence detector. Analytical Chemistry, 73(7):1622–1626, 2001.

[74] Q. Lu and G.E. Collins. Microchip separations of transition metal ions via led absorbance detection of their par complexes. Analyst, 126:429–432, 2001.

[75] S. Wang, X. Huang, Z.Fang, and P.K. Dasgupta. A miniaturized liquid core waveguide-capillary electrophoresis system with flow injection sample introduction and fluorometric detection using light-emitting diodes. Analytical Chemistry, 73(18):4545–4549, 2001.

[76] T. Zhang, Q Fang, S.L.Wang, L.F. Qin, P Wang, Z.Y. Wu, and Z.L. Fang. Enhancement of signal-to-noise level by synchronized dual wavelength modulation for light emitting diode fluorimetry in a liquid-core-waveguide microfluidic capillary electrophoresis system. Talanta, 68(1):19–24, 2005.

[77] B. Valeur. Molecular Fluorescence. WILEY-VCH, 2001.

[78] A.P. de Silva, H.Q.N. Gunaratne, T. Gunnlaugsson, A.J.M. Huxley, C.P. McCoy, J.T. Rademacher, and T.E. Rice. Signaling recognition events with fluorescent sensors and switches. Chemical Reviews, 97:1515–1566, 1997.

[79] B. Valeur and I. Leray. Design principles of fluorescent molecular sensors for cation recognition. Coordination Chemistry Reviews, 205:3–40, 2000.

[80] L. Fabbrizzi, M. Licchelli, P. Pallavicini, A. Perotti, A. Taglietti, and D. Sacchi. Fluorescent sensors for transition metals based on electron-transfer and energy-transfer mechanism. Chemistry - A European Journal, 2:75–82, 1996.

[81] Y. Al Shihadeh, A. Benito, J.M. Lloris, R. Martinez-Manez, T. Pardo, J. Soto, and M.D. Marcos. Polyaza and azaoxa macrocyclic receptors functionalised with fluorescent subunits; hg2+ selective signalling. Journal of the Chemical Society, Dalton Transactions(7):1199–1205, 2000.

[82] J. Ishikawa, H. Sakamoto, S. Nakao, and H. Wada. Silver ion selective fluoroionophores based on anthracene-linked polythiazaalkane or polythiaalkane derivatives. The Journal of Organic Chemistry, 64:1913–1921, 1999.

[83] R. Metivier, I. Leray, and B. Valeur. Lead and mercury sensing by calixarene-based fluoroionophores bearing two or four dansyl fluorophores. ChemistryąłA European Journal, 10:4480–4490, 2004.

[84] M.H. Ha-Thi, M. Penhoat, V. Michelet, and I. Leray. Highly selective and sensitive phosphane sulfide derivative for the detection of hg^{2+} in an organoaqueous medium. Organic letters, 9(6):1133–1136, 2007.

[85] M.V. Alfimov, Y.V. Fedorov, O.A. Fedorova, S.S. Gromov, R.E. Hester, I.K. Lednev, J.N. Moore, V.P. Oleshko, and A.I. Vedernikov. Synthesis and spectroscopic studies of novel photochromic benzodithiacrown ethers and their complexes. Journal of the Chemical Society, Perkin Transactions 2(2):1441–1447, 1996.

[86] I. Leray, J.-P. Lefevre, J.-F. Delouis, J. Delaire, and B. Valeur. Synthesis and photophysical and cation-binding properties of mono- and tetranaphthylcalix[4]arenes as highly sensitive and selective fluorescent sensors for sodium. Chemistry-A European Journal, 7(21):4590–4598, 2001.

[87] X. Peng, J. Du, F. Fan, J. Wang, Y. Wu, J. Zhao, S. Sun, and T. Xu. A selective fluorescent sensor for imaging cd^{2+} in living cells. Journal of the American Chemical Society, 129:1500–1501, 2007.

[88] H. Zhang and D.M. Rudkevich. A fret approach to phosgene detection. Chemical Communications, (12):1238–1239, 2007.

[89] H.J. Kim, S.Y. Park, S. Yoon, and J.S. Kim. Fret-derived ratiometric fluorescence sensor for cu^{2+}. Tetrahedron, 64(7):1294–1300, 2008.

[90] J.A. Sclafani, M.T. Maranto, T.M. Sisk, and S.A. Van Arman. An aqueous ratiometric fluorescence probe for zn(ii). Tetrahedron Letters, 37(13):2193–2196, 1996.

[91] B. Bodenant and F. Fages. Synthesis, metal binding, and fluorescence studies of a pyrene-tethered hydroxamic acid ligand. Tetrahedron Letters, 36(9):1451–1454, 1995.

[92] Y. Shiraishi, K. Ishizumi, G. Nishimura, and T. Hirai. Effects of metal cation coordination on fluorescence properties of a diethylenetriamine bearing two end pyrene fragments. The Journal of Physical Chemistry B, 111:8812–8822, 2007.

[93] M.C. Neuman and A.W. McIntosh. Metal Ecotoxicity, Concepts and Applications. Lewis Publishers, Chelsea, MI, 1991.

[94] G.R. Boyd, N.K. Tarbet, G. Kirmeyer, B.M. Murphy, R.F. Serpente, and M. Zammit. Selecting lead pipe rehabilitation and replacement technologies. Journal of the American Water Works Association, 93(7):74–87, 2001.

[95] P. Jackson, T. van den Hoven, I. Wagner, and P. Leroy. The financial and economic implications of a change of the mac for lead. European Commission Report, 1995.

[96] World Health Organization. Guidelines for drinking water quality, 2nd edition., volume 2. Recommendations, World Health Organization, Geneva, 1996.

[97] World Health Organization. Guidelines for drinking water quality, 3rd edition., volume 1. Recommendations, World Health Organization, Geneva, 2004.

[98] E. Destandau, J.P. Lefevre, A.C.F. Eddine, S. Desportes, M.C. Jullien, R. Hierle, I. Leray, B. Valeur, and J.A. Delaire. A novel microfluidic flow-injection analysis device with fluorescence detection for cation sensing. application to potassium. Analytical and Bioanalytical Chemistry, 387(8):2627–2632, 2007.

[99] C.R.T. Tarley, A.F. Barbosa, M.G. Segatelli, E.C. Figueiredo, and P.O. Lucas. Highly improvedsensitivity of ts-ff-aas for cd(ii) determination at ng l.1 levels using a simple flow injection minicolumn preconcentration system with multiwall carbon nanotubes. Journal of Analytical Atomic Spectrometry, 21:1305–1313, 2006.

[100] N. Pourreza and H. Barisami. Solid phase extraction of zn as xylenol orangecomplex on naphthalene adsorbent and its determination by flame atomic absorption spectrometry. Chemia Analityczna, 52:597–604, 2007.

[101] W. Guo, W. Liu, S. Jin, S. Hu, H. Zhang, and Y. Peng. Determination of trace pb in environmental samples by gf-aas after microsphere phase separation extraction. Bioinformatics and Biomedical Engineering, The 2nd International Conference(16-18):4504–4507, May 2008.

[102] M.T. Naseri, M.R.M. Hosseini, Y. Assadi, and A. Kiani. Rapid determination of lead in water samples by dispersive liquid-liquid microextraction coupled with electrothermal atomic absorption spectrometry. Journal of Hazardous Materials, 75(1):56–62, 2008.

[103] M. Satyanarayanan, V. Balaram, T.G. Rao, B. Dasaram, S.L. Ramesh, R. Mathur, and R.K. Drolia. Determination of trace metals in seawater by icp-ms after preconcentration and matrix separation by dithiocarbamate complexes. Indian Journal of Marine Sciences, 36:71–75, 2007.

[104] S.C. Jacobson, A.W. Moore, and J.M. Ramsey. Fused quartz substrates for microchip electrophoresis. Analytical Chemistry, 67:2059–2063, 1995.

[105] In-H. Chang, J.J. Tulock, J. Liu, W-S Kim, D.M. Cannon, JR., Y. Lu, P.W. Bohn, J.V. Sweedler, and D.M. Cropek. A modular microfluidic architecture for integrated biochemical analysis. Environmental Science and Technology, 39:3756–3761, 2005.

[106] K.A. Shalkh, K.S. Ryu, E.D. Goluch, J.M. Nam, J. Liu, C.S. Thaxton, T.N. Chiesl, A.E. Barron, Y. Lu, C.A. Mirkin, and C. Liu. A modular microfluidic architecture for integrated biochemical analysis. Proceedings of the National Academy of Sciences, 102(28):9745–9750, 2005.

[107] X.S Zhu, C. Gao, J.W. Choi, P.L. Bishop, and C.H. Ahn. On-chip generated mercury microelectrode for heavy metal ion detection. Lab on a Chip, 5:212–217, 2005.

[108] BKH Consulting Engineers, TNO Nutrition, and Food Research. Towards the establishment of a priority list of substances for further evaluation of their role in endocrine disruption. Final report of European Commission DG Environment, 21 June:1–35, 2000.

[109] D.P. Grover, Z.L. Zhang, J.W. Readman, and J.L. Zhou. A comparison of three analytical techniques for the measurement of steroidal estrogens in environmental water samples. Talanta, 78(3):1204–1210, 2009.

[110] C. Bicchi, T. Schilir, C. Pignata, E. Fea, C. Cordero, F. Canale, and G. Gilli. Analysis of environmental endocrine disrupting chemicals using the e-screen method and stir bar sorptive extraction in wastewater treatment plant effluents. Science of the total environment, 407(6):1842–1851, 2009.

[111] A. Hibberd, K. Maskaoui, Z. Zhang, and J.L. Zhou. An improved method for the simultaneous analysis of phenolic and steroidal estrogens in water and sediment. Talanta, 77(4):1315–1321, 2009.

[112] J. Zhao, G. Ying, L. Wang, J. Yang, X. Yang, L. Yang, and X. Li. Determination of phenolic endocrine disrupting chemicals and acidic pharmaceuticals in surface water of the pearl rivers in south china by gas chromatography-negative chemical ionizationĺcmass spectrometry. Science of the total environment, 407(2):962–974, 2009.

[113] A. Manz, D.J. Harrison, E.M.J. Verpoorte, J.C. Fettinger, H. Ludi, and H.M. Widmer. Planar chips technology for miniaturization and integration of separation techniques into monitoring systems: Capillary electrophoresis on a chip. Journal of Chromatography, 593:253–258, 1991.

[114] S.S. Bozkurt, S. Ayata, and I. Kaynak. Fluorescence-based sensor for pb(ii) using tetra-(3-bromo-4-hydroxyphenyl)porphyrin in liquid and immobilized medium. Spectrochimica Acta Part A, 72:880–883, 2009.

[115] L. Ma, Y. Li, Y. Wu, R. Buchet, and Y. Ding. Clarification of the binding model of lead(ii) with a highly sensitive and selective fluoroionophore sensor by spectroscopic and structural study. Spectrochimica Acta Part A, 72(2):306–311, 2009.

[116] L. Guo, S. Hong, X. Lin, Z. Xie, and G. Chen. An organically modified solĺcgel membrane for detection of lead ion by using 2-hydroxy-1-naphthaldehydene-8-aminoquinoline as fluorescence probe. Sensors and Actuators B, 130(2):789–794, 2008.

[117] S. Saito, N. Danzaka, and S. Hoshi. Direct fluorescence detection of pb^{2+} and cd^{2+} by high-performance liquid chromatography using 1-(4-aminobenzyl)ethylenediamine-n,n,n',n'-tetraacetate as a pre-column derivatizing agent. Journal of Chromatography A, 1104:140–144, 2006.

[118] R. Métivier, I. Leray, and B. Valeur. A highly sensitive and selective fluorescent molecular sensor for pb(ii) based on a calix[4]arene bearing four dansyl groups. Chemical Communications, pages 996–997, 2003.

[119] E. Prichard, G.M. MacKay, and J. Points. Trace Analysis: A Structured Approach to Obtaining Reliable Results. Royal Society of Chemistry, Cambridge, 1996.

[120] S.J. Harswell. Atomic Absorbance Spectrophotometry. Theory, Design and Applications. Elsevier, Amsterdam, 1990.

[121] E.L. Silva and S. Roldan Pdos. Simultaneous flow injection preconcentration of lead and cadmium using cloud point extraction and determination by atomic absorption spectrometry. Journal of Hazardous Materials, 161:142–147, 2009.

[122] U. Divrikli, A.A. Kartal, M. Soylak, and L. Elci. Preconcentration of pb(ii), cr(iii), cu(ii), ni(ii) and cd(ii) ions in environmental samples by membrane filtration prior to their flame atomic absorption spectrometric determinations. Journal of Hazardous Materials, 145:459–464, 2007.

[123] Q.F. Hu, G.Y. Yang, Y.Y. Zhao, and J.Y. Yin. Determination of copper, nickel, cobalt, silver, lead, cadmium and mercury ions in water by solid phase extraction and the rp-hplc with uv-vis detection. Analytical and Bioanalytical Chemistry, 375:831–835, 2003.

[124] G.Y. Yang, W.B. Fen, C. Lei, W.L. Xiao, and H.D Sun. Study on solid phase extraction and graphite furnace atomic absorption spectrometry for the determination of nickel, silver, cobalt, copper, cadmium and lead with mci gel chp 20y as sorbent. Journal of Hazardous Materials, 162(1):44–49, 2009.

[125] H. Parham, N. Pourreza, and N. Rahbar. Solid phase extraction of lead and cadmium using solid sulfur as a new metal extractor prior to determination by flame atomic absorption spectrometry. Journal of Hazardous Materials, 163:588–592, 2009.

[126] F. Raoufia, Y. Yaminib, H. Sharghic, and M. Shamsipurd. Solid-phase extraction and determination of trace amounts of lead(ii) using octadecyl silica membrane disks modified with a recently synthesized anthraquinone derivative and atomic absorption spectrometry. Microchemical Journal, 63(2):311–316, 1999.

[127] G.Z. Tsogas, D.L. Giokas, and A.G. Vlessidis. Graphite furnace and hydride generation atomic absorption spectrometric determination of cadmium, lead, and tin traces in natural surface waters: Study of preconcentration technique performance. Journal of Hazardous Materials, 163:988–994, 2009.

[128] C.F. Poole, A.D. Gunatilleka, and R. Sethuraman. Contributions of theory to method development in solid-phase extraction. Journal of Chromatography A, 885:17–39, 2000.

[129] R. Métivier. Ingénierie moléculaire et fluorescence: détection de cations lourds et étude de surfaces d'alumines. ENS CACHAN dissertation, 2003.

[130] O.R. Hashemi, M.R. Kargar, F. Raoufi, A. Moghimi, H. Aghabozorg, and M.R. Ganjali. Separation and preconcentration of trace amounts of lead on octadecyl silica membrane disks modified with a new s-containing schiff's base and its determination by flame atomic absorption spectrometry. Microchemical Journal, 69(1):1–6, 2001.

[131] R. Saxena, A.K. Singh, and D.P.S Rathore. Salicylic acid functionalized polystyrene sorbent amberlite xad-2. synthesis and applications as a preconcentrator in the determination of zinc(ii) and lead(ii) by using atomic absorption spectrometry. Analyst, 120:403–405, 1995.

[132] P.K. Tewari and A.K. Singh. Preconcentration of lead with amberlite xad-2 and amberlite xad-7 based chelating resins for its determination by flame atomic absorption spectrometry. Talanta, 56(4):735–744, 2002.

[133] G. Klein, D. Kaufmann, S. Schürch, and J.-L. Reymond. A fluorescent metal sensor based on macrocyclic chelation. Chemical Communications, 24:561–562, 2001.

[134] P. Domachuk, H.C. Nguyen, B.J. Eggleton, M. Straub, and M. Gu. Microfluidic tunable photonic band-gap device. Applied Physics Letters, 84:1838–1840, 2004.

[135] J.C. Galas, J. Torres, M. Belotti, Q. Kou, and Y. Chen. Microfluidic tunable dye laser with integrated mixer and ring resonator. Applied Physics Letters, 86:264101, 2005.

[136] K.B. Mogensen, Y.C. Kwok, J.C.T. Eijkel, N.J. Petersen, A. Manz, and J.P. Kutter. A microfluidic device with an integrated waveguide beam splitter for velocity measurements of flowing particles by fourier transformation. Analytical Chemistry, 75(18):4931–4936, 2003.

[137] K.W. Ro, K. Lim, B.C. Shim, and J.H. Hahn. Integrated light collimating system for extended optical-path-length absorbance detection in microchip-based capillary electrophoresis. Analytical Chemistry, 77:5160–5166, 2005.

[138] D. Yin, D.W. Deamer, H. Schmidt, J.P. Barber, and A. Hawkins. Single-molecule detection sensitivity using planar integrated optics on a chip. Optics Letters, 31:2136–2138, 2006.

[139] A. Ksendzov and Y. Lin. Integrated optics ring resonator sensors for protein detection. Optics Letters, 30:3344–3346, 2005.

[140] R.A. Potyrailo, S.E. Hobbs, and G.M. Hieftje. Optical waveguide sensors in analytical chemistry: Today's instrumentation, applications and trends for future development. Fresenius' Journal of Analytical Chemistry, 362:349–373, 1998.

[141] E. Krioukov, D.J.W. Klunder, A. Driessen, J. Greve, and C. Otto. Integrated optical microcavities for enhanced evanescent-wave spectroscopy. Optics Letters, 27(17):1504–1506, 2002.

[142] E. Krioukov, J. Greve, and C. Otto. Performance of integrated optical microcavities for refractive index and fluorescence sensing. Sensors and Actuators B, 90:58–67, 2003.

[143] C. Monat, P. Domachuk, and B.J. Eggleton. Integrated optofluidics: A new river of light. Nature Photonics, 1:106–114, 2007.

[144] A.M. Armani and K.J. Vahala. Heavy water detection using ultra high q microcavities. Optics Letters, 31:1896–1898, 2006.

[145] E. Krioukov, D.J.W. Klunder, A. Driessen, J. Greve, and C. Otto. Sensor based on an integrated optical microcavity. Optics Letters, 27:512–514, 2002.

[146] C.Y. Chao, W. Fung, and L.J. Guo. Polymer microring resonators for biochemical sensing applications. IEEE Journal of Selected Topics in Quantum Electronics, 12:134–142, 2006.

[147] C.Y. Chao and L.J. Guo. Biochemical sensors based on polymer microrings with sharp asymmetrical resonance. Applied Physics Letters, 83(8):1527–1529, 2003.

[148] Q. Xu, B. Schmidt, S. Pradhan, and M. Lipson. Micrometre-scale silicon electro-optic modulator. Nature, 435:325–327, 2005.

[149] M. Lebental, J. S. Lauret, R. Hierle, and J. Zyss. Highly directional stadium-shaped polymer microlasers. Applied Physics Letters, 88:031108.1–031108.3, 2006.

[150] M. Lebental, N. Djellali, C. Arnaud, J.S. Lauret, and J. Zyss. Inferring periodic orbits from spectra of simply shaped microlasers. Physical Review A, 76(2):023830, 2007.

[151] F. Vollmer and S. Arnold. Whispering-gallery-mode biosensing: label-free detection down to single molecules. Nature Methods, 5(7):591–596, 2008.

[152] F.P. Schafer. Dye lasers: topics in applied physics 1. Springer, 3rd edn.:Heidelberg, 1990.

[153] Jr TF Johnston. Tunable dye lasers, encyclopedia of physical science and technology. Academic, New York, 14:96–141, 1987.

[154] F.S. Bates and G.H. Gredrickson. Block copolymers - designer soft materials. Physics Today, 52:32–38, 1999.

[155] S. Forster and T. Plantenberg. From self-organizing polymers to nanohybrid and biomaterials. Angewandte Chemie International Edition, 41(5):688–714, 2002.

[156] R. Segalman, A. Hexemer, R. Hayward, and E. Kramer. Ordering and melting of block copolymer spherical domains in 2 and 3 dimensions. Macromolecules, 36(9):3272–3288, 2003.

[157] M.F. Schulz, A.K. Khandpur, and F.S. Bates. Phase behavior of polystyrene-poly(2-vinylpyridine) diblock copolymers. Macromolecules, 29(8):2857–2867, 1996.

[158] A. Sidorenko, I. Tokarev, S. Minko, and M. Stamm. Ordered reactive nanomembranes/ nanotemplates from thin films of block copolymer supramolecular assembly. Journal of the American Chemical Society, 125:12211–12216, 2003.

[159] C.D. Liang, K.L. Hong, G.A. Guiochon, J.W. Mays, and S. Dai. Synthesis of a large-scale highly ordered porous carbon film by self-assembly of block copolymers. Angewandte Chemie International Edition, 43(43):5785–5789, 2004.

[160] R. Saito, S. Okamura, and K. Ishizu. Introduction of colloidal silver into a poly(2-vinyl pyridine) microdomain of microphase separated poly(styrene-b-2-vinyl pyridine) film. Polymer, 33(5):1099–1101, 1992.

[161] K.W. Cheng and W.K. Chan. Morphology of rhenium complex-containing polystyrene-block-poly(4-vinylpyridine) and its use as self-assembly templates for nanoparticles. Langmuir, 21(12):5247–5250, 2005.

[162] D. Yin, S. Horiuchi, and T. Masuoka. Lateral assembly of metal nanoparticles directed by nanodomain control in block copolymer thin films. Chemistry of materials, 17(3):463–469, 2005.

[163] E. Verpoorte. Microfluidic chips for clinical and forensic analysis. Electrophoesis, 23:677–712, 2002.

[164] D.R. Reyes, D. Iossifidis, P.A. Auroux, and A. Manz. Micro total analysis systems. 1. introduction, theory, and technology. Analytical Chemistry, 74(12):2623–2636, 2002.

[165] D. Jed Harrison, K. Fluri, K. Seiler, Z. Fan, C.S. Effenhauser, and A. Manz. Micromachining a miniaturized capillary electrophoresis-based chemical analysis system on a chip. Science, 261:895–897, 1993.

[166] A.T. Woolley, K. Lao, A.N. Glazer, and R.A. Mathies. Capillary electrophoresis chips with integrated electrochemical detection. Analytical Chemistry, 70(4):684–688, 1998.

[167] W.R. Vandaveer IV, S.A. Pasas-Farmer, D.J. Fischer, C.N. Frankenfeld, and S.M. Lunte. Recent developments in electrochemical detection for microchip capillary electrophoresis. Electrophoresis, 25:3528–3549, 2004.

[168] P.A. Auroux, D.R. Reyes, D. Iossifidis, and A. Manz. Micro total analysis systems. 2. analytical standard operations and applications. Analytical Chemistry, 74(12):2637–2652, 2002.

[169] A. Kitahara and A. Watanabe(Eds). Electrical Phenomena at Interfaces. Marcel Dekker, 1984.

[170] J. Gaudioso and H.G. Craighead. Characterizing electroosmotic flow in microfluidic devices. Journal of Chromatography A, 971:249–253, 2002.

[171] D.R. Baker. Capillary Electrophoresis. Wiley, 1995.

[172] R.J. Linhardt and T. Toida. Ultra-high resolution separation comes of age. SCIENCE, 298:1441–1442, 2002.

[173] S. Terabe, K. Otsuka, K. Ichikawa, A. Tsuchiya, and T. Ando. Electrokinetic separations with micellar solutions and open-tubular capillaries. Analytical Chemistry, 56:111–113, 1984.

[174] U. Pyell. Fresenius' Journal of Analytical Chemistry, 371:691–703, 2001.

[175] Y. Allen, A.P. Scott, P. Matthiessen, S. Haworth, J.E. Thain, and S. Feist. Survey of estrogenic activity in united kingdom estuarine and coastal waters and its effects on gonadal development of the flounder platichthys flesus. Environmental Toxicology and Chemistry, 18:1791–1800, 1999.

[176] G.W. Aherne and R.J. Briggs. The relevance of the presence of certain synthetic steroids in the aquatic environment. Journal of Pharmacy and Pharmacology, 41:735–736, 1989.

[177] T. Colborn, F.S.V. Saal, and A.M. Soto. Developmental effects of endocrine-disrupting chemicals in wildlife and humans. Environmental Health Perspectives, 101(5):378–384, 1993.

[178] G.A. Fox. Effects of endocrine disrupting chemicals on wildlife in canada: Past, present and future. Water Quality Research Journal of Canada, 36:233–251, 2001.

[179] S. Jobling, D. Sheahan, J.A. Osborne, P. Matthiessen, and J.P. Sumpter. Inhibition of testicular growth in rainbow trout (oncorhynchus mykiss) exposed to estrogenic alkylphenolic chemicals. Environmental Toxicology and Chemistry, 15:194–202, 1996.

[180] C.E. Purdom, P.A. Hardima, V.J. Bye, N.C. Eno, C.R. Tyler, and J.P. Sumpter. Estrogenic effects of effluents from sewage-treatment works. Chemistry and Ecology, 8:275–285, 1994.

[181] T.B. Hayes, A. Collins, M. Lee, M. Mendoza, N. Noriega, A.A. Stuart, and A. Vonk. Hermaphroditic, demasculinized frogs after exposure to the herbicide atrazine at low ecologically relevant doses. Proceedings of the National Academy of Sciences, 99:5476–5480, 2002.

[182] L.J. Guillette, T.S. Gross, G.R. Masson, J.M. Matter, H.F. Percival, and A.R. Woodward. Developmental abnormalities of the gonad and abnormal sex hormone concentrations in juvenile alligators from contaminated and control lakes in florida. Environmental Health Perspectives, 102:680–688, 1994.

[183] S.N. Wiemeyer, T.G. Lamont, C.M. Bunk, C.R. Sindelar, F.J. Gramlich, and J.D. Frasherand M.A. Byrd. Organochlorine pesticide, polychlorobiphenyl, and mercury residues in bald eagle eggs–1969-79–and their relationships to shell thinning and reproduction. Archives of Environmental Contamination and Toxicology, 13(5):529–549, 1984.

[184] D.M. Fry and C.K. Toone. Ddt-induced feminization of gull embryos. Science, 213:922–924, 1981.

[185] E.K.Sheiner, E. Sheiner, R.D. Hammel, G. Potashnik, and R. Carel. Effect of occupational exposures on male fertility. Industrial Health, 41:55–62, 2003.

[186] P.S. Guzelian. Comparative toxicology of chlordecone (kepone) in humans and experimental animals. Annual Review of Pharmacology and Toxicology, 22:89–113, 1982.

[187] R.M. Sharpe and N.E. Skakkebaek. Are oestrogens involved in falling sperm counts and disorders of the male reproductive tract? The Lancet, 341(8857):1392–1395, 1993.

[188] S.H. Safe. Is there an association between exposure to environmental estrogens and breast cancer? Environmental Health Perspectives Supplements, 105:675–677, 1997.

[189] A. Giwercman, E. Carlsen, N. Keiding, and N.E. Skakkebaek. Evidence for increasing incidence of abnormalities of the human testis: a review. Environmental Health Perspectives Supplements, 101:65–71, 1993.

[190] E. Carlsen, A. Giwercman, N. Keiding, and N.E. Skakkebaek. Evidence for decreasing quality of semen during past 50 years. British Medical Journal, 305(6854):609–613, 1992.

[191] C.H. Groshart and P.C. Okkerman. Toward the establishment of a priority list of substances for further evaluation of their role in endocrine disruption: Preparation of a candidate list of substances as a basis for priority setting. final report. European Commission DG Environment, June 2000.

[192] B. Thiele, K. Gunther, and M.J. Schwuger. Alkylphenol ethoxylates: Trace analysis and environmental behavior. Chemical Reviews, 97(8):3247–3272, 1997.

[193] T. Zacharewski. In vitro bioassays for assessing estrogenic substances. Environmental Science and Technology, 31:613–623, 1997.

[194] S.F. Arnold, M.K. Robinson, P.M. Collins, P.M. Vonier, L.J. Guilette, and J.A. McLachlan. A yeast estrogen screen for examining the relative exposure of cells to natural and xenoestrogens. Environmental Health Perspectives, 104:544–548, 1996.

[195] S. Jobling, T. Reynolds, R. White, M.G. Parker, and J.P. Sumpter. A variety of environmentally persistent chemicals, including some phthalate plasticizers, are weakly estrogenic. Environmental Health Perspectives, 103:582–587, 1995.

[196] S. Jobling and J.P. Sumpter. Detergent components in sewage effluent are weakly oestrogenic to fish: An in vitro study using rainbow trout (oncorhynchus mykiss) hepatocytes. Aquatic Toxicology, 27:361–372, 1993.

[197] M. Nasu, M. Goto, H. Kato, Y. Oshima, and H. Tanaka. Study on endocrine disrupting chemicals in wastewater treatment plants. Water Science and Technology, 43(2):101–108, 2001.

[198] K. Fujii, S. Kikuchi, M. Satomi, N. Ushio-Sata, and N. Morita. Degradation of 17β-estradiol by a gram-negative bacterium isolated from activated sludge in a sewage treatment plant in tokyo, japan. Applied and Environmental Microbiology, 68:2057–2060, 2002.

[199] H.B. Lee and D Liu. Degradation of 17β-estradiol and its metabolites by sewage bacteria. Water, Air, and Soil Pollution, 134:353–368, 2002.

[200] H. Tanaka, Y. Yakou, A. Takahashi, T. Higashitani, and K. Komori. Comparison between estrogenicities estimated from dna recombinant yeast assay and from chemical analyses of endocrine disruptors during sewage treatment. Water Science and Technology, 43(2):125–132, 2001.

[201] C. Planas, J.M. Guadayol, M. Droguet, A. Escalas, J. Rivera, and J. Caixach. Degradation of polyethoxylated nonylphenols in a sewage treatment plant. quantitative analysis by isotopic dilution-hrgc/ms. Water Research, 36:982–988, 2002.

[202] N. Garcia-Reyero, E. Grau, M. Castillo, M.J.L. Dealda, D. Barcelo, and B. Pina. Monitoring of endocrine disruptors in surface waters by the yeast recombinant assay. Environmental Toxicology and Chemistry, 20:1152–1158, 2001.

[203] M. Ahel and W. Giger. Determination of alkylphenols and alkylphenol mono- and diethoxylates in environmental samples by high-performance liquid chromatography. Analytical Chemistry, 57:1577–1583, 1985.

[204] W. Giger, E. Stephanou, and C. Schaffner. Persistent organic chemicals in sewage effluents: I. identifications of nonylphenols and nonylphenolethoxylates by glass capillary gas chromatography / mass spectrometry. Chemosphere, 10:1253–1263, 1981.

[205] A.D. Corcia, R. Samperi, and A. Marcomini. Monitoring aromatic surfactants and their biodegradation intermediates in raw and treated sewages by solid-phase extraction and liquid chromatography. Environmental Science and Technology, 28:850–858, 1994.

[206] S. Chiron, E. Sauvard, and R. Jeannot. Determination of nonionic polyethoxylate surfactants in wastewater and sludge samples of sewage treatment plants by liquid chromatography-mass spectrometry. Analusis, 28:535–542, 2000.

[207] A.A. Boyd-Boland and J.B. Pawliszyn. Solid-phase microextraction coupled with high-performance liquid chromatography for the determination of alkylphenol ethoxylate surfactants in water. Analytical Chemistry, 68:1521–1529, 1996.

[208] P.L. Ferguson, C.R. Iden, A.E. McElroy, and B.J. Brownawell. Determination of steroid estrogens in wastewater by immunoaffinity extraction coupled with hplc-electrospray-ms. Analytical Chemistry, 73:3890–3895, 2001.

[209] A. Marcomini, F. Filipuzzi, and W. Giger. Aromatic surfactants in laundry detergents and hard-surface cleaners: Linear alkylbenzenesulphonates and alkylphenol polyethoxylates. Chemosphere, 17(5):853–863, 1988.

[210] M.A. Blackburn, S.J. Kirby, and M.J. Waldock. Concentrations of alkyphenol polyethoxylates entering uk estuaries. Marine Pollutution Bulletin, 38(2):109–118, 1999.

[211] H. Sabik S. Cathum. Determination of steroids and coprostanol in surface water, effluent and mussel using gas chromatography-mass spectrometry. Chromatographia, 53:S394–S399, 2001.

[212] H. Sabik S. Cathum. Simultaneous determination of alkylphenol polyethoxylate surfactants and their degradation products in water, effluent and mussel using gas chromatography-mass spectrometry. Chromatographia, 53:S400–S405, 2001.

[213] W. Ding and J. Fann. Application of pressurized liquid extraction followed by gas chromatographyĺcmass spectrometry to determine 4-nonylphenols in sediments. Journal of Chromatography A, 866:79–85, 2000.

[214] H.B. Lee and T.E. Peart. Determination of 4-nonylphenol in effluent and sludge from sewage treatment plants. Analytical Chemistry, 34:1976–1980, 1995.

[215] A.P. Scott, R.M. Inbaraj, and E.L.M. Vermeirssen. A. p. scott, r. m. inbaraj and e. l. m. vermeirssen, use of a radioimmunoassay which detects c21pleuronectes platessa. General and Comparative Endocrinology, 105:62–70, 1997.

[216] J.H. Willman, T.B. Martins, T.D. Jaskowski, H.R. Hill, and C.M. Litwin. Heterophile antibodies to bovine and caprine proteins causing false-positive human immunodeficiency virus type 1 and other enzyme-linked immunosorbent assay results. Clinical and Diagnostic Laboratory Immunology, 6(4):615–616, 1999.

[217] E.J. Routledge, D. Sheahan, C. Desbrow, G.C. Brighty, M. Waldock, and J.P. Sumpter. Identification of estrogenic chemicals in stw effluent. 2. in vivo responses in trout and roach. Environmental Science and Technology, 32:1559–1565, 1998.

[218] C. Desbrow, E.J. Routledge, G.C Brighty, J.P. Sumpter, and M. Waldock. Identification of estrogenic chemicals in stw effluent. 1. chemical fractionation and in vitro biological screening. Environmental Science and Technology, 32:1549–1558, 1998.

[219] M.J. Lopez de Alda and D Barcelo. Determination of steroid sex hormones and related synthetic compounds considered as endocrine disrupters in water by liquid chromatography-diode array detectionĺcmass spectrometry. Journal of Chromatography A, 892:391–406, 2000.

[220] L.B. Clark, R.T. Rosen, T.G. Hartman, J.B. Louis, I.H. Suffet, R.L. Lippincott, and J.D. Rosen. Determination of alkylphenol ethoxylates and their acetic acid derivatives in drinking water by particle beam liquid chromatography/mass spectrometry. International Journal of Environmental Analytical Chemistry, 47:167–180, 1992.

[221] S.N. Pedersen and C. Lindhost. Quantification of the xenoestrogens 4-tert.-octylphenol and bisphenol a in water and in fish tissue based on microwave assisted extraction, solid-phase extraction and liquid chromatography-mass spectrometry. Journal of Chromatography A, 864:17–24, 1999.

[222] K. Otsuka, M. Higashimori, R. Koike, K. Karuhaka, Y. Okada, and S. Terabe. Separation of lipophilic compounds by micellar electrokinetic chromatography with organic modifiers. Electrophoresis, 15:1280–1283, 1994.

[223] P.L. Desbene and C.M. Rony. Determination by high-performance capillary electrophoresis of alkylaromatics used as based of sulfonation in the preparation of industrial surfactants. Journal of Chromatography A, 689:107–121, 1995.

[224] C. Mardones, A. Rios, and M. Valcarcel. Determination of chlorophenols in human urine based on the integration of on-line automated clean-up and preconcentration unit with micellar electrokinetic chromatography. Electrophoresis, 20:2922–2929, 1999.

[225] G. Janini, G. Muschik, and H. Issaq. Electrokinetic chromatography in suppressed electroosmotic flow environment: Use of a charged cyclodextrin for the separation of enantiomers and geometric isomers. Electrophoresis, 17:1575–1583, 1996.

[226] F. Regan, A. Moran, B. Fogarty, and E. Dempsey. Development of comparative methods using gas chromatography-mass spectrometry and capillary electrophoresis for determination of endocrine disrupting chemicals in bio-solids. Journal of Chromatography B, 770:243–253, 2002.

[227] Q.C. Chu, M Lin, C.H. Geng, and J.N. Ye. Determination of uric acid in human saliva and urine using miniaturized capillary electrophoresis with amperometric detection. Chromatographia, 65:179–184, 2007.

[228] A. Lagana, A. Bacaloni, I.D. Leva, A. Faberi, G. Fago, and A. Marino. Analytical methodologies for determining the occurrence of endocrine disrupting chemicals in sewage treatment plants and natural waters. Analytica Chimica Acta, 501:79–88, 2004.

[229] M Katayama, Y Matsuda, and T Sasaki. Determination of bisphenol a and 10 alkylphenols in serum using sds micelle capillary electrophoresis with γ-cyclodextrin. Biomedical Chromatography, 15:437–442, 2001.

[230] S.L. Tao, K. Popat, and T.A. Desai. Off-wafer fabrication and surface modification of asymmetric 3d su-8 microparticles. Nature Protocols, 1(6):3153–3158, 2006.

[231] C.H. Lin, G.B. Lee, L.M. Fu, and S.H. Chen. Integrated optical-fiber capillary electrophoresis microchips with novel spin-on-glass surface modification. Biosencors and Bioelectronics, 20:83–90, 2004.

[232] H. Gampp, M. Maeder, C.J. Meyer, and A.D. Zuberbuhler. Calculation of equilibrium constants from multiwavelength spectroscopic data - i.mathematical considerations. Talanta, 32:95–1014, 1985.

[233] H. Gampp, M. Maeder, C.J. Meyer, and A.D. Zuberbuhler. Calculation of equilibrium constants from multiwavelength spectroscopic data - ii. specfit: Two user-friendly programs in basic and standard fortran 77. Talanta, 32:257–264, 1985.

[234] J. Buffle and M.L. Tercier-Waeber. Voltammetric environmental trace-metal analysis and speciation: from laboratory to $in\ situ$ measurements. Trends in Analytical Chemistry, 24(3):172–191, 2005.

[235] C.T. NGUYEN. Polymer-based Photonic Devices for Optical Telecoms. Course of Master Erasmus Mundus MONABIPHOT, 2008.

List of Tables

List of Figures